



TECHNISCHE
UNIVERSITÄT
WIEN

Vienna University of Technology

DISSERTATION

Local reaction kinetics of CO oxidation on heterogeneous Platinum, Palladium and Palladium oxide surfaces

ausgeführt zum Zwecke der Erlangung des akademischen Grades eines
Doktors der Naturwissenschaften unter der Leitung von

Univ.Prof. Mag.rer.nat. Dr.rer.nat. Günther Rupprechter

Assoc.Prof. Dipl.-Phys. Dr.rer.nat. Yuri Suchorski

Institut für Materialchemie (E165)

eingereicht an der Technischen Universität Wien

Fakultät für Technische Chemie

von

Dipl.-Phys. Diana Vogel

Matrikelnummer 0828534

Rueppgasse 27/15

1020 Wien

Wien, den 17.09.2012

KURZFASSUNG

Das Ziel der vorliegenden Dissertation war es, die Reaktionskinetik der CO-Oxidationsreaktion ortsaufgelöst auf heterogenen Platin, Palladium und Palladiumoxid Oberflächen unter Hochvakuumbedingungen zu untersuchen. Zu diesem Zweck wurde neben der konventionellen (über die Probemittelnden) Massenspektroskopie (MS) eine ortsaufauflösende Methode, die Photoelektronenemissionsmikroskopie (PEEM), verwendet, um die katalytische CO-Oxidationsreaktion lokal und *in situ* auf polykristalline Pt- und Pd-Folien sowie auf "Aluminiumoxid geträgeres" Pd und PdO Pulver zu untersuchen.

Durch die Kombination von MS und PEEM ist es möglich, die globale und lokale Reaktionskinetik der CO-Oxidationsreaktion im Bereich der Bistabilität gleichzeitig für die gesamte Pt- bzw. Pd-Folie sowie für einzelne μm -große kristalline Körner unterschiedlicher (hkl) Orientierung auf den polykristallinen Folien zu verfolgen. Mit MS wurde die globale, von allen Körnern der Folie produzierte, CO_2 Rate aufgenommen und die kinetischen Übergänge zwischen den stationären Zuständen hoher und niedriger katalytischer Aktivität wurden bestimmt. Sowohl für die Pt- als auch die Pd-Folie wurden diese globalen kinetischen Übergänge in einem *globalen kinetischen Phasendiagramm* zusammengefasst. Solch ein kinetisches Phasendiagramm gibt die Reaktivitätszustände eines katalytischen Systems im (p, T) -Parameterraum effektiv wieder, so dass ein direkter Vergleich unterschiedlicher Systeme möglich ist.

Parallel zu den mit MS durchgeführten globalen kinetischen Messungen wurde die Reaktion mit PEEM auf den einzelnen Körnern (Domänen) der Pt- bzw. Pd-Folie *in situ* verfolgt. Ein wichtiges Ergebnis dieser PEEM-Messungen war, dass die individuellen, unterschiedlich orientierten (hkl) Domänen auf Pt- bzw. Pd-Folie sich unabhängig voneinander und den entsprechenden Einkristallen analog verhalten. Dies spiegelte sich zum Beispiel darin wieder, dass die Reaktionsdiffusionsfronten innerhalb der Konrgrenzen eingeschränkt waren. Die Unabhängigkeit des Reaktionsverhaltens der einzelnen Domänen bietet daher die einzigartige Möglichkeit, die Reaktionseigenschaften verschiedener Orientierungen mit PEEM *in situ* und unter exakt denselben Bedingungen zu vergleichen.

Die Idee, lokale Reaktionskinetik mit Hilfe von PEEM zu bestimmen, beruht darauf, dass die lokale Photoemissionsintensität über die lokale Austrittsarbeit direkt von der lokalen CO- bzw. Sauerstoffbedeckung abhängt. Diese wiederum bestimmt die Bildungsrate von CO_2 , so dass die lokale PEEM-Bildintensität die lokale Reaktionsrate widerspiegelt. Auf diese Weise können mit Hilfe von Intensitätsanalyse der video-PEEM Daten die lokalen kinetischen Phasenübergänge und damit die *lokalen kinetischen Phasendiagramme* für unterschiedlich orientierte Domänen polykristalliner Proben erhalten werden. Dies wurde für [111]-, [100]- und [100]-orientierte Pt- und Pd-Domänen durchgeführt. Die Orientierung dieser Domänen wurde zuvor für beide Proben mit EBSD (electron

backscatter diffraction) bestimmt. Es wurde gezeigt, dass das lokale Reaktionsverhalten der einzelnen Domänen untereinander sich deutlich unterscheidet: so nimmt die Reaktivität der einzelnen Domänen sowohl für Pt- als auch Pd-Folie mit abnehmender atomarer Dichte der Oberfläche zu, d.h. in der Reihenfolge $(111) < (100) < (110)$.

Auf einer Pt(100) Domäne der Pt-Folie wurde die Ausbreitung von Reaktionsfronten mit Hilfe von PEEM ausführlicher untersucht. Dabei wurde eine Änderung des Mechanismus der Reaktionsfrontausbreitung mit der Temperatur beobachtet. Damit eng verbunden sind auch reaktionsinduzierte Änderungen der Morphologie, die mit Hilfe von AFM-Messungen festgestellt wurden.

Der direkte Vergleich des Reaktionsverhaltens von Pt und Pd (hkl) Oberflächen auf den jeweiligen Folien zeigt, dass Pd der geeignetere Katalysator für die Oxidation von CO ist, in dem Sinne, dass Pd eine höhere Toleranz gegenüber CO-Vergiftung und eine höhere Fähigkeit zur Reaktivierung aufweist. Diese Ergebnisse wurden mit neuesten DFT-Rechnungen und Ergebnissen kinetischer Reaktionsmodellierung verglichen.

Neben der isothermen Bestimmung der globalen und lokalen kinetischen Übergänge von Pt- und Pd-Folie, wie in der Oberflächenforschung zu Reaktionskinetik üblich, wurden auch isobare Experimente zur "Zündung" bzw. "Auslöschung" der Reaktion, wie aus der technischen Katalyse bekannt, durchgeführt. Es konnte gezeigt werden, dass unter den vorliegenden Reaktionsbedingungen beide Herangehensweisen äquivalente Ergebnisse lieferten.

Nicht nur die kristallografische Orientierung einer Oberfläche sondern auch Oberflächendefekte können eine wichtige Rolle für die katalytischen Eigenschaften spielen. Um den Einfluss der Defekte auf die Reaktionskinetik der CO-Oxidation zu untersuchen, wurden künstliche Defekte auf der Pd-Folie durch zusätzlichen Beschuss mit Ar^+ Ionen vor den kinetischen Experimenten erzeugt. Global wurde eine Verschiebung des kinetischen Phasendiagramms zu höheren CO Drücken beobachtet, was auf eine höhere Toleranz gegenüber CO-Vergiftung und eine höhere Fähigkeit zur Reaktivierung der defektreichen Pd-Folie hinweist. Lokal verschwindet die Strukturempfindlichkeit der Reaktion aufgrund der eingeführten ähnlichen Defektdichte auf den unterschiedlichen Körnern scheinbar, was auf Basis von vergleichenden STM-Experimenten auf einem Pd(111) Einkristall verstanden werden konnte. Die beobachtete Eingrenzung der Reaktionsfronten innerhalb der Konrgrenzen im Falle der ausgeheilten Pd-Folie wurde durch die künstliche Defekterzeugung aufgehoben.

Neben den polykristallinen Folien als katalytische Modellsysteme, wurden die Eigenschaften eines realitätsnäheren Modellsystems für technische Katalysatoren, nämlich eines in oxidierte Aluminiumfolie eingepressten Pd-Pulvers (" Al_2O_3 -geträgerte Pd-Teilchen"), untersucht. Ein globales kinetisches Phasendiagramm wurde für diese Probe aufgestellt und mit dem der Pd-Folie verglichen. Der Einfluss der äußerst defektreichen Oberflächenstruktur der Pulverprobe verglichen mit den wohl definierten μm -großen Körnern der Pd-Folie auf die Reaktionskinetik spiegelte sich in einer generell höheren Toleranz gegenüber CO-Vergiftung wieder, wenngleich das kinetische Phasendiagramm

des Pd-Pulvers auch einen breiteren Bistabilitätsbereich aufwies. Ähnlich wie auf der Pd-Folie wurden mit PEEM sich ausbreitende Reaktionsfronten beobachtet.

Die Rolle von Oxiden in der CO-Oxidationsreaktion auf Pd wurde mit PEEM, MS und XPS (Photoelektronenspektroskopie) unter gleichen Bedingungen untersucht. Dabei standen zwei verschiedene Arten von Oxiden im Mittelpunkt: (i) Siliziumoxid, das unter oxidierenden Bedingungen auf der Pd-Folie durch die Segregation von Siliziumverunreinigungen gebildet wurde, und (ii) Aluminiumoxid geträgertes PdO Pulver. Auf der Pd-Folie wurde in Anwesenheit von Sauerstoff eine verstärkte Segregation von Siliziumverunreinigungen aus dem Festkörper zur Oberfläche hin gefunden, die durch die höhere Bindungsstärke von Silizium auf einer Sauerstoff-bedeckten Pd-Oberfläche verursacht wird. Das darauffolgend an der Oberfläche gebildete Siliziumoxid mit dem mit XPS bestimmten Oxidationszustand Si^{2+} verursacht eine starke Deaktivierung der Pd-Oberfläche gegenüber der CO-Oxidation. Die PdO Pulverprobe erschien in dem betrachteten Druckbereich solange katalytisch inaktiv gegenüber der CO-Oxidationsreaktion, bis unter Reaktionsbedingungen eine teilweise Reduktion zu metallischem Pd hin einsetzte, was mit Hilfe der Kombination aus MS und XPS verfolgt werden konnte.

ABSTRACT

The aim of the present thesis was to study the reaction kinetics of the CO oxidation reaction on heterogeneous platinum, palladium and palladium oxide surfaces in a *laterally-resolved* way, under high-vacuum conditions. For this purpose, besides conventional (averaging over the whole sample) mass spectrometry (MS), a spatially resolving technique, photoemission electron microscopy (PEEM), was applied to study the catalytic CO oxidation reaction locally and *in situ* on polycrystalline Pt and Pd foils and on "alumina supported" Pd and PdO powders.

The combination of MS and PEEM allowed to follow simultaneously the global and local reaction kinetics of the CO oxidation reaction in the bistability regime for the entire Pt or Pd foil, respectively, and for the individual μm -sized domains of different (hkl) orientation on the polycrystalline foils. By MS, the global CO_2 rate produced by all grains of the foil was monitored and the kinetic transitions between the steady states of high and low catalytic activity were determined. For both Pt and Pd foil, these global kinetic transitions were summarized in *global kinetic phase diagrams*. Such a kinetic phase diagram represents effectively the reactivity states of a catalytic system in the (p, T) parameter space, thus allowing for a direct comparison of different catalytic systems.

Parallel to the global kinetic measurements by MS, the reaction was followed by PEEM *in situ* on the individual domains of Pt and Pd foil, respectively. An important result of the PEEM experiments was that the individual differently oriented (hkl) domains of Pt and Pd foil exhibit an independent single-crystal-like behavior reflected by a confinement of the propagating reaction-diffusion fronts within the grain boundaries. Thus, the independence of the reaction behavior of the individual domains provides the unique possibility to compare the reaction properties of different orientations by PEEM *in situ* under exactly the same conditions.

The idea to determine local reaction kinetics by PEEM is based on the fact that the local photoemission yield directly depends on the local CO or oxygen coverage (via the local work function). The CO or oxygen coverage, in turn, governs the CO_2 formation rate, thus the local PEEM intensity reflects the local reaction rate. In this way, by intensity analysis of the video-PEEM data local kinetic transitions and the *local kinetic phase diagrams* for differently oriented domains of polycrystalline samples can be obtained. This was performed for [100]-, [110]- and [111]-oriented Pt and Pd domains whose orientation was determined in advance by EBSD (electron backscatter diffraction). It could be shown that the local reaction behavior of the individual domains significantly differs from each other: the reactivity of the individual domains increases with decreasing atomic density, i.e. in the order $(111) < (100) < (110)$, for both Pt and Pd foil.

On a Pt(100) domain on Pt foil, the propagation of reaction-diffusion fronts was studied by PEEM in more detail. A change of the mechanism of the reaction front propagation with temperature was

observed which is also related to reaction-induced morphology changes on this domain observed by AFM measurements.

The direct comparison of the reaction behavior of Pt and Pd (hkl) surfaces on the corresponding foils yielded that Pd is the more suitable catalyst for CO oxidation, in the sense that Pd has a higher tolerance towards CO-poisoning and a higher reactivation ability. These results were compared to newest DFT calculations and results of kinetic reaction modeling.

Besides the isothermal determination of the global and local kinetic transitions on Pt and Pd foil, as usually applied in surface science studies of reaction kinetics, isobaric "ignition" and "extinction" experiments which are more common in technical catalysis were performed. It was demonstrated that under the present reaction conditions both approaches yield equivalent results.

Not only the crystallographic orientation of a surface, but also surface defects play a significant role for the catalytic properties. To study the influence of the defects on the kinetics of the CO oxidation reaction, artificial defects were created on the Pd foil by additional Ar⁺ ion sputtering before the kinetic experiments. Globally, a shift of the kinetic phase diagram to higher CO pressures was observed, indicating a higher CO-tolerance and reactivation ability of the defect-rich Pd foil. Locally, the structure sensitivity of the reaction vanished apparently due to the introduced similar defect density on the different grains, as was rationalized by comparative STM experiments on Pd(111) single crystal. The observed confinement of the reaction fronts within the grain boundaries in case of the annealed Pd foil was lifted upon the artificial defect creation.

In addition to the polycrystalline foils as catalytic model system, the properties of a more realistic model system for technical catalysts, a Pd powder sample impregnated into an oxidized Al foil ("Al₂O₃-supported Pd particles"), were studied. A (global) kinetic phase diagram was constructed for this sample and compared to that of Pd foil. The influence of the highly defected surface morphology of the powder sample compared to the well defined μm-sized grains of the Pd foil on the reaction kinetics was reflected in a generally higher tolerance towards CO poisoning, though the kinetic phase diagram of the Pd powder also exhibited a broader bistability range. Similar as in case of the Pd foil, propagating reaction fronts were observed by PEEM.

The role of oxides in the CO oxidation reaction on Pd was studied by PEEM, MS and XPS (X-ray photoelectron spectroscopy) under the same conditions. Two different types of oxides were investigated: (i) silicon oxide, formed under oxidizing conditions on the Pd foil by bulk impurity segregation, and (ii) alumina supported PdO powder. On Pd foil, an enhanced segregation of silicon bulk impurities to the Pd surface was found in the presence of oxygen caused by the higher bonding strength of Si on an oxygen-covered Pd surface. The subsequently formed surface silicon oxide with the oxidation state Si²⁺ determined by XPS strongly deactivates the Pd surface towards CO oxidation. The Pd oxide powder sample appeared catalytically inactive towards the CO oxidation reaction in the considered pressure range, until partial reduction to metallic Pd has set in under reaction conditions, as could be followed by the combination of MS and XPS.

ACKNOWLEDGEMENTS

I would like to thank...

*...my supervisors **Prof. Günther Rupprechter** and **Prof. Yuri Suchorski** for their guidance, the valuable discussions and for their support during all stages of this thesis.*

*...**Prof. Robert Schlögl** for his willingness to review this work and for financial and scientific support.*

*...The **Max-Planck-Society** (Fritz-Haber-Institute Berlin, Dept. of Inorganic Chemistry) for providing me financial support in form of a PhD grant.*

*...**Prof. Henrik Grönbeck** for the DFT calculations, **Prof. Michael Schmid** for the STM measurements, **Dr. Michael Stöger-Pollach** for the EBSD measurements and **Alexander Urich** for the AFM measurements.*

*...**Fonds zur Förderung der wissenschaftlichen Forschung (FWF)**, in particular the Special Research Program "Functional Oxide Surfaces and Interfaces" (SFB F45 "FOXSI"), the **Österreichischer Austauschdienst** (projects 77ÖU14 and 84Ö2U5) and the Vienna University of Technology (Innovatives Projekt "Spectromicroscopy of Surfaces by Metastable He atoms (He-SMS) ") for financially supporting my research.*

*...**Christian Spiel** for the great collaboration and a lot of (not always scientific) discussions.*

*...**Johannes Frank** for improving and extending the experimental setup.*

*...all **colleagues** at the Institute of Materials Chemistry (IMC) for the great atmosphere.*

*...my **family and friends** for their support.*

*...**Alex.***

CONTENTS

1	Introduction	1
1.1	General introduction	1
1.2	Outline of the thesis	3
2	Experimental	5
2.1	The ultrahigh vacuum system	5
2.1.1	PEEM chamber	7
2.1.2	Load lock	10
2.1.3	XPS chamber	11
2.2	Methods	12
2.2.1	Photoemission Electron Microscopy (PEEM)	12
2.2.1.1	Theoretical background	13
2.2.1.2	Image contrast	16
2.2.1.3	Layout of the microscope	16
2.2.2	Quadrupole Mass Spectrometry (QMS)	17
2.2.3	X-Ray Photoelectron Spectroscopy (XPS)	19
2.2.4	Scanning Tunneling Microscopy (STM)	24
2.2.5	Atomic Force Microscopy (AFM)	25
2.2.6	Electron Backscatter Diffraction (EBSD)	27
2.3	Samples	28
2.3.1	Metal foils	28
2.3.2	Powder samples	29

Contents

2.3.3	Identification of the (hkl) domains on Pt and Pd foil	30
2.4	Experimental procedure	33
3	CO oxidation on Pt group metals	34
3.1	Low Miller index planes of platinum and palladium	35
3.2	Interaction of adsorbates with Pt and Pd surfaces	37
3.2.1	CO Adsorption on Pt(hkl) and Pd(hkl) surfaces	37
3.2.2	Oxygen adsorption on Pt(hkl) and Pd(hkl) surfaces	40
3.2.2.1	Oxygen chemisorption	40
3.2.2.2	Subsurface oxygen	43
3.2.2.3	Formation of surface oxides	44
3.2.3	CO ₂ adsorption	45
3.3	CO oxidation on Pt group metals	46
3.3.1	Langmuir Hinshelwood mechanism	46
3.3.2	Bistability and kinetic phase diagram	50
3.3.3	Role of surface oxides in CO oxidation	52
4	Local reaction kinetics of CO oxidation on polycrystalline platinum	55
4.1	Introduction	56
4.2	Experimental details	58
4.3	Results	59
4.3.1	Global and local reaction kinetics of Pt foil	59
4.3.2	Surface morphology and reaction fronts on (100)-type grains on Pt foil	64
4.4	Summary	72
5	Local catalytic ignition during CO oxidation on low-index Pt and Pd surfaces	73
5.1	Introduction	74
5.2	Experimental approach to global and local catalytic ignition/extinction	75
5.3	Results	77
5.3.1	Isothermal <i>versus</i> isobaric kinetic transitions on Pd foil	77
5.3.2	Palladium <i>versus</i> platinum in CO oxidation	79
5.4	Summary	86
6	Role of defects in the local reaction kinetics in CO oxidation on Pd foil	87
6.1	Introduction	88
6.2	Experimental details	89

Contents

6.3	Results	91
6.3.1	Global kinetics of annealed and sputtered Pd foil	91
6.3.2	Scanning tunneling microscopy measurements	93
6.3.3	Local kinetics of annealed and sputtered Pd foil	94
6.4	Summary	98
7	Reactivity of oxides on Pd in CO oxidation	99
7.1	Introduction	100
7.2	Peculiarities of the experiment	101
7.3	Surface silicon oxide in CO oxidation on Pd foil	104
7.3.1	Global and local reaction kinetics upon surface SiO _x formation	104
7.3.2	XPS results	107
7.4	CO oxidation on Pd powder and PdO powder supported on alumina	111
7.4.1	Reaction kinetics of alumina supported Pd powder	111
7.4.2	Reactivity of PdO powder in CO oxidation	114
7.5	Summary	115
8	Conclusions	117
	References	121
	Publications	136
	Curriculum vitae	143

INTRODUCTION

1.1 General introduction

Heterogeneous catalysts are of great practical importance for many industrial processes and for pollution control. In chemical industry, more than 90% of all products come into contact with at least one catalyst during the production since the use of catalysts for chemical reactions is often the only economic way. The probably best example for an everyday life catalyst is the automobile three-way catalyst (TWC) which reduces the high amount of toxic pollutants in the exhaust gas produced by an automobile engine.

In the early days of catalysis, the main objective was to increase the activity of the catalyst defined by W. Ostwald already in 1894 and later specified by IUPAC as a "substance that increases the rate of reaction without modifying the overall standard Gibbs energy change in the reaction" [1–3]. Since the underlying mechanisms of catalysis were not understood to that time and due to the lack of suitable analytical techniques, the "design" of a catalyst with the aim to increase the yield of a particular product was based on a pure trial and error approach.

Nowadays, the requirements to an effective catalyst have changed significantly: not only a high activity, but also the selectivity towards the desired product to avoid byproducts which can be poisonous to the environment is important to industry. In order to be able to tailor the properties of a catalyst in the desired way, a fundamental understanding of the elementary steps of the reaction, the role of the atomic structure and of the active sites of the catalyst under reaction conditions is mandatory. The first step towards such understanding of heterogeneous catalysts was provided by the pioneering work on adsorption kinetics and

1 Introduction

chemical reactions at surfaces of I. Langmuir in the 1920's [4, 5]. However, in real catalysis many factors still complicate a proper understanding of the underlying mechanisms: real catalysts usually consist of oxide supported metallic nanoparticles of non-unique particle size distribution which exhibit many nanofacets with differing surface orientation. The catalytic properties are not only influenced by the size and the shape of the metal particles, but can also be affected by the metal-support interaction. In addition, real catalysts operate under high pressure conditions, thus mass transport limitations, heat generation or oxide formation can play a significant role. Since all these effects also can influence each other, it is often hardly possible to estimate the importance of the single contributions.

Another challenge of real catalysis is the circumstance that it is difficult to gain information about the exact atomic structure and the chemical composition of a catalyst under reaction conditions. Only a few experimental techniques are available which are surface sensitive in the technological more relevant pressure regime of mbar to bar and can be applied during an ongoing reaction on catalytic model systems, such as high pressure STM, high pressure XPS, PM-IRAS or SFG [6–8].

Therefore, the nowadays knowledge about the fundamentals of chemical reactions at surfaces is mainly based on the surface science approach to catalysis: the elementary steps of a surface chemical reaction, such as adsorption of the reactants, adsorbate diffusion and reaction, are studied on well defined surfaces with highly reduced complexity, i.e. single crystal surfaces, under well defined conditions, mostly under (ultra)high vacuum. With the development of modern surface science techniques in the last decades many processes could be revealed even on the atomic scale [9] and the highly valuable findings resulted in the Nobel Prize awarded to Gerhard Ertl in 2007 "for his studies of chemical processes on solid surfaces" [10].

Although the single crystal studies performed in the past are highly important for a fundamental understanding of the basic principles of heterogeneous catalysis, single crystals rather poorly represent the complex systems used in "real" catalysis. Thus, the results performed on such model systems under high vacuum conditions are only to a limited extent transferable to technological catalysis, a circumstance known as *pressure and material gap*. To bridge this gap, either the pressure under reaction conditions can be increased stepwise on still well-defined surfaces or the complexity of the studied systems has to be increased step by step under still defined reaction conditions asking for experimental techniques which are capable to resolve dynamic processes at least on the μm scale. The latter approach is chosen for the present thesis and two different types of catalytic model systems along the "complexity axis" (see Fig. 1.1) are studied, namely (i) polycrystalline metal foils

1 Introduction

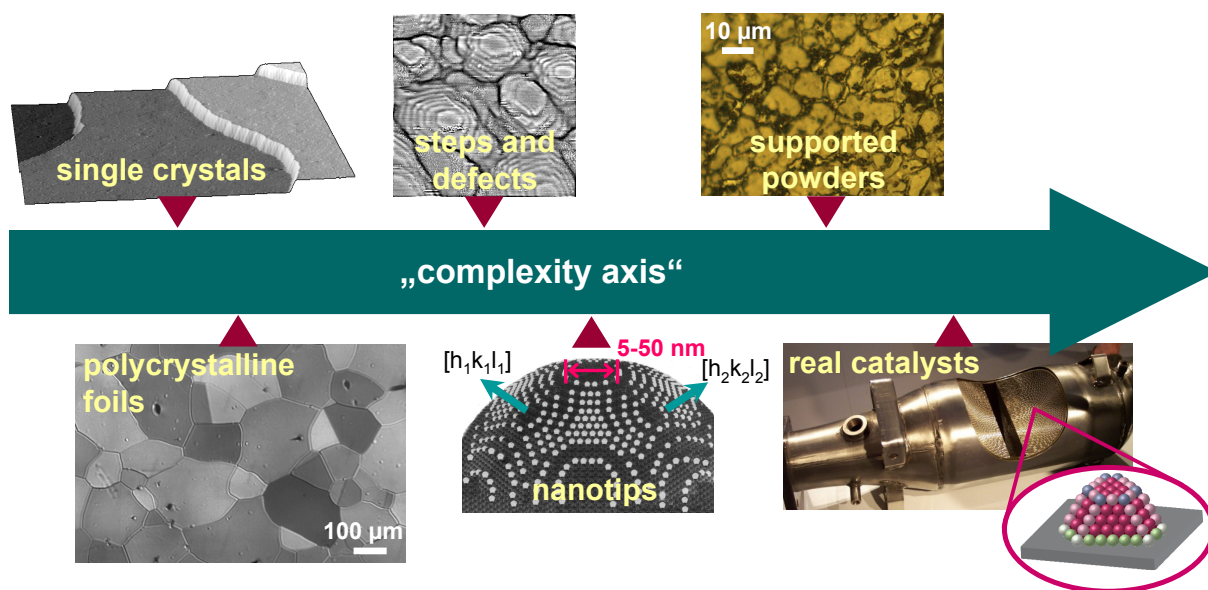


Figure 1.1: Catalytic model systems in surface science along the "complexity axis".

(Pt and Pd) consisting of μm -sized single-crystal-like entities, and (ii) Pd and PdO powder samples impregnated into oxidized aluminum foil, thus serving as a more realistic model system. The studied reaction, the catalytic oxidation of carbon monoxide to CO_2 is not only of high practical meaning for pollution control as one of the three reactions ongoing in a TWC, but can also serve as a suitable model reaction due to its relatively simple Langmuir-Hinshelwood reaction mechanism. By the usage of photoemission electron microscopy it is possible to obtain the local reaction kinetics of this reaction on the μm -scale on both types of samples what is usually not accessible by conventional techniques such as mass spectrometry due to their averaging character.

1.2 Outline of the thesis

The present thesis is structured as follows:

In chapter 2, the experimental setup which was used for most of the experiments is introduced. The theoretical background of the applied experimental techniques is detailed and the studied samples are presented.

Chapter 3 provides an overview of the properties of the studied materials and the interaction of CO, oxygen and CO_2 with the various (hkl) surfaces of Pt and Pd is detailed. The mechanism of the CO oxidation reaction and some of its peculiarities as the bistability

1 Introduction

behavior is presented. An overview of the state-of-the-art of the role of oxides for the CO oxidation reaction on palladium is given.

Chapter 4 presents the results on the local reaction kinetics of the CO oxidation reaction in the bistability regime for individual grains of polycrystalline Pt foil, obtained by the new experimental approach that combines local PEEM analysis and MS for kinetic studies. The peculiarities of the morphology and the reaction front propagation mechanism of a single [100]-oriented domain on Pt foil is detailed.

In chapter 5, the local kinetic properties of the Pt(hkl) domains on Pt foil are contrasted to those of Pd(hkl) domains on Pd foil and the differences are discussed by means of newest micro-kinetic simulations. Two different approaches to obtain kinetic transitions of the reaction, the isothermal variation of the CO pressure at otherwise constant external parameters usually applied in surface science studies and the isobaric temperature variation more common in technical catalysis, are compared to each other.

The role of defects for the kinetic properties of the Pd(hkl) domains on Pd foil is addressed in chapter 6 and rationalized by STM measurements on Pd(111) single crystal.

In chapter 7, the role of extrinsic oxides such as SiO₂ on Pd and of the intrinsic palladium oxide for the CO oxidation reaction is discussed. The oxidation state and the correlation to the reactivity is controlled by XPS. Furthermore, the CO oxidation reaction is studied by PEEM and MS on a model system with higher complexity than the metal foil, namely the alumina supported Pd powder.

Finally, in chapter 8 the most important results of this thesis are summarized.

EXPERIMENTAL

In section 2.1 of this chapter the complex experimental setup, an ultrahigh vacuum system consisting of two separable experimental chambers in which most of the experiments of this PhD thesis were performed, is introduced. Section 2.2 details the theoretical background of the applied experimental methods: the methods most of the experiments were performed with, namely photoemission electron microscopy (PEEM), quadrupole mass spectrometry (QMS) and X-ray photoelectron spectroscopy (XPS) are described in detail, whereas the methods which were used to gather supportive information, namely scanning tunneling microscopy (STM), atomic force microscopy (AFM) and electron backscatter diffraction (EBSD), are only briefly outlined. In section 2.3, the investigated samples are introduced and in section 2.4 the usual experimental procedure is briefly sketched.

2.1 The ultrahigh vacuum system

Most of the experiments described in this thesis were performed in an ultrahigh vacuum (UHV) system consisting of two separable chambers which are connected to each other by a sample transfer system and a load lock. Fig. 2.1a shows a photographic image of the whole UHV system and Fig. 2.1b depicts the system schematically. On the right side of the setup in Fig. 2.1a the PEEM chamber is installed. In this chamber, sample preparation and the kinetic experiments by PEEM and MS were performed. In course of this thesis, the XPS chamber, on the left side of Fig. 2.1a, was developed and mounted. This chamber is equipped with a commercial analyzer (SPECS) and connected to the PEEM chamber by a home-made load lock allowing for a quick sample change without breaking the vacuum in

2 Experimental

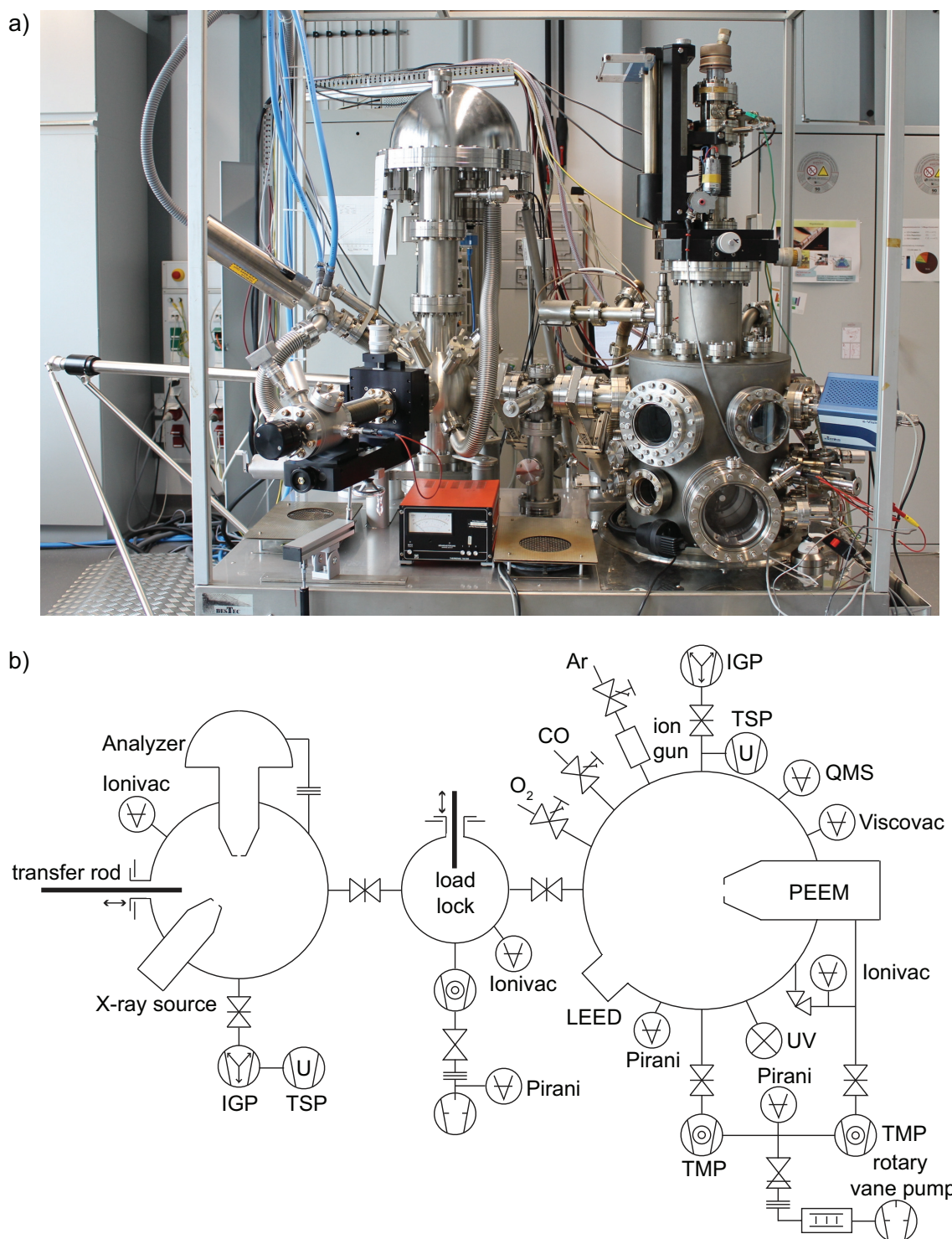


Figure 2.1: a) The UHV system consisting of the PEEM (right side) and the XPS chambers (left side), the load lock in between and the transfer rod attached to the XPS chamber. b) Scheme of the experimental setup.

2 Experimental

the two main chambers. The customized transfer rod (left) allows for quick sample transfer between the two chambers and the load lock without vacuum breaking.

2.1.1 PEEM chamber

The ultrahigh vacuum (base pressure of 10^{-9} mbar) necessary to maintain a contaminant-free atmosphere is achieved in the PEEM chamber (right side in Fig. 2.1) by a turbomolecular pump (TMP; TMU 260, Balzers) and a rotary vane backing pump (TriVac D8B, Leybold) which generates a fore-vacuum of $10^{-2} - 10^{-3}$ mbar. To reduce backdiffusion of oil mist from the rotary vane pump to the TMP, an oil mist filter is integrated between fore-pump and turbomolecular pump. In addition, a fore-vacuum safety valve is integrated in the fore-vacuum line which closes the connection to the UHV in case of a power cut. The rotary vane pump also generates the fore-vacuum for the second turbomolecular pump (TMU 071P, Pfeiffer Vacuum) which is used for differential pumping of the electron optics of the PEEM. In this way, experiments at a pressure of up to 10^{-4} mbar in the main chamber can be performed while the pressure in the PEEM does not exceed 5×10^{-7} mbar what is necessary to protect the sensitive multichannel plate. Furthermore, an ion getter pump (IGP; Vacion Plus 500, Varian) is attached to the chamber to maintain the base pressure, as well as a titanium sublimation pump (TSP; Varian) for removal of hydrogen (H_2) from the residual gas. To remove effectively water (H_2O) from the residual gas, the whole setup can be baked out at a temperature of up to $200^\circ C$ using a heating tent and two fan heaters which are integrated in the movable table on which the stainless steel chambers are mounted. Baking out the parts which are not within the heating tent (e.g. the parts below the table as the ion getter pump) proceeds by heating tapes.

The pressure in the fore-vacuum line as well as in the UHV chamber during beginning of evacuation is controlled by thermal conductivity Pirani gauges (ThermoVac, Leybold). A Bayard-Alpert hot cathode ionization gauge (Varian) is used for permanent monitoring of the pressure in the main chamber or, after closing the angle valve, in the electron optics of the PEEM during the experiments. A spinning rotor gauge (ViscoVac VM212, Leybold) monitors the total pressure in the chamber during the experiments in the range between 10^{-6} and 10^{-4} mbar and the mass spectrometer measures the partial pressures of the reactants and the reaction product (see section 2.2.2). Besides, the pressure in the ion getter pump is controlled by the pump itself.

In addition to the photoemission electron microscope (PEEM 150, STAIB Instruments), the PEEM chamber is equipped with a quadrupole mass spectrometer (QMS; e-Vision+,

2 Experimental

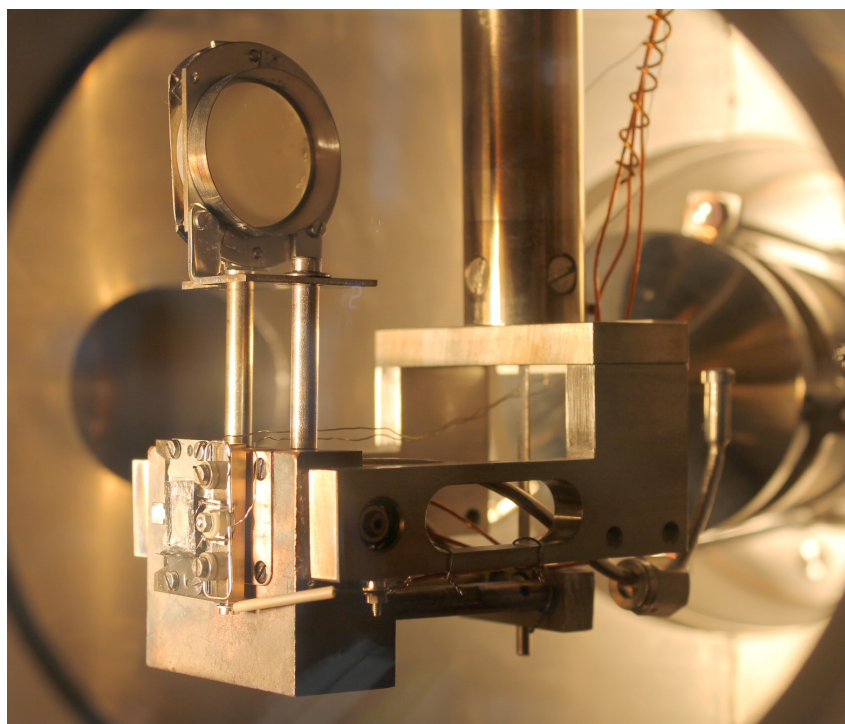


Figure 2.2: The manipulator end with the sample holder in 75 mm off-axis position.

MKS Instruments), a low-energy electron diffraction (LEED) device (SPECTALEED, Omicron NanoTechnology), an Ar^+ ion sputter gun (IQE 11/35, SPECS) and a water-cooled deuterium discharge UV lamp (D200, Heraeus) with an intensity maximum at approximately 6.5 eV photon energy. The high purity gases used in the experiments and for sputtering (CO: 99.97%, Linde; O_2 : 99.999%, Ar: 99.999%, Messer Austria) are dosed to the chamber from 1 L gas bottles (MINICAN[®]) through variable leak valves (Varian).

The manipulator in the PEEM chamber, on which the sample is mounted, is 360° rotatable, ± 25 mm movable in the horizontal x- and y-directions and 200 mm movable in vertical z-direction. The sample holder can be tilted by a few degrees in both directions what is highly important for PEEM measurements since the sample surface normal has to be adjusted *exactly* parallel to the microscope axis of the PEEM for a uniform illumination of the field of view. The distance between the sample and the first lens of the PEEM has to be approximately 5 – 10 mm, therefore the sample holder at the bottom of the manipulator is L-shaped and the sample is mounted 75 mm *off-axis* as can be seen in Fig. 2.2 showing the end of the manipulator within the UHV chamber.

The samples are spot-welded to home-made stainless steel or molybdenum sample holder plates based on the Omicron/ SPECS design (Fig. 2.3a). The sample holder plate is in-

2 Experimental

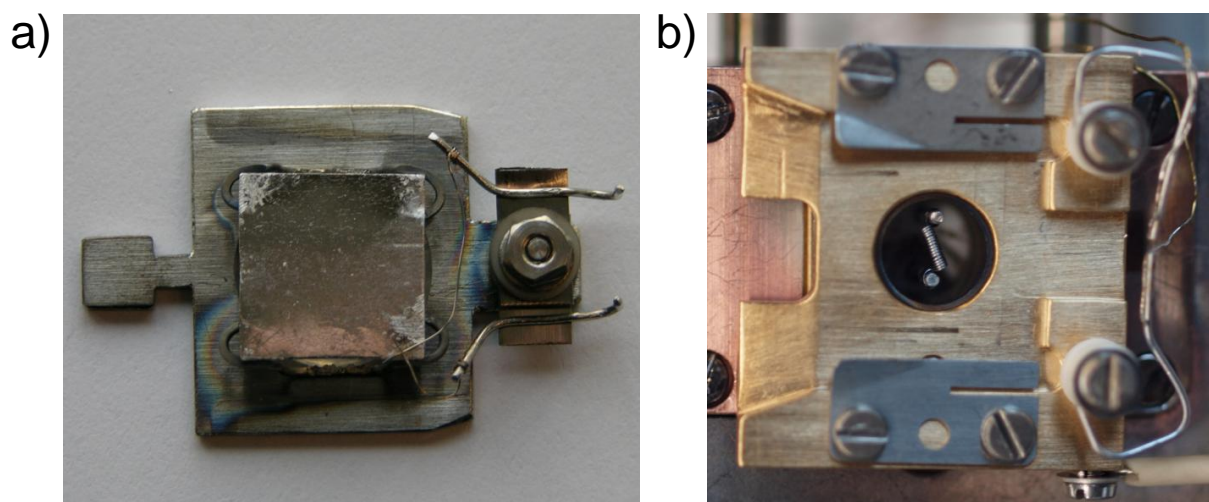


Figure 2.3: a) Pd foil sample mounted on the stainless steel sample holder plate with the transfer clutch on the left side; b) gold-coated copper sample holder adapter mounted at the very end of the manipulator.

served horizontally into the (also home-made) gold-coated copper sample holder which is mounted at the bottom of the manipulator (Fig. 2.3b). By the clutch on the left side of the plate, the sample holder plate can be easily picked up by the transfer rod and directly transferred between the chambers without the usage of a wobble-stick. The gold-coated sample holder is, in fact, a three-part sandwich adapter which was constructed to make the direct sample transfer possible without modification of the original sample stage at the bottom of the manipulator. The middle part of the adapter is a thin sapphire plate which is needed for electrical insulation of the sample. The electrical contact to the sample acquired for sample grounding is realized by a Kapton-insulated wire which is screwed to the front part of the adapter.

The sample can be heated by electron bombardment heating. In the back of the sample a self-made filament fabricated from coiled thoriated tungsten wire which is spot-welded to two pins is placed within the sample holder (see also Fig. 2.3b). The filament is electrically shielded to the surrounding by a cylindrical alumina (Al_2O_3) tube. For electron bombardment heating, the filament is set to maximum 1 kV high voltage and the sample is grounded. With 2 – 2.5 A filament current, an emission current of 10 – 15 mA and a maximum temperature of $\sim 1200\text{ K}$ can be reached. Due to frequent operation of the filament in 10^{-5} mbar oxygen, its lifetime is limited to approximately one year. The temperature of the sample is measured by a NiCr/Ni thermocouple (type-K) spot-welded to the front side of the sample (Fig. 2.3a). The thermovoltage is transferred to the spring clamps on the right side of the sample holder adapter (Fig. 2.3b) and then led outside the UHV chamber

2 Experimental

through electrical feedthroughs via Kapton-insulated thermowires. In addition, an external type-K thermocouple is mounted to the chamber on a linear motion feedthrough. It is used to crosscheck the internal thermocouple values and to verify the absence of a temperature gradient across the sample surface (a maximum temperature difference of 5 K was found between different spots of the sample surface).

2.1.2 Load lock

Between the PEEM and the XPS chamber, a custom-made load lock (Fig. 2.4) is integrated which is separated from the two main chambers by two gate valves (VAT). The load lock is pumped by a turbomolecular pump (HiPace 80, Pfeiffer Vacuum), which is also equipped with a vent valve, and a rotary vane pump (Duo 5, Pfeiffer Vacuum) separable by a valve from the high vacuum part. The pressure in the load lock can be controlled by a hot cathode ionization gauge (MVC-3, Vacom). At the end of a linear motion feedthrough (MDC Vacuum) which is attached to the load lock a sample holder is mounted which is used for exchange and subsequent transfer of the sample to one of the two chambers by means of the transfer rod.

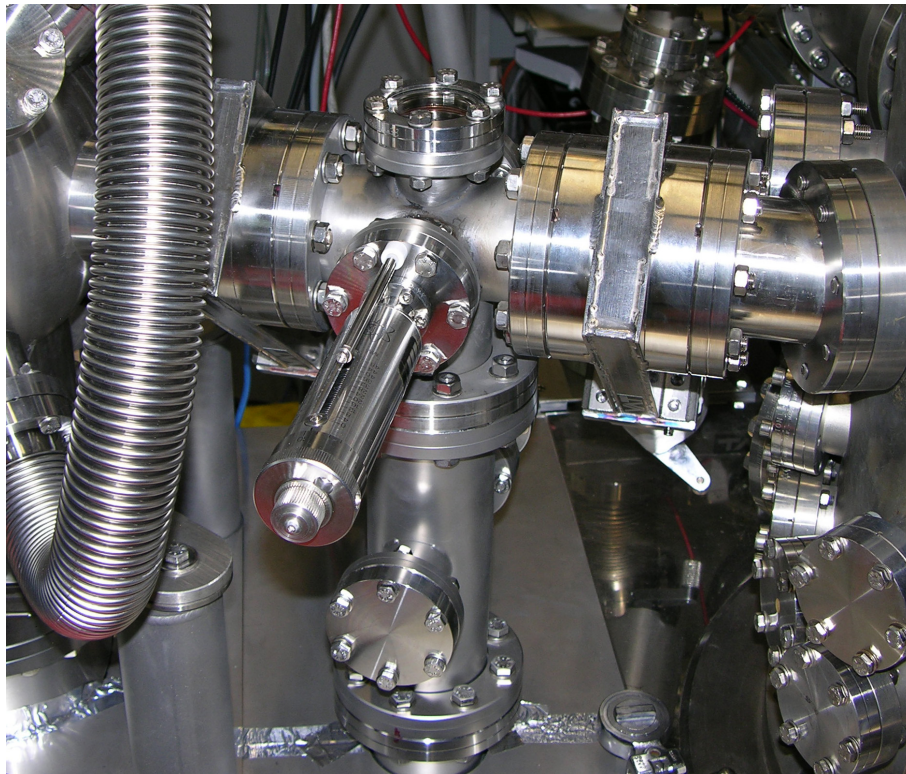


Figure 2.4: The load lock with the linear motion feedthrough in the front.

2 Experimental

2.1.3 XPS chamber

The XPS chamber is equipped with a hemispherical electron energy analyzer (HSA; Phoibos 100, SPECS) which is mounted vertically to the chamber. Instead of a single channeltron, a micro-channel plate and a 2D-CCD detector is used for electron detection, so in principle spatially resolved XPS measurements are possible with this device. Under the "magic" angle of 54.7° to the sample normal an X-ray source (XR 50, SPECS) is attached to the chamber on a linear motion feedthrough which allows to position the X-ray source close to the sample surface. The X-ray source is water-cooled and a water interlock system prevents operation of the source without water cooling. Both, the hemispherical analyzer and the X-ray source are additionally connected by flexible metal hoses to the chamber for better pumping conditions. The horizontally mounted manipulator (VAB) is 360° rotatable, ± 12.5 mm movable in the (vertical) x,y-plane and 100 mm movable along the (horizontal) z-axis. As in the PEEM chamber, the sample can be heated by electron bombardment with a coiled filament (SPECS) placed in the back of the sample within the sample holder. Temperature measurement proceeds also via a type-K thermocouple.

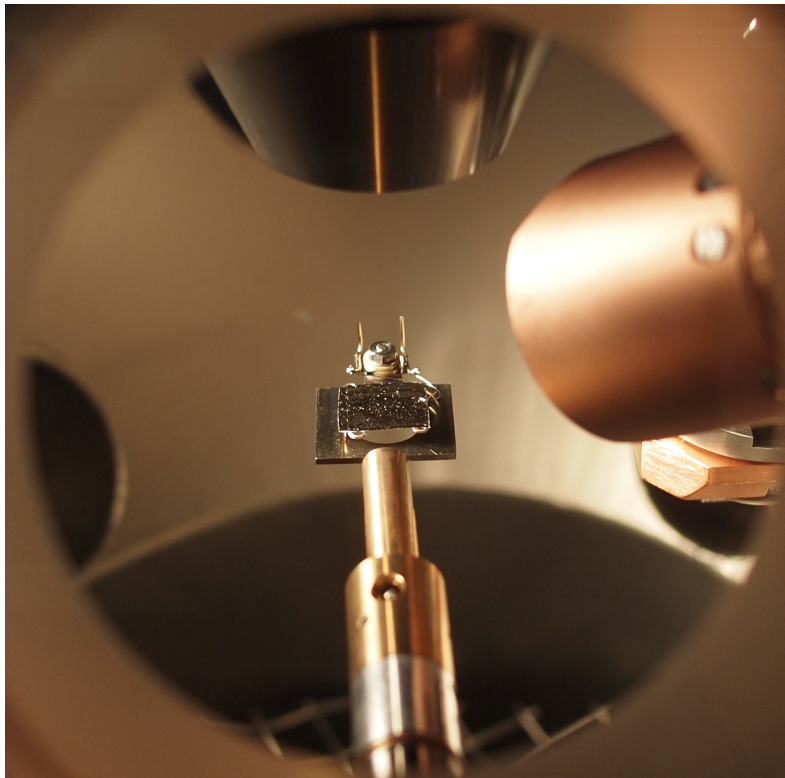


Figure 2.5: View through a CF40 window into the XPS chamber: the sample is held by the transfer rod in the front. On the right side, the end of the manipulator as well as the cone of the X-ray source can be seen. From the top, the energy analyzer is visible.

2 Experimental

The transfer rod which is used for sample transfer between the two chambers is attached to the XPS part of the setup. In the front of the photographic image in Fig. 2.5 the end of the transfer rod can be seen within the XPS chamber with the sample attached to it. At the top, one can see the entrance cone of the analyzer and on the left, the X-ray source covers partly the sample holder.

To evacuate the XPS chamber, the gate valve to the load lock is opened and the XPS chamber is pumped by the turbomolecular pump of the load lock. To maintain the ultrahigh vacuum (base pressure of 10^{-9} mbar), an ion getter pump (StarCell 300, Varian) is attached. Like in the PEEM chamber, in addition a titanium sublimation pump is mounted to the XPS chamber. The pressure is controlled by an ionization gauge (MVC-3, Vacom) equivalent to the one in the load lock, so the same control unit can be used for both pressure gauges.

2.2 Methods

In this section, the experimental techniques which were applied in this work are presented. The majority of the experiments were performed by photoemission electron microscopy (PEEM), quadrupole mass spectrometry (QMS) and X-ray photoelectron spectroscopy (XPS) in the experimental setup presented in section 2.1. These techniques are described in more detail, whereas scanning tunneling microscopy (STM), atomic force microscopy (AFM) and electron backscatter diffraction (EBSD) are only briefly sketched since they were used to gather supportive information in different other setups.

2.2.1 Photoemission Electron Microscopy (PEEM)

In (UV-)photoemission electron microscopy, the image is created by electrons emitted from the imaged surface and the image contrast is given by the distribution of the local work function across a metallic sample surface. The first photoelectron emission microscope was already developed in the early 1930's [11], but the technique has found wide application only after the development of UHV-compatible PEEM-devices by the groups of W. Engel [12–14] and E. Bauer [15]. One of the main advantages of PEEM, the real-time observation of dynamic processes at surfaces, was successfully exploited in the past by the group of G. Ertl to investigate the spatio-temporal pattern formation during catalytic surface reactions at single crystal surfaces [10, 16–18].

2.2.1.1 Theoretical background

The working principle of PEEM is based on the *photoelectric effect* which was discovered by Heinrich Hertz and Wilhelm Hallwachs in 1887 [19, 20] and later explained by Albert Einstein [21] (awarded with the Nobel Prize in 1921 "for his services to Theoretical Physics, and especially for his discovery of the law of the photoelectric effect"). The image in PEEM is created by photoelectrons which are emitted from the metal surface upon irradiation by UV light. In Fig. 2.6 the photoelectric effect is illustrated: upon irradiation of a metal surface by photons with the energy $h\nu$, *photoelectrons* with a certain kinetic energy E_{kin} are emitted from the surface. The kinetic energy of an emitted photoelectron depends on the energy of the impinging photons, the binding energy E_B of the electron within the metal and on its work function Φ :

$$E_{kin} = h\nu - E_B - \Phi. \quad (2.1)$$

The work function Φ of the metal is defined by

$$\Phi = E_{Vac} - E_{Fermi} \quad (2.2)$$

as the difference between the vacuum level E_{Vac} and the Fermi level E_{Fermi} of the metal (see also Fig. 2.6).

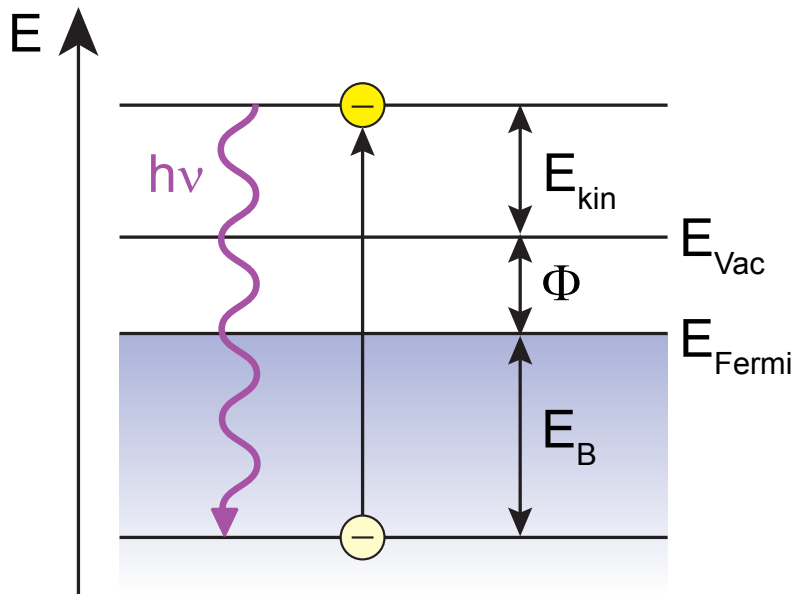


Figure 2.6: Energetic scheme of the photoelectric effect. The kinetic energy of the emitted electron depends on the energy of the incoming photon, the binding energy and the sample work function.

2 Experimental

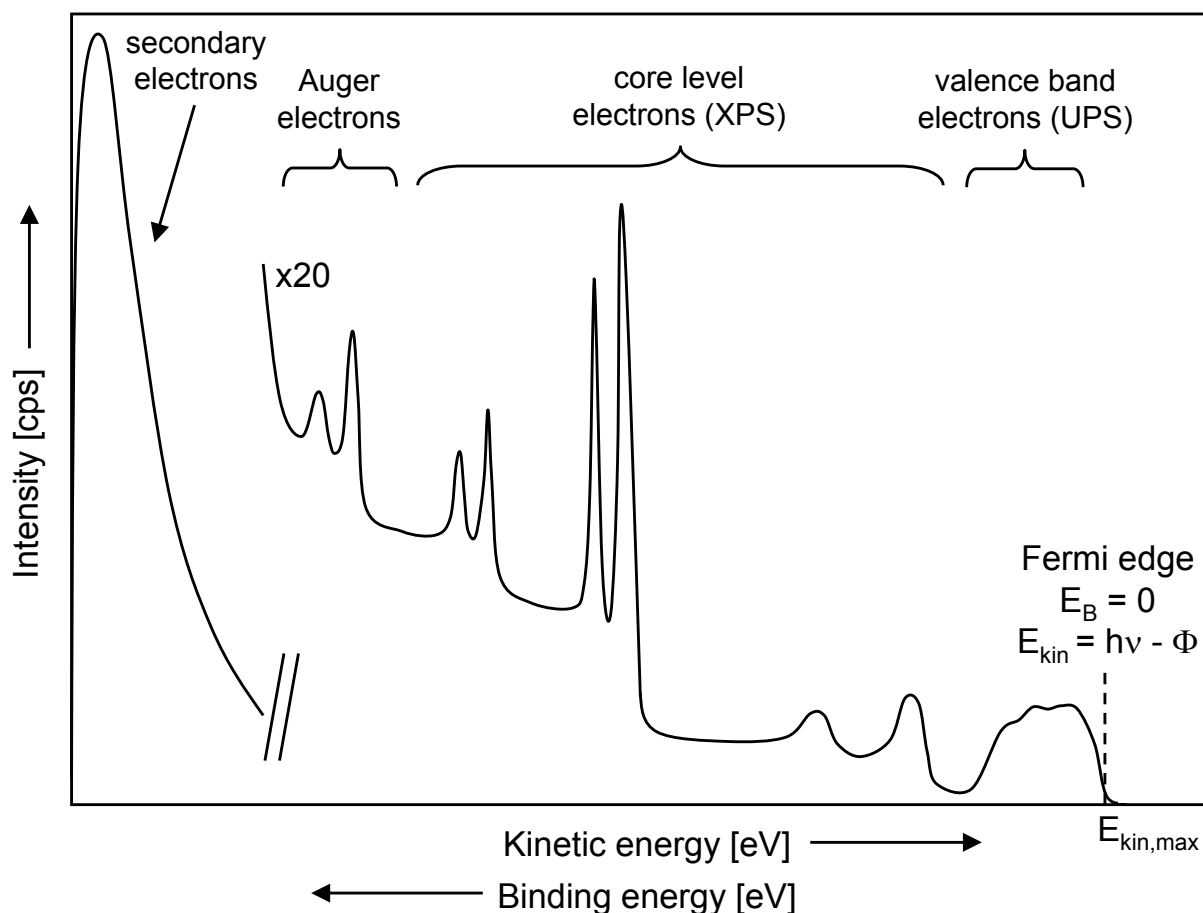


Figure 2.7: Scheme of a typical photoemission spectrum for incident photon energies in the X-ray range. The majority of emitted electrons are inelastically scattered secondary electrons.

Generally, if the incident photon energy is high enough, as it is for example the case in XPS (see also section 2.2.3), the energetic spectrum of the emitted photoelectrons exhibits the characteristics depicted in Fig. 2.7. The electrons with the highest kinetic energy correspond to a binding energy of zero, i.e. $E_{kin,max} = h\nu - \Phi$. The electrons with high kinetic energy (i.e. low binding energies) stem from the valence band of the investigated material and are usually accessible by UV photoelectron spectroscopy (UPS). With decreasing kinetic energy (increasing binding energy!) the electrons from the core levels are excited and can be detected by XPS (see section 2.2.3). At even lower kinetic energy, the Auger electrons can be detected: these electrons do not originate directly from the initially excited core level. Rather, an electron from a higher energetic level fills the emptied core level and transfers its energy to the then detected Auger electron. The high amount of electrons with very low kinetic energy is attributed to electrons which are inelastically scattered on their way from the "bulk" (i.e. from 0.5 – 2 nm below the surface corresponding to the inelas-

2 Experimental

tic mean free path of the electrons within the material [22]) to the sample surface. These electrons, for spectroscopic applications rather disturbing, are used in PEEM for imaging.

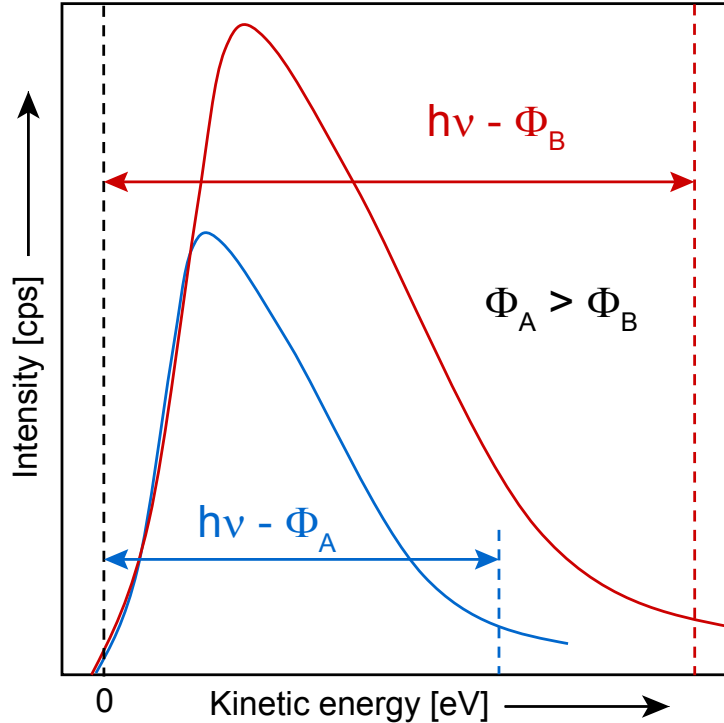


Figure 2.8: Photoemission spectrum for a photon energy close to the sample work function. The photoemission yield from a sample with a high work function Φ_A is considerably lower than from a sample with a lower work function $\Phi_B < \Phi_A$.

A spectrum as it is shown in Fig. 2.7 is typical for an incident photon energy of 1000 – 2000 eV, i.e. for energies in the X-ray range. In (UV-)PEEM, the incident photon energy is usually chosen to be just above the sample work function, i.e. $h\nu_0 \sim 5 - 7$ eV. Typical laboratory light sources are for example mercury ($E_{max} = 4.9$ eV) or deuterium lamps ($E_{max} = 6.8$ eV). Therefore, in a "photoemission spectrum" achieved by illumination with such a source a small fraction of electrons from the valence band, but mainly inelastically scattered electrons with a very low kinetic energy in the range between the excitation energy and the work function appear. Since this range is very narrow, the *amount* of the emitted electrons which yield the brightness of the PEEM image depends very strongly on small variations of the sample work function. This is illustrated in Fig. 2.8: for a sample work function Φ_A higher than Φ_B , the amount of the inelastically scattered electrons (i.e. the intensity peak area) and therefore the PEEM image brightness is considerably lower. This leads to the high image contrast in PEEM already for very small work function differences across the sample. PEEM as used in the present work is not an energy-resolving

2 Experimental

technique, since only the amount of emitted electrons is detected. However, in the last years energy-resolving PEEM instruments are more common.

2.2.1.2 Image contrast

As described in the previous section, the image contrast in PEEM is determined by variations of the sample work function. The work function of a sample depends on a diversity of factors: First of all, the material itself determines the work function value. For platinum and palladium surfaces, it varies between 5 and 6 eV. Furthermore, the crystallographic orientation of a surface plays an important role. Following the Smoluchowski theorem [23], the work function of a surface increases with its atomic density. Therefore, the closest-packed (111) surface of fcc metals is usually the one with the highest work function. The adsorption of atoms or molecules from the gas phase alters the work function of a sample considerably. PEEM, as a parallel imaging method, is a very suitable tool to investigate surface chemical reactions, especially on polycrystalline materials such as metal foils. A metal foil consists of grains of different crystallographic orientation with a typical size of 10 – 100 μm . Since the field of view in PEEM used in the present work is approximately 500 μm , it is possible to observe several differently oriented grains simultaneously and to compare *directly* their behavior in a specific surface reaction in one experiment in real time.

However, the image brightness in PEEM may also be influenced by the topography of the surface. The roughness of the surface, or more precisely the curvature of the accelerating field for the photoelectrons around topographical features of the surface as e.g. grain boundaries, scratches or any kind of defect sites (holes, protrusions etc.), leads to a variation of the local photoemission yield and therefore of the local image brightness. Generally, this effect results in a decrease of the spatial resolution.

2.2.1.3 Layout of the microscope

An image in PEEM is created by the emission of photoelectrons from a grounded metallic sample surface. The electron optical lenses which are used for the imaging are all of electrostatic nature. A scheme of the lens system of the PEEM-150 instrument is depicted in Fig. 2.9. The distance between the sample and the entrance cone of the PEEM is approximately 5 – 10 mm, so the illuminating UV light has to incide under a relatively flat angle (15°). The entrance cone of the PEEM is set to an anode voltage of $U_A = 15 - 20 \text{ kV}$ to attract and accelerate the photoelectrons. The first lens, the objective lens set to a voltage of $U_{OL} = 2 - 4 \text{ kV}$, forms the first real image of the sample which is further magnified by the in-

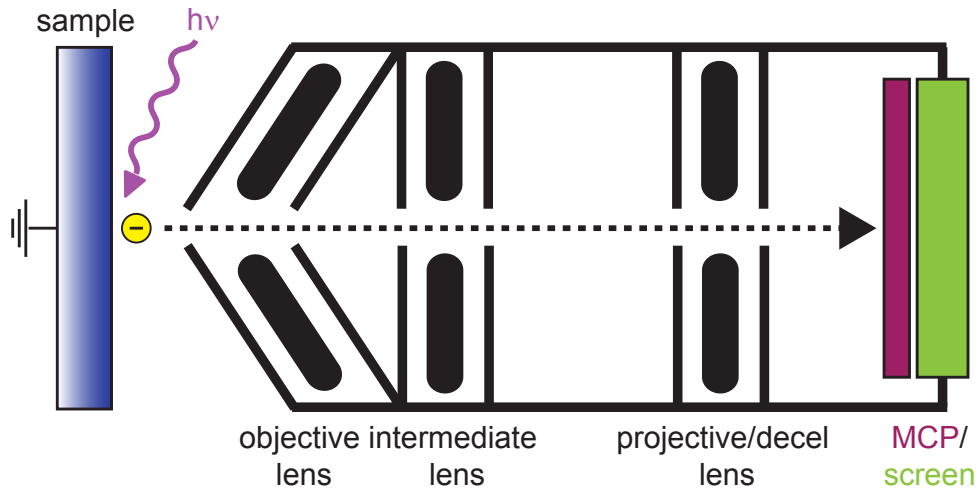


Figure 2.9: Layout of the electrostatic lens system of the PEEM microscope.

intermediate lens ($U_{IL} = 0 - U_A$). The projective and decelerating lenses ($U_{PL} = 1.58 \text{ kV}$, $U_{DL} = 1.25 \text{ kV}$) decrease the kinetic energy of the photoelectrons because the multichannel plate (MCP, $U_{MCP} = 700 - 750 \text{ V}$) which amplifies the electron signal has its sensitivity maximum for an impinging electron energy between 200 and 2000 eV. Finally, the electrons are accelerated to a phosphorous screen ($U_{screen} = 3 \text{ kV}$) which is recorded through a window by a CCD-camera outside the vacuum system. To protect the multichannel plate and to avoid flashovers inside the electron optical column, the PEEM can be pumped differentially through a CF40 flange by a turbomolecular pump under "high pressure" operation (i.e. for a maximum pressure of $\sim 10^{-4}$ mbar within the vacuum chamber).

The magnification achievable by the PEEM-150 allows imaging on the mesoscopic scale, the typical lateral resolution is in the low μm range and the field of view is approximately $500 \mu\text{m}$. Due to the parallel imaging principle the temporal resolution is only determined by the latency of the phosphorous screen and the employed camera system. Since a high-speed CCD camera (Hamamatsu) was used in this thesis, a temporal resolution in the low μs range is in principle achievable.

2.2.2 Quadrupole Mass Spectrometry (QMS)

Quadrupole mass spectrometry is a very widely used method for residual gas analysis under low pressure conditions. The main advantage of QMS is that it is possible to monitor not only the *total* pressure of the gas atmosphere but also the *partial pressure* of the residual gas components. In the PEEM chamber of the UHV setup, a quadrupole mass spectrometer is installed which was mainly used for controlling and recording the partial

2 Experimental

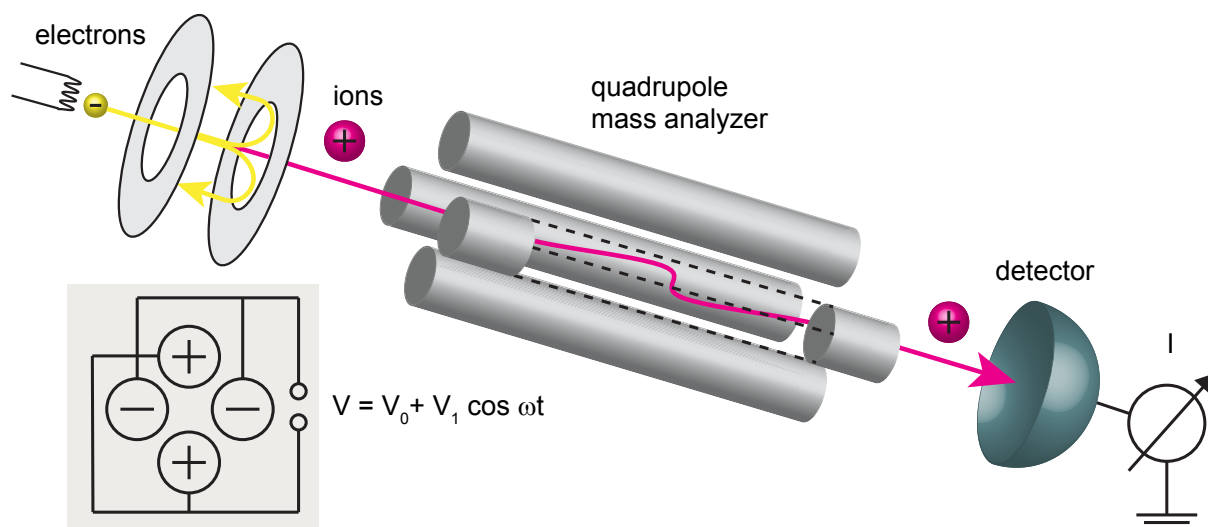


Figure 2.10: Scheme of the QMS. Residual gas atoms are ionized by electron bombardment, mass-separated in the quadrupole mass analyzer and detected either by a Faraday cup or a secondary electron multiplier. The inset shows the polarity of the four quadrupole rods.

pressures of the reactants (CO and O_2) and the reaction product (CO_2) during the kinetic experiments. Besides, it was also used as a leak check device after evacuation of the UHV chamber: flanges or newly installed devices were scanned outside the chamber with a helium gas beam while *inside* the chamber the helium trend was controlled.

The working principle of a QMS is illustrated in Fig. 2.10. The residual gas atoms are ionized in a so-called ion source by an electron beam emitted from a cathode. The positively charged ions are accelerated towards the detector which is placed *after* the quadrupole mass analyzer. The mass analyzer consists of four parallel rods arranged in a square which form a quadrupole electric field. Each opposite pair of rods is electrically connected while a voltage

$$V = V_0 + V_1 \cos \omega t \quad (2.3)$$

is applied between the two rod pairs (inset in Fig. 2.10). From the equations of motion of the ions near the axis of the filter it follows that only ions with a mass-to-charge ratio of

$$\frac{m}{z} = \text{const.} \times \frac{V_1}{\omega} \quad (2.4)$$

are able to pass the mass filter. Therefore, by varying either the voltage V_1 or the frequency ω of the AC voltage the mass-to-charge ratio of the passing ions can be scanned.

The ions are usually detected either by a Faraday cup for large ion currents or by a *channeltron* for small ion currents. The Faraday cup is a metal cup which directly measures

2 Experimental

the current of the impinging ions via the electron current needed for their neutralization. The sensitivity of a Faraday cup is relatively low, so it cannot be used for small pressures (i.e. small ion currents). In that case, a channeltron is used for detection. The channeltron amplifies the signal of the impinging ion by an avalanche of secondary electrons emitted from the walls of the multiplier. The sum of these secondary electrons is then detected by measuring the total electron current.

The evaluation of a mass spectrum is complicated by the appearance of higher charged ions (e.g. $\text{CO}^{++} = 14$), isotopes (e.g. for O_2 a signal at 32 and 34 is detected) or charged fragments of the original molecules. Fragments appear especially in case of hydrocarbons: for example, a methane molecule would lead to a signal at the m/z -ratios ranging from 16 to 12 according to CH_4^+ , CH_3^+ and so forth. However, such fragments or isotopes can be utilized for an unambiguous identification of the gas phase components due to their characteristic distribution.

2.2.3 X-Ray Photoelectron Spectroscopy (XPS)

X-ray photoelectron spectroscopy (XPS), originally named electron spectroscopy for chemical analysis (ESCA), has been first successfully realized by in the mid 1960's K. Siegbahn [24, 25] who was awarded with the Nobel Prize in 1981 "for his contribution to the development of high-resolution electron spectroscopy". Due to its high surface sensitivity and the possibility to reveal the electronic structure (i.e. the chemical composition) of a surface, XPS has become one of the most powerful standard techniques in surface science.

Like in the case of PEEM, the working principle of XPS is based on the photoelectric effect. However, the energy of the incident X-ray radiation is considerably higher than the excitation energy in an (UV-)PEEM being sufficient to excite electrons from the core levels of the sample (Mg $K\alpha$: 1253.6 eV, Al $K\alpha$: 1486.6 eV). The emitted photoelectrons are detected in dependence of their kinetic energy leading to a typical photoemission spectrum as it was shown schematically in Fig. 2.7. The kinetic energy of the electrons is measured respective to the Fermi level of the analyzer, which is directly related to the Fermi level of the sample via the applied voltage U . Therefore, the measured kinetic energy of the photoelectrons is given by

$$E_{kin,analyzer} = h\nu - E_B - eU - \Phi_{analyzer}. \quad (2.5)$$

The corresponding energy scheme is also illustrated in Fig. 2.11.

The photoelectrons emitted from the sample surface are separated according to their kinetic energies in a concentric hemispherical analyzer as it is shown schematically in Fig.

2 Experimental

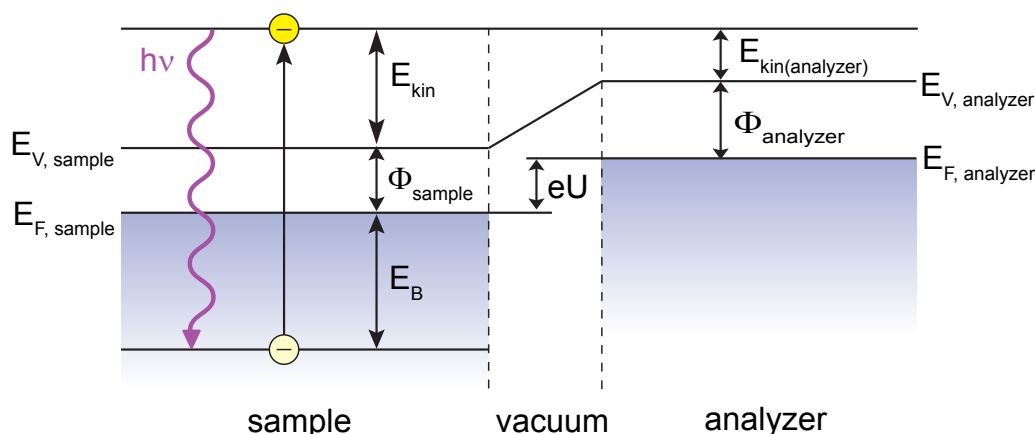


Figure 2.11: Energy levels in XPS. The kinetic energy of the photoelectrons is measured with respect to the Fermi level of the analyzer.

2.12. Such an analyzer consists of two concentric hemispheres with radii R_{in} (inner) and R_{out} (outer) to which the voltages V_1 and V_2 are applied, respectively (with $V_2 > V_1$). Only electrons with a certain energy, the so-called *pass energy*, which is determined by the applied voltages can pass the analyzer. The energy resolution amounts to some percent of the pass energy. The energy of the electrons is usually scanned at *fixed analyzer transmission*, i.e. by varying the voltages at the entrance slit and a fixed pass energy.

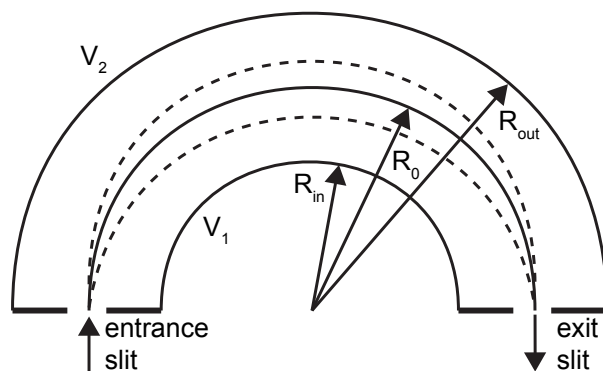


Figure 2.12: Schematic cross section through a concentric hemispherical analyzer.

In Fig. 2.13 a photoemission spectrum of metallic Pd foil excited by the Al $K\alpha$ X-ray source is shown. The wide energy range survey spectrum exhibits no significant contaminations of the sample except for traces of carbon at ~ 285 eV (C 1s peak). Several elastic peaks corresponding to the 3s, 3p, 3d, 4s and 4p core levels of Pd are distinguishable. However, core levels below the 3s level are not accessible since the energy of the Al $K\alpha$ source is not sufficient to excite the electrons from the 1s, 2s and 2p levels of Pd.

2 Experimental

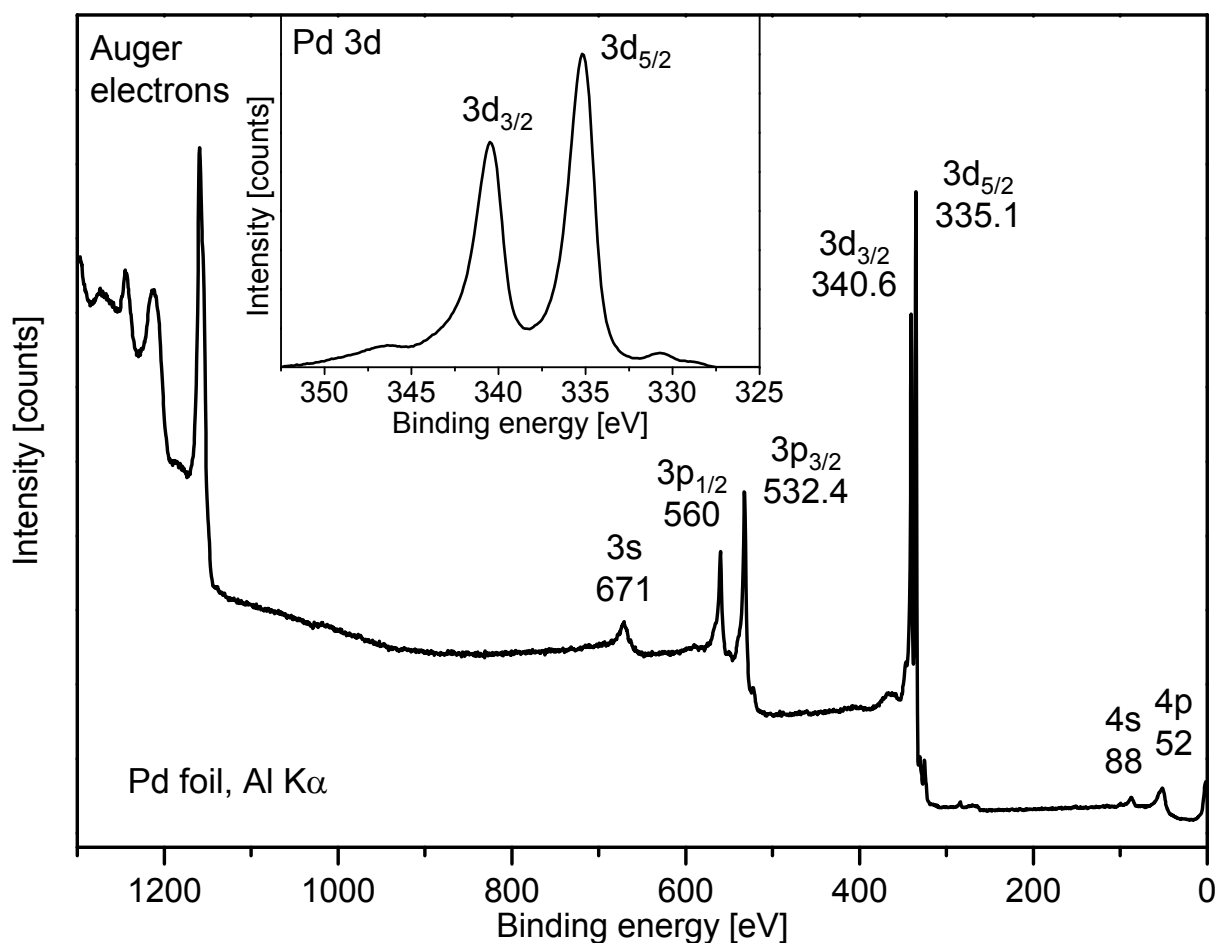


Figure 2.13: X-ray photoelectron spectrum of Pd foil measured with the Al $K\alpha$ source (1486.6 eV). The inset shows a high-resolution scan of the Pd 3d region.

The survey spectrum and also the high-resolution spectrum of the Pd 3d region in the inset of Fig. 2.13 exhibit a splitting of the peaks corresponding to atomic orbitals with an angular momentum quantum number l higher than 0 (here p and d). This splitting is a result of the spin-orbit coupling: the total angular momentum j is the sum of l and the spin momentum quantum number s , which can be either $+$ or $-1/2$. For example in case of the p-state, j can be either $1/2$ or $3/2$. The intensity ratio of a spin-orbit doublet is determined by the $(2j+1)$ -degeneracy of the corresponding energy levels, i.e. for example in case of the p-state the ratio of the peak areas of the $1/2$ and $3/2$ peaks is 1:2.

The peaks at binding energies higher than ~ 1000 eV originate from the Auger process which was already described in section 2.2.1.1. These Auger peaks can easily be distinguished from the "real" photoemission peaks by changing the incident X-ray energy. The kinetic energy of the Auger peaks is independent from the excitation energy of the X-ray

2 Experimental

source, therefore the "apparent" binding energy of the Auger electrons is shifted when the photon energy is altered by changing the X-ray anode in contrast to the source-independent binding energies of the photoelectrons.

Beside the photoelectric peaks and the Auger lines, several other processes contribute to the intensity in XPS spectra. So-called *X-ray satellite peaks* occur, if the used X-ray source is non-monochromatic (as in the experiments presented here). In this case, the X-ray emission spectrum consists not only of one characteristic line but also of several minor X-ray components at higher photon energies. Therefore, the X-ray satellite peaks always occur at lower binding energies than the primary photoemission line in a certain distance and with a certain intensity characteristic for the utilized X-ray anode material. At binding energies higher than the photoelectric peak, *shake-up lines* may occur. Such lines are attributed to a process where the emitted electron leaves the atom in an excited state, i.e. part of its kinetic energy is transferred to an other electron, so the kinetic energy of the emitted electron is reduced. The *background signal* is always higher at the high binding energy site (left) of a photoelectric peak than on the low-energy site. This is due to the inelastically scattered photoelectrons which leave the surface with a lower kinetic energy than the unscattered photoelectrons. Here, also resonant scattering of the electrons may occur leading to so-called *plasmon peaks*. Plasmons are collective excitations of the electron gas within the material. Therefore, sharp plasmon peaks are characteristic for metals, whereas plasmon peaks in less or non-conductive materials (e.g. silicon dioxide) are rather broad.

The principal advantage of XPS over other surface-analytical techniques is its sensitivity toward changes of the electronic structure of an element. The binding energies of the core level electrons depend also on the chemical surrounding of the element, so changes of the chemical surrounding lead to the so-called *chemical shift* of the corresponding photoelectric lines. If for example a metal is oxidized, the valence electrons of the metal atom are partially transferred to the oxygen atom. Since the valence electrons have a finite probability to be located close to the nucleus of the metal atom, they partially shield the innerlying orbitals from the nuclear charge. This shielding effect is reduced in case of oxidation of the metal atom, so the binding energies of the core level electrons in oxidized metal are shifted to higher values (up to 5 eV [26, 27]). In this way, the oxidation state of an element can be determined with high accuracy.

2 Experimental

Besides the qualitative analysis, XPS also provides the possibility to quantify the surface composition. The area of an XPS peak is directly proportional to the concentration of a surface species according to the following relation:

$$I = k\sigma(i, h\nu, X)f(\alpha) \int n_i(z) \exp\left(\frac{-z}{\lambda(E_{kin}) \cos\theta}\right) dz. \quad (2.6)$$

Here, k is an instrumental constant that includes the X-ray flux, and the transmission and detection probability of the analyzer for electrons with kinetic energy E_{kin} . $\sigma(i, h\nu, X)$ is the effective cross section of the element i for photoemission upon excitation of a line X by a photon energy $h\nu$. Further, $n_i(z)$ is the concentration of the element i in the probing depth z , $\lambda(E_{kin})$ is the mean free path of the escaping electrons with E_{kin} and θ is the exit angle of the electrons (to the surface normal). $f(\alpha)$ is the so-called asymmetry parameter which is 1 if the angle α between the X-ray beam and the emitted electrons is exactly 54.7° (*magic angle*). This means, that the X-ray source has to be mounted under the magic angle relative to the analyzer to maximize the intensity.

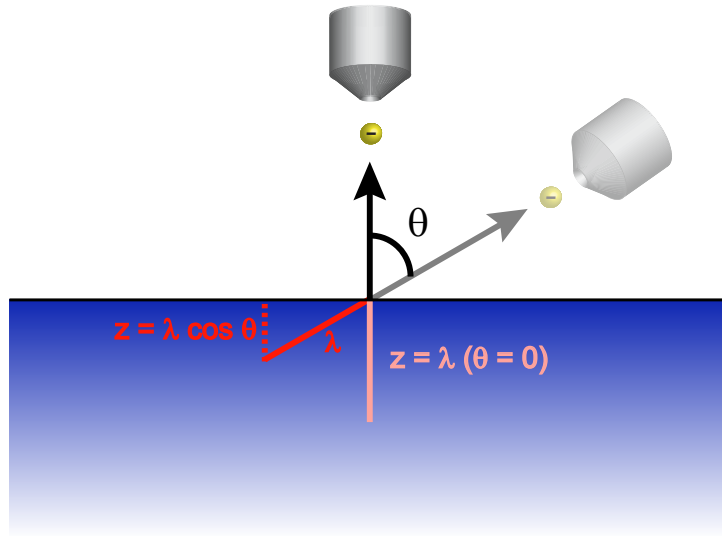


Figure 2.14: Enhancement of the surface sensitivity by tilting the sample with respect to the analyzer: The information depth z is decreased with increasing tilting angle θ .

The high surface sensitivity of XPS can be deduced from the short inelastic mean free path λ of the electrons within the sample. While the incident X-ray radiation penetrates the surface as deep as μm , λ is less than 2 nm for the kinetic energies of the photoelectrons usual in XPS ($E_{kin} = 10 - 1000 \text{ eV}$) [22]. This means 95% of the XPS signal originate from the first 2-20 atomic layers. The surface sensitivity is even increased if the sample is tilted as illustrated in Fig. 2.14. The information depth z is equal to the inelastic mean free path λ ,

2 Experimental

if elastic scattering can be neglected, [28] and the photoelectron is emitted perpendicular to the surface, i.e. if the angle θ between surface normal and analyzer is zero. If the sample is tilted by an angle θ , the information depth is given by

$$z = \lambda \cos \theta. \quad (2.7)$$

Since λ is constant for a given kinetic energy, the probing depth z is decreased and the surface sensitivity increased with an increasing angle θ .

2.2.4 Scanning Tunneling Microscopy (STM)

Scanning tunneling microscopy (STM) was used in this thesis to study the impact of Ar⁺ ion bombardment on the surface of a Pd(111) single crystal and to transfer these results to the Pd foil (see chapter 6).

STM has been developed in the early 1980's by Gerd Binnig and Heinrich Rohrer who were awarded with the Nobel Prize in 1986 "for their design of the scanning tunneling microscope" [29]. The working principle of STM depicted in Fig. 2.15 is based on the quantum mechanical tunnel effect. The surface of a conductive sample is raster scanned with a sharp metal tip at a distance of approximately 0.5 – 1.5 nm. Due to the tunnel effect, electrons can tunnel between the tip and the surface with a certain probability. In a simple (1-dimensional) quantum mechanical picture, the wave function $\psi(z)$ of an electron (with mass m) within a potential barrier with the height Φ between tip and sample decays exponentially:

$$\psi(z) \propto e^{-\kappa z} \quad \text{with} \quad \kappa = \sqrt{\frac{2m\Phi}{\hbar^2}}. \quad (2.8)$$

If the width of the barrier is d , the transmission probability of the electron and the resulting tunnel current are proportional to $|\psi|^2$, i.e.

$$I \propto e^{-2\kappa d}. \quad (2.9)$$

This tunnel current is highly sensitive to variations of the distance d between tip and sample and is used to image the surface. Usually, tunneling microscopes are operated in the constant current mode in which the tip is adjusted by a piezoelectric feedback mechanism such, that the tunnel current remains constant. Since the electrons tunnel from filled electronic states from one solid to the empty states of the other solid, the tip follows rather the contours of constant local density of states (LDOS) than the actual surface topography,

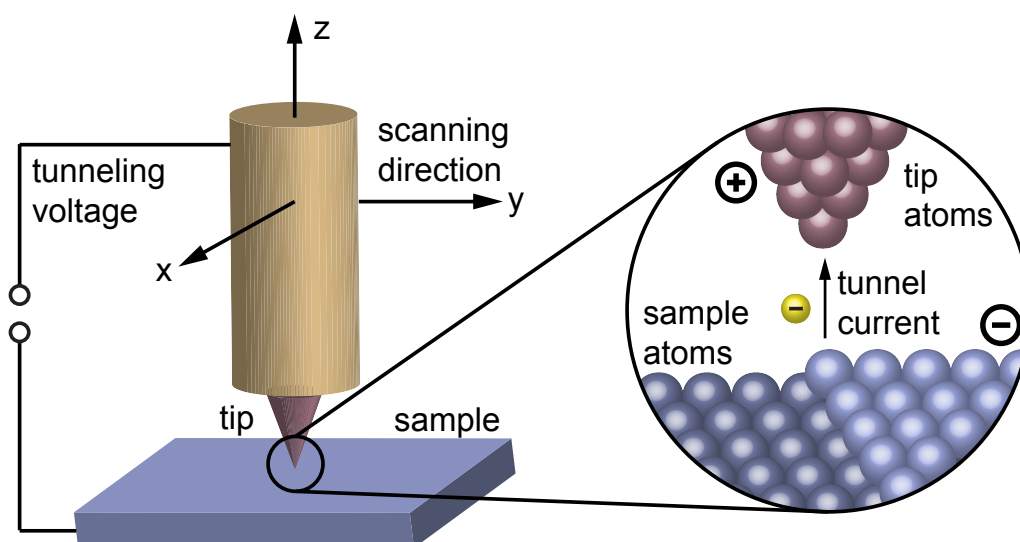


Figure 2.15: Working principle of STM. An atomically sharp tip is raster scanned across the conducting sample and the resulting tunnel current between tip and sample is used to image the surface.

thus imaging a convolution of the electronic structure of the surface near the Fermi level with its topography.

The lateral resolution in STM is restricted by the curvature radius of the used tip. Therefore, the end of the tip consists ideally of one single atom to achieve the best lateral resolution of $\sim 0.2\text{\AA}$. The sensitivity in z-direction is exceptionally high in STM, since the tunnel current decreases exponentially with the distance between tip and surface. Therefore, a resolution of up to 1 pm is achievable in vertical direction. The high sensitivity of the tunnel current towards height variations represents also a major challenge of STM: to achieve a high vertical resolution, it is necessary to maintain the tip approximately 1 nm above the surface with a certainty of 1 – 2%. Therefore, an excellent vibration isolation is compulsory which is nowadays usually realized by mechanical springs or gas spring systems.

The STM experiments performed for this thesis were carried out in a separated UHV setup with a base pressure below 10^{-10} mbar in both the preparation and analysis chambers at the Institute of Applied Physics at the Vienna University of Technology.

2.2.5 Atomic Force Microscopy (AFM)

Another scanning probe microscopy technique, the atomic force microscopy (AFM) which was developed on the basis of the STM-principle in 1986 [30], was applied in this work to image the surface of individual grains of the Pt foil (see chapter 4). AFM was chosen over STM for this purpose, since the dynamic range in z-direction is much higher in case of

2 Experimental

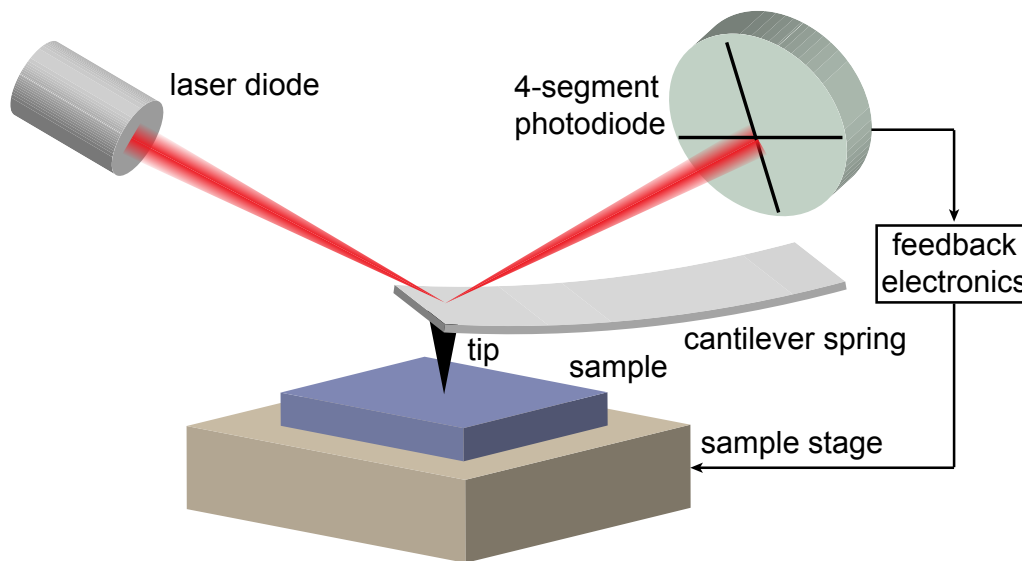


Figure 2.16: Working principle of AFM. A (vibrating) tip is scanned across the sample surface. The deflection of the tip due to mechanical forces between tip and sample is detected by a laser system and used to image the surface.

AFM. This is particularly important for topographical measurements of the grain boundaries, which are up to several μm deep and thus, are not accessible by STM. Besides, the used AFM instrument could be operated under ambient pressure conditions, though without atomic resolution.

The working principle of AFM, which is based on the detection of forces between the sample and the probe, is illustrated in Fig. 2.16. Like in the case of STM, the probe for topographical imaging of the sample surface is a very sharp tip with a nominal tip radius in the low nm range that is used to scan the sample. The tip is positioned at the end of a cantilever spring. A laser beam is focused on the backside of the cantilever and reflected towards the center of a four-segment photodiode. If the cantilever is deflected due to irregularities of the surface, the laser beam is also deflected in vertical direction and the sample stage is adjusted via a feedback mechanism in z-direction in that way, that the laser beam hits the center of the photodiode again, thus yielding the topography of the sample surface.

There are several different modes the AFM can be operated in to image the surface topography:

- In the *contact mode*, the tip is scanned over the sample in mechanical contact to the surface. The repulsive force between tip and sample which can be attributed to their overlapping wave functions and the associated repulsion according to the Pauli principle is measured and kept constant via the feedback electronics.

2 Experimental

- In the *non-contact mode* and *tapping mode*, the attractive force between the tip and the sample is measured. In both cases, the cantilever is oscillated near its resonance frequency (but with different amplitudes) which is decreased when attractive forces like the van der Waals force or capillary forces of a thin liquid film (if operated in air) act on the tip. By the feedback mechanism, a constant distance of the tip to the surface is adjusted.

The AFM measurements in this PhD thesis were all performed with a commercial AFM (NanoMan VS, Veeco) at the center for micro- and nanostructures (ZMNS) at the Vienna University of Technology. The measurements were performed under ambient conditions in tapping mode with a probe (Nanosensors) with a nominal tip radius below 10 nm.

2.2.6 Electron Backscatter Diffraction (EBSD)

Electron backscatter diffraction (EBSD) is a widely used method in materials science for quantitative analysis of polycrystalline materials such as metal foils [31]. By EBSD, it is possible to unambiguously identify the crystallographic orientation of individual grains of such a foil. EBSD measurements are usually carried out in a scanning electron microscope (SEM) equipped with an EBSD detector. The electron beam of the SEM is raster scanned across the sample which is mounted under an angle of 60 – 70° relative to the horizontal (Fig. 2.17). The electrons diffract a few times among the crystallographic planes and by exiting, they produce a characteristic pattern composed of intersecting bands (*Kikuchi bands*) which directly reflect the crystal lattice structure of the sample spot [32, 33]. These Kikuchi patterns are recorded by an EBSD detector with a CCD camera for each raster pixel and a computer software automatically analyzes the diffraction pattern for each spot and composes a so-called *orientation map* of the sample. In such an orientation map, each color corresponds to a certain crystallographic orientation according to the *inverse pole figure* which prescribes this correlation.

In this work, EBSD measurements have been carried out to identify the crystallographic structure of the grains of polycrystalline Pt and Pd foil and to prove the results which were obtained by PEEM work function analysis (see section 2.3.3). The measurements were performed in a scanning electron microscope (Quanta200F, FEI) in a separate setup at the USTEM facility (University Service Center for Transmission Electron Microscopy) of the Vienna University of Technology.

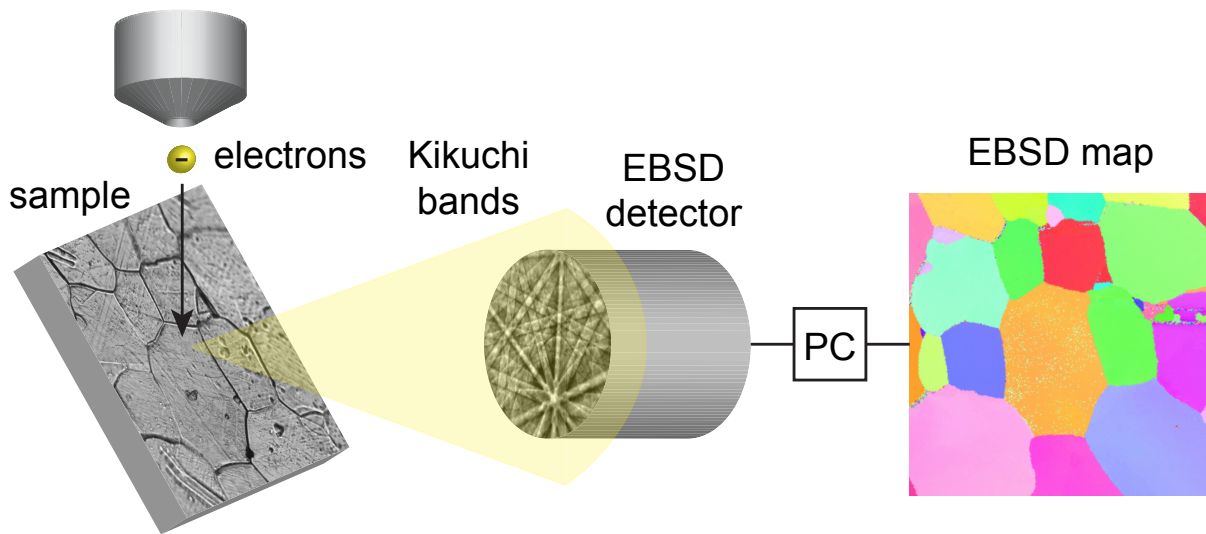


Figure 2.17: EBSD working principle. The sample is scanned by an electron beam of a SEM and the resulting characteristic Kikuchi patterns are analyzed by a software for each sample spot.

2.3 Samples

The experiments presented in this thesis were performed on two polycrystalline metal foils, a platinum and a palladium foil, described in section 2.3.1 and on Pd and PdO powder samples introduced in section 2.3.2. In section 2.3.3 the identification of the crystallographic orientation of the individual grains on Pt and Pd foil is described in detail.

2.3.1 Metal foils

The polycrystalline samples investigated in this thesis were a $10 \times 10 \text{ mm}^2$ large and 0.25 mm thick Pt foil (MaTecK, 99.99%) and a Pd foil of the same dimensions (AlfaAesar, 99.9%). Before mounting the samples in the UHV chamber, they were mechanically polished, flame annealed in air (Pt foil) and cleaned in an ultrasonic bath with acetone. To ensure the formation of grains with low Miller-index orientation, the samples were heated in UHV for several hours at 1000 – 1100 K. Figure 2.18 shows two optical micrographs recorded with a differential interference contrast microscope (Polyvar 2 MET from Reichert Microscope Services, $NA = 0.95$) as well as the corresponding PEEM images of the same sample spots of the Pt and Pd foil, respectively. The optical micrographs were used to calibrate the magnification of the PEEM images. Well-developed grains of up to $\sim 100 \mu\text{m}$ size in diameter are distinguishable on both, Pt and Pd foil. The determination of the surface orientation of the grains will be discussed in section 2.3.3. Prior to the experiments, the samples

2 Experimental

were cleaned from remaining contaminants such as carbon or sulfur by repeated cycles of Ar^+ ion sputtering perpendicular to the surface at $p_{\text{Ar}} = 1 \times 10^{-5}$ mbar and 1 keV energy (at 10 mA emission current) resulting in a typical sample current of 3.5 – 4.5 μA and consecutive annealing between 1000 and 1100 K. Despite the very low pressure of 10^{-9} – 10^{-8} mbar, before each experiment another cycle of 15 minutes sputtering, annealing and consecutive heating in oxygen at $p_{\text{O}_2} = 5 \times 10^{-7}$ mbar and 623 K (for oxidative removal of carbonaceous contaminants) was necessary. The cleanliness of the samples was finally checked by XPS.

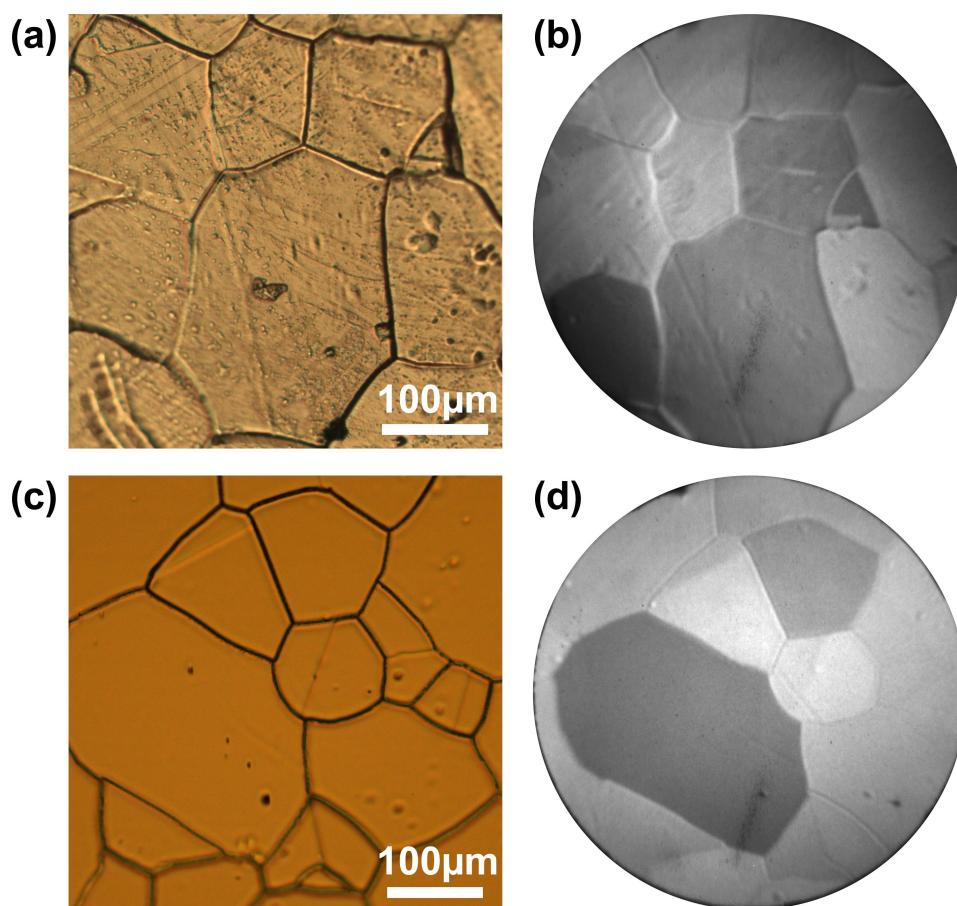


Figure 2.18: (a) Optical micrograph of the Pt foil. (b) PEEM image of the same sample spot on the Pt foil. (c) Optical micrograph of the Pd foil. (d) PEEM image of the corresponding sample spot on the Pd foil.

2.3.2 Powder samples

In addition to the metal foils, two powder samples, Pd black (Fluka AG) and Pd(II)O (Sigma Aldrich, 99.998%) powder, have been investigated in course of this thesis. Both powders

2 Experimental

have been impregnated with a press into an (oxidized) aluminum foil serving as the model support. In both cases, a $10 \times 10 \text{ mm}^2$ large sample was prepared and fixed onto the sample holder using a tantalum frame. This is shown in Fig. 2.19a for the Pd powder and in Fig. 2.19b for the PdO powder sample. In chapter 7, the characterization of the powder samples is described in more detail.

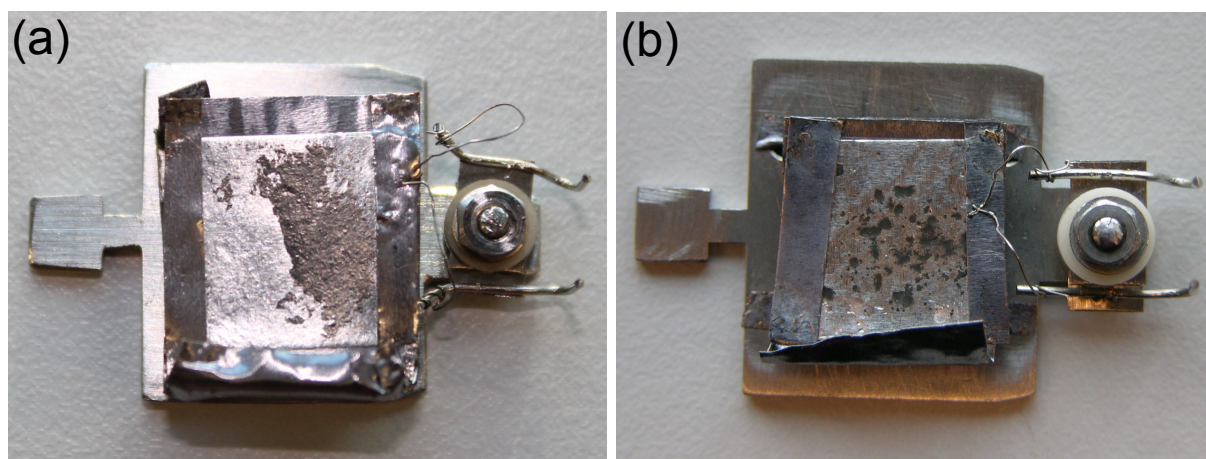


Figure 2.19: a) Pd black powder impregnated into aluminum foil and mounted onto the sample holder plate by tantalum stripes. (b) PdO powder, prepared in a similar way as the Pd powder sample.

Before mounting the powder samples in UHV, they were cleaned in an ultrasonic bath with acetone. In the UHV chamber, the preparation procedure was limited by the relatively low melting point of aluminum (660°C). Even for temperatures below 400°C , the mechanical stability of the samples was not guaranteed due to a considerable bending of the aluminum foil. Therefore, a maximum annealing temperature of 350°C was chosen. Before each experiment, the powder samples were additionally heated in oxygen to remove carbonaceous impurities at $250 - 350^\circ\text{C}$, the Pd black sample in $p_{\text{O}_2} = 5 \times 10^{-7} \text{ mbar}$ to avoid Pd oxidation and the PdO powder in $p_{\text{O}_2} = 1.3 \times 10^{-5} \text{ mbar}$. Preceding sputtering was only possible in case of the Pd black powder, since Ar^+ ion bombardment of the PdO sample led to the reduction of the oxide to the metallic state. Therefore, the PdO sample was additionally pretreated for impurity removal before mounting in UHV in an oxygen-nitrogen flux (1:1 ratio) of 50 ml/min at 500°C for $2\frac{1}{2} \text{ h}$.

2.3.3 Identification of the (hkl) domains on Pt and Pd foil

The main advantage of the used polycrystalline samples is that they consist of μm -sized domains with different surface orientation which are exposed during the experiment to ex-

2 Experimental

Table 2.1: Work function values for the three low Miller-index planes of Pt and Pd, respectively for the clean, the CO covered and the oxygen covered surfaces.

	clean [eV]	CO covered [eV]	oxygen covered [eV]
Pt(110)	5.49 [34, 35]	5.80 [35]	6.50 [35]
Pt(100)	5.84 [36]	6.04 [37]	6.30 [37, 38]
Pt(111)	5.93 [34]	6.13 [37]	6.38 [37]
Pd(110)	5.20 [39]	6.45 [40]	5.90 [40]
Pd(100)	5.65 [39]	6.64 [40]	not reported
Pd(111)	5.95 [39]	6.88 [40]	6.75 [40]

actly the same experimental conditions such as temperature or reactant pressures. Therefore, by PEEM the reaction can be followed in parallel on different surface orientations *in one experiment*. But to exploit the local kinetic results in a meaningful way, it is necessary to know the crystallographic orientation of the individual domains, i.e. the Miller indices of the domains have to be determined.

As explained in section 2.2.1, the image contrast in PEEM is based on local differences of the work function on the sample. Since the work function of a surface depends on its surface orientation and on the adsorbate, it can be used to identify the orientation of the individual domains. Table 2.1 summarizes the work function values of the three clean, CO-covered and oxygen-covered low Miller-index planes of Pt and Pd, respectively. For both metals, the order of the work function values of the clean surfaces corresponds to their atomic density ($(110) < (100) < (111)$), following Smoluchowski's theorem [23]: Increasing atomic density of the surface leads in general to an increase in the work function. Adsorbed CO increases the work function of the Pt(hkl) terminations by roughly ~ 0.2 eV and the work functions of the Pd(hkl) domains by ~ 1 eV, whereby the order of the work function values is not changed upon CO adsorption. Adsorption of oxygen on Pt(hkl) domains leads to a much stronger increase of the work function and in addition, to a change of the order: $\Phi_{\text{O/Pt}(100)} < \Phi_{\text{O/Pt}(111)} < \Phi_{\text{O/Pt}(110)}$. Especially this circumstance makes a unique identification of the crystallographic orientation of the Pt(hkl) domains possible by comparing the changes of their relative brightness in the PEEM images upon CO and oxygen adsorption. In Fig. 2.20 PEEM images of the clean, the CO- and the oxygen-covered Pt foil are shown. Since in PEEM surfaces with higher work function appear dark, the PEEM image of the oxygen covered Pt surface is the darkest. The Miller-indices of the individual domains determined by a comparison of the relative brightness with the work function values are indicated in Fig. 2.20 a.

2 Experimental

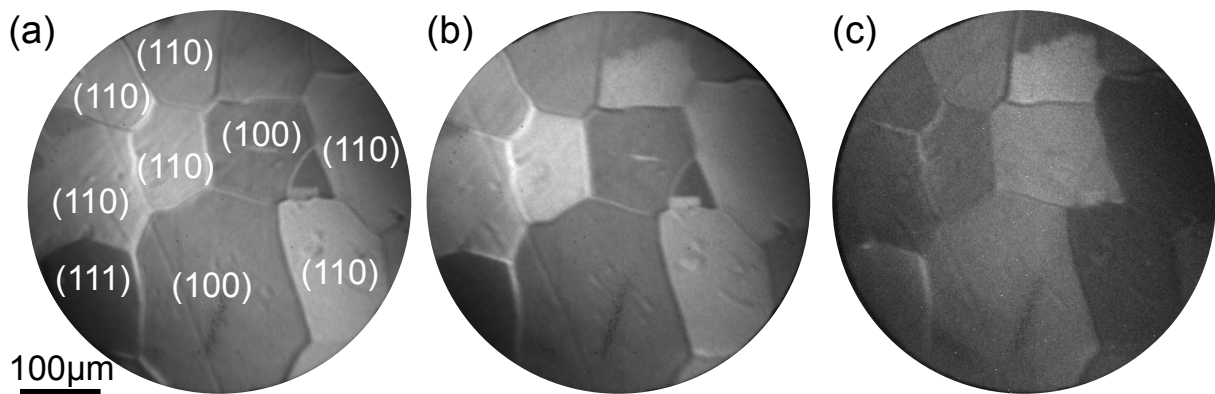


Figure 2.20: (a) PEEM image of the clean Pt foil. The surface orientation of the individual grains is indicated. (b) PEEM image of the CO-covered Pt foil. (c) PEEM image of the oxygen-covered Pt foil. The surface appears dark in PEEM since adsorbed oxygen increases the work function of Pt more than CO does.

Unfortunately, not all work function values of oxygen covered Pd(hkl) surfaces are known, so for Pd, another method is required for an unambiguous identification of the surface orientation. Therefore, electron backscatter diffraction was performed on the sample spot of the Pd foil where most of the kinetic measurements were carried out. As described in section 2.2.6, in EBSD a color-coded "map" of the sample surface is produced (Fig. 2.21a) where each color corresponds to a certain Miller index according to the inverse pole figure also shown in Fig. 2.21a (right). In Fig. 2.21b the Miller indices which are derived from the EBSD measurement are indicated within the corresponding PEEM image of the Pd sample.

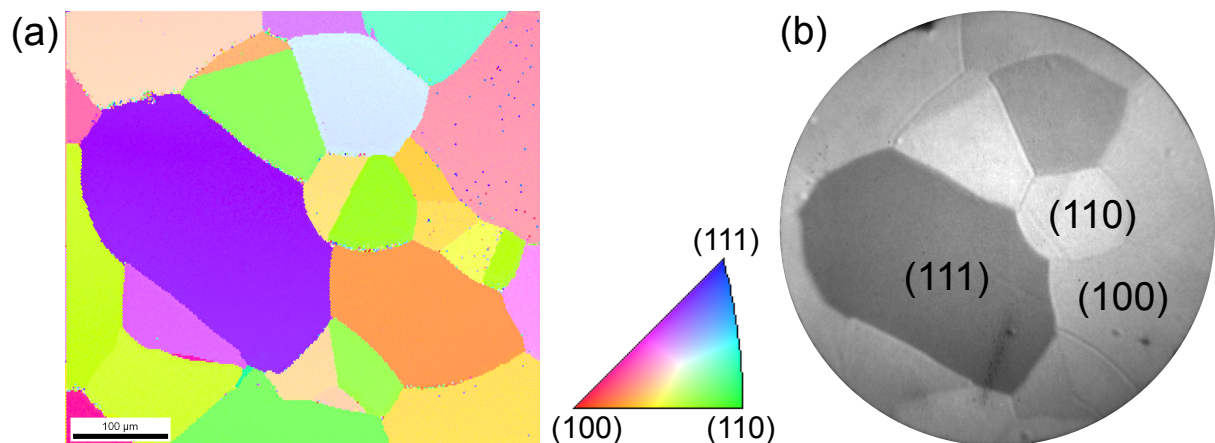


Figure 2.21: (a) EBSD map of the Pd surface. (b) Corresponding PEEM image of the same sample spot. The Miller indices derived from the EBSD are indicated as well. See also chapter 6.

2.4 Experimental procedure

During the kinetic experiments, the partial pressures of the reactants, i.e. CO and oxygen, and of the reaction product (CO₂) are monitored by the mass spectrometer, which is positioned close to the PEEM in the UHV chamber. The mass spectrometer scans over a mass-to-charge ratio (m/z) range from 27 to 45, including therefore CO ($m/z = 28$), O₂ ($m/z = 32$) and CO₂ ($m/z = 44$) in one scan. The duration of one scan is approximately 3–4 s. In parallel, the screen of the PEEM is recorded by a high-speed CCD camera with a maximum time resolution of 5 μ s. However, the usual time resolution applied in the kinetic experiments was 100 – 250 ms. Before each experiment, the brightness of the PEEM image was adjusted by slight variation of the sample position, especially of the distance between the sample and the transfer lens of the PEEM (ca. 4 – 10 mm) and the rotation and the tilt angles. The UV lamp focusing and the PEEM voltage settings also play an important role for brightness adjustments. For evaluation of the recorded PEEM video-frames, the intensity of a chosen region-of-interest within the field of view can be temporally correlated with the MS-dataset by computer software, yielding the pressure dependence of the PEEM intensity.

CO OXIDATION ON PT GROUP METALS

In this chapter, the two metals serving as the catalysts for the CO oxidation reaction in this PhD thesis, namely platinum and palladium, are introduced and the fundamentals that are important to understand the reaction mechanism, as e.g. the interaction between the metal surfaces and different adsorbates, are presented.

In section 3.1, the low Miller index surfaces of platinum and palladium are described which are due to their stability the most relevant surface orientations. Hereby, also some peculiarities as the reconstruction of the Pt(100) and Pt(110) surfaces are captured.

The adsorption properties of carbon monoxide, oxygen and carbon dioxide on all low Miller index (hkl) planes of platinum and palladium are summarized in section 3.2. Since oxygen interaction especially with palladium, is quite complex, not only simple chemisorption but also subsurface oxygen and surface oxide formation are described in detail.

Due to the necessity of pollution emission control, CO oxidation is one of the most important and also the most investigated surface reactions in heterogeneous catalysis. Moreover, its relative simplicity -only two quite simple reactants are involved- makes it a suitable model reaction and facilitates its study, both experimentally and theoretically. In section 3.3, the well-known Langmuir-Hinshelwood (LH) mechanism of the CO oxidation reaction is depicted. As a result of the LH mechanism, the complex phenomenon of bistability occurs in a certain range in $(p_{\text{O}_2}, p_{\text{CO}}, T)$ -parameter space, what can be gathered by *kinetic phase diagrams*, also described in section 3.3. The state-of-the-art concerning the influence of (Pd) surface oxides on the reactivity in CO oxidation is outlined in section 3.3.3.

3.1 Low Miller index planes of platinum and palladium

Platinum and palladium both have a face-centered cubic (fcc) lattice structure with a lattice constant of $a_{\text{Pt}} = 3.92\text{\AA}$ and $a_{\text{Pd}} = 3.88\text{\AA}$, respectively. The three low Miller index planes (100), (110) and (111) have the lowest surface energy [41], i.e. these surfaces are most stable and a metal foil is expected to recrystallize upon heating in crystallites with mainly these surface orientations. In fig. 3.1a the three unreconstructed [100]-, [110]- and [111]-oriented surfaces of an fcc metal are shown as a ball model. The lattice constants for the isotropic cubic (100) and hexagonal (111) orientations are the same as the nearest neighbor distance $a'_{(100)} = b'_{(100)} = a'_{(111)} = b'_{(111)} = a/\sqrt{2}$, i.e. $a_{\text{Pt}}^{\text{nn}} = 2.77\text{\AA}$ and $a_{\text{Pd}}^{\text{nn}} = 2.74\text{\AA}$. The lattice constants of the anisotropic (110) surface of platinum are $a'_{(110)} = a_{\text{Pt}}^{\text{nn}} = 2.77\text{\AA}$ in $[1\bar{1}0]$ direction and $b'_{(110)} = a_{\text{Pt}} = 3.92\text{\AA}$ in $[001]$ direction, and correspondingly for Pd $a'_{(110)} = 2.74\text{\AA}$ in $[1\bar{1}0]$ direction and $b'_{(110)} = 3.88\text{\AA}$ in $[001]$ direction. In contrast to the Pd(hkl) and the Pt(111) surfaces, the clean Pt(100) and Pt(110) surfaces are thermodynamically only stable in a reconstructed state. Figure 3.1b shows the reconstruction of these two surfaces.

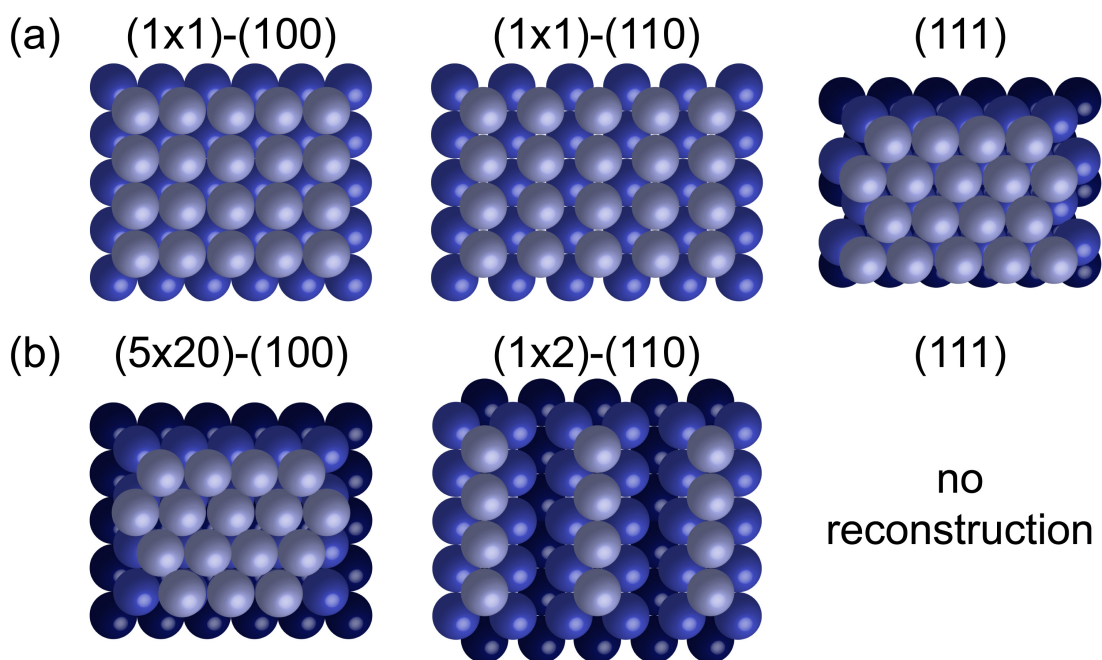


Figure 3.1: (a) Surface structure of the unreconstructed (1x1)-(100), -(110) and -(111) surfaces. (b) Reconstructed Pt(5 × 20)-(100) and (1 × 2)-(110) surfaces.

Pt(100) reconstructs in a so-called (hex) or (5 × 20) reconstruction [42] which is lifted upon CO and oxygen adsorption. In case of CO the lifting of the reconstruction starts already at the very low critical coverage of $\Theta_{\text{crit}} = 0.05\text{ML}$ (monolayer) and is finished at

3 CO oxidation on Pt group metals

$\Theta_{\text{CO}} = 0.5\text{ML}$ [43–47]. Oxygen lifts the reconstruction at a critical coverage of $\Theta_{\text{crit}} = 0.1\text{ML}$ [38, 48–50]. To restore the (hex) reconstruction, the coverage needs to drop below $\Theta_{\text{CO}} = 0.3\text{ML}$ or $\Theta_{\text{O}} = 0.4\text{ML}$, respectively [44, 49]. It is also possible to prepare a clean (1×1) -Pt(100) surface [51] which is then in a metastable state since the transformation into the (hex) phase is activated by an energy ranging from 0.76 eV [52] up to 0.87 – 1.09 eV [53, 54]. The reconstruction of the Pt(100) surface is called "hex" due to a quasi-hexagonal rearrangement of the topmost surface atoms which is oriented along the $[0\bar{1}1]$ direction of the underlying (1×1) "substrate" and exhibits a corrugation of $\sim 1\text{\AA}$ in height and 14\AA in length perpendicular to this direction [55–58]. Such a corrugation is formed since the hexagonal surface layer is only poorly matching the underlying cubic lattice what is also reflected in the large (5×20) LEED periodicity [42, 59]. The adsorbate-induced surface phase transition (SPT) from the hexagonal to the (1×1) reconstruction is associated with a strong surface roughening since the $\sim 20\%$ higher atomic density of the (hex) phase has to be compensated during the transformation to the (1×1) structure. This proceeds via a collective ejection of entire rows of Pt atoms along the $[0\bar{1}1]$ direction forming elongated ad-islands between $\sim 15\text{\AA}$ [58] and 70\AA [57] size depending on the temperature, i.e. the (hex) $\rightarrow (1 \times 1)$ surface phase transition proceeds in a highly anisotropic way [58, 60, 61]. This effect has a significant influence on the propagation of reaction-diffusion fronts during the CO oxidation on Pt(100) domains what will be discussed in more detail in chapter 4.

Pt(110) reconstructs in a (1×2) or so-called "missing row" structure [62–64], since every second row along the $[1\bar{1}0]$ direction of the topmost atomic layer is missing as can be seen in Fig. 3.1b. The activation energy for the $(1 \times 1) \rightarrow (1 \times 2)$ SPT is with $E_A = 0.26\text{eV}$ considerably lower than in case of Pt(100) what is explained by the circumstance that the (hex) reconstruction of the (100) surface is not in registry with the (1×1) substrate [65, 66]. The reconstruction of the Pt(110) surface is driven by the lowering of the surface energy upon formation of (111) microfacets. It is lifted upon CO adsorption above the critical coverage of $\Theta_{\text{crit}} = 0.2\text{ML}$ and is finished at a coverage of 0.5ML [66–70], oxygen does not lift the reconstruction. As in case of Pt(100), this surface phase transition is also associated with a noticeable mass transport of 50% of the topmost monolayer. However, on Pt(110) faceting occurs only during the CO oxidation reaction, i.e. with CO *and* oxygen present on the surface [71, 72], thereby enhancing the catalytic activity of the Pt(110) surface [73].

3.2 Interaction of adsorbates with Pt and Pd surfaces

3.2.1 CO Adsorption on Pt(hkl) and Pd(hkl) surfaces

Carbon monoxide adsorption on Pt group metals is the most extensively studied and probably the best understood adsorption system in surface science. On both, Pt and Pd, CO adsorbs non-dissociatively with the carbon atom pointing towards the metal surface. The bonding between CO and the metal surface can be described by the so-called *Blyholder-model* [74] which is illustrated in figure 3.2. The electrons of the filled 5σ molecular orbital, which is the *highest occupied molecular orbital* (HOMO) of CO, are partially transferred to the d-band of the metal (donation). At the same time, a backdonation process via transfer of electrons from the metal d- and p-orbitals to the antibonding $2\pi^*$ orbital, i.e. the *lowest unoccupied molecular orbital* (LUMO), of CO occurs. On one side, this leads to a strengthening of the CO-metal bond, but on the other side, the internal carbon-oxygen bond is weakened in comparison to the gas-phase molecule. This is for example reflected in a shift

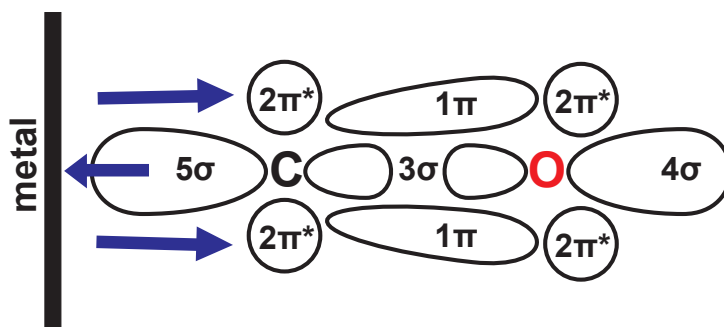


Figure 3.2: Blyholder model of CO adsorption on metal surfaces. [74]

of the CO stretching frequency to lower values compared to the gas phase molecule in infrared experiments [75]. The nature of the adsorption site of CO also plays a significant role: on Pt group metals CO can adsorb *on top* of a metal atom, be *bridge-bonded* between two metal atoms, *hollow-bonded* in an fcc site of a (111) surface or 4-fold coordinated between 4 atoms of a (100) surface. The strength of the backdonation increases with increasing coordination number and therefore, the frequency shift to lower wavenumbers is also higher for higher coordination number. The stronger backdonation for higher-coordinated CO molecules is also reflected in the coverage dependence of the work function of CO-covered Pt. Most of the well studied Pt(hkl) surfaces exhibit a local minimum in the relative work function at low CO coverages, but at saturation coverage the work function of Pt is *increased* in comparison to adsorbate-free Pt. This is explained by the increased backdonation for

3 CO oxidation on Pt group metals

bridge-bonded CO resulting in a net charge transfer from the metal to the CO molecule and leading to an opposite resulting dipole moment in comparison to onefold coordinated CO [66, 75].

The adsorption properties of CO depend strongly on the orientation of the underlying surface. On *Pt(100)*, the *initial sticking coefficient* s_0 of CO, i.e. the probability that a molecule from the gas phase hitting the clean surface adsorbs, was found to be 0.6-0.75 [44, 51], independent of whether it adsorbs on the (hex) or on the (1×1) phase. Also a value of 1 for s_0 has been reported [48]. The *initial heat of adsorption* E_{ads}^0 on (hex)-*Pt(100)* is 179 kJ/mol and 215 kJ/mol on the unreconstructed (1×1) -*Pt(100)* surface [47]. Since the surface phase transition to the (1×1) phase already starts at $\Theta = 0.05$ ML, no further adsorption properties of CO on the (hex)-*Pt(100)* surface can be listed. On the (1×1) phase, CO first forms a $c(2 \times 2)$ superstructure at $\Theta_{\text{CO}} = 0.5$ ML adsorbing only in *on top* positions, then, at $\Theta_{\text{CO}} = 0.66$ ML, a $(\sqrt{2} \times 3\sqrt{2})R45^\circ$ superstructure is formed involving also *bridge* positions, and finally CO saturates in a $c(4 \times 2)$ superstructure at a coverage of 0.75 ML [46, 51]. CO desorption from the (1×1) -*Pt(100)* surface, as determined from thermal desorption spectroscopy (TDS), starts with an α -"shoulder" at $\sim 400 - 450$ K resulting in the main desorption peak (β) at $500 - 520$ K [44, 48].

In turn, on the *Pt(110)* surface the initial sticking coefficient of CO is $0.8 - 1$ [67, 76-79], the initial heat of adsorption is $E_{\text{ads}}^0 = 183$ kJ/mol [79]. Upon CO adsorption below $T = 250$ K, the (1×2) reconstruction of *Pt(110)* is not lifted and CO forms a $c(8 \times 4)$ LEED superstructure whereby the CO molecules adsorb perpendicular to the substrate only in *on top* positions of the topmost surface layer [63, 69, 80-83]. It has to be noted that additional adsorption of 22° tilted CO molecules on *bridge* sites of the (111) microfacets has also been reported for this superstructure [84]. Adsorption at room temperature leads, as already mentioned, to the surface phase transition to the (1×1) phase, the driving force of which is the higher binding energy of CO on low-coordinated Pt atoms (the number of low-coordinated Pt atoms available for CO adsorption is doubled upon the SPT) [70]. At room temperature (RT), the CO molecules do not form an ordered superstructure resulting in an unchanged (1×1) LEED pattern [69, 84]. By cooling the *Pt(110)* surface in CO from 600 K to RT, an ordered $(2 \times 1)p2mg$ structure can be formed [70, 84] which was first assigned as $(2 \times 1)p1g1$ [66, 67, 69, 77]. At this structure the saturation coverage is $\Theta = 1$ and the molecules are adsorbed only in *on top* positions. Since the van der Waals distance of CO molecules is larger than the nearest neighbor distance of Pt (3.2 \AA vs. 2.77 \AA), the CO molecules are tilted [67, 70, 83, 84] by an angle of $\sim 22^\circ$. Similar as in case of *Pt(100)*,

3 CO oxidation on Pt group metals

CO desorbs from Pt(110) in two states, an α state at 400 – 430K and a β state at $T \sim 520$ K [67, 68, 76–78].

The reported initial sticking coefficient s_0 of CO on *Pt(111)* varies between 0.34 and 0.84 [76, 85]. Steininger *et al.* even found a maximum of the sticking coefficient at a coverage of $\Theta_{\text{CO}} = 0.1$ of 0.85 while the initial value was 0.56 [75]. On oxygen covered Pt(111) the sticking coefficient of CO was found to be still 0.7 [86]. The initial heat of adsorption is $E_{\text{ads}}^0 = 180$ kJ/mol [86]. CO forms a $(\sqrt{3} \times \sqrt{3})R30^\circ$ superstructure at $\Theta = 0.33$ adsorbing first only in *on top* positions. At $\Theta = 0.5$ the CO superstructure transforms into a $c(4 \times 2)$ structure with additional *bridge* positions [86–88]. The saturation coverage at room temperature is 0.5, but a "compression structure" with $\Theta \sim 0.7$ can also be prepared at low temperatures [76, 86, 87]. The desorption maximum of CO from Pt(111) in TDS spectra lies between 400K and 450K [75, 76, 85, 87, 88].

On the (100) surface of *palladium* CO adsorbs with a sticking probability of $s_0 = 0.6 - 0.8$ and an initial heat of adsorption E_{ads}^0 of 165 kJ/mol [89, 90]. At room temperature, a $(2\sqrt{2} \times \sqrt{2})R45^\circ$ LEED pattern is formed, which corresponds to a coverage of $\Theta = 0.5$ ML with CO bonded in *bridge* positions [90–94]. Higher coverages of 0.67 ML and 0.75 ML with corresponding $(3\sqrt{2} \times \sqrt{2})R45^\circ$ and $(4\sqrt{2} \times \sqrt{2})R45^\circ$ structures can also be achieved by succent exposure to CO at lower temperatures, with the CO molecules also adsorbed in *bridge* sites, but tilted to compensate for the dipole-dipole repulsion [95]. CO desorbs from Pd(100) between 480K and 515K [90, 92].

CO adsorption on *Pd(110)* has been investigated with LEED in one of the very first surface science studies by Ertl and Rau [96]. The initial sticking coefficient of CO on Pd(110) is 1 on the clean surface and still 0.9 for a surface already covered with 0.4 ML of CO. However, if the surface is precovered with 0.4 ML of oxygen, the sticking probability for CO decreases to a value of 0.5 [97]. The heat of adsorption was determined to be 167 kJ/mol [98]. Above a critical coverage of 0.3 ML, a (4×2) LEED pattern has been observed which is associated with a starting reconstruction of the (110) surface to the (1×2) -missing row structure due to a higher heat of adsorption of CO on the (1×2) structure than on the unreconstructed surface [99]. The reconstruction nucleates in patches and is fully converted at the room temperature saturation coverage of 0.75 ML [99–101]. CO is located in *bridge* positions on the ridges and in the grooves of the reconstructed Pd(110)- (1×2) surface. Higher coverages up to 1 ML may be achieved by CO adsorption at lower temperatures or pressures above 10^{-6} Torr. In that case, the reconstruction of the Pd(110) "substrate" is lifted again and a $(2 \times 1)p2mg$ LEED pattern is observed [98, 99, 101]. Also for this structure, the favored adsorption sites are on *bridge* positions whereby the CO molecules form an alternate

3 CO oxidation on Pt group metals

tilted overlayer or so-called "herring-bone" structure [93, 101–105]. Desorption of CO from Pd(110) occurs in three different states, namely an α -state at 330K and two β -states at 400K and 475K [106].

On *Pd(111)* CO adsorbs with a probability near unity [107] and an adsorption energy of 142kJ/mol [98]. With increasing exposure to CO, six different LEED patterns have been observed, the most important of which are the $(\sqrt{3} \times \sqrt{3})R30^\circ$ structure at $\Theta = 0.33$ ML, the $c(4 \times 2)$ structure at the room temperature saturation coverage of 0.5ML and the (2×2) structure at the coverages of 0.66ML and 0.75ML at 200K and 90K, respectively [108, 109]. When the surface is covered with a third of a monolayer, the CO molecules adsorb on fcc hollow sites [91], at saturation coverage additional on top positions are occupied [109, 110]. The desorption temperature is reported to be between 450K and 500K [108, 109].

3.2.2 Oxygen adsorption on Pt(hkl) and Pd(hkl) surfaces

In general, oxygen adsorption on Pt group metals is more complicated than CO adsorption since a dissociation step is involved in the adsorption process. Therefore, oxygen adsorbs on all three (hkl) surfaces of Pt and Pd in a molecular state at low temperatures before it chemisorbs dissociatively. In addition, oxygen is able to penetrate the topmost surface layer(s) of the substrate to form subsurface oxygen on platinum and palladium and different surface oxides on palladium. Since these effects are relatively complex, they are treated in the separate subsections 3.2.2.2 and 3.2.2.3.

3.2.2.1 Oxygen chemisorption

On the (hex) reconstruction of *Pt(100)* oxygen adsorbs at low temperatures in the molecular state, e.g. at 123K with a sticking coefficient of $s_0 = 0.13$ and a saturation coverage of $\Theta_{\text{sat}}(\text{O}_2) = 0.38$ ML [111]. Upon heating, the oxygen molecules do not dissociate but only desorb at 144K and the initial sticking coefficient for the *dissociative* oxygen adsorption on the (hex)-Pt(100) surface is only $10^{-4} - 10^{-3}$ [38]. On (1×1) -Pt(100) the molecular adsorption of oxygen at 123K occurs with a sticking coefficient of 0.4, but in contrast to the (hex) surface, only $\sim 10\%$ of the molecular O_2 present on the surface desorbs upon heating above 144K while the rest dissociates. Consequently, room temperature adsorption on the metastable (1×1) phase leads to dissociative chemisorption with a sticking probability of 0.1 [38]. The saturation coverage is $\Theta_{\text{sat}}(\text{O}) = 0.63$ ML exhibiting a "complex" LEED pattern [49], while for a coverage of 0.44ML a (3×1) LEED pattern has been observed. The *bridge* position has been determined to be most favorable for atomic oxygen adsorption on

3 CO oxidation on Pt group metals

(1 × 1)-Pt(100) [50, 112, 113]. Desorption takes place in two main states, first at 660 – 675 K accompanied by a transition of the LEED pattern from "complex" to (3 × 1) and second at 700 – 710 K with a transition of the LEED pattern to the clean (hex) phase [38, 48]. A third desorption state at 950 K was assigned to desorption from defect sites [38].

As already mentioned, oxygen does not lift the (1 × 2) reconstruction of *Pt(110)*. Molecular oxygen physisorbs on Pt(110) below 60 K and chemisorbs with a sticking coefficient of 0.9 below 160 – 200 K [114–116]. Heating the chemisorbed molecular oxygen layer to 300 K leads partially to desorption of O₂ at ~ 200 K and partially to dissociation of the oxygen, resulting in a pure layer of atomic oxygen with a coverage of $\Theta = 0.7$ ML. The sticking probability for adsorption at room temperature is only 0.3 – 0.4 [79, 117, 118], the saturation coverage in this case is $\Theta = 0.3$ ML exhibiting a $c(4 \times 2)$ LEED pattern [114] and the initial heat of adsorption is $E_{\text{ads}}^0 = 335$ kJ/mol [79]. A coverage of up to 0.85 ML can be achieved by successive room temperature adsorption and additional oxygen exposure at lower temperatures [115, 116]. The preferred adsorption sites are proposed to be fcc sites on the (111) microfacets of the reconstructed Pt(110) surface [116–118]. The atomic oxygen desorbs from Pt(110) under recombination at 700 – 750 K [114, 118].

On *Pt(111)* oxygen can adsorb in three different states: as a physisorbed multilayer of molecular oxygen with a sticking coefficient near unity below $T = 40$ K, as chemisorbed molecular oxygen below 150 K and as atomic oxygen up to ~ 700 K [119–121]. In both, the physisorbed and the chemisorbed molecular state, the oxygen molecule is oriented parallel to the metal surface and is located in hollow sites [122–124]. The atomic chemisorption can be achieved either by oxygen exposure above 150 K leading directly to dissociative adsorption with a sticking coefficient of $s_0 = 0.06$ and an initial heat of adsorption of $E_{\text{ads}}^0 = 339$ kJ/mol [86] or by heating the molecularly adsorbed phase above 150 K whereby the molecular oxygen partially desorbs and partially dissociates [120, 121, 123–126]. The atomic oxygen forms a $p(2 \times 2)$ overlayer at a saturation coverage of $\Theta = 0.25$ ML adsorbing only in threefold hollow sites [113, 124, 127, 128]. The desorption maximum in TDS spectra of atomic oxygen desorbing from Pt(111) is approximately at $T = 700$ K [120, 121, 123, 125, 126].

On the (100) surface of *palladium*, oxygen is also able to adsorb in a molecular state below 120 K, but already at these temperatures atomic oxygen is present on the surface [129]. At room temperature, only dissociative adsorption of oxygen occurs on Pd(100), with an initial sticking coefficient s_0 varying from 0.1 [130] to 0.75 [131]. In general, the sticking probability of oxygen on low-Miller index Pd surfaces is much higher than on the corresponding Pt(hkl) surfaces. Adsorption of 0.25 ML oxygen on Pd(100) at room temperature

3 CO oxidation on Pt group metals

leads to a $p(2 \times 2)$ LEED structure and increasing the coverage to 0.5ML leads to a $c(2 \times 2)$ structure [92, 130]. For both structures, the oxygen atoms are adsorbed in fourfold hollow sites [94]. Further exposure of oxygen to Pd(100) at more elevated temperatures leads to the formation of several surface oxides which will be discussed in more detail in section 3.2.2.3 [130, 132]. Desorption of oxygen occurs at approximately 700K and 840K [92]. If silicon impurities are present in the bulk of the Pd crystal, exposure to oxygen at temperatures above $\sim 1000\text{K}$ may induce the formation of a non-reactive $\text{PdO}_x\text{-SiO}_y$ species which will be discussed later in more detail (see section 7.3) [130].

Like the adsorption of CO, oxygen adsorption on $\text{Pd}(110)$ has been investigated already in a very early LEED study by Ertl and Rau where a sequence of different LEED patterns with increasing oxygen coverage has been observed [96]. At 100K, 1ML of oxygen is adsorbed molecularly and atomically, but even at these low temperatures, only 10% molecular oxygen are present on the surface [106, 133, 134]. Heating this surface leads to a sequence of a "pseudo- (2×1) ", $c(2 \times 6)$ and a $c(2 \times 4)$ (at RT) LEED patterns, with only atomic oxygen left above 200K [133, 134]. Above 160K the sticking coefficient for dissociative adsorption varies between $s_0 = 0.86$ [106] and 0.96 [135]. Depending on the coverage, two different LEED structures have been observed upon oxygen adsorption between 400 and 500K: a "pseudo- (1×3) " or $(2 \times 3) - 1D$ structure corresponding to a coverage of $\Theta = 0.23\text{ML}$ and a $c(2 \times 4)$ structure associated with the saturation coverage of 0.5ML [106, 134–136]. Both LEED structures involve a reconstruction of the Pd(110) surface, namely a (1×3) reconstruction for the lower coverage and a (1×2) reconstruction for the higher coverage, i.e. either every second row along the $[1\bar{1}0]$ direction of the topmost surface layer is missing or every third row [134, 137–144]. For both reconstructions, the oxygen atoms are adsorbed in a zigzag chain configuration in the threefold hollow (fcc) positions of the (111) microfacets. The (1×2) reconstruction is metastable, it can be stabilized by hydrogen reduction of the $c(2 \times 4)$ -O layer, but it returns to the (1×1) configuration for $T > 355\text{K}$ [139]. The main desorption peaks of oxygen from Pd(110) in TDS spectra are located at $T_\alpha = 120\text{K}$ associated with molecular oxygen desorption, $T_{\beta_1} \sim 700\text{K}$ and $T_{\beta_2} \sim 800\text{K}$ [133, 135, 145]. The β_1 state was associated with subsurface oxygen, since it only evolves after low temperature and high exposure adsorption [133].

The dissociative adsorption of oxygen on $\text{Pd}(111)$ is associated with a sequential population of several molecular precursor states, namely one physisorbed and three different chemisorbed states which occur upon adsorption of oxygen below 80K [146, 147]. Heating the Pd(111) surface precovered with molecularly adsorbed oxygen above 200K leads to the complete dissociation of the oxygen molecules and an associated (2×2) LEED pat-

3 CO oxidation on Pt group metals

tern [146]. The sticking coefficient of oxygen for room temperature adsorption reported in the literature varies between 0.3 and 0.74 [107, 108, 147–150]. The saturation coverage at room temperature is $\Theta_{\text{sat}} = 0.25\text{ML}$ and the corresponding LEED structure is $p(2 \times 2)$ [107, 108, 148, 149, 151], but a higher coverage of 0.33ML with a corresponding $(\sqrt{3} \times \sqrt{3})R30^\circ$ LEED pattern may also be achieved [148]. The favored adsorption sites for both, the precursor states and the atomic adsorption, are fcc hollow sites [148, 152]. Oxygen desorbs at a temperature of 850K from Pd(111), but also diffuses into the bulk [108, 148]. This process already takes place when the Pd(111) surface is exposed to oxygen at $T = 523\text{K}$: oxygen migrates into the subsurface region and a surface oxide is formed [149] (see section 3.2.2.3). Also a "high temperature resistant surface oxide" can be formed by high temperature oxygen adsorption which can only be removed by sputtering [148]. Such a phase is most probably due to SiO_x formation by silicon impurities which are dissolved in the bulk (see section 7.3).

3.2.2.2 Subsurface oxygen

Besides the relatively simple chemisorption of oxygen on platinum and palladium surfaces, oxygen is also able to penetrate the topmost surface layer to form a variety of more strongly bound oxygen-metal species called "subsurface oxygen", "subsurface oxide" or "surface oxide". Subsurface oxygen is defined as oxygen located between the first two layer of metal atoms at interstitial sites and manifests in a higher apparent coverage Θ than the saturation coverage of chemisorbed oxygen. Subsurface oxygen has been observed on a Pt(100) [153, 154] and a Pt(110) single crystal [155–157] in PEEM experiments, and also on Pt(210) [158] and Pt(111) [159]. In the PEEM experiments, oxygen islands, which appear dark in PEEM corresponding to high work function values, were converted on Pt(100) as well as on Pt(110) under certain conditions to bright patches (i.e. regions of *low* work function) what was explained by an inversion of the dipole moment at the surface caused by the negative oxygen atoms now located below the positively charged surface metal atoms. In both cases, surrounding CO was found to accelerate the inversion, so a mechanism was established which made surface restructuring responsible for subsurface oxygen formation [160]. Reaction of the subsurface oxygen with CO is rather slow [153], it desorbs only at temperatures around 1000K [161], and also under CO oxidation reaction conditions it was found to be quite stable [154]. However, in case of the Pt(111) single crystal a lowering of the reactivity of the surface in the CO oxidation reaction has also not been found [159].

On Pd(110), subsurface oxygen formation which is also accompanied by a work function decrease [133, 162] was discussed to be responsible for the observed oscillations in the CO_2

3 CO oxidation on Pt group metals

reaction rate during CO oxidation at elevated pressures ($p_{\text{O}_2} > 10^{-3}$ Torr), i.e. to modulate the catalytic activity of the surface [162, 163]. Later, subsurface oxygen on Pd(110) was regarded to nucleate an oxide phase [164] which might be responsible for the oscillations in CO oxidation at elevated oxygen pressures. On Pd(111), after the first oxygen incorporation into the surface, a surface oxide is immediately formed [165]. The *surface oxides* are treated in the next section.

3.2.2.3 Formation of surface oxides

Before "real" oxidation of a metal takes place, i.e. the formation of bulk MeO_x , the surface of the metal is oxidized. In some cases, e.g. on Pd(111) and Pd(100), this happens via the formation of surface oxides whose structures are distinct from the corresponding bulk oxides [132, 166–175]. Therefore, the catalytic properties of such surface oxides may also differ strongly from the corresponding bulk oxides and since under conditions applied in real catalysis palladium surface oxides may be formed, the role of them for oxidation reactions, in particular the CO oxidation reaction, is strongly debated and will be discussed in section 3.3.3 [176–183].

On Pd(111), oxygen exposure at intermediate pressures in the range of $10^{-6} - 10^{-4}$ mbar and elevated temperatures above ~ 500 K leads to migration of oxygen into the surface associated with apparent oxygen coverages higher than the 0.25 ML saturation coverage of chemisorbed oxygen [149, 184]. The migrated oxygen was found to almost immediately create an oxidic phase distinct from bulk PdO [164, 165, 185]. The structure of this surface oxide, which is regarded as an intermediate state between metallic Pd and PdO during the oxidation of Pd [166, 169], was finally determined by STM, SXRD, HRCLS and DFT to be Pd_5O_4 with a $(\sqrt{6} \times \sqrt{6})$ LEED periodicity and no stoichiometric or structural resemblance to bulk PdO [167, 168, 186]. The oxygen and palladium atoms within the twodimensional surface oxide layer are coordinated as a O-Pd-O trilayer with oxygen bound on top or at bridge site of the Pd(111) "substrate" [165, 167]. Pd_5O_4 grows (and decays) via several, kinetically stabilized intermediate surface oxide phases [170, 171], but the Pd_5O_4 is the only thermodynamically stable surface oxide of Pd(111) [169]. At even higher pressures above 0.1 mbar bulk PdO is formed: the surface oxide starts to grow into the subsurface region followed by the structural transformation to PdO via formation of small PdO clusters as a precursor on the Pd_5O_4 surface oxide [172, 173, 186].

The surface oxide of the Pd(100) surface was already described by Orent *et al.* in 1982 [130]: at $T = 473$ K, the LEED pattern changes from the $c(2 \times 2)$ structure corresponding to an oxygen coverage of 0.5 ML to a $p(5 \times 5)$ pattern ($\Theta = 0.7$ ML), and at 573 K a $(\sqrt{5} \times \sqrt{5})R27^\circ$

3 CO oxidation on Pt group metals

LEED pattern is formed corresponding to $\Theta = 0.8\text{ML}$. The surface oxide was related to low-index planes of bulk PdO. In a similar way as the Pd_5O_4 , the $(\sqrt{5} \times \sqrt{5})R27^\circ$ surface oxide of Pd(100) formed at $p_{\text{O}_2} = 5 \times 10^{-6}\text{mbar}$ and 600K has been characterized by STM, HRCLS and DFT [132]. The surface oxide consists of a O-Pd-O trilayer of bulk PdO grown in [101] direction which is not a preferred growth direction of PdO crystallites [187] and is therefore stabilized by a strong coupling to the Pd(100) substrate. The surface oxide has been observed even at atmospheric pressure at 575K, but above 600K already at 1 mbar restructuring of the PdO(101) surface oxide to a rough PdO film with predominantly PdO(001) orientation of the ordered domains begins [175].

In the case of Pd(110), surface oxides are not formed, but at 350°C and 10^{-2}mbar oxygen pressure, the surface transforms directly from the metallic phase densely packed by chemisorbed oxygen to PdO [188]. In a similar way, oxidation of platinum surfaces leads via the formation of oxide nanoislands on the surface as a precursor phase directly to bulk PtO_2 , but it is hardly possible to form PtO_2 under high vacuum conditions and it requires much harsher conditions as pressures in the mbar range [189–191] or oxidation by ozone [192]. The role of the Pt surface oxides for the reactivity in the CO oxidation reaction at elevated pressures (i.e. in the mbar pressure range) is also controversial and will be discussed in section 3.3.3.

3.2.3 CO₂ adsorption

CO₂ adsorbs only very weakly and non-dissociatively on both, platinum and palladium surfaces [193]. Physisorbed CO₂ could only be observed at stationary CO₂ pressures between 10^{-7} and 10^{-5}Torr and sample temperatures below 100K, e.g. on polycrystalline Pt foil with an estimated adsorption energy of $\sim 42\text{kJ/mol}$ [194, 195], on Pd(100) single crystal [196] and on Pt(111) single crystal [197]. Since CO₂ desorbs already at temperatures between 110 and 185K [194, 196], i.e. well below the temperatures relevant for the catalytic CO oxidation on Pt and Pd, during the reaction it is immediately released to the gas phase just after formation [108] and therefore, does not effect the catalytic performance of the metal surface.

3.3 CO oxidation on Pt group metals

After the interaction between carbon monoxide and oxygen with the platinum and palladium (hkl) surfaces has been detailed in the previous section, an overview over the CO oxidation reaction on platinum group metals is given in the following.

3.3.1 Langmuir Hinshelwood mechanism

The catalytic CO oxidation reaction on platinum group metals has been investigated in numerous studies since the early days of catalysis, including the pioneer work of Langmuir [4, 5], and is nowadays one of the best-understood reactions in heterogeneous catalysis. It is well established that on metal surfaces the reaction underlies the Langmuir-Hinshelwood (LH) mechanism, where the reaction occurs between both reactants adsorbed on the catalyst surface and which is described by the following three elementary reaction steps and illustrated in Fig. 3.3 [108, 198, 199]:



The first two equations describe the adsorption of CO and oxygen (see also Fig. 3.3a). CO chemisorbs molecularly and therefore, needs only one free adsorption site (indicated by an asterisk), and oxygen chemisorbs dissociatively occupying two adjacent free sites (the index "ad" denotes the adsorbed species). The molecules in the gas phase and on the surface are in an adsorption-desorption equilibrium, depending on gas phase pressure and surface temperature: In the temperature range relevant for the CO oxidation reaction, only CO desorption has to be taken into account. The adsorbed CO molecule can diffuse on the surface whereas the slow oxygen diffusion in this temperature range can be neglected. Therefore, the CO molecules diffuse towards the oxygen atoms and react with them to CO₂. The CO₂ molecules are immediately desorbed from the surface due to their low binding energy to the surface and leave two free adsorption sites behind (Fig. 3.3b). These freed sites can be filled again with adsorbing oxygen or CO, the reaction cycle is closed.

Beside the catalytically active steady state where the surface is covered by a relatively open oxygen adlayer and coadsorption (and therefore reaction) with CO as presumed in

3 CO oxidation on Pt group metals

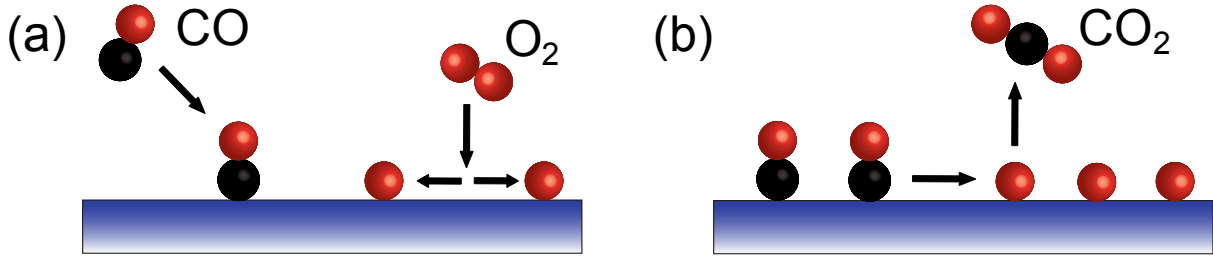


Figure 3.3: (a) Molecular adsorption of carbon monoxide and dissociative adsorption of oxygen. (b) Diffusion of CO towards oxygen, reaction to carbon dioxide and immediate desorption of CO₂.

the Langmuir-Hinshelwood mechanism is possible, the system may also be under certain conditions in a catalytically inactive, CO-poisoned steady state.

The saturation coverage of CO is very high on all (hkl) surfaces of Pt and Pd and in contrast to CO oxygen needs two free adjacent sites for dissociative adsorption. Therefore, if the surface is covered by CO, the dissociative oxygen adsorption is very effectively blocked by the carbon monoxide, the surface is "CO-poisoned". These differences in the adsorption properties of CO and oxygen also lead to an asymmetric inhibition of the reaction, the surface exhibits a bistable behavior. Depending on external control parameters as temperature or pressure *and* on the prehistory of the system, it can be either in the active or in the inactive steady state. Taking into account the different adsorption properties of the reactants, the CO oxidation reaction on platinum group metals can be described mathematically by a set of coupled differential equations [200, 201]:

$$\frac{d\Theta_{\text{CO}}}{dt} = k_{\text{CO}}^{\text{ad}}(T)p_{\text{CO}}s_{\text{CO}} - k_{\text{CO}}^{\text{des}}(T)\Theta_{\text{CO}} - k^r(T)\Theta_{\text{CO}}\Theta_{\text{O}} + D_{\text{CO}}\nabla^2\Theta_{\text{CO}} \quad (3.2a)$$

$$\frac{d\Theta_{\text{O}}}{dt} = k_{\text{O}_2}^{\text{ad}}(T)p_{\text{O}_2}s_{\text{O}_2} - k^r(T)\Theta_{\text{CO}}\Theta_{\text{O}}. \quad (3.2b)$$

The temporal evolution of the CO coverage Θ_{CO} is determined by the adsorption rate of CO, which is described by the first term in eq. 3.2a, the desorption rate of CO (second term), the reaction rate with oxygen (third term, corresponds to the CO₂ formation rate R_{CO_2}) and surface diffusion of CO (4th term). Analogous, the oxygen coverage Θ_{O} changes with oxygen adsorption and reaction with CO (as mentioned above, desorption and diffusion of oxygen can be neglected in the temperature range relevant for CO oxidation). The adsorption rate depends on the *adsorption coefficient* k_i^{ad} , the partial pressure p_i and the sticking coefficient s_i of CO or oxygen, respectively. The desorption rate is described by the *desorption coefficient* k^{des} and the coverage of CO and the reaction rate is composed of the *reaction*

3 CO oxidation on Pt group metals

rate constant k^r of CO oxidation and the surface coverages of CO and oxygen. The diffusion term of CO is determined by the *diffusion coefficient* D_{CO} of CO.

The sticking coefficients and rate coefficients in the equations 3.2a and 3.2b can be expressed by the following terms:

$$s_{\text{CO}} = s_{\text{CO}}^0 \left(1 - \left(\frac{\Theta_{\text{CO}}}{\Theta_{\text{CO}}^{\text{sat}}} \right)^q \right) \quad (3.3a)$$

$$s_{\text{O}_2} = s_{\text{O}_2}^0 \left(1 - \frac{\Theta_{\text{CO}}}{\Theta_{\text{CO}}^{\text{sat}}} - \frac{\Theta_{\text{O}}}{\Theta_{\text{O}}^{\text{sat}}} \right)^2 \quad (3.3b)$$

$$k^{r, \text{des}} = \nu_{r, \text{des}} \exp(-E_A^{r, \text{des}} / RT) \quad (3.3c)$$

$$k_i^{\text{ad}} = \frac{1}{\sqrt{2\pi m_i kT}}. \quad (3.3d)$$

The values of the sticking coefficients depend on the initial sticking coefficients s^0 , the coverages and the saturation coverages of CO and oxygen, respectively. By the variable q in 3.3a, the precursor kinetics of CO adsorption is taken into account. The sticking coefficient decreases with increasing coverage and reaches zero at saturation coverage. In case of oxygen (3.3b), the dependence of the sticking coefficient on the CO coverage considers the asymmetric inhibition, and the square dependence accounts for the necessity of two adsorption sites for oxygen adsorption. The rate constants for desorption and reaction follow the Arrhenius law with a pre-exponential factor ν and the exponential dependence on the activation energy E_A and the Boltzmann factor kT . The adsorption constant k^{ad} is determined by kinetic gas theory and depends on mass and temperature.

The solution of the coupled differential equations 3.2 is depicted in Fig. 3.4(a) and leads directly to the (experimentally accessible) hysteresis behavior of the CO oxidation reaction on Pt group metals upon cyclic variation of one control parameter (e.g. CO partial pressure) at otherwise constant parameters. The isothermal CO pressure-dependence of the coverages at constant oxygen pressure is shown in Fig. 3.4a and a scheme of the resulting CO_2 formation rate is depicted in Fig. 3.4b. At a low CO pressure, the surface is predominantly oxygen covered and the reaction rate is practically zero. With increasing CO pressure, the reaction rate increases linearly, since in this range only the availability of CO molecules is rate limiting. The CO coverage does not change significantly, whereas the oxygen coverage constantly decreases due to the reaction with CO. In this pressure range, the surface is in a steady state of high reactivity and the solution of the differential equations is monostable.

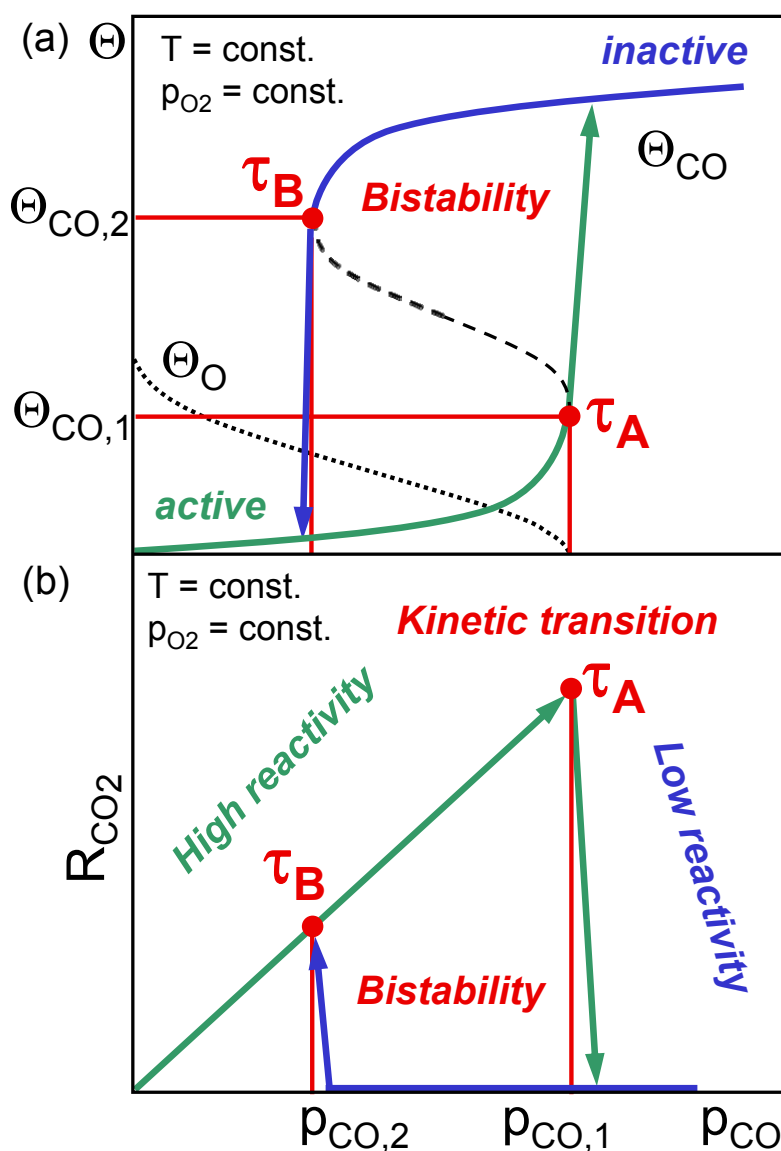


Figure 3.4: Bistability in CO oxidation: (a) Scheme of the CO (solid lines) and oxygen coverage (dotted line) in dependence of the CO partial pressure as obtained as isothermal solution of the differential equations 3.2. The dashed line indicates the unstable solution within the bistability range. The transitions τ_A and τ_B are marked by the arrows. (b) Scheme of the experimentally accessible hysteresis in the CO₂ formation rate in dependence of the CO pressure at constant oxygen pressure and temperature. Adapted from [201].

At a certain critical CO partial pressure $p_{CO,1}$, the monostable solution gets unstable (indicated by the dashed line in Fig. 3.4a) and a first-order kinetic phase transition to the CO-covered state occurs. This transition point, a *saddle-node bifurcation point* indicating the change of the number of stable states of the system, is called τ_A . Above τ_A , the adsorbed CO molecules block oxygen adsorption, the oxygen coverage and the CO₂ forma-

3 CO oxidation on Pt group metals

tion rate become zero and an increase of the CO pressure does not change the reaction rate anymore. Upon decreasing the CO pressure again, the monostable solution gets stable at the transition point τ_B at a CO pressure $p_{\text{CO},2} < p_{\text{CO},1}$ and the system switches back to the oxygen-covered high reactivity state. Between τ_A and τ_B the system is bistable: in the experimentally accessible CO_2 formation rate a hysteresis occurs upon the cyclic variation of the CO partial pressure (see Fig. 3.4b and Fig. 3.5a), it depends on the prehistory of the system whether it is high or low reactive.

Besides the conventional mean field modeling (MF) performed in numerous studies under various assumptions [200–203], a kinetic Monte Carlo (kMC) approach can be applied to model the system under consideration on an atomistic scale [204–206]. By MC simulations microscopic phenomena can be taken into account which are difficult to treat analytically (i.e. by the conventional MF method) like density fluctuations, spatial correlations or the local distribution of adsorbants, the surface structure and composition on the nm-scale. For example, fluctuation-induced transitions between the activity branches in a bistable reaction, e.g. the CO oxidation reaction on a Pt field emitter tip, could be modeled successfully by Monte Carlo simulations [207–209]. Other examples are the incorporation of the average size of the (1×1) and (hex) patches on a Pt(100) surface to model the CO oxidation reaction [210] or the study of the stability of thin surface oxide films in reactive environments [211, 212]).

3.3.2 Bistability and kinetic phase diagram

In Fig. 3.5a, a measured R_{CO_2} hysteresis loop as a function of CO pressure at the constant oxygen pressure $p_{\text{O}_2} = 1.3 \times 10^{-5}$ mbar and a temperature of 453K is shown for a Pt(111) single crystal [213]. The curve exhibits qualitatively the same behavior as in the scheme in Fig. 3.4a, i. e. at low CO pressures the CO_2 rate increases linearly with p_{CO} , at a certain CO pressure $p_{\text{CO}}^{\tau_A}$ the reactivity decreases rapidly due to CO-poisoning of the surface and upon cyclic variation of p_{CO} the reverse transition to the high reactivity state occurs at a lower CO pressure $p_{\text{CO}}^{\tau_B}$ than $p_{\text{CO}}^{\tau_A}$ because of the asymmetric inhibition of the reaction. The width of the bistability region varies strongly with surface temperature, so a plot of the transition points as a function of one external parameter (e.g. the temperature), while the other external parameter is held constant, can be constructed illustrating this behavior very effectively. For example, in Fig. 3.5b such a plot as a function of the temperature at constant $p_{\text{O}_2} = 1.3 \times 10^{-5}$ mbar is shown for the Pt(111) single crystal studied in Ref. [213]. This type of presentation is called *kinetic phase diagram* in analogy to equilibrium thermodynamics

3 CO oxidation on Pt group metals

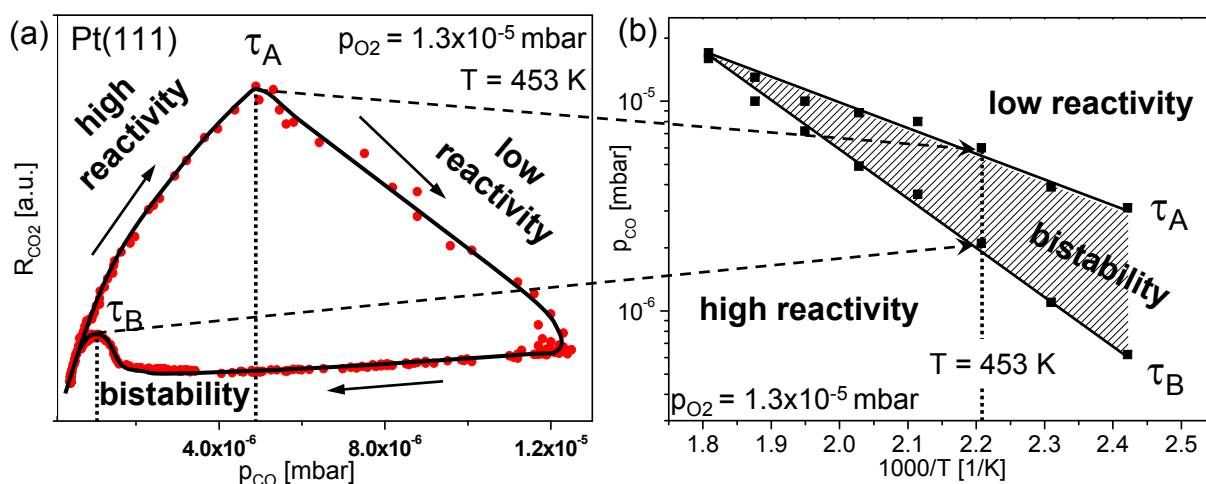


Figure 3.5: (a) Hysteresis in the CO_2 formation rate at 453K for a Pt(111) single crystal at constant $p_{\text{O}_2} = 1.3 \times 10^{-5}$ mbar. (b) Kinetic phase diagram for the Pt(111) single crystal deduced from the transition points τ_A and τ_B in the R_{CO_2} hysteresis. The dashed region indicates the bistability regime. With permission from [213].

[214–216]. The term *kinetic phase diagram* has been justified by the circumstance that the state of both equilibrium and non-equilibrium systems changes qualitatively, when a critical point is passed upon variation of an external parameter (e.g. pressure or temperature). Due to its characteristic shape it has been also referred to as *cross-shaped diagram* [217] or *bifurcation diagram* [218]. Kinetic phase diagrams provide a very useful and straightforward characterization of the kinetic properties of a catalytic system because the different regions of high and low reactivity and the region of bistability in parameter space, i.e. the different possible catalytic states of a system, are summarized in one plot and are thus directly accessible. Therefore, the kinetic properties of different systems, e.g. different metals as Pt and Pd or different crystallographic orientations, can be directly compared. Furthermore, the effect of surface modifications as sputtering or surface oxidation can be easily illustrated.

In the past, kinetic phase diagrams have been obtained for various single crystals as Pd(110) [219], Pd(111) [203], Pt(210) [218] or Pt(111) [213, 220]. Among the more complex model systems, kinetic phase diagrams are rather scarce, only one study of a Pt field emitter tip is reported [217].

For some of the single crystal surfaces of the Pt group metals (e.g. Pt(110) and Pt(100)) bistability during CO oxidation is not the only observed phenomenon. Reaction rate oscillations and spatio-temporal pattern formation have been studied experimentally and theo-

retically over the years mainly by Ertl and co-workers [18, 35, 155, 202, 221–227] culminated in the Nobel Prize in Chemistry awarded to Gerhard Ertl in 2007 [10].

Numerous possible mechanisms have been proposed to explain the observed reaction rate oscillations (e.g. [228]), but finally the surface reconstruction model by Ertl and coworkers has been generally accepted for oscillations on Pt(100) and Pt(110) under high vacuum conditions: the rate oscillations have been attributed to the reversible surface phase transition between the different reconstructions of the Pt(100) and Pt(110) surfaces altering the adsorption properties of CO and oxygen and thus altering also the catalytic activity. In turn, oscillations on a Pd(110) surface at intermediate pressures ($\sim 10^{-3} - 10^{-1}$ mbar) were described by reversible surface oxide formation and reduction [228]. However, since the reaction rate oscillations have been extensively studied in the past, they are not further considered in this thesis.

3.3.3 Role of surface oxides in CO oxidation

In section 3.2.2.3 it was shown that under certain conditions, especially in the mbar pressure range, i.e. at reactant pressures very similar to the technological conditions of CO oxidation (automotive three-way catalysts, industrial catalysis, etc.), surface oxides may form on different Pt and Pd surfaces. The role of these surface oxides in the CO oxidation reaction is not unambiguous and the mechanistic details of the reaction under high-pressure conditions were the subject of a vivid discussion concerning the question of the most active phase in the reaction in the recent past [176–183, 229–231]. Even the well-established mechanism of the reaction (Langmuir-Hinshelwood) is questioned with regard to the surface oxide formation and a Mars-van-Krevelen like mechanism is favored in some studies [176, 177].

Nowadays, new surface sensitive techniques have been developed which can be operated in the high pressure regime (mbar to atmospheric pressure), such as high-pressure STM (scanning tunneling microscopy), high-pressure SXRD (surface x-ray diffraction), PM-IRAS (polarization modulation infrared absorption spectroscopy) or high-pressure XPS (X-ray photoelectron spectroscopy) [6, 232]. In several studies, surface oxides, e.g. on Pt(110) or Pd(100), were observed in parallel with an activity increase during the oxide formation [176, 177, 183, 233]. A Mars-van Krevelen mechanism has been proposed in which the less stable "highly reactive" oxide is consumed and reformed during the reaction, being the source of oxygen for the CO oxidation reaction. Therefore, the surface oxides were sug-

3 CO oxidation on Pt group metals

gested to be the active phases of CO oxidation, whereas the metallic surface was believed to be rather inactive.

To the same time, it has been shown that PdO_x can hardly be reduced by CO, especially the higher the oxidation state of the Pd surface is chosen: In a comparative CO titration study by Gabasch *et al.* [229], chemisorbed oxygen on a metallic Pd(111) single crystal exhibited the highest affinity to react with the CO, followed by the oxygen incorporated in the Pd_5O_4 surface oxide, the PdO_x thin film suboxide and in silica supported PdO nanoparticles. The reason for this behavior is the lack of adsorption sites for CO on the oxidic Pd surface and the necessity of high mass-transport for the (re-)formation of the metallic Pd phase on the deeply oxidized Pd samples. In other studies, the "surface oxide" on Pd(100) or Pt(110) is removed by CO only little slower than chemisorbed oxygen [191, 234], while also a very high stability of the oxide towards CO reduction has been observed for a Pt(100) surface [189]. In the latter case, the surface was also deactivated completely for the CO oxidation reaction in the mbar pressure range.

Concerning the catalytic behavior of the surface oxides on Pt and Pd (hkl) surfaces *under CO oxidation reaction conditions*, Goodman and co-workers have convincingly shown that also in the high pressure regime the Langmuir-Hinshelwood mechanism may still predict the kinetics of the CO oxidation reaction and that the oxygen-covered metallic surface still appears as the most active phase as it is known from the low pressure regime. However, under elevated pressures, the highly active, oxygen-covered metallic surface appears to be only transient between the CO-inhibited metallic surface and an oxidic surface at which the CO_2 reaction rate is higher than on the CO-poisoned metallic surface but lower than on the transient oxygen-covered metallic surface. Furthermore, with increasing surface oxidation a deactivation of the catalyst was observed [178, 179, 182, 230]. Also for Al_2O_3 -supported Pd nanoparticles, the oxygen-covered metallic Pd was determined to be the active phase in contrast to fully oxidized PdO nanoparticles exhibiting activity only after partial reduction by CO [231]. Substoichiometric partially oxidized $\text{PdO}_{x<1}$ was not stable under reaction conditions due to facile reducibility by CO resulting in a similar activity as the metallic Pd nanoparticles, so it was concluded that "metallic Pd will always dominate under technically relevant conditions" being the active phase in CO oxidation. In case of Pd nanoparticles supported on an Fe_3O_4 film on Pt(111) single crystal, a dynamical formation and decomposition of an oxide at the interface of the Pd particles and the support has been observed. The oxide serves as an oxygen reservoir for the CO oxidation reaction which is still taking place mainly on the metallic part of the Pd particles due to the weak CO adsorption capa-

3 CO oxidation on Pt group metals

bility on the Pd oxide, i.e. on the oxygen-covered metallic Pd CO oxidation is fast and on the Pd oxide the reaction is slow because of the involved oxide reduction step [235–237].

Taking into account the mean-field modeling of the bistable reaction kinetics of CO oxidation on Pt involving surface oxide formation by Carlsson et al. [238] based on the Sales-model of alternating surface oxidation and reduction during the reaction [228], a complete picture is formed which is also compatible with the experiments of Singh et al. on supported Pt nanoparticles where an oxidic phase after ignition, i.e. in the high reactive regime was observed [239, 240], and which was basically already suggested by Goodman and co-workers [178]. In the mbar-bar pressure regime under oxygen-rich atmosphere and relatively high temperatures, (surface) oxides are formed on Pt and Pd surfaces under reaction conditions, i.e. for example in a typical ignition experiment three distinct reactivity regimes can be observed: at low temperatures, the surface is in the metallic, but CO-poisoned and therefore inactive state; with increasing temperature, the carbon monoxide reacts with the oxygen and at a certain point, the surface is in the (transient) oxygen-covered highly reactive *metallic* state which might be overlooked at very oxidizing conditions as were applied in the experiments by Frenken and co-workers; then, as a consequence and due to CO mass-transfer limitations the oxygen starts to partially oxidize the metallic surface at which the reaction still follows the Langmuir-Hinshelwood mechanism, but with a lower reaction rate due to lower CO and oxygen adsorption capabilities [238]. Thus, the discrepancies in literature arise mainly by the incorrect comparison of metal surfaces in the CO-inhibited regime with surfaces exposed to the oxidizing regime, where the reaction rate is considerably lower than on the metallic surface with chemisorbed oxygen, but still higher than on the completely inactive CO-poisoned metallic surface. Besides, on the oxidic surfaces, even a small fraction of metallic surface would provide a catalytic activity incomparable higher than the whole surface poisoned by CO. Therefore, under elevated pressures, surface oxide formation repeatedly observed in several studies does play an important role, though the metallic surface still seems to serve as the most active phase for the CO oxidation reaction.

LOCAL REACTION KINETICS OF CO OXIDATION ON POLYCRYSTALLINE PLATINUM

As a first step towards bridging the materials gap in model catalysis between the well-studied single crystals and the highly complex real catalysts, the CO oxidation reaction on individual grains of a polycrystalline Pt foil is studied in this chapter. Besides the averaged global reaction kinetics in the bistability range as measured by mass spectrometry (MS), the locally-resolved reaction kinetics of CO oxidation on individual μm -sized (100)-, (110)- and (111)-type grains of the polycrystalline Pt foil, as obtained by local Photoemission Electron Microscopy (PEEM) intensity analysis, is presented. For all three orientations the reaction conditions of high activity, low activity and bistability are determined and domain-specific kinetic phase diagrams for CO oxidation are obtained. Possible coupling mechanisms between the differently oriented grains and the role of the grain boundaries are discussed by means of the construction of an "artificial" global kinetic phase diagram, which is based on the PEEM-derived local kinetic phase diagrams and compared to the global reaction kinetics experimentally measured by MS.

In the second part of this chapter, the reaction-induced surface morphology changes on a (100)-oriented grain on Pt foil, studied by optical differential interference contrast microscopy and atomic force microscopy (AFM), are presented. The mechanism of the reaction front propagation for CO and oxygen fronts as observed by PEEM is discussed in a wide temperature range.

4.1 Introduction

The surfaces of noble metal single crystals such as Pt(111) have served in the past as successful model systems for heterogeneous catalysts. To account for the fact that supported Pt nanoparticles of technological catalysts typically exhibit different low Miller-index facets to the reactive gases, single-crystal studies were most frequently carried out for Pt(111), Pt(110) and Pt(100) terminations. Catalytic reaction properties were, for example, determined by temperature-programmed methods or molecular beam studies (both relying on mass spectroscopic product analysis) or, in case of atmospheric pressure conditions, by gas chromatography. In order to evaluate and compare the catalytic properties of the different crystallographic orientations, a relatively large parameter space of reactant gas pressure and reaction temperature must be investigated. Since this represents a significant body of work, there is hardly any catalytic system with a complete set of reported reactivity data.

However, although catalytic CO oxidation on Pt group metals is one of the most extensively studied surface reactions in heterogeneous (model) catalysis [10], the detailed comparison of the catalytic behavior of differently-oriented surfaces is still difficult. The problems are mainly related to limitations of creating exactly the same experimental conditions for different samples, since even small variations of temperature or pressure near the transition points may induce kinetic transitions from a catalytically active to an inactive state or vice versa [201]. A practicable approach in surface physics, when e.g. adsorption or diffusion are studied in parallel on differently-oriented facets on the same field emitter tip [241], fails in the case of surface reactions due to noise-induced transitions on the small (nm) sized facets [208] (i.e. rapid adsorbate diffusion "wipes out" structural differences).

In this work, an alternative approach is presented that allows for the determination of the catalytic properties of different crystallographic orientations in a more efficient way. Photoemission Electron Microscopy (PEEM) was employed to study the CO oxidation reaction on polycrystalline Pt foil, consisting of micrometer-sized domains of (100), (110) and (111) orientation. PEEM imaging was performed *in situ*, that is, during the ongoing CO oxidation reaction. The idea to apply PEEM for such spatially-resolved studies is based on the correlation of the work function with catalytic activity, as observed earlier in averaging studies on Pt single crystal surfaces [18]. Translated to the local studies on individual grains of a polycrystalline Pt foil, this idea allows to pursue the kinetic transitions during the reaction and to create local kinetic phase diagrams for the individual (100), (110) and (111) crystalline grains, as is described in detail below. It is important to note that at a given

4 Local reaction kinetics of CO oxidation on polycrystalline platinum

time the reactant gas pressure and temperature were identical for all orientations, allowing a direct simultaneous comparison of their catalytic properties.

Kinetic phase transitions on the Pt(111) single-crystal surface have been previously observed by PEEM (by averaging the whole image intensity, since the homogeneity of such a surface did not ask for spatially-resolved analysis [220]) and PEEM images of CO oxidation on Pt foil have been reported (but without analysis of phase transitions and in a rather qualitative way [37, 242]). However, in this thesis it is shown how local kinetic phase diagrams of a catalytic reaction can be obtained for individual differently oriented domains of a polycrystalline material. The oxidation of CO on platinum surfaces is a seemingly simple reaction, but it exhibits several complex phenomena such as hysteresis (bistability), oscillations, dissipative structures and chaotic behavior [10]. Herein, the CO oxidation reaction was examined deliberately only in the bistability regime, whereas the parameter space (higher temperature and pressures) of oscillations was not considered since it was extensively studied before [10, 226].

To account for possible coupling mechanisms as diffusion or gas-phase coupling between the different (100), (110) and (111) domains which might synchronize their kinetic transitions the (weighted) local kinetic phase diagrams of the individual domains as measured by PEEM were summed up and compared to the global kinetics as measured by MS. In this context, also the role of the grain boundaries for the overall reaction kinetics is discussed.

Further in this chapter, the morphology of an individual [100]-oriented grain of a Pt foil and its change induced by the CO oxidation reaction is treated, since this reaction on Pt(100) single crystal surfaces has already been studied intensively: temporal oscillations in the CO₂ reaction rate were observed and could be correlated to work function oscillations [221] and to periodic variations of the LEED pattern corresponding to (hex) and (1x1) reconstructions [38, 44, 45, 49, 243]. In early attempts, the existence range of oscillations was evaluated by a $p_{\text{CO}}-p_{\text{O}_2}$ -diagram at fixed temperature [222], a predecessor of the currently-used kinetic phase diagrams [217–219]. Scanning photoemission microscopy was first applied to monitor the Pt(100) surface during the CO oxidation reaction [244, 245], but a real time imaging of the spatio-temporal patterns formed during the reaction was only possible after the development of photoemission electron microscopy (PEEM), due to its parallel imaging principle [10, 16]. In a first systematic PEEM study of the CO oxidation reaction on a Pt(100) single crystal in the oscillatory regime the kinetic oscillations of the CO₂ production rate could be clearly correlated to the spatio-temporal pattern formation [225]. The propagation of reaction-diffusion fronts on Pt(100) was investigated in more detail using

4 Local reaction kinetics of CO oxidation on polycrystalline platinum

LEEM and selected-area LEED [246–249]. In further PEEM studies, the formation of sub-surface oxygen species could be observed at the boundary of oxygen and CO-covered regions [250] and a mechanism for the formation of this oxygen species could be established [153]. In several studies some characteristic morphological structures have been reported. Lauterbach et al. have observed "a pronounced texture with parallel furrows" on the (100)-type grains of a polycrystalline platinum foil by SEM, the size of the furrows ranging from 200 nm up to several μm [37]. In a LEEM study on a Pt(100) single crystal a characteristic step and terrace structure with a mean terrace width of approximately 700 nm to $1\mu\text{m}$ is reported [248]. Other authors have shown that the CO oxidation reaction can induce a strong roughening of the platinum surface up to a length scale of 0.1 – $1\mu\text{m}$ [251, 252]. Nevertheless, the formation of these features is still not entirely understood. Using PEEM and AFM in the present work a model that may explain the mechanism under which these characteristic features (up to the μm range) are developed is presented.

4.2 Experimental details

The experiments were performed in the multifunctional UHV chamber with a base pressure below 10^{-9} mbar described in detail in chapter 2. For the experiments presented in this chapter, the PEEM, the quadrupole mass spectrometer, the sample preparation facilities for sputtering and annealing, and the gas supply system with the high-purity reactive gases (O_2 : 99.999%, CO: 99.97%) were used. The sample studied in this chapter was the $10 \times 10\text{mm}^2$ large polycrystalline Pt foil (99.99%), which was treated by flame annealing in air prior to mounting. In UHV, the sample was cleaned by the standard UHV cleaning procedure described in section 2.3.1. The temperature was measured by a NiCr/Ni thermocouple spot-welded to the back of the sample.

The PEEM-image is created by photoelectrons emitted from the sample surface which is irradiated by a UV deuterium discharge lamp (D200, Heraeus) with a cut-off photon energy of 6.8 eV. The intensity of the emitted photoelectrons depends strongly on the local sample work function. This allows to identify the surface orientation of individual grains on the Pt foil by selected-area intensity analysis, as described in detail in section 2.3.3 and in Refs. [253, 254]. In turn, the local work function varies strongly with the local adsorbate coverage, so it is possible to follow the CO oxidation reaction *in situ* on individual grains of the Pt foil. By analyzing the local PEEM intensities during the reaction also local kinetic information can be obtained. The local PEEM data can be correlated with the global CO_2 reaction rate measured simultaneously by the mass spectrometer placed in vicinity of the sample.

4 Local reaction kinetics of CO oxidation on polycrystalline platinum

The surface topography of the (100) domains on the Pt foil was studied with a commercial AFM (NanoMan VS, Veeco) at ambient conditions in tapping mode. A PPP-NCHR probe (Nanosensors) with a nominal tip radius below 10 nm was used. An optical microscope was coupled with the AFM for a preselection of a region of interest from which AFM images were taken. AFM image analysis including linear height profiles was carried out using the Gwyddion Software. In addition, differential interference contrast microscopy (Polyvar 2 MET from Reichert Microscope Services, $NA = 0.95$) was utilized to obtain optical micrographs with enhanced contrast of the Pt foil.

4.3 Results

4.3.1 Global and local reaction kinetics of Pt foil

To illustrate the kinetic behavior of polycrystalline Pt foil, the global (overall) reaction kinetics in the bistability range of CO oxidation measured by mass spectroscopy is summarized in Fig. 4.1, where Figs. 4.1a, b show PEEM images of the clean and adsorbate covered sample, respectively, and Figs. 4.1c, d the CO_2 production rate and the kinetic phase diagram, respectively. The surface orientation of the grains was determined by comparison of the local PEEM intensity with single crystal work function data (see section 2.3.3). As typical for CO oxidation on Pt, the surface is in a high reactivity steady state (predominantly oxygen-covered, Fig. 4.1b) at low CO pressures with the CO_2 production rate increasing with increasing CO partial pressure (at constant oxygen partial pressure and constant temperature; Fig. 4.1c, $p_{\text{O}_2} = 1.3 \times 10^{-5}$ mbar). At a certain CO to oxygen pressure ratio CO adsorption prevails over oxygen adsorption, thus drastically reducing the CO_2 production. Adsorbed CO inhibits the dissociative adsorption of oxygen and a kinetic transition to the low reactivity steady state occurs [201]. This transition point in the parameter space is termed transition point τ_A whereas the point of the reverse transition is called τ_B (Fig. 4.1c). Due to the effective blocking of adsorption sites for oxygen by CO the reverse transition from the inactive to the active state takes place at a lower CO partial pressure τ_B than the transition τ_A . This leads to the hysteresis in the CO_2 production rate as shown in Fig. 4.1c for three different temperatures (417 K, 453 K and 477 K). Higher temperatures lead to a shift of the hysteresis curves: higher CO partial pressures are required for the kinetic transition and the CO_2 reaction rate is higher. This behavior can be summarized in a plot called "kinetic phase diagram", based on the analogy to phase transitions in equilibrium

4 Local reaction kinetics of CO oxidation on polycrystalline platinum

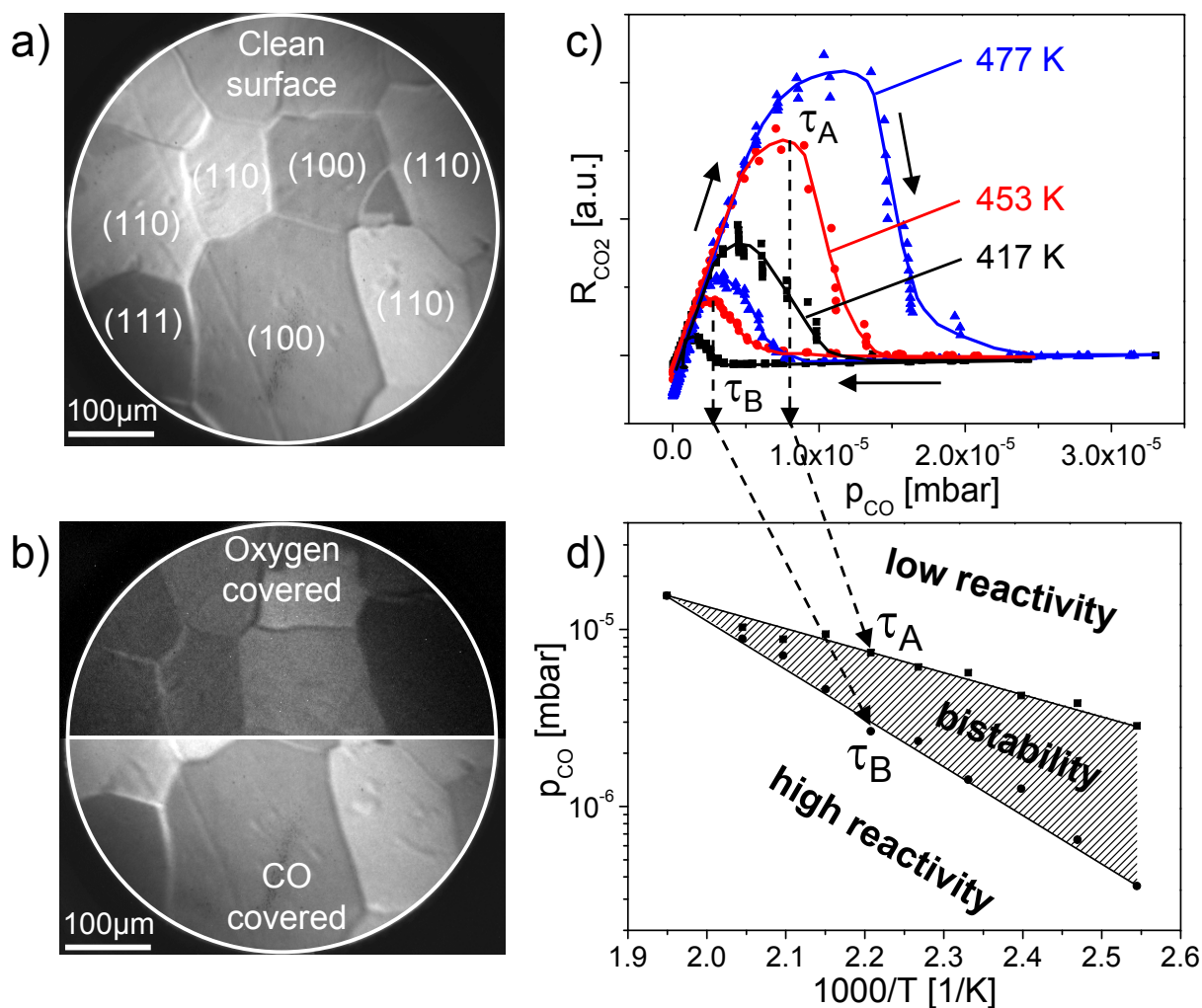


Figure 4.1: Global kinetics of CO oxidation on Pt foil. (a) PEEM image of the clean Pt foil. The surface orientation of the individual grains is indicated. (b) PEEM images of the oxygen-covered (top) and the CO-covered (bottom) Pt foil. The oxygen-covered surface appears dark in PEEM since adsorbed oxygen increases the work function of the Pt surface. (c) Hysteresis in the global CO₂ production rate at cyclic variation of the CO pressure at constant O₂ pressure of 1.3×10^{-5} mbar and at temperatures of 417 K (black squares), 453 K (red dots) and 477 K (blue triangles). The τ_A and τ_B values deduced from the hysteresis curves were used for the kinetic phase diagram in Fig. 4.1d. (d) Global kinetic phase diagram of CO oxidation on polycrystalline Pt foil, obtained by mass spectroscopy.¹

thermodynamics [214, 215] (in Fig. 4.1d for the temperature range 393 to 513 K). Such a diagram is a useful representation of the kinetic behavior of the reaction system, i.e. of the regions of high and low reactivity, bistability and oscillations, and may also effectively illus-

¹In further work, corrections due to an improved temperature measurement method were applied to the kinetic phase diagram data of Pt foil, cf. chapter 5.

4 Local reaction kinetics of CO oxidation on polycrystalline platinum

trate the role of reaction promoters (altering the adsorption/desorption kinetics, sticking etc.) [217, 218].

The contrast mechanism of PEEM based on work function changes due to adsorbed oxygen or CO provides the basis for monitoring the local kinetic transitions in the ongoing $\text{CO} + \text{O}_2$ reaction on individual grains of Pt foil. The principle of the local kinetic experiments is illustrated in Fig. 4.2a: In parallel to the measurement of the global CO_2 production rate by MS, we monitor the local PEEM intensity of a defined area, typically an individual grain of the Pt foil (a [100]-oriented facet = "region of interest" is depicted in frame 1), during cyclic variation of the CO partial pressure at a constant temperature and constant oxygen partial pressure. The video-frames 1 – 4 represent characteristic points in the hysteresis cycle and the inset below the frames presents the corresponding integrated local PEEM intensity curve for the (100) grain, plotted as a function of p_{CO} . The drops/jumps in the local PEEM intensity reflect the local kinetic transitions characteristic for this particular crystalline Pt grain. In frame (1) the surface is oxygen-covered (high-reactivity steady state; high work function, dark), frame (2) reflects the transition τ_A . Bright CO fronts are propagating across the (100) facet, resulting in a sharp increase of the intensity that corresponds to a drop in the simultaneously measured CO_2 production rate (note that the PEEM intensity axis has an opposite direction to the MS axis in Fig. 4.1c). Frame (3) corresponds to a CO covered surface (low-reactivity steady state; low work function, bright) and frame (4), in turn, shows a sharp decrease of the intensity at the transition point τ_B when the surface switches back to an oxygen-covered state. Note the propagating dark oxygen fronts in this frame. The transition points τ_A and τ_B obtained from series of such measurements at different temperatures result in the local kinetic phase diagram shown in Fig. 4.2b, which is displayed together with the global diagram of Fig. 4.1d. At first glance, the differences between the global and the local diagram seem rather insignificant, thus questioning this approach. However, comparison of the local diagrams measured for the specific Pt(100) facet and for neighboring Pt(110) and Pt(111) grains (cf. Fig. 4.1a) shows significant differences, as evident from Fig. 4.2c. The clear differences between the local diagrams for [100]-, [110]- and [111]-oriented facets indicate a rather independent catalytic behavior of individual crystalline grains of mesoscopic size with respect to the CO oxidation reaction. This independent reaction behavior of the individual domains, also manifested in the observation that propagating reaction fronts were confined within grain boundaries (i.e. reaction fronts did not propagate across domain boundaries; cf. frames 1 – 4 in Fig. 4.1) can be rationalized by considering potential mechanisms of reactive coupling (synchronization) between the facets. Diffusion coupling was made responsible for synchronization of local

4 Local reaction kinetics of CO oxidation on polycrystalline platinum

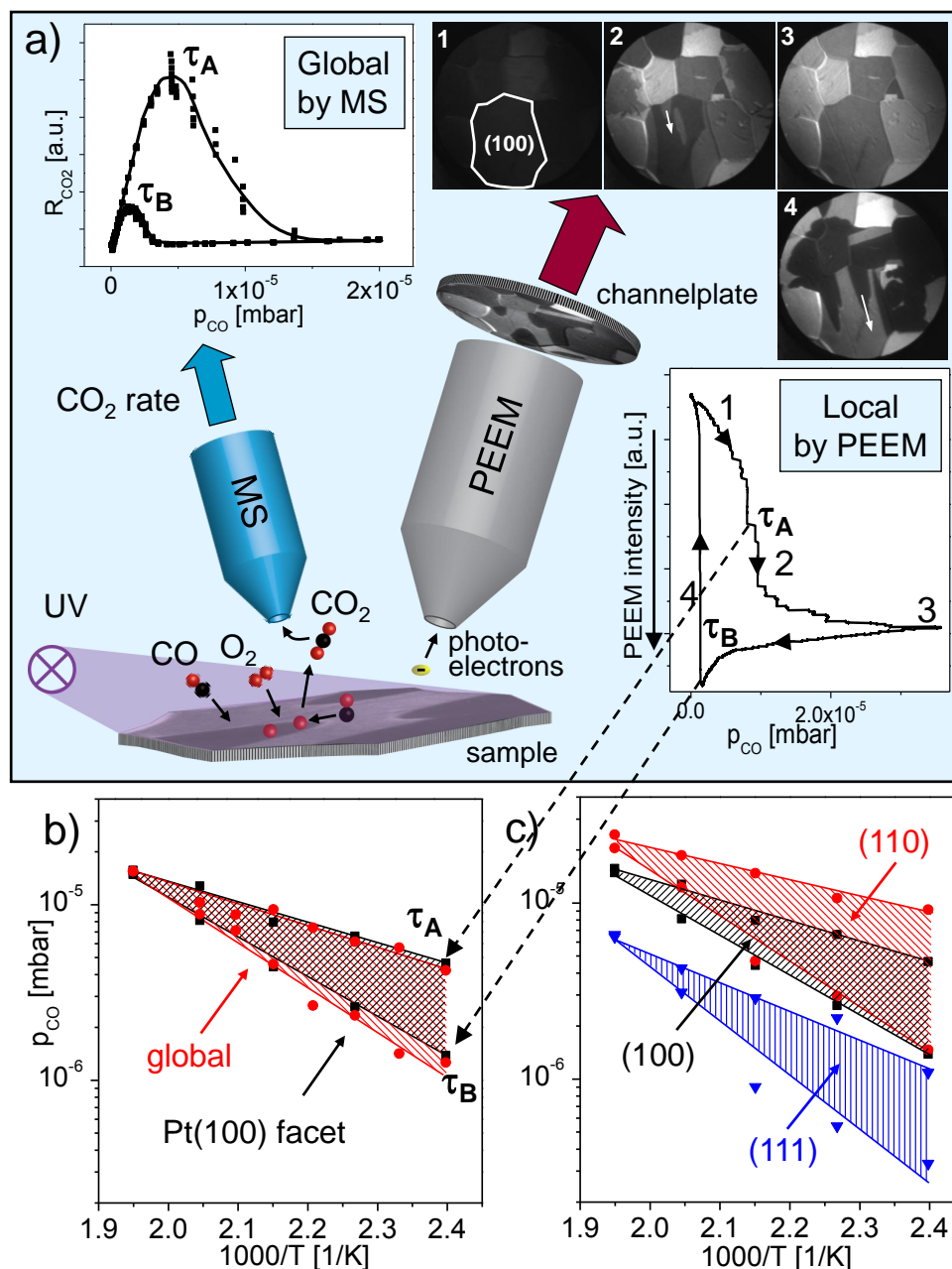


Figure 4.2: Local kinetics of CO oxidation on individual crystalline grains of a Pt foil. (a) Principle of the local kinetic measurements by PEEM. Left inset: Global CO₂ production rate versus CO partial pressure as measured by MS during catalytic CO oxidation at $T = 417\text{K}$ and $p_{\text{O}_2} = 1.3 \times 10^{-5}\text{mbar}$. Right inset: Hysteresis plot of the local PEEM intensity of an individual Pt(100) facet versus CO partial pressure, as measured *in situ* by PEEM at the same reaction conditions. The selected domain is indicated in frame (1). The numbers along the hysteresis curve indicate the corresponding PEEM frames. (b) Corresponding kinetic phase diagram for a Pt(100) facet (black squares) in comparison to the global (MS-measured) diagram (red dots). (c) The same as in (b), but in comparison to a local diagram for a Pt(110) facet (red dots).

4 Local reaction kinetics of CO oxidation on polycrystalline platinum

transitions at small length scales [255]. At pressures higher than 10^{-4} mbar, gas-phase coupling provides the synchronization [256, 257], and at atmospheric pressure, heat transfer contributes significantly or even dominates spatial coupling [258, 259]. Apparently, the domain boundaries effectively hinder the diffusion coupling and the total pressure (10^{-5} mbar) seems insufficient for synchronization via gas-phase coupling.

In a further step we have modeled the global reaction kinetics of Pt foil by summing up the weighted contributions (weighted average of the transition pressures) of the different domains, based on the domain area distribution of annealed foil of (100) : (110) : (111) = 2 : 2 : 1 (Figure 4.3) [37]. Indeed, the global phase diagram constructed from the superposition of domain specific local phase diagrams of the individual (100), (110) and (111) orientations (based on local PEEM intensity analysis) perfectly coincides with the experimental global phase diagram obtained by MS. This indicates that the PEEM imaging/analysis monitored all relevant surface catalytic processes and that the facets, rather than the domain boundaries, governed the reaction rate. Otherwise, there would have been a deviation between global MS rates (accounting for all active surface sites) and the weighted sum of local PEEM rates (including only "visible" domain sites in the field of view).

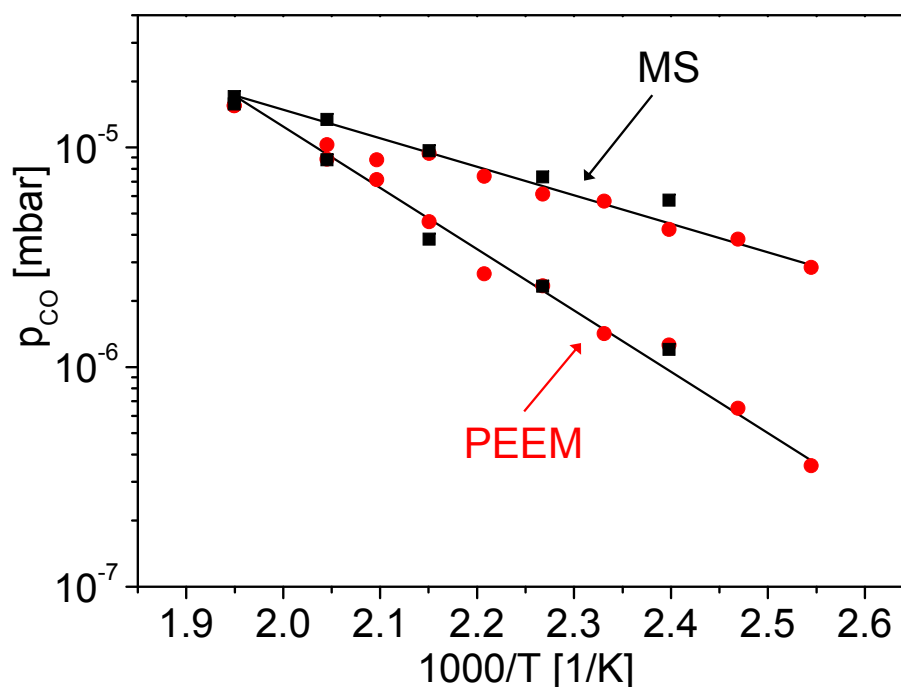


Figure 4.3: Global kinetic phase diagram of a Pt foil, based on the domain specific diagrams deduced from local PEEM intensities (black squares, cf. Fig. 4.2) at constant O_2 pressure (1.3×10^{-5} mbar), compared to the kinetic phase diagram of the same Pt foil obtained from the mass spectroscopic CO_2 rate (red dots).

4.3.2 Surface morphology and reaction fronts on (100)-type grains on Pt foil

In the following we focus on the propagation of reaction-diffusion fronts on specific Pt(100) grains and its correlation to the surface morphology. Figure 4.4 shows a series of PEEM image frames recorded during a CO pressure scan at 417K and constant $p_{\text{O}_2} = 1.3 \times 10^{-5}$ mbar, illustrating the transition from the CO-covered (inactive) to the oxygen-covered (active) state. The dark regions represent the propagating oxygen fronts whereas the brighter regions are still CO-covered. The fronts exhibit a pronounced anisotropy, although both possible phases of the (100) surface are expected to be isotropic (i.e. the quasi-hexagonal structure of the clean surface, typically referred to as the (hex) phase [42], and the unreconstructed (1×1) phase formed upon CO or oxygen adsorption [44, 45, 53]. STM observations, however, have revealed a strong surface roughening during the adsorbate-induced surface transition from the (hex) to the (1×1) phase upon which entire rows of Pt atoms are collectively ejected and form elongated ad-islands [58]. This can be explained by the required compensation of the difference in the surface atom density: the (hex) phase is $\sim 20\%$ more densely packed than the (1×1) phase [60] (see also corresponding ball models in Fig. 4.8). The size of the "ejected islands" depends on temperature and varies between $\sim 15 \text{ \AA}$ at 300K [58] and 70 \AA at 460K [57]. Therefore, even in the "ideal" case neither of the surface configurations can be considered as isotropic. Nevertheless, at first glance the observed high degree of the front anisotropy is astonishing, particularly when compared to that on the neighboring (110) grain (visible e.g. in frames 1 to 3 of Fig. 4.4). On (110), elliptical fronts are formed due to the known atomic scale anisotropy of the (110) substrate, with a ratio of ~ 2 for the front velocities along the $[1\bar{1}0]$ and $[001]$ directions [254, 260], well in agreement with single crystal data [261].

To understand the striking degree of the front anisotropy on (100) domains, we have investigated the surface morphology of the two neighboring [100]-oriented grains highlighted in PEEM frame 1 of Fig. 4.4. The surface morphology was examined in more detail by using optical differential interference contrast microscopy and AFM and our observations were compared to earlier STM reports by Borg et al. [58].

Figures 4.5a, b show PEEM frames of the clean Pt surface (a) and of the Pt surface with propagating oxygen fronts on the two neighboring (100) domains, with the propagation directions significantly differing from each other (b). In turn, the optical micrograph (Fig. 4.5c) taken after many reaction cycles clearly shows a hill-and-valley surface morphology, which coincides with the front propagation directions. Figures 4.5d and 4.5e display cor-

4 Local reaction kinetics of CO oxidation on polycrystalline platinum

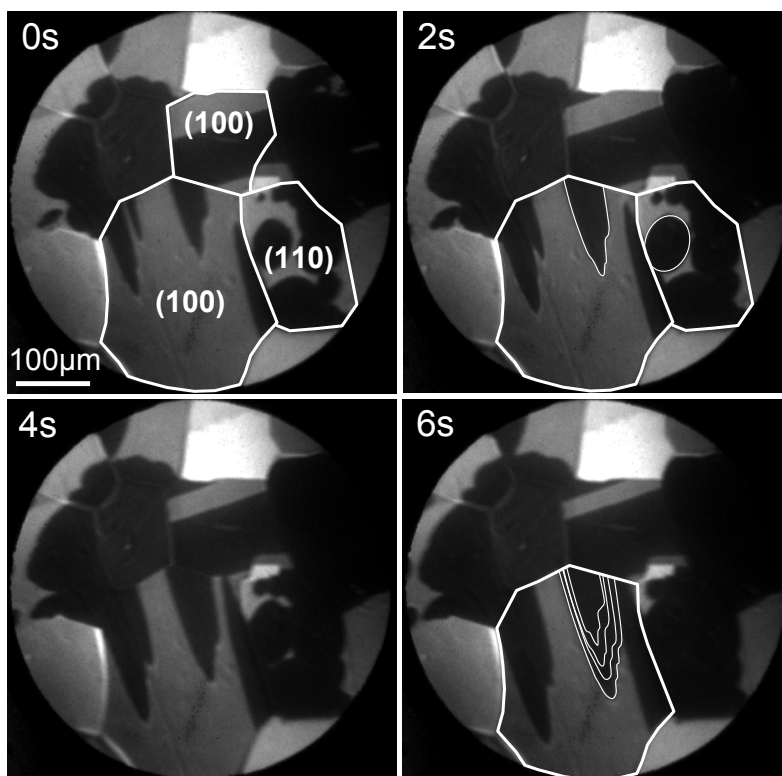


Figure 4.4: Propagation of reaction fronts (here oxygen fronts) on polycrystalline Pt foil during catalytic CO oxidation at $T = 417\text{K}$ and $p_{\text{O}_2} = 1.3 \times 10^{-5}\text{mbar}$ (image frames recorded at an interval of 2s). Regions of interest (two Pt(100) domains in comparison with a Pt(110) domain) are marked in the frame "0s". Note the different shape of the propagating fronts on the (100) and (110) domains as marked in the frame "2s". In the frame taken at 6s, the front positions at 0s, 2s, 4s and 6s are outlined in white.

responding AFM micrographs of the two neighboring grains revealing ca. 20nm deep and 400 – 600nm wide grooves aligned along the propagation directions. Surface structures of similar size have been previously reported in the context of catalytic CO oxidation on Pt surfaces: using scanning electron microscopy Lauterbach et al. have observed parallel furrows (size range of 200nm up to several μm) on (100)-type grains of a polycrystalline Pt foil, the direction of which correlated with the propagating reaction fronts [37]. Swiech et al. observed a step and terrace structure on a Pt(100) single crystal surface with a mean terrace width of approximately 700nm [248], which was assigned to a miscut of their single crystal.

The formation of such grooves on (100)-type grains can be explained in the following way: As already mentioned, the adsorbate-induced surface phase transition from the (hex) to the (1×1) phase is accompanied by the formation of elongated (ad-)islands [58, 60]. Upon removing the adsorbate a reverse transition takes place, when the less densely packed

4 Local reaction kinetics of CO oxidation on polycrystalline platinum

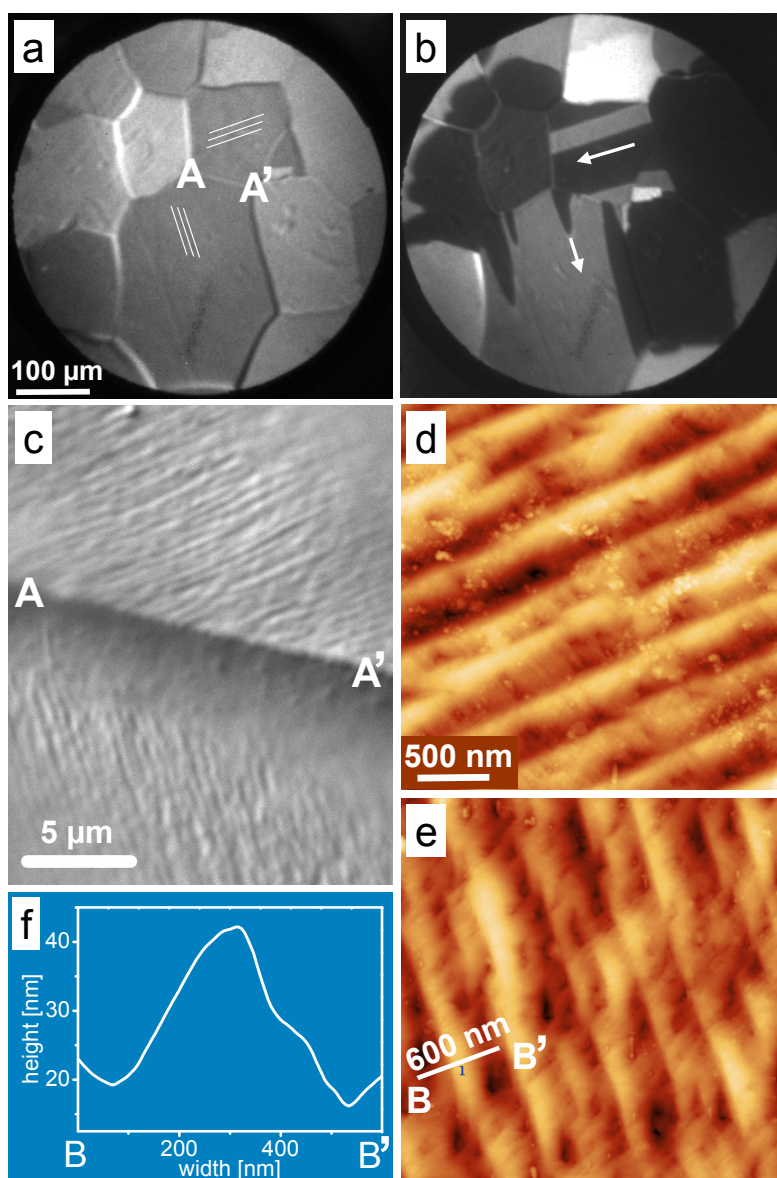


Figure 4.5: (a) Clean Pt foil imaged by PEEM. The AA' line denotes the grain boundary between two (100) domains. (b) Snap-shot during the transition τ_B : anisotropic propagation directions of the reaction fronts on the neighboring (100) domains differ from each other. (c) Optical micrograph of the grain boundary region AA'. (d) and (e) AFM images of the neighboring (100) domains. (f) Line scan across the BB' line in (e). The grooves imaged in (c)-(e) are schematically indicated in (a). The reaction front propagation directions (b) coincide with the directions of the grooves in (c) and are indicated in (a).

(1 × 1) phase covered with ~ 20% of ad-islands has to transform back into the close-packed (hex) reconstruction. This may proceed not simply through a direct absorption of the adatoms into the (sub)surface layer, which would require quite extensive mass transport,

4 Local reaction kinetics of CO oxidation on polycrystalline platinum

but may proceed via creation of subsurface vacancies, which can coalesce by diffusion to steps and additionally increase the total surface roughness [61]. The CO oxidation reaction additionally enhances the roughening of the surface, since the reaction front propagation involves the surface phase transition, so one can conclude that after numerous repeats of the adsorbate-induced surface phase transition, mesoscopic grooves on the order of several hundred nm width and around 20 nm height are created. Once the grooves are formed, they may have, in turn, an influence on the direction of the reaction front propagation.

To learn more about the propagation of the reaction-diffusion fronts, the role of the reaction temperature was also studied. Figure 4.6 shows the behavior of propagating CO fronts during the transition from the active (dark) to the inactive (bright) state at constant oxygen pressure $p_{\text{O}_2} = 1.3 \times 10^{-5}$ mbar, at two different temperatures of 417 K and 513 K. The PEEM images in Fig. 4.6a, b reveal that at both temperatures the CO fronts are highly anisotropic and oriented along the grooves of the (100) domain. For the whole temperature range, bright fringes are observed separating the CO- and oxygen-covered regions, which are illustrated by intensity line scans (Fig. 4.6c, d). Figure 4.6e shows the temperature dependence of the CO front velocities, which is strong along the grooves (black squares) and basically negligible across the grooves (red dots). The values which are in the low $\mu\text{m/s}$ range are in qualitative agreement with literature data on Pt(100) single crystals [225]. We apply Luther's equation $v(T) \approx a\sqrt{k(T) \cdot D(T)}$ describing the temperature dependence of the propagation velocity $v(T)$ of a reaction-diffusion front [262]. $D(T)$ is the CO diffusion coefficient and $k(T)$ is the effective first-order reaction rate constant of the reaction. The corresponding fit to the front propagation along the grooves obtained with the $D(T)$ and $k(T)$ values from single crystal studies [222] is in good agreement with our experimental data. This indicates that the reaction fronts along the "faster direction" on the individual (100) domains of the polycrystalline foil behave very similar as on the corresponding Pt(100) single crystal. The velocity along the "slower direction" can hardly be fitted with the literature data of the Pt(100) single crystal, since the surface structure profile in this direction can be rather compared to a stepped (100) surface (see discussion below), for which the surface diffusion is different from the "flat" Pt(100) [263]. Therefore, the fitting parameters were set free and a value of 11.3 kcal/mol for the effective activation energy was obtained from the red line in Fig. 4.6e.

The mechanism of CO front propagation was proposed already in 1994 (for the oscillating CO oxidation) [225]: on the oxygen covered surface, CO adsorbs at some defects (in the present case at the domain boundaries) and CO_2 is formed, leaving behind a region where the adsorbate coverage is low enough to initiate the $(1 \times 1) \rightarrow (\text{hex})$ surface phase transition.

4 Local reaction kinetics of CO oxidation on polycrystalline platinum

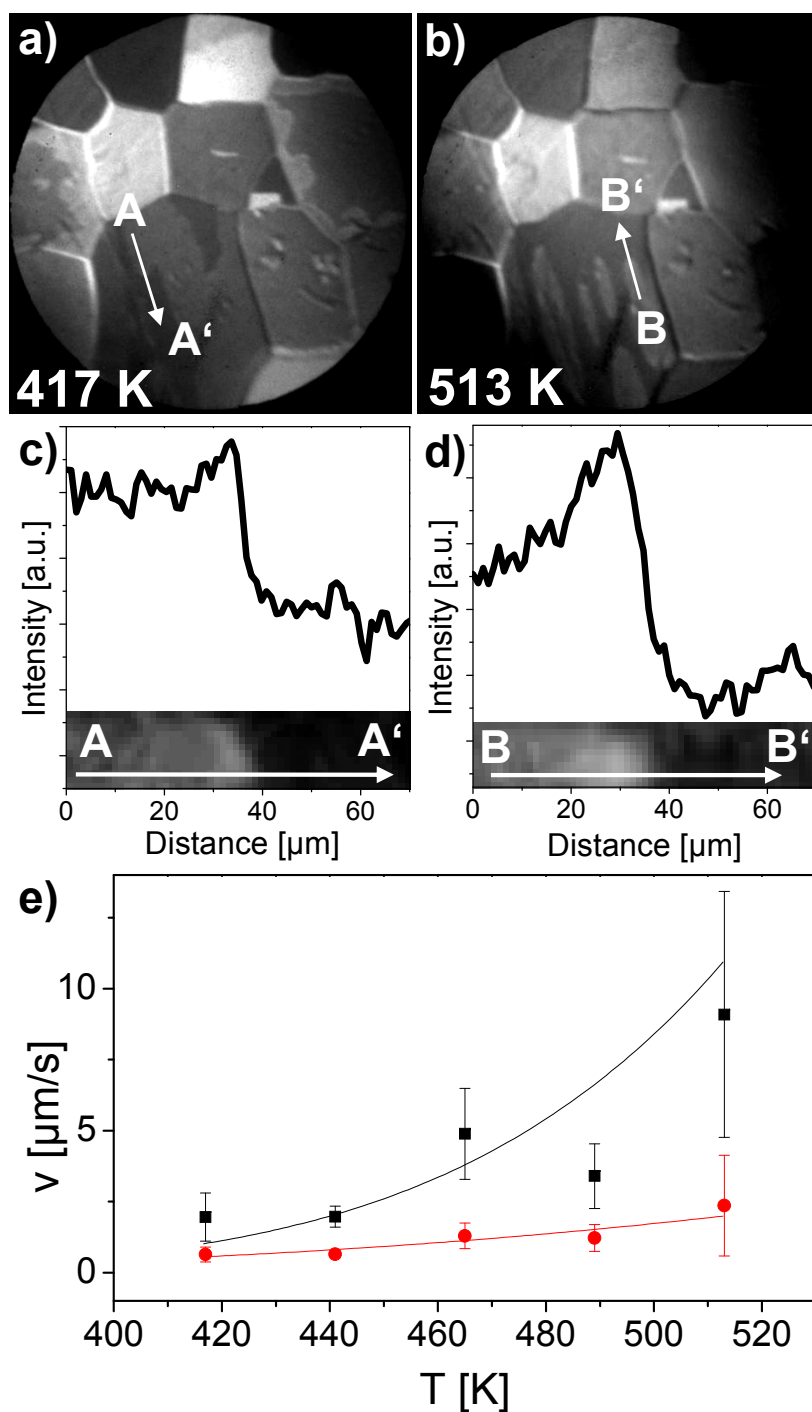


Figure 4.6: Temperature dependence of the CO front propagation. (a) and (b) PEEM images of the CO fronts recorded during the transition τ_A at $p_{\text{O}_2} = 1.3 \times 10^{-5}$ mbar, at 417 K and 513 K, respectively. (c) and (d) Intensity line scans across the CO front along AA' and BB'. (e) Temperature dependence of the front propagation velocities along (black squares) and across (red dots) the grooves on the (100) domain (see Fig. 4.5). The solid lines are fits using Luther's equation (see text).

4 Local reaction kinetics of CO oxidation on polycrystalline platinum

Since the sticking coefficient for oxygen is lowered to approximately 10^{-3} – 10^{-4} on the (hex) phase from ~ 0.1 on the (1×1) phase [49], oxygen is unlikely to adsorb in this region and the CO molecules can diffuse towards the (preadsorbed) oxygen. The bright fringe at the border of the CO fronts was assigned to the clean hexagonally reconstructed surface. This mechanism is still in agreement with the current results on Pt foil.

Next, we consider the behavior of the oxygen fronts. Figure 4.7 shows the behavior of the oxygen fronts propagating during the transition τ_B at different temperatures. At low temperature the oxygen fronts are highly anisotropic, similar to the CO fronts (Fig. 4.7a). However, with increasing temperature the fronts become almost completely isotropic (Fig. 4.6b), in strong contrast to the CO fronts, where the anisotropy is maintained at high temperature. Also the appearance of the $\text{CO}_{ad}/\text{O}_{ad}$ border in the oxygen fronts differs significantly from that of the CO fronts (Fig. 4.7c, d): for low temperatures (e.g. 417 K), the oxygen front exhibits a very bright fringe between the oxygen- and CO-covered regions. In contrast, at 489 K the fringe has vanished, indicating a different front structure at high temperature. A plot of the ratio of the v_x/v_y , where v_x is the velocity along the grooves and v_y across them (Fig. 4.7e), demonstrates this convincingly: this ratio decreases from a factor of approximately 8 at 417 K to a factor smaller than 2 at 513 K.

Both the disappearance of the front anisotropy and of the bright fringes indicate a change in the propagation mechanism for oxygen fronts upon increasing the temperature. The oxygen front propagation mechanism (again for oscillatory reaction conditions) has been described in the following way [225]: On the CO-covered surface, which is in the (1×1) phase, oxygen can nucleate at its excess in the gas phase at surface defects. Since the oxygen pressure is roughly 10 times higher than the CO pressure, oxygen adsorption in this region prevails over CO diffusion, so the oxygen front propagates via the subsequent adsorption of oxygen onto free sites and the (1×1) structure is continuously present across the front line. This mechanism can, in principle, be applied to our high temperature case (489 K–513 K). It is clear that for a continuous (1×1) structure across the propagating front, no bright fringe should be observed, as also observed in our experiments.

At lower temperatures, we observe a front structure different from that proposed in [225]. Here, the much lower CO diffusion rate leads to a broader front zone than at higher temperature. In this front zone a stronger CO coverage gradient exists and the overlap of the CO_{ad} and O_{ad} coverages is not sufficient to keep the (1×1) structure "stable", thus a nearly adsorbate-free area exists between the oxygen and CO covered regions (therefore a bright fringe is observed, Fig. 4.7c) which reconstructs to the (hex) phase. The reconstruction is thermally activated starting at temperatures above 390 K [53] and is thus expected to oc-

4 Local reaction kinetics of CO oxidation on polycrystalline platinum

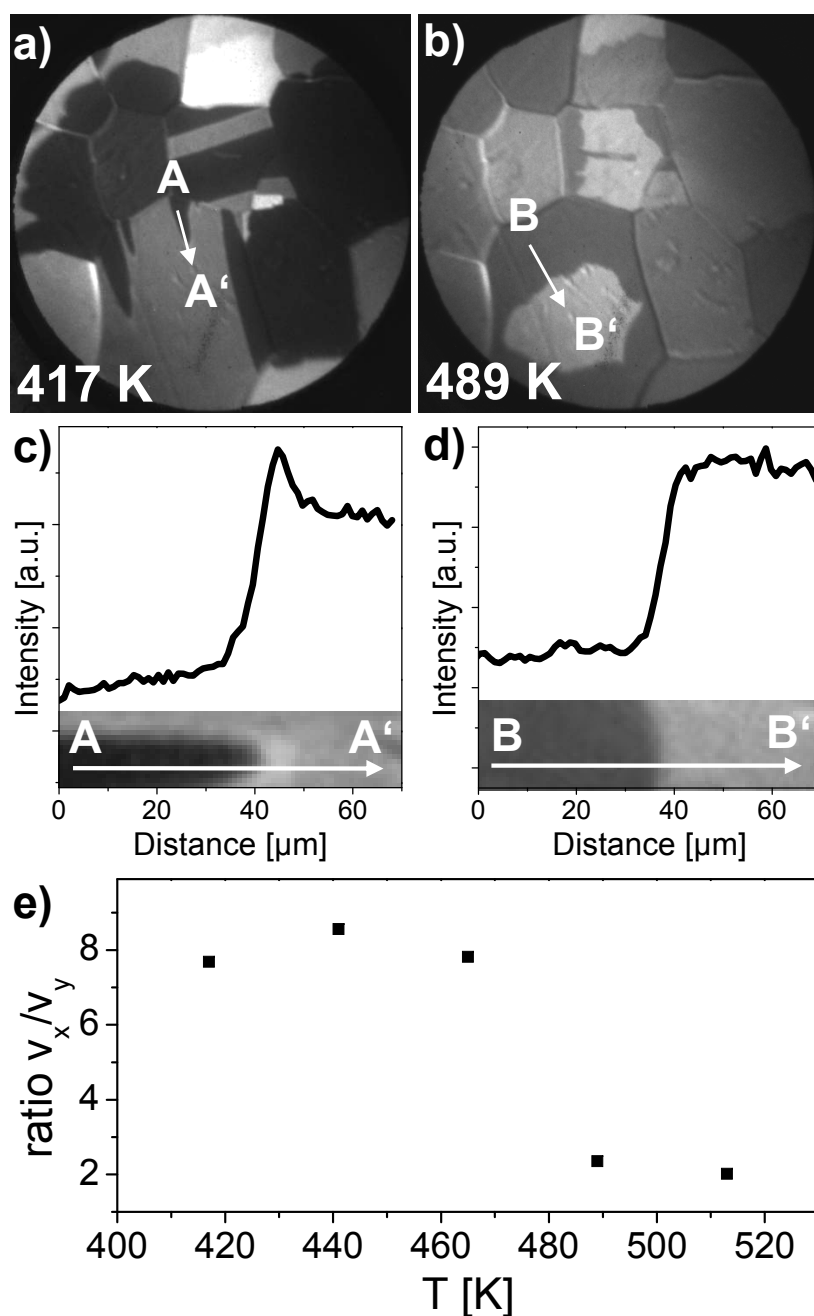


Figure 4.7: Oxygen front propagation at two different temperatures of 417K and 489K. (a) and (b) PEEM images of oxygen fronts during the transition τ_B at $p_{\text{O}_2} = 1.3 \times 10^{-5}$ mbar, at 417K and 513K, respectively. (c) and (d) Corresponding intensity line scans across the oxygen front along AA' and BB'. The bright fringe between the CO- and oxygen-covered regions disappears at the higher temperature. (e) Temperature dependence of the ratio of the propagation velocities along (v_x) and across (v_y) the prolonged grooves on the (100) facet. The anisotropy decreases with increasing surface temperature.

4 Local reaction kinetics of CO oxidation on polycrystalline platinum

cur under the experimental conditions in Fig. 4.7c. Interestingly, a similar fringe formation for oxygen fronts was observed earlier [225], but the formation of the (hex) phase within the boundary was excluded as reason, maybe because the fringe-free fronts at which the hex-phase disappears were not observed in Ref. [225].

To finally explain the high anisotropy of the CO-fronts (and the oxygen fronts at temperatures up to 465K) we refer to the results of the STM study by Borg et al. [58]: the growth of the (1 × 1) phase is highly anisotropic, thus it is clear that the CO and the oxygen islands, both nucleating the (1 × 1) structure on the (hex) phase, grow in an anisotropic way as was directly observed in [58] in adsorption experiments. Thus the fronts which propagate in this case via anisotropic island formation, are also anisotropic as is schematically depicted in Fig. 4.8a and b. In turn, on the already existing continuous (1 × 1) phase the propagation of the reaction front is driven mainly by adsorption which is an isotropic process, thus the anisotropy vanishes for oxygen fronts at $T > 465\text{K}$, as is observed in the present experiments and is sketched in Fig. 4.8c.

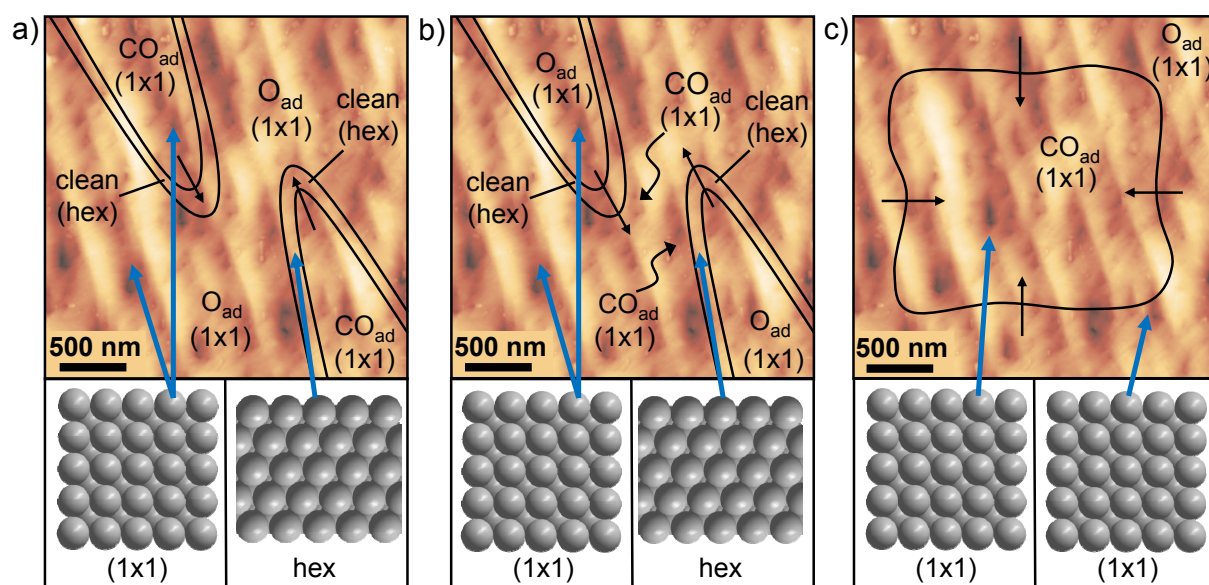


Figure 4.8: Scheme of the front propagation mechanism for (a) CO fronts at all studied temperatures, (b) oxygen fronts at temperatures up to 465 K, (c) oxygen fronts at temperature above 465 K. The AFM image shown in Fig. 4.5 is used as a background.

Last but not least, we mention the role of the reaction-induced mesoscopic "hill and valley" morphology on the surface: it seems that it rather plays a minor role in the observed anisotropy of the reaction front propagation, apart of an apparent effect of the projection of the 3D folded surface to a 2D image in which a circle appears as an ellipse. Our estimations based on the 3D geometry deduced from AFM indicate just a 0.5% contribution to the

anisotropy. However, a higher density of steps may be expected across the grooves leading to a certain CO diffusion asymmetry, the contribution of which can be hardly estimated at present.

4.4 Summary

The domain-specific kinetics of the CO oxidation reaction on individual [100]-, [110]- and [111]-oriented domains on a polycrystalline Pt foil were examined by PEEM. The kinetic phase diagrams for CO oxidation on single Pt(100), Pt(110) and Pt(111) domains were obtained by intensity analysis of *in situ* video-PEEM sequences. Such a local kinetic phase diagram provides information within the parameter space (p_{CO}, p_{O_2}, T) for regions of high and low reactivity and the bistability region, for an individual μm -sized Pt(hkl) region confined by grain boundaries.

The local (PEEM-determined) kinetic phase diagrams for the Pt(hkl) domains differ significantly from the averaged (MS-measured) diagram for the entire polycrystalline sample, stressing the necessity of local kinetic studies on heterogeneous samples. The observed confinement of the propagating reaction fronts within grain boundaries indicates a quasi-independent behavior of the individual domains. The micrometer-size of the domains and the low total pressure (10^{-5} mbar) hinder the reactive synchronization via adsorbate diffusion or gas phase coupling, respectively. Based on the PEEM-derived local kinetic phase diagrams, a global phase diagram was constructed by summing up the weighted contributions of the (100), (110) and (111) domains. The constructed global phase diagram was in excellent agreement with the global phase diagram experimentally measured by (averaging) mass spectroscopy, indicating that PEEM imaging/ analysis detected all relevant surface catalytic processes.

PEEM monitoring of the reaction front propagation on Pt(100) domains reveals a high degree of propagation anisotropy both for oxygen and CO fronts (on the apparently isotropic Pt(100) surface). The anisotropy vanishes for oxygen fronts at temperatures above 465 K, but remains for CO fronts at all temperatures studied, in the range of 417 to 513 K. A change in the front propagation mechanism is proposed to explain the observed effects. In turn, the reaction-induced mesoscopic "hill and valley" morphology on the surface, observed by AFM, seems to play rather a minor role in the observed anisotropy of the reaction front propagation.

LOCAL CATALYTIC IGNITION DURING CO OXIDATION ON LOW-INDEX Pt AND Pd SURFACES

In this chapter, a study of the local reaction kinetics in the CO oxidation, including catalytic ignition, on individual grains of polycrystalline platinum and palladium foil samples by photoemission electron microscopy (PEEM), mass spectrometry (MS), density functional theory (DFT) and micro-kinetic modeling is presented. The catalytic behavior of the Pt foil and the individual (hkl) domains on Pt foil is contrasted to the Pd foil and the Pd(hkl) grains, respectively. Hereby, not only the isothermal kinetic transitions are studied, which are used to construct the kinetic phase diagrams, but also the isobaric kinetic transitions, which are more commonly studied in technical catalysis and are termed as catalytic ignition and extinction of the reaction. The question is addressed at which surfaces, Pt(hkl) or the corresponding Pd(hkl) domains, the catalytic ignition occurs easier and how the isothermal determination of kinetic transitions, commonly used in surface science under high-vacuum conditions, compares to the isobaric reactivity monitoring usually applied in technical catalysis.

In addition, new DFT-calculated adsorption energies for oxygen and CO adsorption on the three low-Miller indexed orientations of Pt and Pd, calculated reaction barriers for the CO oxidation reaction on Pt and Pd and micro-kinetically simulated ("local") kinetic phase diagrams for the Pt and Pd(hkl) surfaces are used to rationalize the experimentally observed differences between Pt and Pd and the individual (hkl) domains, respectively.

5.1 Introduction

Although modern catalytic converters significantly reduce pollution from automobile engines, a major amount of pollutants is still emitted just after "cold-start", i.e. until the catalytic converter warms up to the reaction "ignition" temperature, at which the reaction rate rapidly switches from low to high conversion. There is thus substantial interest of manufacturers to reduce emissions during the start-up period of automotive catalyts. Consequently, sophisticated catalyst heating processes have been developed to quickly reach the critical temperature. Methods include operation at lean air-to-fuel ratio, exhaust system combustion devices, secondary air injection into the exhaust, electrically heated catalyts, etc [264]. Alternatively, as an "energy-neutral" approach, lowering the critical temperature seems more promising.

Catalytic ignition has originally been considered as a sole heat balance problem [265], with the critical ignition temperature being defined as the temperature when the heat generated by the exothermic reaction exceeds the dissipated heat (i.e. the catalyst heats up and no external heating is required anymore; "light-off"). In fact, the catalytic ignition process represents a convolution of reaction kinetics and heat generation, since the produced heat is governed by the reaction rate which in turn is determined by the reaction kinetics [266, 267].

However, for CO oxidation under (ultra)high-vacuum on metallic model catalyts, the heat generation by the reaction can be neglected, and the catalytic ignition problem can thus be reduced to the "pure kinetics", that is, to the temperature-triggered kinetic transition from the low-rate steady state regime to a high-rate steady state [268, 269]. Such a transition in the CO oxidation reaction is a phenomenon of purely kinetic origin [201, 270] which is well studied, mainly via varying the CO/O₂ ratio [213, 219, 220, 253].

In this chapter an experimental study of catalytic ignition in the CO oxidation reaction under high vacuum conditions (10⁻⁵ mbar range) for μm-sized (hkl) domains of polycrystalline Pt and Pd foil is presented. Emphasis is put on local kinetic measurements enabling a direct comparison of the reaction properties of low-Miller-index Pt(hkl) and Pd(hkl) domains, whereby the different metals and different terminations have been evaluated under basically identical reaction conditions, yielding the inherent reaction behavior. The results of the isothermal and the isobaric determination of reactivity states are compared in the considered pressure regime for the CO oxidation on Pt and Pd foil. The catalytic performance of Pd foil is compared to that of Pt foil, regarding the reactivity ranges in (*p*, *T*)-parameter space, that is, regarding the CO-tolerance and the reactivation ability. The ex-

perimental findings are supported and explained by newly performed Density Functional Theory (DFT) calculations and micro-kinetic modeling.

In chapter 4, an experimental approach based on the analysis of local PEEM (Photoemission Electron Microscopy) intensities has been presented, which allows the *in situ* observation of kinetic phase transitions on individual differently oriented grains of a polycrystalline Pt foil [253]. The idea of the experiment is based on the fact that the local photoemission yield is directly dependent on the local CO or oxygen coverage (via the local work function). Since the CO or oxygen coverage governs the rate of CO₂ formation [18], the local PEEM image intensity serves as an indicator for the local reaction rate, which allows "imaging" of the kinetic phase transitions on the μm-scale. In chapter 4, such an analysis has been used to construct kinetic phase diagrams for the CO oxidation reaction in the 10⁻⁵ mbar pressure range for individual [100]-, [110]- and [111]-oriented grains of a Pt foil [253]. The single (hkl) domains exhibited independent reaction properties, analogous to the corresponding single crystals, and the sum of the local kinetic diagrams for individual grains is equal to the global kinetic diagram obtained for the whole sample by MS (indicating that the grain boundaries do not contribute directly to the overall reactivity and that all relevant catalytic processes were monitored by this approach) [253]. In the present chapter, this approach has been extended to Pd samples and to the reaction light-off on Pt and Pd foil at isobaric conditions.

5.2 Experimental approach to global and local catalytic ignition/extinction

A series of ignition/extinction experiments has been performed in the PEEM chamber of the UHV setup described in detail in chapter 2. The studied samples were the polycrystalline Pd (AlfaAesar, 99.9%) and Pt (MaTeck, 99.99%) foil, described in section 2.3.1, both consisting of up to ~ 100 μm large crystallites of different surface orientation, as determined by work function analysis [253]. Before each experiment, the samples were cleaned by the standard UHV cleaning procedure described in section 2.3.1.

The reaction was followed *in situ* (Fig. 5.1a), simultaneously by photoemission electron microscopy (PEEM) and by quadrupole mass spectrometry (QMS). QMS provides the average CO₂ formation rate originating from all grains of the polycrystalline foil (Fig. 5.1b), whereas the recorded PEEM-sequences deliver the local photoemission yield from individual grains (Fig. 5.1c). The latter provides laterally-resolved kinetic information from

5 Local catalytic ignition during CO oxidation on low-index Pt and Pd surfaces

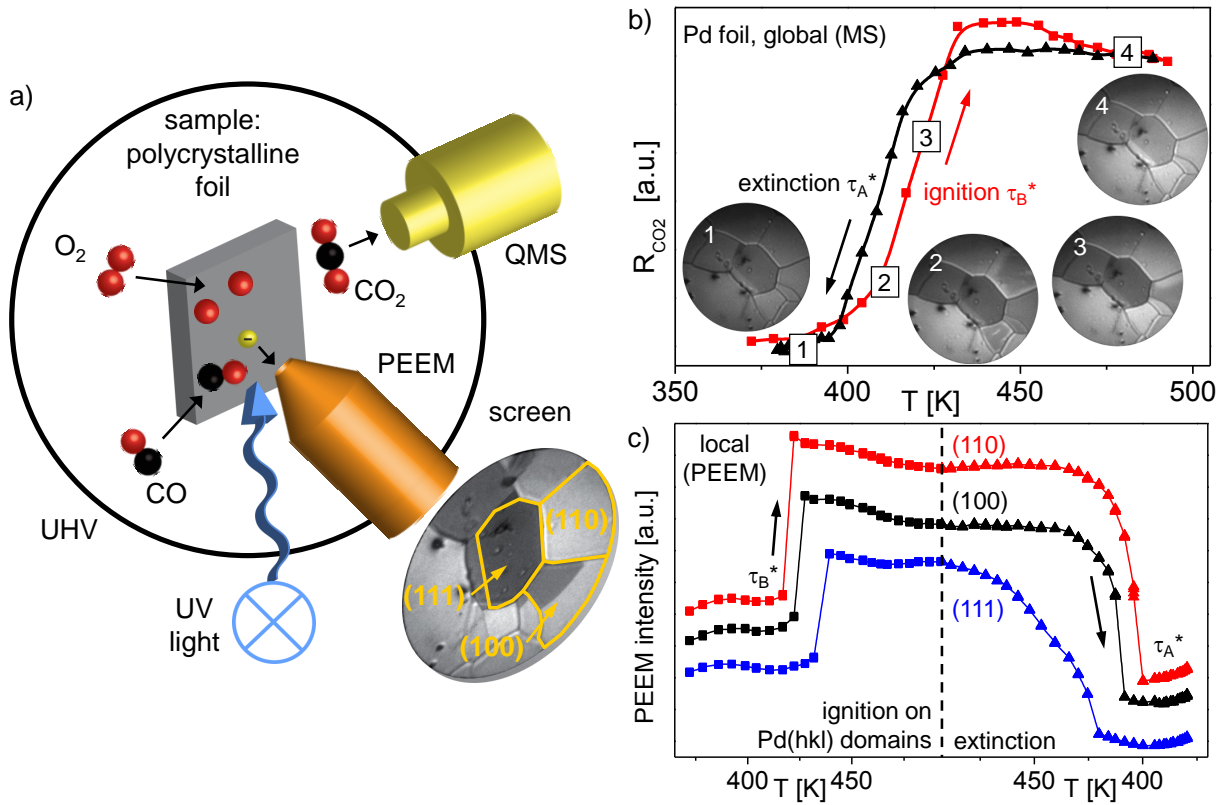


Figure 5.1: a) Scheme of the experiment: CO oxidation reaction on polycrystalline Pd (Pt) foil is simultaneously followed by MS and PEEM. Three different domains, Pd(110), Pd(100) and Pd(111) are exemplary identified in the PEEM image. b) Ignition (red squares) and extinction curves (black triangles) on Pd foil, as CO₂ production rate measured globally by MS at cyclic variation of the sample temperature (rate: 0.5K/s) at constant $p_{\text{CO}} = 5.8 \times 10^{-6}$ mbar and $p_{\text{O}_2} = 1.3 \times 10^{-5}$ mbar. Simultaneously recorded PEEM video-sequences illustrate the ignition process: Frame (1) - inactive, CO covered surface; (2) - ignition begins on (110)-domains; (3) - ignition continues on (100) domains; (4) - oxygen covered, active surface. c) Laterally resolved ignition/extinction measurements: local PEEM intensity for the individual (110), (100) and (111) domains during the same cyclic temperature scan as in (b). The vertical dashed line indicates the turning point from heating to cooling.

the different domains at exactly identical experimental conditions, since all domains of the foil are exposed to the same gas phase composition at the same temperature. In this way, the global (Fig. 5.1b) and local (Fig. 5.1c) kinetics for the Pd foil can be compared, e.g. for a typical temperature scan from 372K to 493K, with a rate of 0.5K/s at constant $p_{\text{CO}} = 5.8 \times 10^{-6}$ mbar and $p_{\text{O}_2} = 1.3 \times 10^{-5}$ mbar. Following the temperature ramp, the global CO₂ rate suddenly increases indicating the transition τ_{B}^* from the state of low catalytic activity (CO-poisoned surface; video-frame 1 in Figure 5.1b, dark contrast) to the state of high catalytic activity at which the surface becomes oxygen covered (frame 4; bright contrast). Analogous to the MS signal in the overall CO₂ reaction rate, the jumps in the

local PEEM intensity represent the local kinetic transitions on the individual grains (Fig. 5.1c). These transitions do not occur simultaneously on the different orientations but show a pronounced structure sensitivity with clearly identifiable critical temperatures of 417K for Pd(110), 423K for Pd(100) and 432K for Pd(111). A similar observation was made for the reaction extinction, i.e. for the transition τ_A^* from the high reactivity to the low reactivity state upon cooling the sample. Again, the curve of the *global* CO₂ production rate appears to be "smoothened out" (black curve in Fig. 5.1b), whereas *local* extinction on the individual grains occurs rather sharply and independently from each other (Fig. 5.1c). This clearly shows the limitation of averaging techniques such as mass-spectroscopy, which can not reveal the important local kinetics.

5.3 Results

5.3.1 Isothermal *versus* isobaric kinetic transitions on Pd foil

Usually, kinetic transitions in CO oxidation are experimentally studied under high vacuum conditions by varying the CO/O₂ pressure ratio at constant temperature [219, 220, 253]. Such an experiment is illustrated for Pd foil in the right inset of Fig. 5.2a, at constant $p_{O_2} = 1.3 \times 10^{-5}$ mbar and $T = 449$ K. Similar to the case of Pt foil [253, 254, 271], the global CO₂ formation rate exhibits a pronounced hysteresis upon cyclic variation of the CO partial pressure manifested in the gap between the kinetic transition τ_A from the high reactivity to the low reactivity state and the reverse transition τ_B . In between, the system is bistable, i.e. it can be either in the high or in the low reactivity steady state, depending on the pre-history. The τ_A and τ_B points are temperature-dependent, thus a (global) kinetic phase diagram can be constructed for the Pd foil, summarizing the kinetic transitions (Fig. 5.2a).

For comparison, the kinetic transition points (τ_A^*/τ_B^*) extracted from isobaric ignition/extinction experiments (shown in the left inset of Fig. 5.2a for constant $p_{CO} = 5.8 \times 10^{-6}$ mbar and $p_{O_2} = 1.3 \times 10^{-5}$ mbar) are also plotted into the isothermally obtained diagram in Figure 5.2a. The *isobaric* variation of the reaction temperature results in kinetic transitions which are quantitatively matching the kinetic phase diagram obtained by the isothermal variation of the CO pressure. In Fig. 5.2b the result of the local PEEM analysis of the same transition for an individual Pd(100) domain is shown: again, the left inset shows the ignition/extinction experiment and the right inset presents the transitions obtained via variation of the CO pressure at constant T and p_{O_2} . As in the case of the (global) MS-data, the transition points obtained from isobaric experiments are in quantitative agreement with

5 Local catalytic ignition during CO oxidation on low-index Pt and Pd surfaces

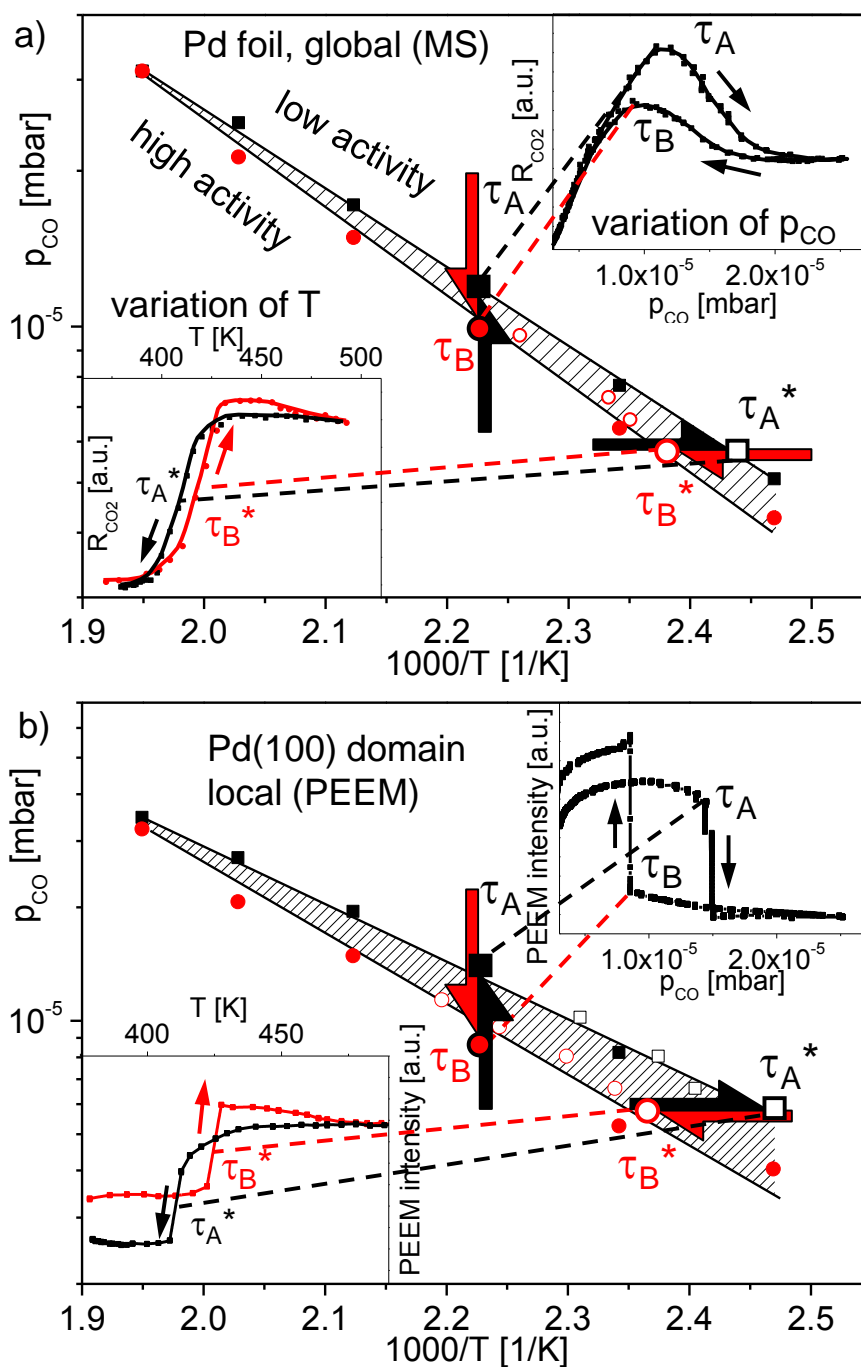


Figure 5.2: Global (a) and local (b) kinetic phase diagram illustrating the CO oxidation reaction on polycrystalline Pd foil (a) and on a single Pd(100) domain of the Pd foil (b). Note the agreement of the transition points τ_A^* and τ_B^* obtained at varying T (from the ignition/extinction curves shown in the left insets, open symbols) with the diagram obtained via cyclic variation of p_{CO} (from the poisoning/reactivation curves in the right insets, filled symbols). The dashed regions indicate the range of bistability.

the isothermal experiments, thus linking the typical surface science (isothermal) approach and the typical technical catalysis (isobaric) approach.

5.3.2 Palladium *versus* platinum in CO oxidation

To compare the reaction behavior of Pt and Pd foil, global ignition and extinction measurements for Pt foil were performed in analogy to the Pd foil experiments by mass spectrometric monitoring of the CO₂ reaction rate at constant $p_{\text{O}_2} = 1.3 \times 10^{-5}$ mbar and $p_{\text{CO}} = 6.6 \times 10^{-6}$ mbar, as illustrated in Fig. 5.3a. The global extinction curve appears to be smoothed out and a distinct "global extinction temperature" can hardly be assigned. This "smoothing" effect is caused by sequential extinction of differently oriented Pt(hkl) domains, i.e. at isobaric conditions the local extinctions on the individual Pt(hkl) domains occur sequentially within a broad temperature range which covers almost the whole global hysteresis loop. For comparison, a global R_{CO_2} hysteresis curve obtained under isothermal conditions upon cyclic variation of the CO partial pressure is shown in Fig. 5.3b. The smooth appearance of the transition τ_A upon CO pressure variation reflects again the sequential CO-poisoning of the (hkl) domains.

Parallel to the global MS measurements shown in Figs. 5.3a and b, the local PEEM intensities from individual grains of the Pt foil were monitored, as shown in Figure 5.3c and d for a (100) domain. For both type of measurements, variation of temperature (Fig. 5.3c) and variation of CO partial pressure (Fig. 5.3d), the local kinetic transition points τ_A^*/τ_B^* and τ_A/τ_B , respectively, are much more pronounced than in the global MS measurements (Figs. 5.3a, b).

In Fig. 5.4, the PEEM video-frames of the local ignition and extinction of Pt(hkl) domains which were recorded during the MS-monitoring in Fig. 5.3a (and c) are shown. Details of the identification of the surface orientation of the individual Pt(hkl) domains and the contrast mechanism (CO-covered surface appears bright in comparison to oxygen covered surface) were described in section 2.3.3. Note that on Pt, contrary to Pd, the oxygen covered surface appears darker in PEEM than CO covered regions.

In Fig. 5.5a, the *global* reaction behavior of Pt and Pd foil is compared, whereas in Fig. 5.5b the local kinetic transitions of the individual Pt(hkl) domains are contrasted to those of the Pd(hkl) domains. The most striking differences between Pt and Pd are: (i) the global and the respective local kinetic phase diagrams of Pd foil are situated at significantly higher CO partial pressure and (ii) the bistability range is much narrower for Pd than for Pt foil. In particular, this means that for Pd the transition τ_A from the high to the low reactivity state

5 Local catalytic ignition during CO oxidation on low-index Pt and Pd surfaces

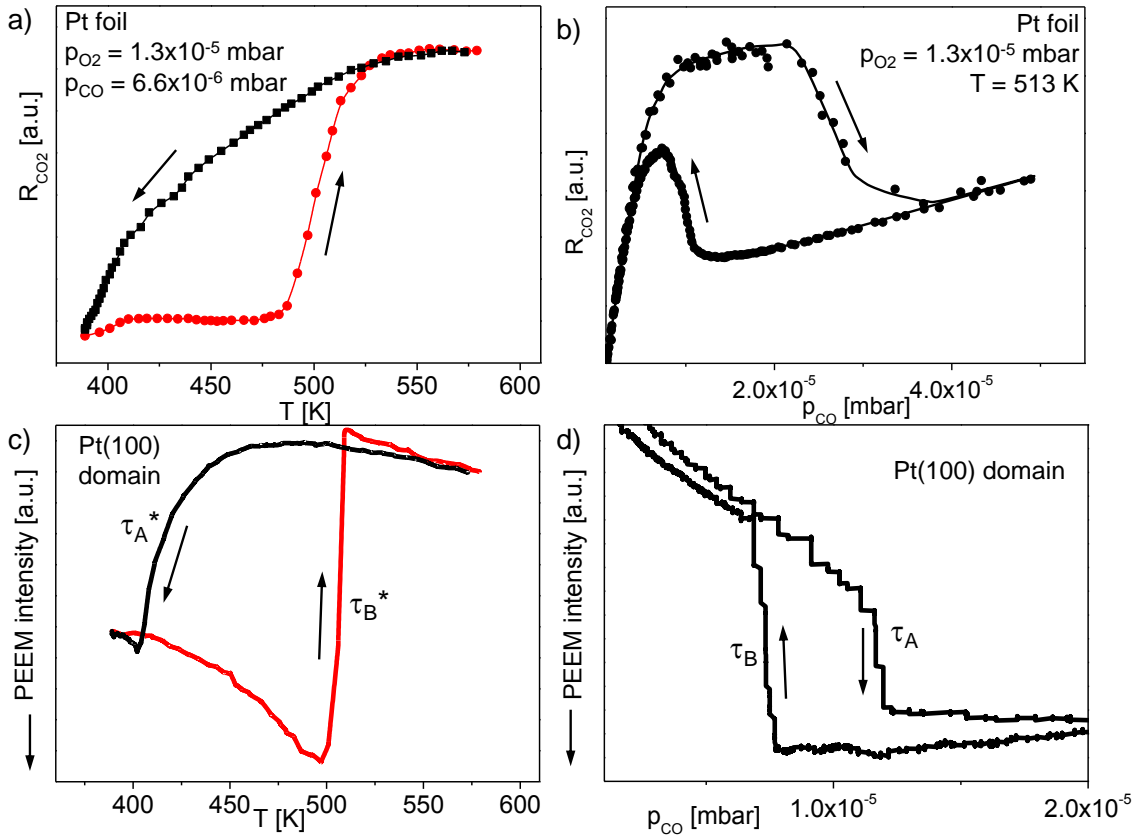


Figure 5.3: a) Global ignition (red) and extinction (black) R_{CO_2} curves obtained for Pt foil upon cyclic temperature variation at constant $p_{CO} = 6.6 \times 10^{-6}$ mbar and $p_{O_2} = 1.3 \times 10^{-5}$ mbar; b) global hysteresis in the CO₂ rate upon p_{CO} variation at $T = 513$ K, at the same oxygen pressure as in a); c) local PEEM intensity during ignition/extinction on a Pt(100) domain, simultaneously obtained with the R_{CO_2} curve in a); d) local PEEM intensity hysteresis on a Pt(100) domain during CO pressure variation as shown in b).

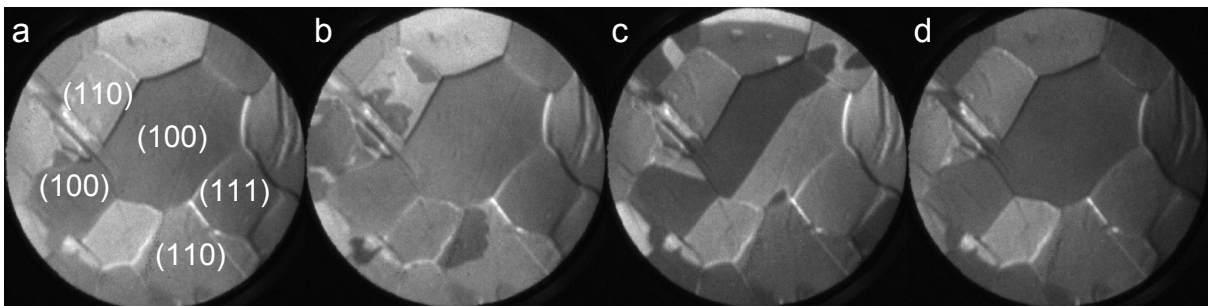


Figure 5.4: Sequence of PEEM images during the ignition τ_B^* on Pt foil at constant $p_{CO} = 6.6 \times 10^{-6}$ mbar and $p_{O_2} = 1.3 \times 10^{-5}$ mbar. The temperature is ramped with a heating rate of ~ 0.5 K/s from 483 K in frame (a) (CO-covered), to 492 K and 506 K in frame (b) and (c) (ignition on (110) and (100) domains) and to 568 K in frame (d) (oxygen covered). The orientation of the individual domains is indicated in frame a).

5 Local catalytic ignition during CO oxidation on low-index Pt and Pd surfaces

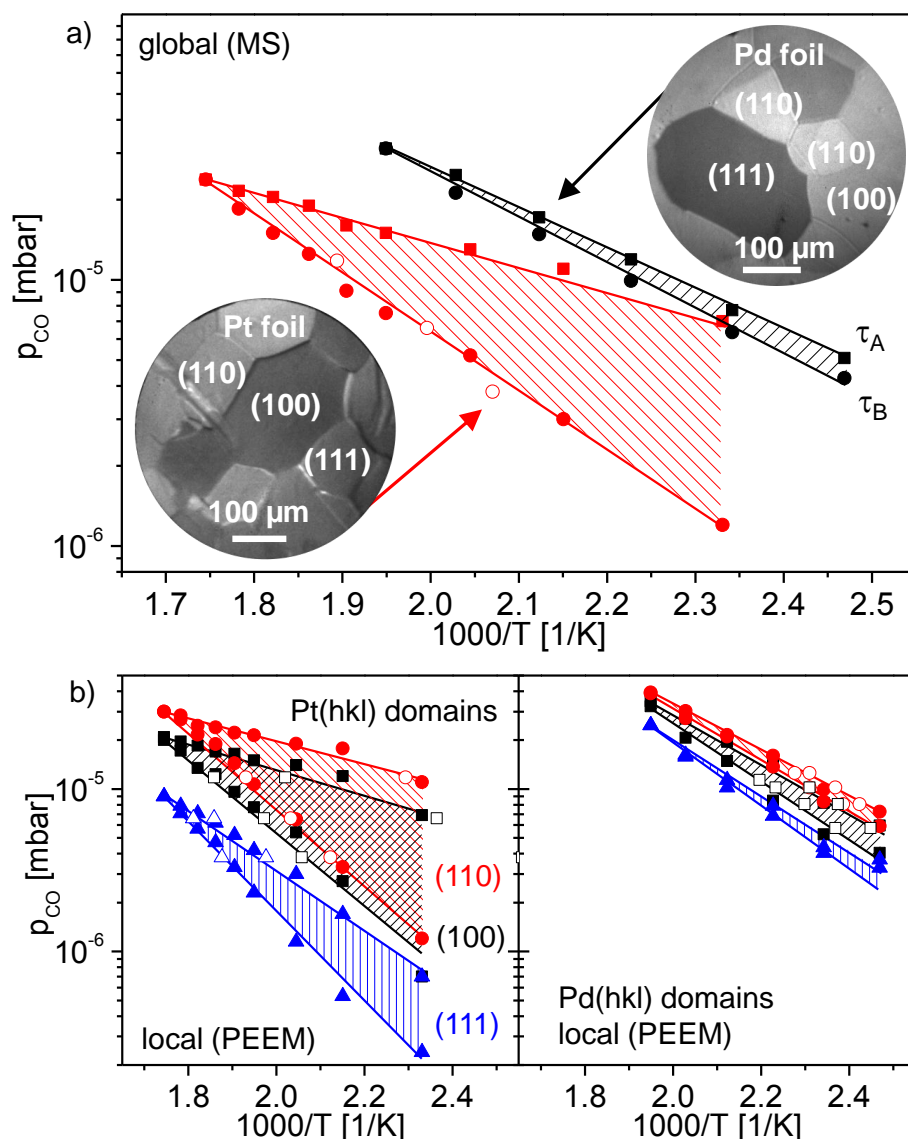


Figure 5.5: Palladium versus platinum in CO oxidation. a) Comparison of the global kinetic phase diagrams (by MS) at constant oxygen pressure ($p_{O_2} = 1.3 \times 10^{-5}$ mbar) of polycrystalline Pt (filled red squares and circles) and Pd (black squares and circles)¹. Open circles are ignition points for Pt. b) Corresponding local kinetic phase diagrams for individual Pt(hkl) domains (left) and Pd (right), obtained by local PEEM intensity analysis. Open symbols are the local ignition and extinction points.

occurs at higher CO partial pressure than for Pt, and that the reverse transition τ_B also occurs at a higher CO-to-oxygen ratio than for Pt. In other words, Pd is the better (more CO-tolerant) catalyst than Pt under the current conditions because *more* CO is needed to poison the Pd surface and a *lower* oxygen-to-CO ratio is sufficient to "reactivate" the Pd

¹An improved temperature measurement method was used in comparison to chapter 4, with the corresponding correction being applied to the Pt data.

5 Local catalytic ignition during CO oxidation on low-index Pt and Pd surfaces

Table 5.1: Adsorption energies of CO and O₂ and the barrier (E_r) to form CO₂ from adsorbed CO and O on the three low Miller index planes of Pt, as well as the sticking coefficients of CO and oxygen and the desorption temperature of CO, as known from literature. The energies are reported in eV. The sticking coefficients used in the simulations are given in parentheses. The preferred adsorption sites are indicated for CO and O; atop (t), bridge (b), hcp hollow (h) and fcc hollow (fcc).

	Pt(110)	Pt(100)	Pt(111)
$E_{\text{ads}}(\text{CO})$ [eV]	2.00 (t)	2.02 (b)	1.76 (fcc)
$E_{\text{ads}}(\text{O}_2)$ [eV]	2.40 (h)	2.14 (b)	2.28 (fcc)
E_r	0.96	0.55	0.95
$s_0(\text{O}_2)$	0.3-0.4 [117] (0.4)	$10^{-3}/0.1$ [38] (0.1)	0.06 [86] (0.1)
$s_0(\text{CO})$	0.8-1 [76] (0.9)	0.6-0.75 [51] (0.6)	0.6-0.8 [85] (0.9)
$T_{\text{des}}(\text{CO})$ [K]	500-520 [76]	~ 520 [44]	400-450 [87]

surface. In addition, the bistability regime of Pd disappears at a lower temperature than in the case of Pt, namely at $T_{\text{Pd}} = 513\text{K}$ in contrast to $T_{\text{Pt}} = 573\text{K}$, so CO poisoning on Pd occurs generally at a lower temperature than on Pt.

In order to explain these observations, density functional theory (DFT) calculations of the adsorption energies of CO and oxygen on clean Pd(hkl) and Pt(hkl) domains, as well as of the reaction barriers (cf. Tables 5.1 and 5.2) recently performed by Henrik Grönbeck at Chalmers University of Technology, Sweden, were used. These calculations were performed in a real space grid implementation [272, 273] of the projector augmented wave (PAW) method [274] with a grid spacing of 0.18\AA . The frozen core and projectors were generated with scalar relativistic corrections for Pd and Pt. Exchange and correlation contributions were described by the spin-polarized Perdew-Burke-Ernzerhof (PBE) functional [275]. Reciprocal space integration over the Brillouin zone was approximated with finite sampling [276, 277]. An effective temperature of 0.1eV was used to smear the Fermi discontinuity. Activation energies were evaluated with the nudged-elastic band method [278] or constrained optimization.

Three surfaces were considered for Pd and Pt, namely (111), (100) and the missing row reconstructed (110). Four atomic layers were used to model the slabs. The calculations were performed with an adsorption coverage of 0.25. The structural relaxations were performed within the quasi-Newton method. Structures are regarded optimized when the largest element of the gradient was smaller than $0.05\text{eV}/\text{\AA}$.

The energetic results from the DFT are collected in Tables 5.1 and 5.2. Only adsorption of atomic oxygen was considered. Thus, the $E_{\text{ads}}(\text{O}_2)$ value in Tables 5.1 and 5.2 corresponds to the adsorption energy of two oxygen atoms with respect to O₂ in the gas phase. The results are in good agreement with previous reports. It should be noted that the reaction

5 Local catalytic ignition during CO oxidation on low-index Pt and Pd surfaces

Table 5.2: Analogue to Table 5.1, but for Pd(hkl) surfaces.

	Pd(110)	Pd(100)	Pd(111)
$E_{\text{ads}}(\text{CO})$ [eV]	1.97 (h)	1.84 (b)	1.96 (fcc)
$E_{\text{ads}}(\text{O}_2)$ [eV]	2.48 (h)	2.40 (h)	2.50 (fcc)
E_r	-	0.80	1.53
$s_0(\text{O}_2)$	0.96 [135]	0.1-0.75 [130, 131]	0.7 [149] (0.7)
$s_0(\text{CO})$	1 [97]	0.6-0.8 [90]	0.96 [198] (0.7)
$T_{\text{des}}(\text{CO})$ [K]	400/475 [106]	~ 480 [90]	450 [109]

barrier is sensitive to the assumed reaction path. For the (111) surfaces, the barrier is obtained from CO close to an atop position and O in a bridge configuration. CO_2 is in this case formed over an fcc hollow site. Over the (100) surfaces, CO_2 is formed from both CO and O in opposite bridge positions. On (110), the barrier is evaluated with CO in a bridge position on the row and O in a hollow position. The sticking coefficients of CO and oxygen and the desorption temperatures of CO on Pd(hkl) and Pt(hkl), known from literature, are also included in Tables 5.1 and 5.2.

The bistability regions for Pt(111), Pt(100), Pt(110) and Pd(111) have been simulated by a micro-kinetic model based on the conventional Langmuir- Hinshelwood mechanism for CO oxidation:



Here, $*$ denotes a free surface site and X^* an adsorbate X bonded to a surface site. The corresponding rate equations are:

$$\frac{d\theta_{\text{CO}}}{dt} = s_{\text{CO}}^0(1 - \theta_{\text{CO}}^2)p_{\text{CO}}k_{\text{CO}}^a - k_{\text{CO}}^d\theta_{\text{CO}} - k^r\theta_{\text{CO}}\theta_{\text{O}} \tag{5.2a}$$

$$\frac{d\theta_{\text{O}}}{dt} = 2s_{\text{O}}^0(1 - \theta_{\text{CO}} - \theta_{\text{O}})^2p_{\text{O}_2}k_{\text{O}_2}^a - k_{\text{O}_2}^d\theta_{\text{O}}^2 - k^r\theta_{\text{CO}}\theta_{\text{O}}. \tag{5.2b}$$

Here, θ_{CO} and θ_{O} are the coverages, p_{CO} and p_{O_2} are the pressures, and s_{CO}^0 and $s_{\text{O}_2}^0$ the initial sticking coefficients. The rate constants are given by:

5 Local catalytic ignition during CO oxidation on low-index Pt and Pd surfaces

$$k_{\text{CO}}^d = v_{\text{CO}}^d e^{-E_{\text{CO}}^d(1-\alpha\theta_{\text{CO}})/k_B T} \quad (5.3a)$$

$$k_{\text{O}_2}^d = v_{\text{O}_2}^d e^{-E_{\text{O}_2}^d(1-\alpha\theta_{\text{O}})/k_B T} \quad (5.3b)$$

$$k^r = v^r e^{-E^r(1-\beta\theta_{\text{CO}})/k_B T} \quad (5.3c)$$

$$k_X^a = 1/N_0 \sqrt{2\pi M k_B T}. \quad (5.3d)$$

T is the temperature, k_B is the Boltzmann constant, M the mass of the molecule under consideration, and N_0 is the number of sites per area. A linear coverage dependence is introduced for the adsorption energies and the barrier. α and β are in all cases set close to 0.5. The coverage dependence (strength and functional form) could, in principle, be evaluated from first principles. However, here the strategy in Ref. [279] was followed. The desorption of O_2 is included above for completeness. The kinetics is insensitive to this step and it was not included in the simulations. The pre-exponential factors are set to $v_{\text{CO}}^d = 10^{15}$ and $v^r = 10^{14}$, respectively [279].

In Fig. 5.6a the calculated bistability regions are compared for Pd(111) and Pt(111), and in Fig. 5.6b the three low Miller-indexed surfaces of Pt are compared to each other. The right inset in Fig. 5.6a depicts a simulated ignition/extinction curve for the Pd(111) surface, and the left inset shows a simulated hysteresis curve for the Pt(111) surface resulting from p_{CO} variation. In all cases, the kinetic simulations are in good agreement with the experiment: the bistability region of Pd is considerably narrower than in case of Pt, and the kinetic phase diagram of Pd is located at higher CO pressure. The DFT-derived order of the local kinetic phase diagrams of the three Pt surfaces also corresponds to the experimental results: The Pt(100) surface is active at higher CO pressures than Pt(111), and Pt(110) is active at the highest CO pressures.

The DFT calculations and the kinetic modeling provide an unambiguous way to rationalize the experimental findings. The experiments showed that at a given oxygen pressure and temperature the Pt(hkl) domains are deactivated at lower CO pressure than Pd(hkl). This can mainly be attributed to the higher adsorption energies of oxygen on Pd(hkl) than on Pt(hkl) (cf. Tables 5.1 and 5.2), i.e. oxygen is more strongly bound to Pd and thus, the CO-poisoning of the surface occurs at higher CO pressures. Regarding the transition τ_B from the low to the high reactivity state, the Pd foil "reactivates" already at a considerably higher CO pressure than Pt foil. This results from the higher sticking coefficients of oxygen for the Pd(hkl) domains as compared to the Pt(hkl) domains: whereas CO adsorption prop-

5 Local catalytic ignition during CO oxidation on low-index Pt and Pd surfaces

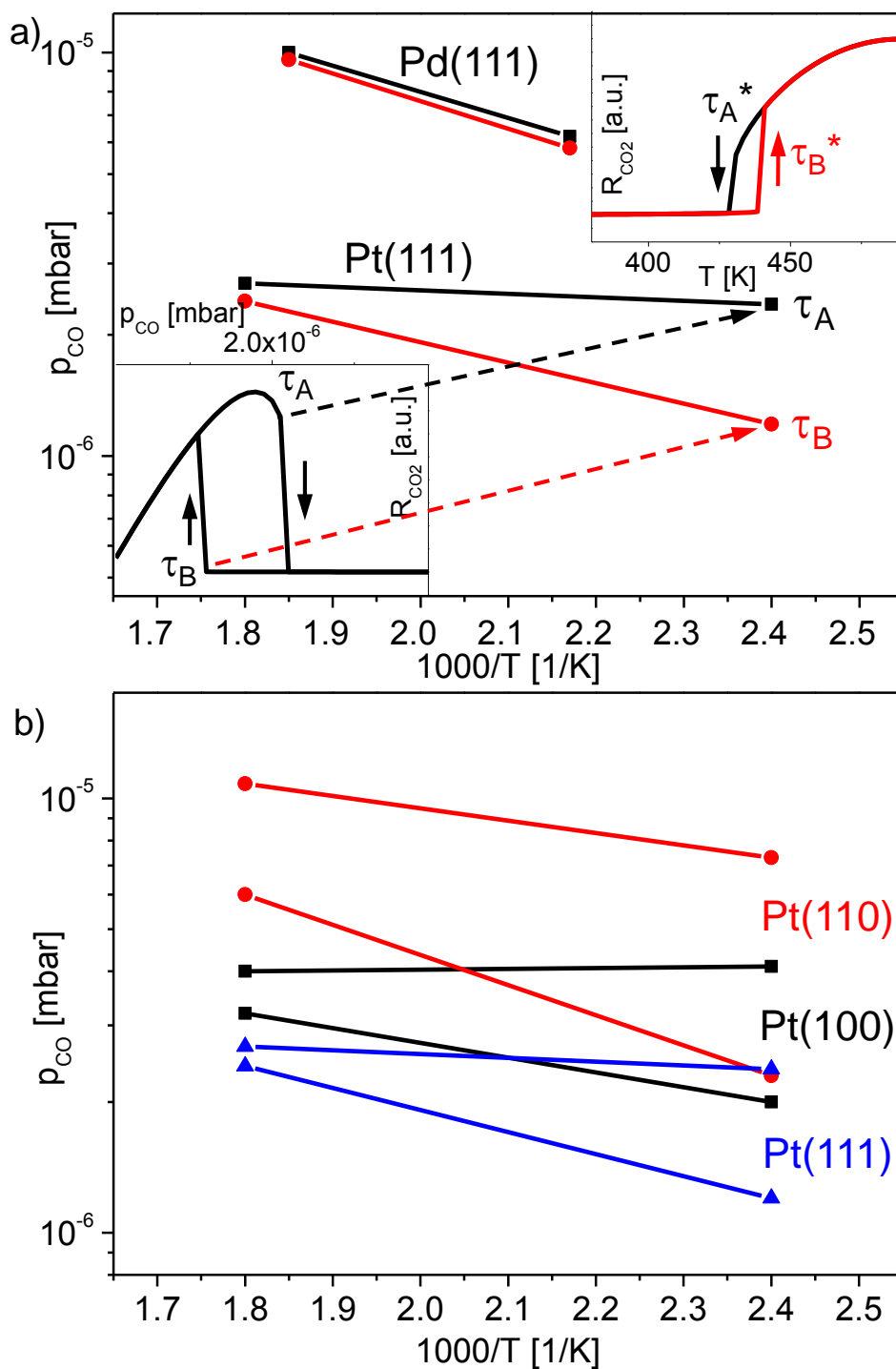


Figure 5.6: a) Simulated kinetic phase diagrams for Pd(111) and Pt(111) at $p_{O_2} = 1.3 \times 10^{-5}$ mbar, as well as a simulated p_{CO_2} hysteresis curve for Pt(111) at 417K (left inset) and a simulated ignition/extinction curve for Pd(111) at $p_{CO} = 5.8 \times 10^{-6}$ mbar (right inset). b) Simulated local kinetic phase diagrams of Pt(110), Pt(100) and Pt(111) at $p_{O_2} = 1.3 \times 10^{-5}$ mbar.

erties are quite similar on Pt and Pd(hkl) surfaces, oxygen adsorption is clearly favored on Pd(hkl). The disappearance of the bistability regime at the so-called "cusp-point" occurs at lower temperature for Pd than for Pt foil. This can be explained by the generally lower desorption temperature of CO on Pd(hkl).

5.4 Summary

In summary, local domain-specific kinetic measurements for individual Pd and Pt crystalline grains have been performed under truly identical reaction conditions, allowing a direct comparison of the inherent catalytic properties of Pt(hkl)- and Pd(hkl)-domains with respect to CO oxidation. In addition to the global and local kinetic phase diagrams for Pt foil and the Pt(hkl) domains, respectively, presented in chapter 4, the global and local kinetics for Pd foil and corresponding Pd(hkl) domains were obtained. The global and local reaction kinetics of Pt and Pd foil are compared to each other and it is demonstrated that the Pd(hkl) domains exhibit a higher tolerance towards CO poisoning and a higher ability to reactivation than the corresponding Pt(hkl) domains, reflected by the fact, that the (local) kinetic phase diagrams for the Pd(hkl) domains are located at higher CO pressures than for the Pt(hkl) domains.

For both, Pt and Pd foil, ignition and extinction experiments were performed, i.e. contrary to the isothermally obtained kinetic phase diagrams, the kinetic transitions were monitored by isobaric temperature variation. It is shown that for the CO oxidation reaction the typical surface science approach for determining reaction kinetics, namely the isothermal monitoring of kinetic transitions, *quantitatively* yields the same results as the common technical catalysis approach, i.e. the isobaric study of the different reactivity regimes, at least in the pressure range of $\sim 10^{-5}$ mbar.

The observed differences in the catalytic activity of Pt(hkl)- and Pd(hkl)-domains, as well as the differences between particular crystallographic orientations, were rationalized by DFT calculated adsorption energies for CO and oxygen and reaction barriers on the Pt and Pd surfaces. By micro-kinetic reaction modeling kinetic phase diagrams for the Pt and Pd(hkl) surfaces were simulated which were in good agreement with the experimental findings.

ROLE OF DEFECTS IN THE LOCAL REACTION KINETICS IN CO OXIDATION ON Pd FOIL

In this chapter, the question is addressed which role defects play for the local reaction kinetics of the CO oxidation reaction on Pd foil. Artificial defects on the Pd foil were introduced by additional Ar⁺ ion sputtering after the usual sample preparation procedure, and simultaneous global and local kinetic measurements analogous to that presented in the previous chapters 4 and 5 were performed. The constructed global and local kinetic phase diagrams for the sputtered Pd foil and the individual (hkl)-oriented domains, respectively, are compared to those of the smooth sample. The impact of the Ar⁺ ion sputtering was estimated by Scanning Tunneling Microscopy measurements on a Pd(111) single crystal exposed to an equivalent Ar⁺ ion dose as the Pd foil in the kinetic measurements. The effect on the local kinetic behavior of the individual (hkl) domains of the Pd foil upon defect creation and on the reaction front propagation observed by PEEM is discussed in terms of the results obtained in the STM measurements.

6.1 Introduction

The structure dependence of reaction rates in heterogeneously catalyzed reactions and the related fundamental question of the nature of catalytically active sites are maybe the most discussed topics since the early days of catalysis [280, 281]. Atomic steps and surface defects are often considered to be particularly suitable to serve as active sites for heterogeneous catalytic reactions [282–284], since these particular sites do not only facilitate the bond breaking [285] but also strengthen the reactant-surface binding [286].

Generally, different reactions exhibit different structure sensitivities and particular active sites. With respect to the CO oxidation reaction on platinum-group metal surfaces, structure sensitivity has been studied mainly by comparing the reaction kinetics on differently oriented single crystal surfaces, measured in independent experiments. Despite of the obvious drawbacks of such measurements caused by the difficulties to keep the conditions and control parameters exactly the same in different experiments, important findings could be distilled, eg. for Pd [179, 287–290]. Since atomic steps seem to play a peculiar role, corresponding efforts have to be made to gain insight into the atomistic details in the processes occurring on stepped surfaces. The detailed knowledge of the role of atomic steps and defects may help not only to understand the reaction peculiarities on real catalysts with all the complexity related to particle size and shape [291–293], but might also help to achieve one of the ultimate goals in heterogeneous catalysis, namely the bottom-up catalyst design beginning from the atomic scale [294].

Basically, two types of studies, where the role of atomic steps and defects is in foreground, are known: either the reaction is studied on vicinal surfaces with steps in the "native" state, such as Pt(335) [295] and Pt(332) [296] or the surface steps and defect sites are created intentionally, e.g. by laser radiation [297]. On a Rh(111) surface, interesting results were obtained by artificial introduction of defects by Ar⁺ ion sputtering of the surface oxide: the sputter induced roughness increased significantly the number of nuclei for the reduction of the surface oxide by H₂ [298]. This suggests the use of Ar⁺ ion sputtering as a method of artificial roughness creation for other surface processes such as e.g. catalytic reactions, since the energy of Ar⁺ ions, the Ar⁺ ion dose and the temperature during sputtering allow a flexible variation of the surface topography.

The PEEM-based method provides new possibilities to study reaction kinetics on stepped or otherwise "defected" surfaces. Due to the parallel imaging principle of PEEM, local kinetic information is obtained simultaneously and under exactly the same conditions for the whole field of view (ca. 500 μm), e.g. for the differently oriented micrograins of the poly-

crystalline foil sample(s) studied in this thesis. Since upon Ar^+ ion sputtering all domains of the polycrystalline sample surface underlie an identical impact, such a parallel analyzing method may provide also the possibility to compare the activities of differently oriented, but similarly "damaged" surfaces and eliminates in this way the main shortcoming of the comparing kinetic measurements for various single crystal surfaces.

In this chapter this possibility is exploited by applying the digital analysis method of *in situ* recorded PEEM video-sequences, to obtain local kinetic information for the CO oxidation reaction on the smooth (sputtered and annealed) and atomically rough (additionally sputtered) individual Pd(hkl) domains of a polycrystalline Pd foil. The degree of the surface modification caused by Ar^+ ion impact was estimated by STM and the global (average) kinetics of the CO oxidation reaction was monitored by MS.

6.2 Experimental details

The PEEM experiments presented in this chapter were performed in the UHV chamber described in detail in chapter 2. The investigated sample was the polycrystalline Pd foil described in section 2.3.1. Before each kinetic experiment, the standard UHV cleaning procedure, namely Ar^+ ion sputtering, annealing at 1073 K and subsequent heating at 523 K in 5×10^{-7} mbar oxygen atmosphere, was performed. In case of the kinetic measurements on the artificially defected Pd foil, the sample was Ar^+ ion sputtered for 15 min at $p_{\text{Ar}} = 8 \times 10^{-6}$ mbar and $E_{\text{kin}} = 1$ keV before each experiment in addition to the cleaning cycle.

The idea of the experimental approach was already presented in the previous chapters and is briefly recapitulated in Fig. 6.1: The global CO_2 formation rate produced by all grains of the Pd foil (Fig. 6.1a) in the CO oxidation reaction is monitored mass-spectroscopically yielding the global reaction kinetics of this reaction on the whole sample (Fig. 6.1b). In parallel, PEEM is applied to visualize the CO oxidation reaction *in situ* on the individual grains of the Pd foil based on work function differences across the sample. The local reaction kinetics is monitored by intensity analysis of specific domains in the recorded PEEM-video sequences (an [110]-oriented domain is indicated in Fig. 1a and the corresponding local reaction kinetics is shown in Fig. 6.1c).

The identification of different grains of a Pd foil by local PEEM image contrast is a challenging task because of the rather small work-function differences of individual orientations. Therefore, Electron Backscatter Diffraction (EBSD) has been applied to prove the crystallographic orientation of the individual grains which was first determined by work function analysis by PEEM. EBSD measurements have been carried out independently in a

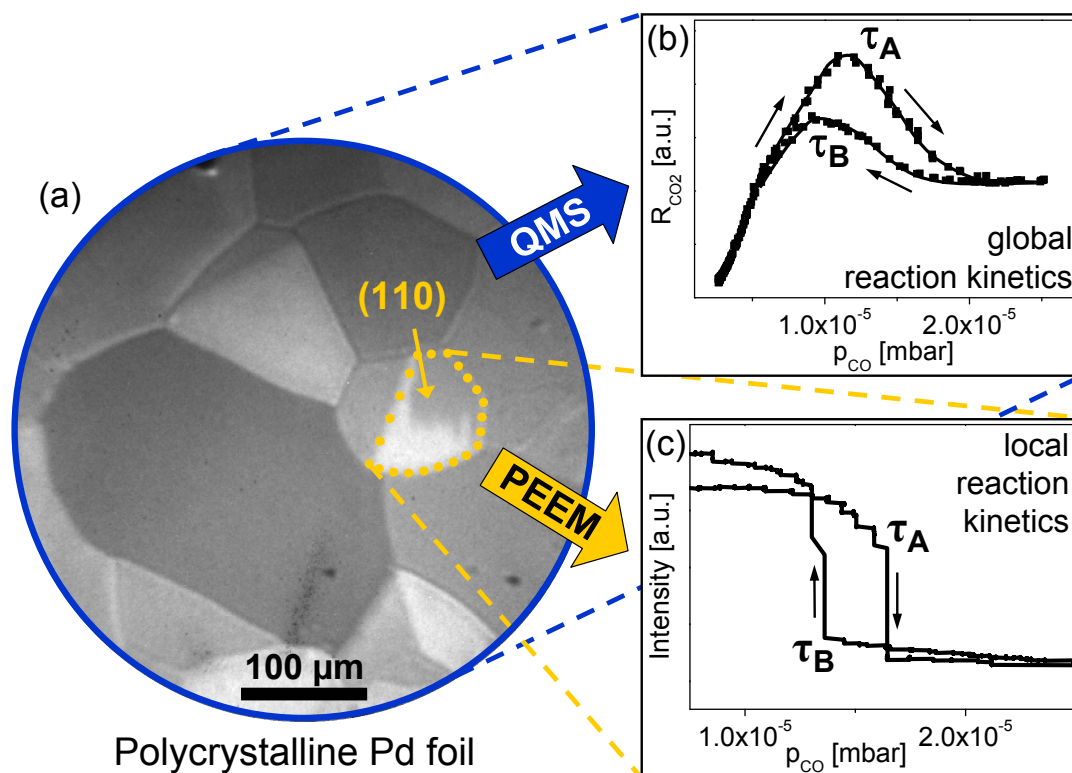


Figure 6.1: Scheme of the experiment. (a) PEEM image of the polycrystalline Pd sample during the CO oxidation reaction ($T = 449\text{K}$, $p_{\text{CO}} = 1.4 \times 10^{-5}\text{mbar}$, $p_{\text{O}_2} = 1.3 \times 10^{-5}\text{mbar}$). (b) Global hysteresis in the overall CO_2 reaction rate measured during a cycle of CO pressure variation at constant $T = 449\text{K}$ and $p_{\text{O}_2} = 1.3 \times 10^{-5}\text{mbar}$ by MS for the whole sample. (c) Local hysteresis as obtained from a corresponding PEEM video sequence for the Pd(110) domain indicated in (a); acquired simultaneously with the MS-measurement in (b).

scanning electron microscope (FEI, Quanta 200F) equipped with an EBSD detector allowing to record the Kikuchi bands, which provide the EBSD pattern of a given sample spot. Figure 6.2 presents the resulting orientation map and a comparison with the PEEM image of a clean sample surface. As can be seen from Fig. 6.2, the EBSD results are in perfect agreement with the independent work function analysis by PEEM. The advantage of EBSD is that one can identify also higher Miller index orientations as e.g. (210) which are often present on the surface, but can hardly be identified on the basis of sole work function measurements.

The STM experiments on the Pd(111) single crystal have been carried out in a separate UHV system with a base pressure below 10^{-10}mbar in both the preparation and analysis chambers, using the same methods as in Ref. [171].

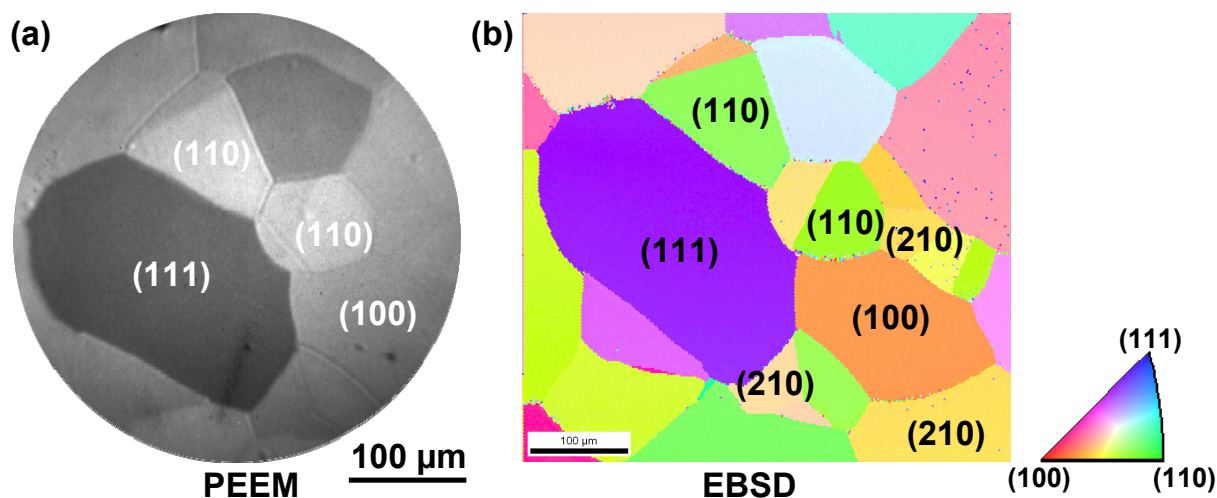


Figure 6.2: Surface domain orientation for a chosen field of view of the polycrystalline Pd foil. (a) as identified by work function differences in PEEM (b) the same, but by EBSD. Note the inverse pole pole figure assigning the corresponding directions.

6.3 Results

6.3.1 Global kinetics of annealed and sputtered Pd foil

Using the combined PEEM-MS approach, a systematic set of kinetic measurements for the CO oxidation reaction on the polycrystalline Pd foil was performed, whereby both the CO₂ reaction rate and the video-PEEM data were recorded simultaneously during cyclic variation of the CO partial pressure in the range of $\sim 10^{-8}$ mbar to $\sim 10^{-4}$ mbar at constant oxygen pressure ($p_{\text{O}_2} = 1.3 \times 10^{-5}$ mbar) and different constant temperatures in the range of 405 K to 513 K. Both, the global CO₂ reaction rate produced by the whole sample and the local PEEM intensities of the individual grains, exhibit a pronounced hysteresis (see Fig. 6.1b and c) characterizing the bistability in the CO oxidation reaction (see section 3.3). The transition points τ_A and τ_B between the steady states of high and low reactivity depend not only on external parameters as the temperature, but also naturally on such intrinsic properties of the studied system as e.g. the crystallographic orientation or the surface structure. Thus, the kinetic phase diagrams introduced in section 3.3 which are constructed from the p_{CO} values of τ_A and τ_B in dependence of the (reciprocal) temperature and characterize the particular system, are well suited to compare different reaction systems and to reveal the influence of different factors such as promoters [213].

The main goal of the present study was to compare the catalytic properties of the nearly ideal, i.e. sputtered and annealed Pd(hkl) surfaces on Pd foil with the same surfaces but

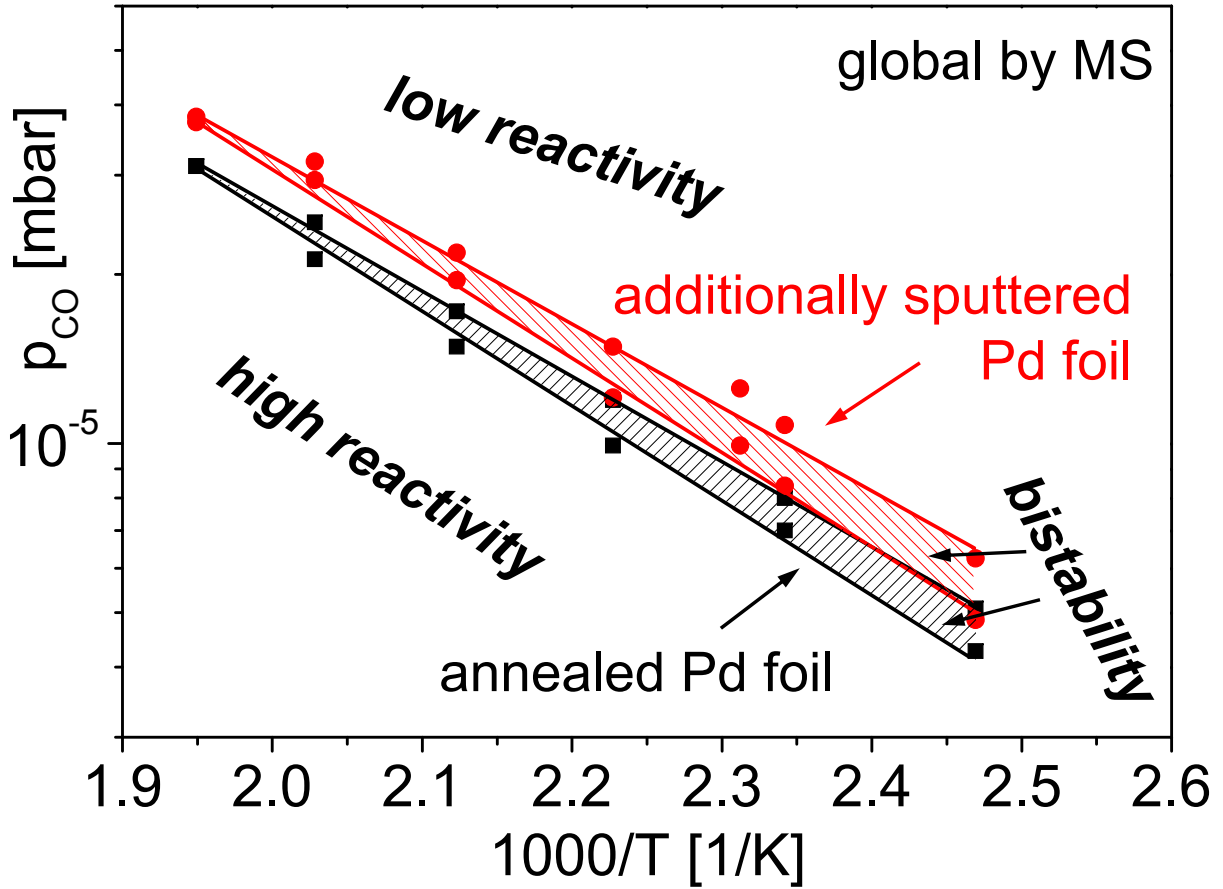


Figure 6.3: Global kinetic phase diagrams for the smooth (sputtered and annealed) Pd foil (black squares) and for the same but additionally sputtered Pd foil (red squares) as obtained by MS at constant $p_{O_2} = 1.3 \times 10^{-5}$ mbar and different constant temperatures in the range between 405 K and 513 K.

artificially modified by additional Ar^+ sputtering ($E_{kin} = 1$ keV). The global kinetic phase diagrams for the smooth and for the additionally sputtered Pd foil, which were determined from the kinetic transition points in the R_{CO_2} hysteresis curves (see Fig. 6.1b), are presented in Fig. 6.3. In these diagrams a remarkable effect is apparent: the diagram for the sputtered foil (red symbols in Fig. 6.3) is shifted significantly towards higher CO pressures in comparison to that of the smooth surface. This means that CO oxidation on the sputtered Pd foil can be inhibited by CO poisoning only at a considerably higher CO partial pressure and the sputtered surface is also reactivated at a higher CO pressure than the annealed Pd foil, i.e. the defect-rich sputtered sample is much more tolerant towards CO poisoning than the smooth Pd surface.

6.3.2 Scanning tunneling microscopy measurements

To understand the above observations, Scanning Tunneling Microscopy (STM) has been applied to a smooth and to an additionally sputtered Pd(111) single crystal surface subjected to Ar^+ sputtering under the same conditions as the Pd foil (energy 1 keV, ion dose $2 \times 10^{16} \text{ cm}^2$, sample at room temperature) at the Institute of Applied Physics, Vienna University of Technology. The corresponding STM images are shown in Figs. 6.4a and b. The freshly prepared (sputtered and annealed) Pd(111) surface exhibits well defined smooth terraces with a typical terrace width of 20–30 nm (Fig. 6.4a). The situation changes dramatically upon sputtering (Fig. 6.4b): ion bombardment of the surface leads to the formation of three-dimensional islands, with a very high density of steps and edges. The uppermost terraces of the mounds have diameters of 2–3 nm, and the slope angles are between 10 and 20°, corresponding to terrace widths of 0.6 to 1.2 nm. This means that about one quarter of all surface Pd atoms are step or kink atoms. With the lattice constant of the Pd(111) surface of 2.74 Å the surface corresponds to a mixture of high-index surfaces with 2-6 atom wide (111) terraces and [100]- and [110]-directed steps, but with an additional very high amount of kink atoms.

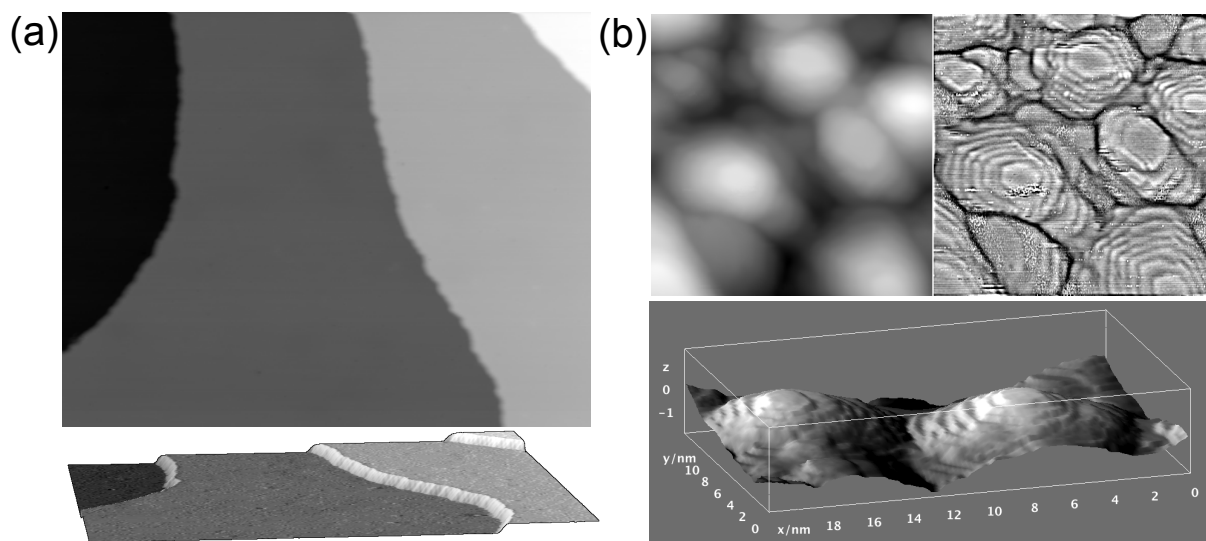


Figure 6.4: a) STM micrograph of annealed Pd(111) surface (100 nm wide). b) same surface after Ar^+ ion sputtering ($20 \times 20 \text{ nm}^2$; the high-pass filtered image shown at the right shows the steps). The bottom of each panel shows a 3D view; enhancement of high frequencies and edge-preserving blur has been used to improve the visibility of steps in the 3D image (b).

It is known that the binding energy of oxygen is considerably higher at low-coordination defect sites than on flat terraces of Pd [299, 300], that is, atomic oxygen binds more strongly to a defect-rich Pd surface. Although the CO binding energy is also altered on such defect

sites on Pd [301], the impact on the CO adsorption kinetics appears to be lower when compared to oxygen [302]. Since the energetics governs the kinetics of the competitive CO and oxygen coadsorption, this might explain why the sputtered Pd surface is poisoned by CO at a significantly higher CO pressure than the smooth surface. The higher CO pressure values for reactivation of the sputtered Pd surface compared to the annealed surface, i.e. the reverse transition τ_B , can be explained directly by the adsorption kinetics rather than the energetics: Due to the high step and defect density, more adsorption sites for oxygen adsorption on a mainly CO-covered surface are available, the sticking probability for oxygen adsorption is considerably higher and therefore, the reactivation occurs at a higher CO-to-oxygen pressure ratio than on the smooth surface.

6.3.3 Local kinetics of annealed and sputtered Pd foil

Although an illustration of the catalytic properties as shown in Fig. 6.3 is useful, it does not provide any local information about the properties of the individual grains due to the averaging character of the measurement method (MS). The PEEM images and the EBSD scan revealed that the sample consists of many grains with differing crystallographic orientation and it might be expected that the impact of sputtering on the catalytic behavior of the individual (hkl) domains is differing due to their different atomic configurations. As already mentioned above, the analysis of the local PEEM-intensities for the selected individual crystalline grains allows to obtain the local hysteresis curves (Fig. 6.1c) which result in turn in the local kinetic phase diagrams as shown in Fig. 6.5 for the three chosen [110]-, [100]- and [111]-oriented domains of the smooth Pd surface. As expected for different orientations, the CO-tolerance and the ability for reactivation are clearly related to the atomic structure: whereas the local kinetic phase diagram of the most open structure among the three studied orientations, i.e. the (110) domain, is located at the highest CO-to-oxygen pressure ratio, the corresponding diagram of the closest-packed (111) domain is situated at the lowest value of the pressure ratio.

The PEEM frames 1-3 in Fig. 6.5 illustrate the transition τ_B from the inactive CO-covered (low work function, dark contrast) state to the highly reactive oxygen covered state (higher work function, bright contrast) at 405K caused by reduction of the CO pressure. In addition, 4 grains of (111), (100), (210) and (110) orientation are denoted in frame 1. In the frames 1-3, corresponding to CO pressures of 5.4×10^{-5} mbar, 4.3×10^{-6} mbar, and 4.0×10^{-6} mbar, bright oxygen fronts propagate across the individual domains, in each case strongly confined within the grain boundaries, i.e. no front propagation across the bound-

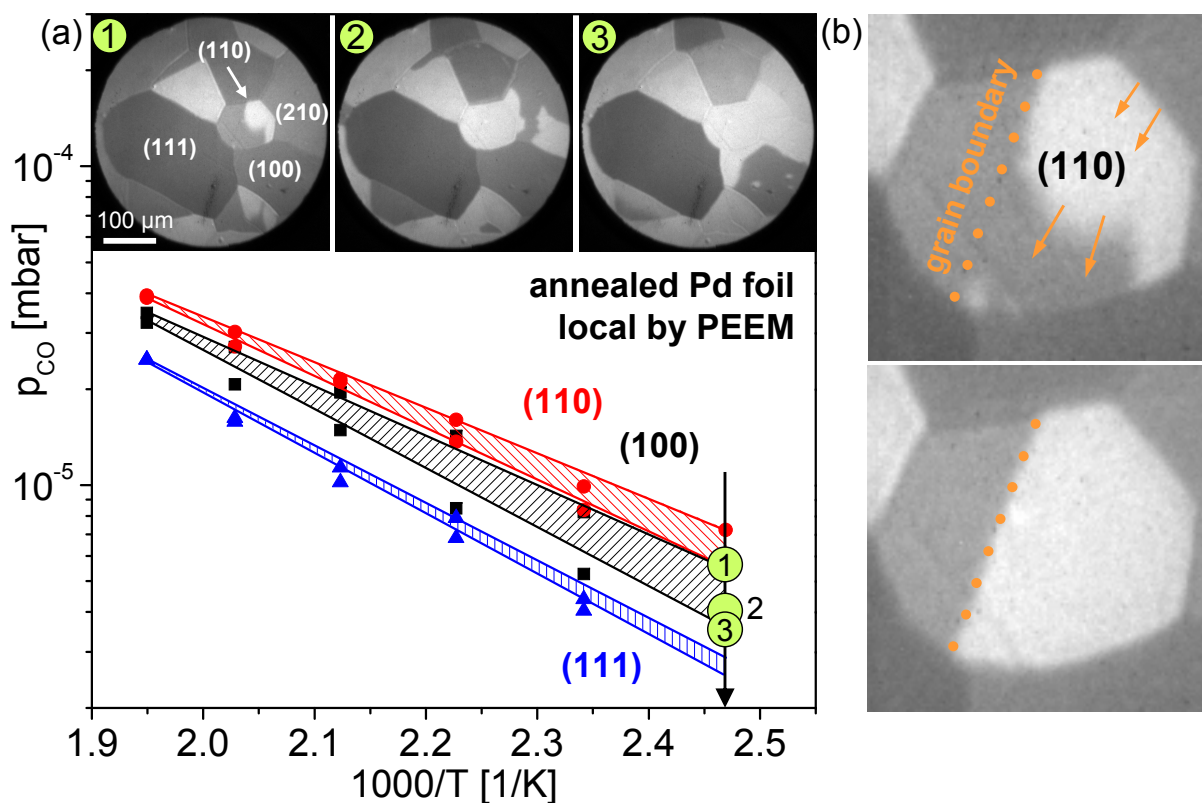


Figure 6.5: CO oxidation on the individual Pd(hkl) domains of a smooth Pd foil. (a) Local kinetic phase diagrams of individual [110]- (red), [100]- (black) and [111]-oriented (blue) domains of Pd foil during CO oxidation at constant $p_{\text{O}_2} = 1.3 \times 10^{-5}$ mbar obtained by PEEM intensity analysis. Frames 1-3 illustrate the transition τ_B from the inactive steady state (CO covered, dark contrast) to the active steady state (oxygen covered, bright contrast) at 405 K, p_{CO} scan from 5.4×10^{-5} mbar to 4.0×10^{-5} mbar. (b) Independence of the domains in the CO oxidation reaction: the reaction fronts are stopped at the grain boundaries, no diffusion coupling between differently oriented grains was observed under present conditions.

aries occurs. Note, that the transition τ_B observed for the (210) domain (frame 2), consisting of (100) terraces and (110) steps, occurs exactly between the transitions on the (110) and the (100) domains (frame 1 and 3, respectively), confirming again the structure-reactivity relation. In Fig. 6.5b, where magnified PEEM images of the (110) domain are displayed, it is visible how the bright oxygen front nucleates at the grain boundary, i.e. in a region of a very high step and defect density, propagates across the domain and is effectively stopped at the surrounding grain boundaries due to the non-suitable conditions for the transition τ_B on the surrounding grains.

The individual domains on a smooth Pd foil behave quasi independently within the complex neighborhood of other differently oriented grains, at least under the current reaction conditions. As already mentioned in chapter 4, such independent single-crystal like reac-

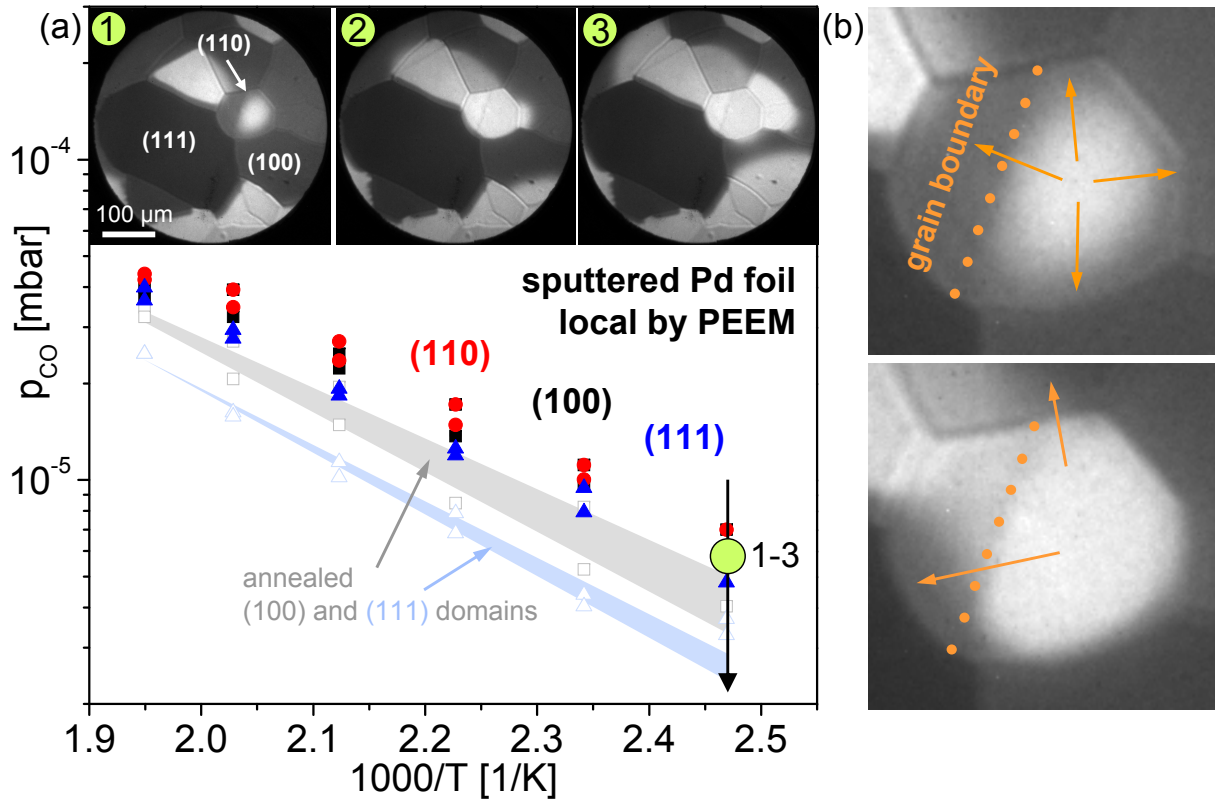


Figure 6.6: CO oxidation on the individual Pd(hkl) domains of a sputtered Pd foil. (a) Local kinetic phase diagrams of the individual [110]- (red), [100]- (black) and [111]-oriented (blue) grains on the additionally sputtered Pd foil, and for comparison of the (100) and (111) domain on annealed Pd foil, at constant $p_{O_2} = 1.3 \times 10^{-5}$ mbar and different constant temperatures. The local kinetic phase diagrams are shifted towards higher CO pressures compared to the local kinetic phase diagrams on the annealed sample (see Fig. 6.5a). In addition, the kinetic phase diagrams of the (sputtered) individual grains are shifted together. Frames 1-3: transition τ_B at 405K on the additionally sputtered Pd foil, $p_{CO} = 5.9 \times 10^{-5}$ mbar. (b) The reaction fronts propagate across the grain boundaries. The independence of the domains is lifted.

tion behavior of the individual grains can be understood by considering possible mechanisms of reactive synchronization (coupling) between the different surface regions: at small (nm-sized) length scales diffusion coupling was made responsible for the synchronization of local transitions [208]. At pressures higher than 10^{-4} mbar, gas-phase coupling provides the synchronization over macroscopic samples [256, 303], and near atmospheric pressure, heat transfer contributes significantly or even dominates spatial coupling [258, 259]. Evidently, under the present pressure conditions, the μm -size of the individual grains is not sufficient to synchronize the kinetic transitions on differently oriented grains via fast CO and oxygen consumption from the gas phase. From the other side, the grain boundaries seem to hinder effectively the diffusion coupling (frames 1-3 in Fig. 6.5).

6 Role of defects in the local reaction kinetics in CO oxidation on Pd foil

Figure 6.6, where the local kinetic phase diagrams of the same [110]-, [100]- and [111]-oriented domains as in Fig. 6.5, but measured after additional Ar⁺ ion bombardment (15 min, 1 keV), are shown, illustrates the change of the local reaction properties of the individual domains upon Ar⁺ sputtering. For comparison, the local kinetic phase diagrams of the annealed (100) and the (111) domains are also shown. Evidently, the local kinetic transitions on all domains are now located at generally higher CO pressures, as expected from the global results (Fig. 6.3). Unexpectedly, the individual kinetic phase diagrams, which were clearly separated from each other in case of the smooth foil, are shifted together and can hardly be distinguished from each other for the sputtered foil. This means, the local kinetic transitions on the individual domains of the sputtered Pd foil occur almost "at once" and not "delayed" in respect to each other, as it is the case for the smooth surface.

The PEEM frames 1-3 in Fig. 6.6a, recorded within a few seconds at the CO partial pressure of 5.9×10^{-6} mbar and showing the transition τ_B at the same temperature of 405 K as in Fig. 6.5, but on the additionally sputtered sample, confirm this suggestion: The bright oxygen fronts do not stop at the grain boundaries and propagate almost instantaneously across the whole foil. It is clear, that on the sputtered Pd foil the differences in the local reaction kinetics are reduced by sputtering due to the similarly defected structure of the different domains, thus the reaction fronts propagate across the grain boundaries, because the conditions necessary for the kinetic transition are similar on the now similarly structured neighboring grains. Also, the grain boundaries do not serve as nucleation centers for the reaction fronts anymore, what can be seen clearly by a comparison of the magnified PEEM images of the (110) domain in Figs. 6.5b and 6.6b. On the additionally sputtered foil, the reaction fronts nucleate primarily in the inner part of the domains rather than on the grain boundaries, i.e. the defects on the roughened surface of the sputtered foil are sufficient to nucleate the reaction fronts (Fig. 6.6b).

Generally, the Ar⁺ sputtering in the applied intensity creates apparently a similarly "damaged" surface structure on the individual low-index Pd domains, lifting in this way their quasi-independent behavior in the CO oxidation and shifting significantly the individual local kinetic phase diagrams. This promises possible future applications with a fine dozed impact of Ar⁺ ions, controlled structure disorder and targeted phase diagram shifts as a step towards tailored catalytic properties. A use of the present approach for bimetallic or oxide covered surfaces is also thinkable.

6.4 Summary

The role of artificially created defects and steps in the local reaction kinetics in CO oxidation on low-index Pd surfaces was studied by PEEM, MS and STM. The reaction kinetics on smooth (Ar^+ sputtered and annealed) and defect-rich (additionally Ar^+ sputtered) Pd(hkl) surfaces was directly compared, using the PEEM-based approach which allows the simultaneous determination of the local kinetic phase transitions on μm -sized grains of a polycrystalline sample.

In case of the smooth Pd foil, the individual Pd(hkl) domains behave independently (single crystal like) with respect to CO oxidation at present conditions, that is, in the 10^{-5} mbar pressure range. In turn, upon sputtering, the domain independence is lifted and the reaction behavior is rather correlated. To estimate the effect of the Ar^+ ion bombardment on the Pd foil, STM measurements were performed on a Pd(111) single crystal which was pre-treated with Ar^+ ions in the same way as the Pd foil. After sputtering of the Pd(111) single crystal, a very high degree of step and kink sites was found altering the adsorption kinetics of the reactants considerably compared to a smooth surface. As a consequence of this high defect density, the kinetic phase diagrams of the different grains on Pd foil approach each other and the reaction fronts propagate unhindered across the grain boundaries. Both the global (MS-measured) and the local (PEEM-measured) kinetic phase diagrams shift towards a higher CO pressure (higher CO tolerance) for the defect-rich surface due to the differently modified oxygen and CO binding energies on the low-coordinated step and defect sites compared to the smooth surface.

The exact identity of the conditions for different crystallographic orientations and the parallel principle of the used technique, which allows the simultaneous monitoring of dynamic processes on different domains, open interesting perspectives for future applications of this approach.

REACTIVITY OF OXIDES ON Pd IN CO OXIDATION

In this chapter, the role of two different kinds of oxides in the CO oxidation reaction on Pd is treated. The first part of this chapter is dedicated to the study of an extrinsic oxide, SiO_x , which is formed under oxidizing conditions at elevated temperatures on the Pd foil by segregation of silicon bulk impurities. The mechanism of the Si segregation and SiO_x formation at the surface of Pd foil in the presence of oxygen dissociatively adsorbed on the metallic Pd are discussed. The influence of the silicon oxide present on the Pd foil on the activity of the Pd towards the CO oxidation reaction is investigated by the mass-spectroscopically measured CO_2 rate and the local properties observed by PEEM.

In the second part, first the reactivity towards CO oxidation of a Pd powder sample impregnated on (oxidized) aluminum foil serving as a more realistic model for technical catalysts is compared to the reactivity of the Pd foil. The impact of the higher defect density on the powder sample compared to the very well defined foil with its μm -sized (hkl) grains on the global reaction kinetics of the CO oxidation reaction is investigated. In a second step, the reactivity of an PdO powder sample which was prepared in the same way as the Pd powder sample is studied. The oxidation state of palladium within the PdO was controlled by XPS after each kinetic experiment and the question was addressed if there exists a correlation between the Pd oxidation state and the reactivity towards CO oxidation.

7.1 Introduction

Although the catalytic CO oxidation on Pt-group metal surfaces is extensively studied in the past and the underlying Langmuir-Hinshelwood mechanism with the involved elementary steps such as molecular adsorption of CO, dissociative adsorption of oxygen, surface reaction and desorption of carbon dioxide is well established by various single crystal studies under UHV conditions [10], this seemingly simple model reaction was found to be quite complex in the case of real systems consisting of oxide supported precious metal particles under ambient conditions.

To overcome the "material gap" between single crystal surfaces and real catalysts, many approaches have been applied, e.g. the investigation of field emitter tips [304], cylindrical single crystals [257] or polycrystalline foils [37, 242, 253]. Polycrystalline foils are particularly suitable model systems since the μm -sized domains of different orientations are automatically exposed to exactly the same external parameters such as partial pressures and temperature, thus precise comparative studies of the catalytic behavior of individual (hkl) orientations, such as the role of surface oxide formation, can be performed.

The role of palladium oxides in the CO oxidation on Pd has become the focus of attention, since new surface sensitive techniques were developed which are also applicable under high pressure conditions (up to atmospheric pressure), for example high-pressure STM, PM-IRAS or high-pressure XPS [6, 232]. Such methods have provided insights to the catalytic CO oxidation reaction under more realistic catalytic conditions, bridging thus the "pressure gap" [176, 178, 179, 305–307]. As was described in detail in section 3.3.3, an intensive contradictory debate about the nature of the most active phase in CO oxidation resulted in the finding that the Langmuir-Hinshelwood mechanism still predicts the kinetics of the CO oxidation reaction on Pt-group metals at both low and high pressures [178, 180, 181]: the O-covered metal surface responsible for the high catalytic activity in UHV, appears also as the most active phase at elevated pressures, unless oxide formation initiates the deactivation, especially for Pd and Rh surfaces.

Despite of the intensive studies of the role of palladium oxides in the CO oxidation on Pd, much less attention is directed to the role of "non-palladium" oxides on the Pd surface in the CO oxidation. Recently it was shown, that such "stranger" oxides present on the platinum-metal surface, can significantly influence the reaction, even at small oxide coverages [213, 308]. It is also known that impurities commonly present in commercially used catalysts, such as Si, might form surface oxides under oxidizing atmosphere [309], but aimed studies of such oxides under reaction conditions are very scarce. In this chapter, the

role of the surface oxides formed by Si impurities in the kinetics of the CO oxidation on Pd is studied by PEEM combined with XPS and MS.

In addition, the same methods are used to study the role of the intrinsic Pd oxide in the CO oxidation reaction. Since the studied sample is a PdO powder sample impregnated into an aluminum foil, first the reaction kinetics of an equivalently prepared metallic Pd powder sample was studied for comparison. In that way, also a more realistic model for technological catalysts, i.e. alumina supported Pd nanoparticles, was produced and its kinetic behavior in comparison to the Pd foil consisting of well-defined single-crystal-like regions of up to $\sim 100\mu\text{m}$ is investigated.

7.2 Peculiarities of the experiment

The experiments presented in this chapter were performed in both chambers of the UHV setup detailed in section 2.1, namely the independently from each other operated PEEM and XPS chambers which are connected by a sample transfer line allowing thus a common reactive gas atmosphere in the 10^{-4} to 10^{-9} mbar range. In the "microscopy" chamber the photoemission electron microscope, the MS, the high purity gas supply system and the sample preparation facilities for cleaning the sample by argon ion sputtering and subsequent annealing were used for the experiments. In the "spectroscopy" chamber the XPS-system consisting of the hemispherical energy analyzer and a twin anode X-ray source were utilized for the measurements. The general configuration of the experimental setup and a scheme of the experiment are shown in Fig. 7.1.

The principle of the local kinetic measurements by PEEM has been described in detail in the previous chapters and is therefore summarized here only briefly (see also Fig. 7.1). The CO oxidation reaction on the sample is monitored simultaneously by MS and by PEEM whereby MS provides the global CO_2 rate produced by the whole polycrystalline sample and PEEM, in turn, provides the laterally-resolved kinetic information from the individual grains (in case of the foil sample). Since the PEEM image reflects the lateral distribution of the local work function across the sample, e.g. grains of different surface orientation and different adsorbates can be distinguished. The PEEM-image is recorded *in situ* with a high-speed CCD-camera, so the intensity of a selected region-of-interest, e.g. one particular grain of the foil sample, can be monitored during a typical CO pressure scan. The XPS analysis provides data on the chemical composition of the samples in UHV or under the same gas atmosphere as in PEEM.

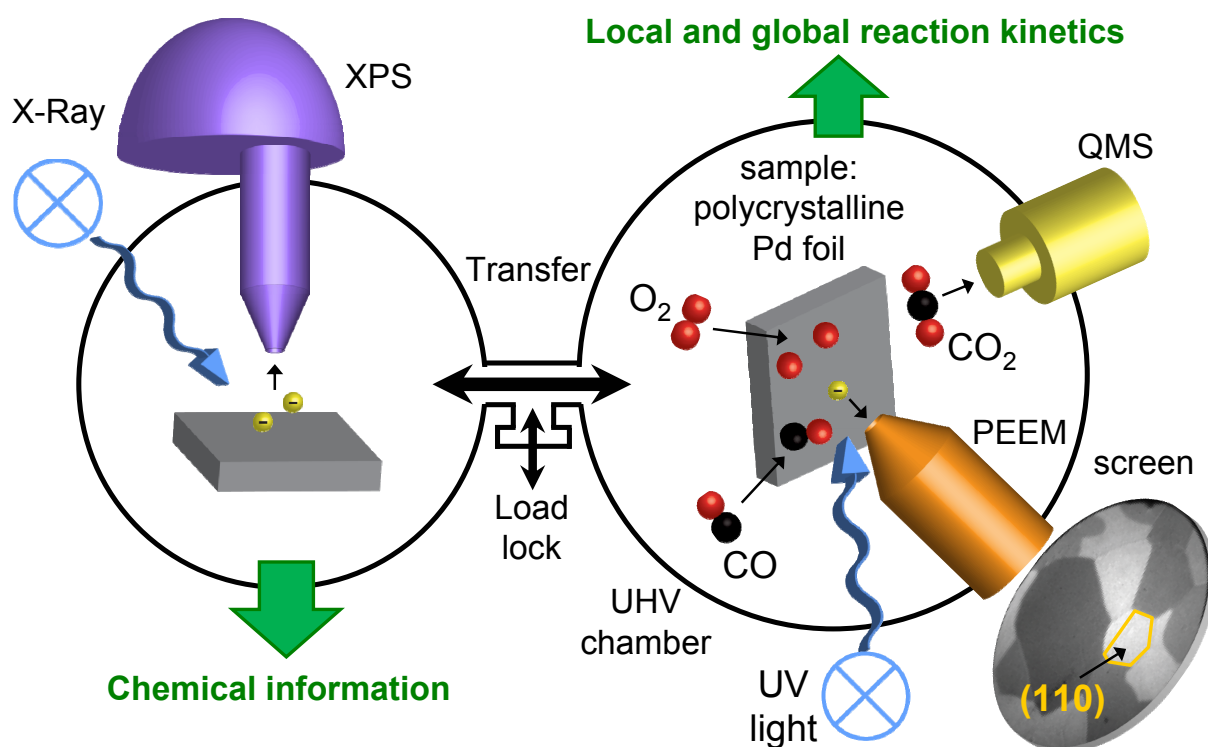


Figure 7.1: Configuration of the experimental setup and scheme of the experiment. The simultaneous monitoring of the ongoing CO oxidation by PEEM and MS provides information on kinetic phase transitions on individual grains of a polycrystalline Pd foil (local PEEM measurements) in parallel with the global MS data. The XPS analysis provides data on the chemical composition of the samples in UHV and under the same gas atmosphere as in PEEM.

The investigated samples were the $10 \times 10 \text{ mm}^2$ polycrystalline Pd foil, consisting mainly of [100]-, [110]- and [111]-oriented grains (see section 2.3.1), and the Pd powder and PdO powder samples supported on a $10 \times 10 \text{ mm}^2$ alumina/aluminum foil.

As already described in section 2.3.2, the Pd and PdO powders have been pressed each into an (oxidized) aluminum foil which was fixed by a tantalum frame to the molybdenum sample holder plate (see Fig. 2.19 in section 2.3.2). Due to the low melting point of aluminum (660°C), the samples could not be heated above 350°C in UHV. The sample temperature was measured by a NiCr/Ni thermocouple spot-welded to the front side of the samples. Ar⁺ ion sputtering was only possible in case of the Pd powder sample, since the PdO powder was considerably reduced to metallic Pd upon sputtering as was proven by XPS. To remove carbonaceous impurities, both samples were heated in oxygen before the kinetic experiments, the metallic Pd powder in $p_{\text{O}_2} = 5 \times 10^{-7}$ mbar and the Pd oxide powder in $p_{\text{O}_2} = 1.3 \times 10^{-5}$ mbar. In Fig. 7.2, optical micrographs and the corresponding PEEM

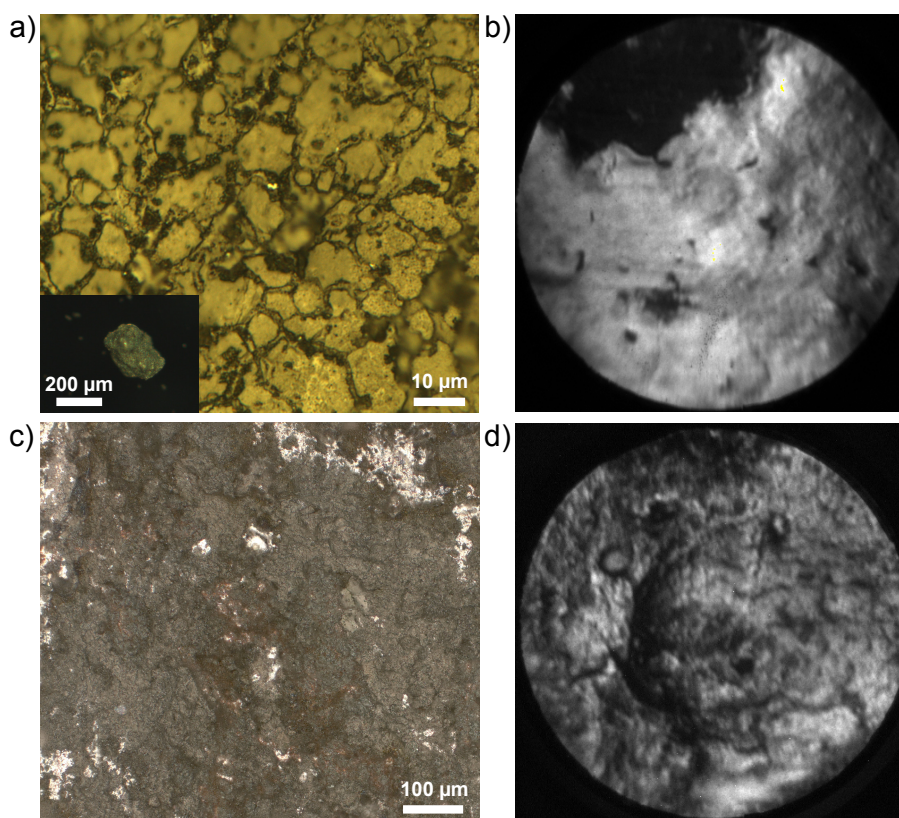


Figure 7.2: (a) Optical micrograph of the Pd black powder impregnated onto aluminum foil. Inset: Pd black powder particle before impregnation. (b) PEEM image of the Pd black sample. (c) Optical micrograph of the PdO powder pressed into aluminum foil. (d) PEEM image of the PdO powder sample.

images of the Pd black and the PdO powder are shown in the subfigures a and b, and c and d, respectively.

The cleanliness of the powder samples has been checked by XPS. In Fig. 7.3a, the Pd 3d region is displayed for the Pd black powder sample. As expected for metallic Pd [310], the 3d_{3/2} and the 3d_{5/2} peak maxima are located at 340.4 eV and 335.1 eV, respectively. In Fig. 7.3b, the same region for the PdO sample is displayed. The Pd 3d peaks are considerably shifted towards higher binding energies (342.3 eV and 336.9, respectively), as it is characteristic for oxidized metal samples (cf. section 2.2.3). Figure 7.3c shows the Al 2p region of the Pd black powder sample. The peak consists of two contributions, with the oxidic one at 75.8 eV being more dominant than the metallic one at 72.9 eV. The large shift of 2.9 eV indicates that the support consists mainly of oxidized aluminum (alumina, Al₂O₃) [310] and can thus serve as a suitable model of a catalytic support. Peak fitting was performed with the CasaXPS software.

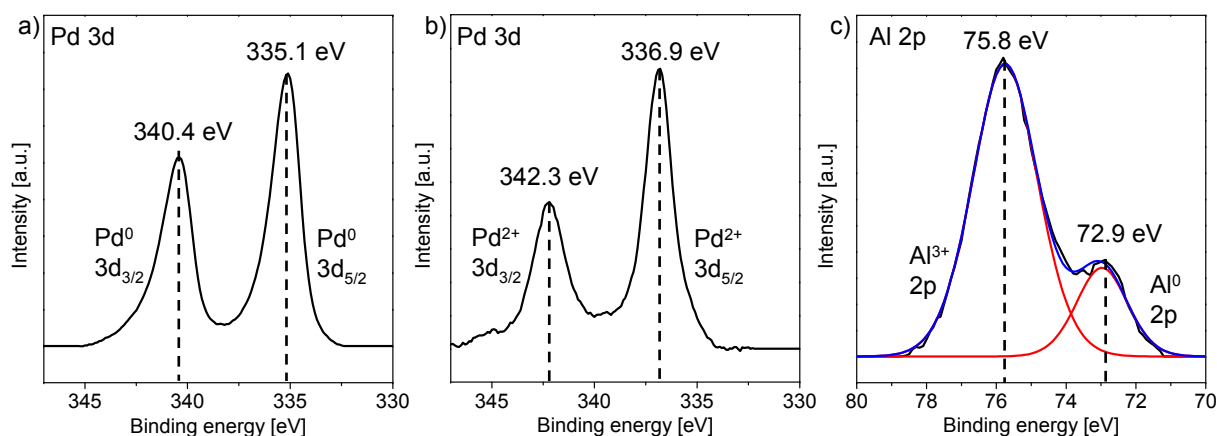


Figure 7.3: (a) XPS of the Pd 3d region of the Pd black powder sample. (b) the same, but for the Pd 3d region of the PdO powder sample. (c) XPS of the Al 2p region of the aluminum support of the Pd black powder sample.

7.3 Surface silicon oxide in CO oxidation on Pd foil

In the first part of the presented results, the formation of an extrinsic oxide, a silicon oxide on the Pd surface, and its influence on the reactivity of Pd is treated. The formation of this silicon oxide is induced by an oxidizing treatment of the Pd foil under elevated temperatures as will be discussed below.

7.3.1 Global and local reaction kinetics upon surface SiO_x formation

To study the influence of an oxidizing treatment of the polycrystalline Pd foil on the kinetic transitions in CO oxidation reaction, global kinetic measurements of the CO_2 reaction rate analogous to those presented in chapter 4 were performed for a clean (Ar^+ sputtered and annealed) Pd foil and for the same but additionally oxygen treated surface. The results are summarized in Fig. 7.4: the upper row (Fig. 7.4a-c) shows PEEM-frames of the clean Pd foil (Fig. 7.4a), the same surface covered by adsorbed oxygen (Fig. 7.4b) and again the same area but after oxygen treatment at 973K and 5×10^{-6} mbar (Fig. 7.4c). The latter PEEM image was brightened for better comparison. In Fig. 7.4a three individual [110]-, [100]- and [111]-oriented grains are indicated, whose crystallographic orientation has been determined by the differences in contrast, as described in detail in section 2.3.3. The lower plots in Fig. 7.4 show the global (MS-measured for the whole sample) CO_2 reaction rate recorded during an isothermal cyclic CO pressure scan at constant oxygen pressure of 1.3×10^{-5} mbar and $T = 473\text{K}$ for the clean, i.e. sputtered and annealed Pd surface (Fig. 2d), and for the same surface treated by oxygen at $p_{\text{O}_2} = 5 \times 10^{-6}$ mbar for 15 min at three different

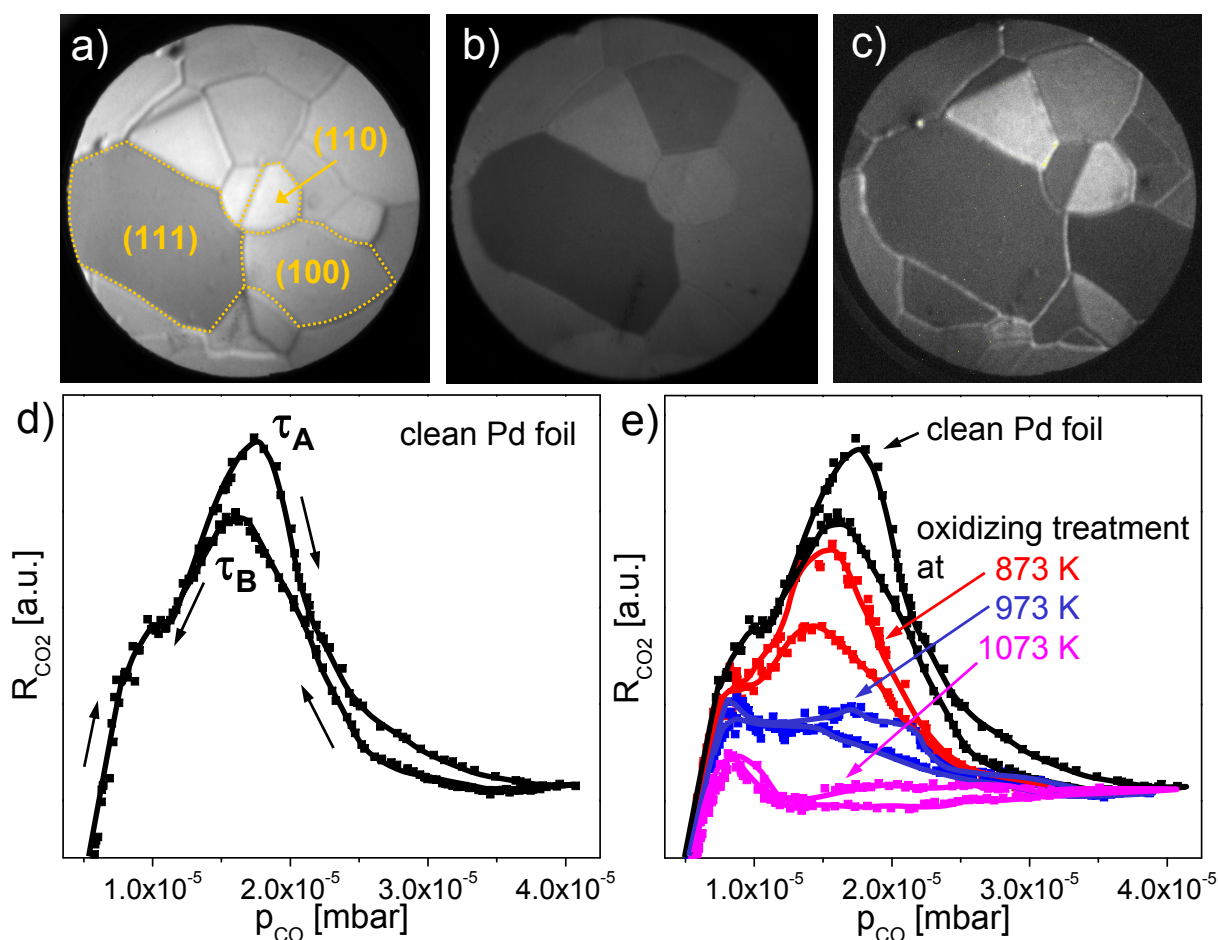


Figure 7.4: CO oxidation on the polycrystalline Pd foil. (a) PEEM image of the clean (Ar^+ sputtered and annealed) Pd surface, three low index domains are exemplary indicated; (b) the same surface, but oxygen covered; (c) the same surface after oxygen treatment at $p_{\text{O}_2} = 5 \times 10^{-6}$ mbar and $T = 973$ K; (d) global CO_2 reaction rate for a clean Pd surface recorded by MS during an isothermal ($T = 473$ K) cyclic CO pressure scan at constant oxygen pressure of 1.3×10^{-5} mbar. Kinetic transitions τ_A and τ_B from the catalytically active to the inactive steady state and vice versa are indicated; (e) the same as in (d) but for the oxygen treated surface ($p_{\text{O}_2} = 5 \times 10^{-6}$ mbar, $T = 873$ K; 973 K; 1073 K, treatment duration 15 min for all temperatures). A CO_2 reaction rate curve for the clean surface is also shown for comparison.

temperatures of 873 K, 973 K and 1073 K, also in comparison with the clean Pd surface (Fig. 7.4e).

In Fig. 7.4d, the CO_2 reaction rate exhibits the typical (for CO oxidation on Pd) hysteresis behavior outlined in section 3.3: the global CO_2 rate almost linearly increases for the surface in the high reactivity steady state (predominantly oxygen-covered), till the kinetic transition τ_A from the high reactivity state to the low reactivity state occurs (Fig. 7.4d). Because of the effective blocking of adsorption sites for oxygen by CO the reverse transition τ_B from

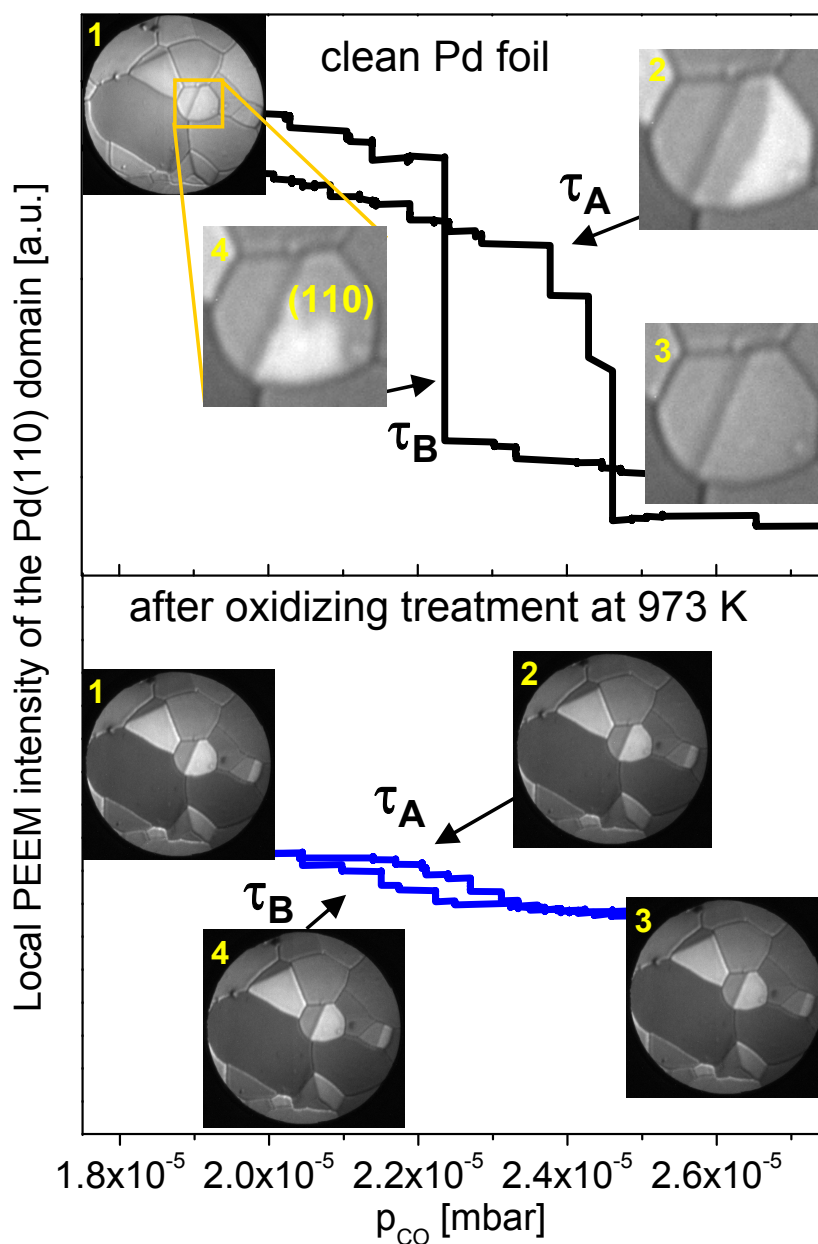


Figure 7.5: Laterally-resolved kinetics of CO oxidation on polycrystalline Pd foil. (a) local intensity of the PEEM image for the Pd(110) domain recorded during the same cyclic CO pressure scan as in Fig. 7.4d. The kinetic transitions τ_A and τ_B are much more pronounced than in the global MS curve in Fig. 7.4d. The PEEM frames correspond to the reaction stages indicated in the PEEM intensity curve; (b) the same as in (a) but after the oxidizing oxygen treatment at 973K. The τ_A and τ_B are almost undiscernible.

the inactive to the active state occurs at a lower CO partial pressure than the transition τ_A resulting in the hysteresis in the CO_2 production rate as is seen in Fig. 7.4d for the sputtered and annealed Pd surface and in Fig. 7.4e for the Pd surface treated at 873K in

7 Reactivity of oxides on Pd in CO oxidation

oxygen at 5×10^{-6} mbar. For the Pd surface treated by oxygen at 873K the CO₂ rate appears considerably lower, but the hysteresis is still present (Fig. 7.4e). Oxygen treatment at higher temperatures causes further decrease of the CO₂ rate (e.g. for 973K, Fig. 7.4e) and even a practical disappearance of the hysteresis (see the 1073K curve in Fig. 7.4e).

For the laterally resolved kinetics of the CO oxidation reaction, the video-PEEM sequences recorded simultaneously with the MS monitoring were analyzed. Figure 7.5a shows an example of such analysis where the local PEEM intensity for a particular domain, in the present case a Pd(110) domain, is shown in analogy to the globally MS-measured CO₂ rate in Fig. 7.4d. The local data result in a clear hysteresis where two sharp drops/jumps of the PEEM intensity (representing the kinetic transitions from one reactivity state of the system to another, but measured locally for one particular grain of interest) are visible. The reason for the much more pronounced local transitions observed by PEEM (in comparison to MS) lies in the averaging effect of the MS measurements: the kinetic transitions of the differently oriented grains occur at different CO pressures, the corresponding drops/jumps in the R_{CO_2} curve overlap smearing out the global τ_A and τ_B .

Again, similarly as in the global case, the treatment of the polycrystalline Pd surface with oxygen at elevated temperature (e.g. at 973K as is shown in Fig. 7.5b) results in the collapse of the hysteresis loop, the local τ_A and τ_B transitions are smeared out and it is not possible to associate the transitions with particular CO pressure values as in the case of the clean Pd surface (Fig. 7.5a). The reason for this behavior will be discussed below, together with the XPS data.

7.3.2 XPS results

To explain the observed reaction behavior, an XPS-analysis of the Pd foil before and after the oxidizing oxygen treatment at constant oxygen pressure of 5×10^{-6} mbar and temperatures between 673K and 973K has been performed. The XPS results are summarized in Figs. 7.6a and b and 7.7, where the high-resolution spectra for the Pd 3d region (Fig. 7.6a), for the Si 2p region (Fig. 7.6b) and the evolution of the Si 2p signal with surface oxidation temperature (Fig. 7.7) are shown.

The Pd 3d spectra demonstrate that no significant formation of palladium oxide has been observed under the present conditions. In turn, the Si 2p spectra reveal an intensive SiO₂ formation on the Pd surface upon the oxidizing treatment of the Pd foil at elevated temperatures. Apparently, the presence of oxygen stimulates the diffusion of the bulk dissolved Si from the near-surface regions towards the surface and enhances thus the segregation of Si

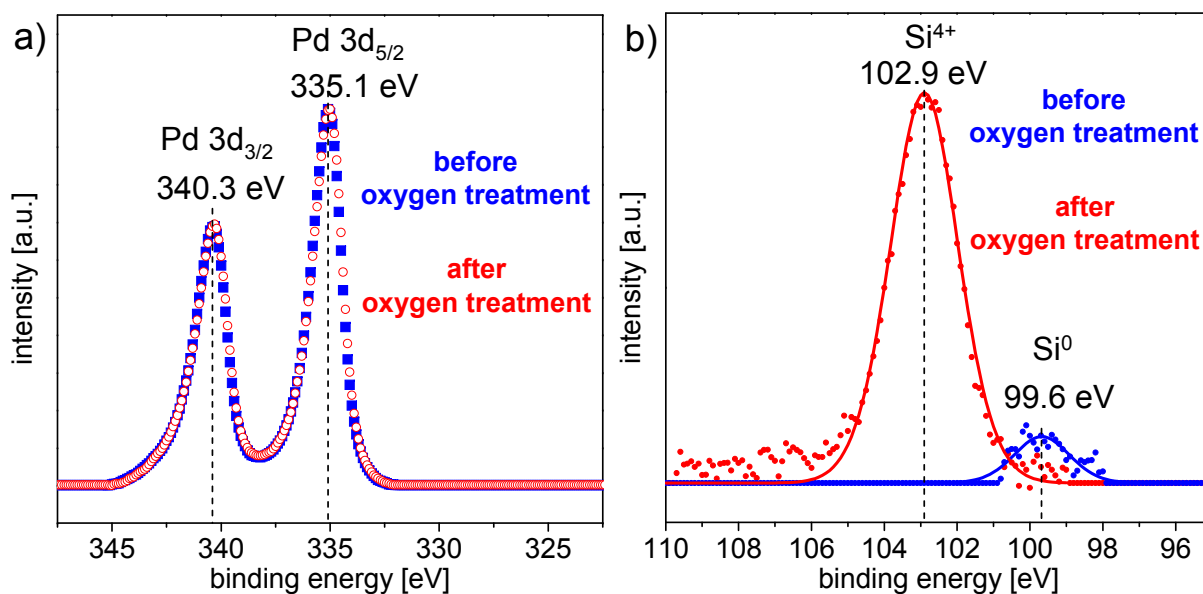


Figure 7.6: Silicon oxide formation on Pd surface: a) Pd 3d XPS spectra before and after oxidizing oxygen treatment at 973 K; b) the same but for the Si 2p spectra.

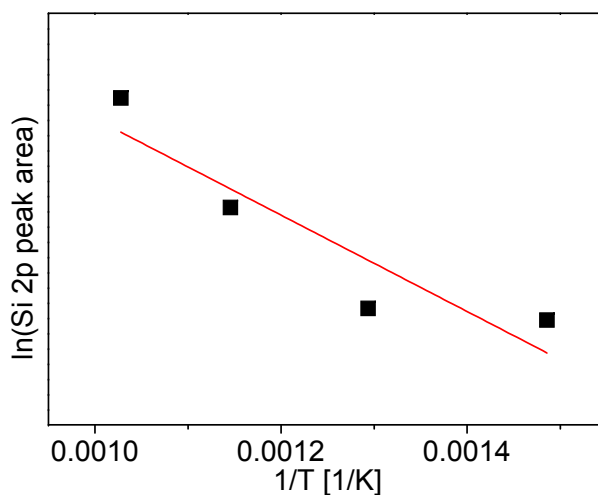


Figure 7.7: Arrhenius plot of the surface silicon oxide formation.

to the Pd surface (compare the Si⁰ and the Si⁴⁺ 2p signals, measured for the Si segregated without and with oxygen atmosphere, respectively). As for any diffusion related process, the segregation limited SiO₂ formation rate appears to be strongly temperature dependent, as demonstrated in Fig. 7.7. An attempt to apply an Arrhenius plot provides an effective activation energy of 0.27 eV, a value which is significantly lower than known values of about 2 eV for thermal Si oxidation [311, 312]. It is clear, however, that in the present case of a submonolayer SiO₂, the Deal-Grove model [311] based on the assumption that Si oxidation

proceeds by the transport of molecular oxygen from the ambient to the Si/SiO₂ interface through already oxidized Si layers does not apply. In our case, the rate limitation does not result from the oxygen diffusion, but from the silicon transport from the Pd subsurface region to the surface. Thus, the activation energy values typical for the oxygen diffusion limited process could not be expected. Recently, unusually small activation energy values (of e.g. 0.13 eV [312] or even lower [313]) were observed for the oxidation procedure where the oxygen diffusion limit was lifted by using atomic oxygen for the Si oxidation.

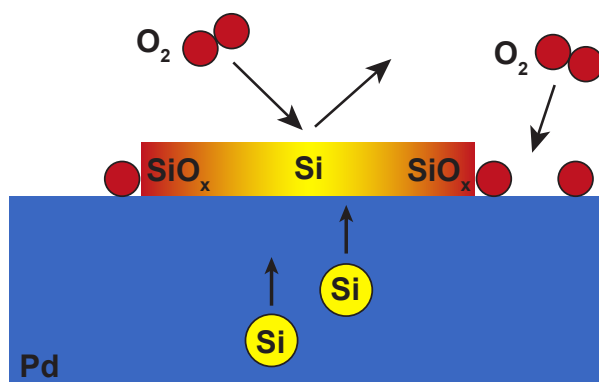


Figure 7.8: Schematic illustration of the SiO_x formation by segregation of Si bulk impurities and subsequent oxidation by atomic oxygen chemisorbed on the Pd surface.

In Fig. 7.8, the process of Si segregation from the Pd subsurface region and subsequent Si oxidation by oxygen atoms already adsorbed on the Pd patches is schematically illustrated. The metal atoms of the substrate "catalyze" the SiO_x formation on the surface via a spillover effect since the interaction of molecular oxygen with silicon is rather low compared to atomic oxygen. Generally, experimental observations are known, which show that the presence of oxygen (even in the 10⁻⁶ mbar range) increases the mobility of Si in Pt-metals causing the precipitation of SiO_x at the surface [314]. Such a very stable, nonreducible, i.e. non-reactive towards CO or H₂, "surface oxide" which can only be removed by Ar ion bombardment or prolonged annealing in UHV at temperatures above ~ 1200 K was first assigned to a transition oxide in the subsurface/surface region of the metal substrate leading to the formation of bulk PdO [117, 130, 148]. However, PdO is thermodynamically not stable under these conditions and it was found that the true nature of these species is a silicon-stabilized oxide [130, 309, 314–316]: bulk dissolved Si impurities segregate to the surface upon heating in the presence of oxygen in the gas phase. The structure of the oxide is mainly characterized by silicon-oxygen bonds rather than Pd-oxygen bonds, with a lattice constant related to, but not necessarily identical with that of SiO₂ [130, 309, 316].

7 Reactivity of oxides on Pd in CO oxidation

The enhanced Si segregation in the presence of oxygen can be rationalized considering energetic arguments: the higher bonding strength of Si on an oxygen covered Pd surface provides an energetic sink for Si atoms due to the chemical potential gradient, similarly as it occurs e.g. in an enrichment of alkali atoms on the oxygen covered surface in CO oxidation on Rh [317] or hydrogen oxidation on Rh [318, 319], or in the formation of concentration patterns of electropositive adsorbates as a result of up-hill diffusion in two-dimensional first order phase transitions under reaction-free conditions [320, 321]. Recently, DFT calculations were performed to identify the stable Si-O bonding structures on the Pd(111) and Pt(111) surfaces [322], where a variety of stable intermediates with stoichiometries between SiO_2 and SiO_3 , depending on the coverage, were found. This might explain the inhibiting effect of the SiO_x growth on the PdO_x formation observed in the present experiments, again due to the energetic arguments which favor the Si rather than the Pd oxidation.

The easiest interpretation of the inhibiting role of the SiO_2 in the CO oxidation reaction would be that SiO_2 simply blocks a part of the active reaction sites on the Pd surface but does not itself participate in the reaction. However, the drastic decrease in the CO_2 formation rate for a rather small coverage of SiO_2 (just a fraction of a monolayer, as follows from the Pd 3d and Si 2p signal relation) forces an additional explanation. It is known, that oxides on the Pt-group metals form monolayer islands at the initial growth stage [213, 323]. The boundary lines between the oxide islands and the remaining "oxide-free" metal surfaces exhibit, due to the local electron density jump from the metal to the oxide surface, different electronic properties which may nanometer-wide extend the promoting effect along the free metal surface around the islands [213].

The promoting effect on the reaction observed in the case of CeO_x islands, which is due to the additional oxygen supply [213], cannot be expected for the SiO_2 because of the poor redox properties of SiO_2 and thus the absence of an oxygen storage ability. Whereas the refilling of the oxygen vacancies in reducible oxides such as CeO_x stimulates the oxygen dissociation on the oxide-island adjacent surface sites, this is not the case for SiO_2 . In turn, the spillover of CO from the SiO_2 islands (a weakly bound mobile CO layer can be formed on the SiO_2 surface [324]) supports the interpretation that the regions around the SiO_2 islands must be rather inactive for the CO oxidation.

7.4 CO oxidation on Pd powder and PdO powder supported on alumina

In this section, the results on the global kinetic measurements for the model systems consisting of alumina supported Pd and PdO powder are presented. In parallel, the reaction was imaged by PEEM. The supported Pd powder serves as a more realistic model for technical catalysts than the Pd foil and the PdO powder allows for an intrinsic study of the role of the palladium oxide in comparison to the metallic Pd powder.

7.4.1 Reaction kinetics of alumina supported Pd powder

Analogue to the global kinetic measurements of the CO oxidation on Pd foil, presented in chapter 5, the CO₂ reaction rate was followed for the Pd powder sample (introduced in section 2.3) during the cyclic variation of the CO partial pressure at constant oxygen pressure ($p_{\text{O}_2} = 1.3 \times 10^{-5}$ mbar) and different constant temperatures in the range between 413K and 563K. Similar to the Pd foil, the CO₂ reaction rate exhibits a pronounced hysteresis (right inset in Fig. 7.9, $T = 433$ K) and plotting the kinetic transition points τ_A and τ_B in dependence of the temperature results in a kinetic phase diagram shown in Fig. 7.9. As was already the case for the Pd foil, the variation of the temperature at constant oxygen and CO pressures, i.e. an ignition/extinction experiment as exemplarily shown for $p_{\text{CO}} = 1 \times 10^{-5}$ mbar in the left inset in Fig. 7.9, results in *isobaric* kinetic transitions which quantitatively match the *isothermally* obtained global kinetic phase diagram.

In Fig. 7.9, the global kinetic phase diagram of the Pd foil is incorporated for comparison. In contrast to the kinetic behavior of the sputtered Pd foil (cf. chapter 6), the global kinetic phase diagram of the powder sample is not shifted as a whole to higher CO partial pressures. Rather, only the kinetic transition τ_A is located at higher CO partial pressures than for the foil sample, i.e. the bistability range of the Pd powder is considerably broader.

Like the sputtered Pd foil, the defect density on the Pd powder sample is very high. In agreement with the results on the sputtered Pd foil, the kinetic transition τ_A from the oxygen to the CO covered state occurs at a considerably higher CO pressure than on the annealed Pd foil. As already in case of the sputtered foil, this can be explained by the higher binding energy of oxygen at defect sites, i.e. more CO is needed to react with the oxygen and to poison the surface (cf. chapter 6). However, the reverse transition τ_B from the CO-poisoned to the oxygen covered state is essentially not changed compared to annealed Pd foil, in contrast to the results on sputtered Pd foil. Such effect may be explained by the

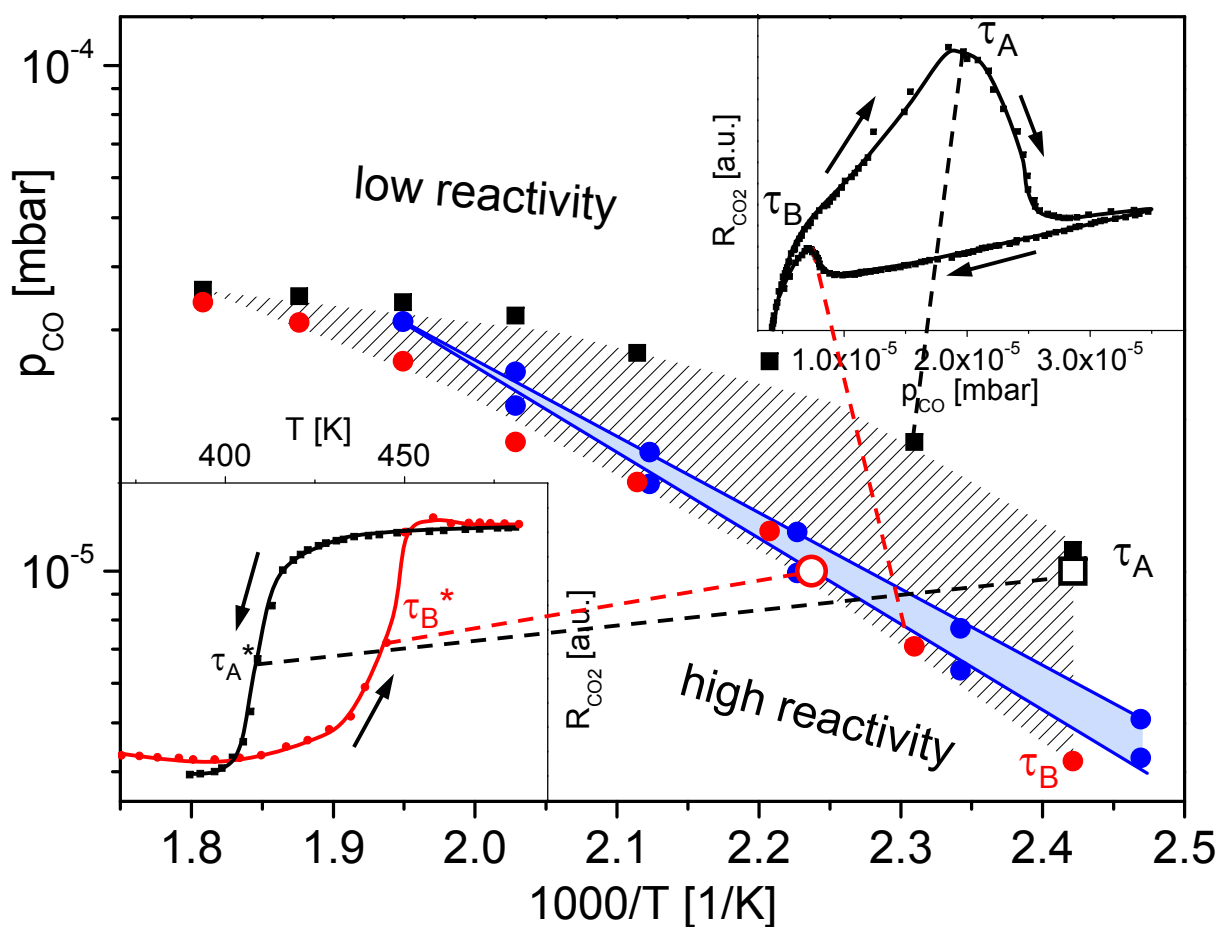


Figure 7.9: Global kinetic phase diagram of the Pd powder sample (black squares: τ_A , red dots: τ_B). The right inset shows an *isobaric* R_{CO_2} hysteresis loop at $p_{\text{O}_2} = 1.3 \times 10^{-5}$ mbar and $T = 433$ K and the left inset shows an *isothermal* ignition/extinction measurement at $p_{\text{CO}} = 1 \times 10^{-5}$ mbar. For comparison, the global kinetic phase diagram of the Pd foil is integrated (blue symbols).

assumption that the defect density on the powder sample is still much higher than on the sputtered foil and hence, the higher adsorption affinity of oxygen at defect sites is compensated by the also increased CO binding energy at these defects. However, to understand this effect in a more profound way, basically more research is necessary, e.g. the morphology of the powder should be known on the atomic scale to draw conclusions from its structure on the adsorption properties.

In parallel to the global MS measurements, the reaction has been followed *in situ* by PEEM. In Fig. 7.10 PEEM frames of the transition τ_B at $p_{\text{O}_2} = 1.3 \times 10^{-5}$ mbar and $T = 453$ K are shown. In general, the PEEM image intensity was considerably higher than in case of Pd foil, in accordance to the Smoluchowski law that the work function of a surface is decreased with increasing defect density [23]. Note also the dark region in the upper left

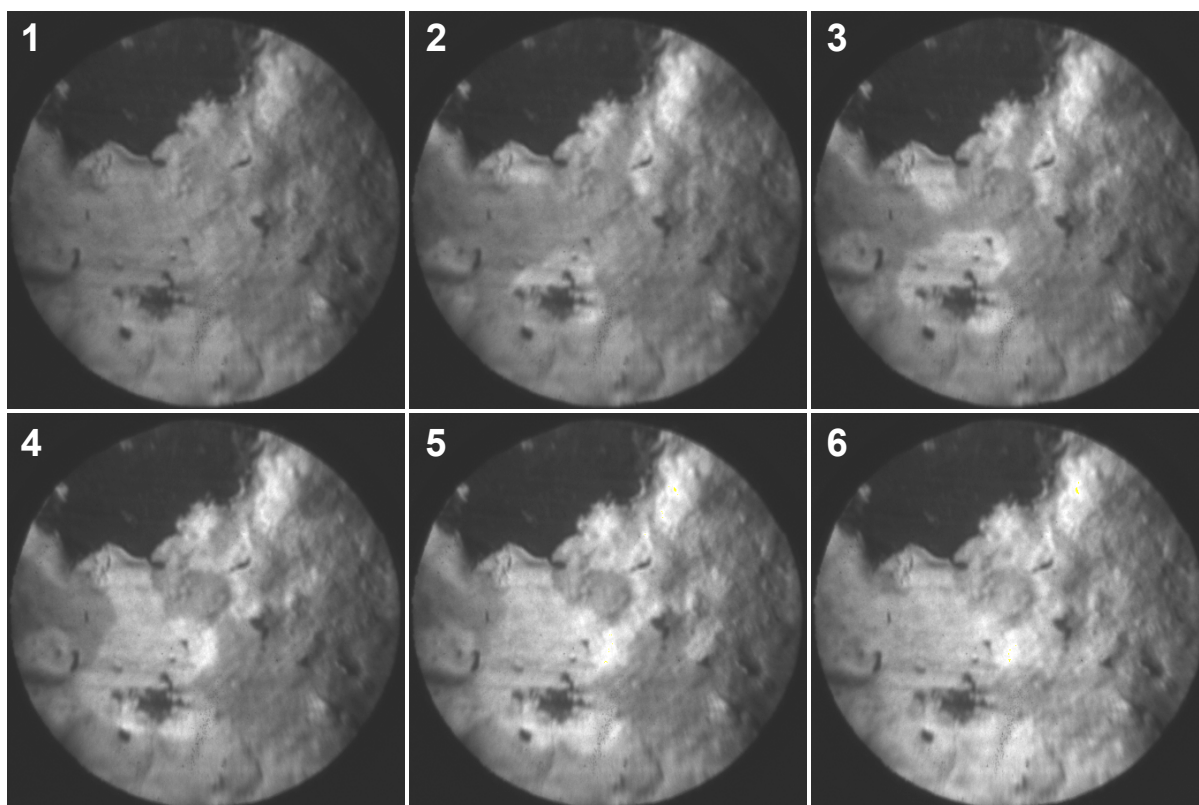


Figure 7.10: PEEM video frames of the transition τ_B on the Pd powder sample at $p_{O_2} = 1.3 \times 10^{-5}$ mbar and $T = 453$ K. CO covered regions appear dark and the bright regions correspond to the propagating oxygen front. The alumina support is represented by the very dark region in the upper left corner.

part of the PEEM images corresponding to the alumina support with a relatively high work function. Like in case of the Pd foil, propagating reaction fronts were observed for both kinetic transitions, τ_A and τ_B . The fronts nucleated usually at regions of elevated defect density as for example the boundaries between Pd and alumina or pits and protrusions and were propagating across the Pd powder regions without preferred direction. It can not be excluded that reactive coupling may occur via heat transfer contributions, since alumina as a poor heat conductor may not or only poorly dissipate the produced heat. The surface of the powder sample is to a certain degree homogeneous in that sense, that no mesoscopic regions of particular (hkl) orientations are present as in case of the Pd foil with its μm -sized domains, thus the construction of a "local" kinetic phase diagram is not very meaningful and would only reproduce the global kinetic phase diagram in the best case.

7.4.2 Reactivity of PdO powder in CO oxidation

It was outlined in section 3.3.3 that the role of Pd (surface) oxides with respect to the CO oxidation reaction under elevated pressure conditions was strongly debated in recent years. To investigate the intrinsic reactivity of Pd oxide towards the CO oxidation reaction, the CO₂ production rate over the PdO powder sample was measured in analogy to the Pd powder during cyclic variation of the CO partial pressure at constant p_{O_2} and temperature. In parallel, the oxidation state of the PdO powder was controlled by XPS after each kinetic experiment. In Fig. 7.11 the corresponding results are presented.

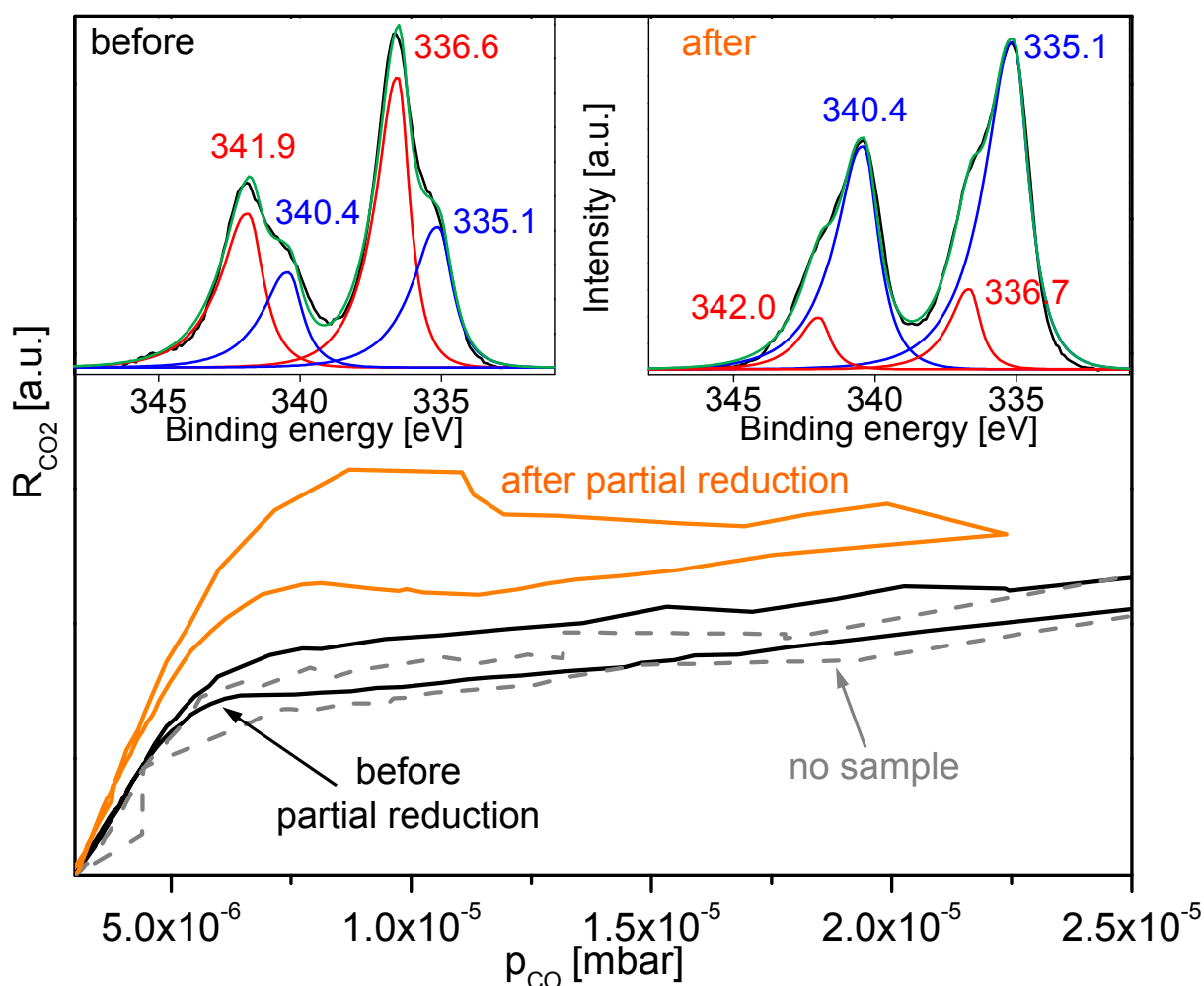


Figure 7.11: Global CO₂ rate in the CO oxidation reaction during cyclic variation of the CO pressure at constant $p_{O_2} = 1.3 \times 10^{-5}$ mbar and $T = 433$ K on the PdO powder sample before (black line) and after partial reduction (orange line) towards metallic Pd by sputtering. For comparison, the background CO₂ rate is also depicted as measured without sample (grey dashed line). The XPS spectra in the insets were recorded directly after the corresponding MS measurements.

7 Reactivity of oxides on Pd in CO oxidation

Before the kinetic measurements of the CO₂ rate over the PdO powder sample, the background CO₂ rate produced by the mass spectrometer was measured without a sample in the UHV chamber at $p_{\text{O}_2} = 1.3 \times 10^{-5}$ mbar and cyclic variation of the CO pressure. The result is represented by the dashed line in Fig. 7.11. It is obvious that the CO₂ rate produced by the (almost pure) PdO powder sample (at $p_{\text{O}_2} = 1.3 \times 10^{-5}$ mbar and $T = 433$ K) represented by the solid black line is equivalent to the background signal, i.e. the PdO powder sample was found to be completely inactive. After this first MS measurement, an XPS spectrum was recorded of the Pd 3d region (left inset): The spectrum showed evidence for a mixture of pure and partially reduced PdO with the main (oxidic) peaks located at 341.9 eV (3d_{3/2}) and 336.6 eV (3d_{5/2}) and the metallic shoulders at 340.4 eV and 335.1 eV. This means, the PdO powder sample was already partially reduced after the first reaction cycle, but still the main body of the sample consisted of PdO. *After* that, the PdO powder sample was sputtered and annealed in $p_{\text{O}_2} = 1.3 \times 10^{-5}$ mbar and another reaction cycle was performed represented by the solid orange line in Fig. 7.11 at the same temperature of 433 K. Now, the sample exhibited already a certain reactivity and the usual hysteresis behavior of Pd was observed. The subsequently recorded XPS spectrum (right inset) showed that the sample was almost completely reduced to metallic Pd: only small oxidic shoulders were observed with the main peak maxima located at the metallic Pd 3d binding energies. Hence, it can be concluded that the increase in reactivity is accompanied by an increase of the metallic Pd component due to the reduction of the PdO powder to metallic Pd. The reduction probably occurs because of the different sputter yields of Pd and oxygen in the PdO (the lighter oxygen atoms are more easily removed by the Ar ions than the heavy Pd atoms). In addition, vacuum is generally a reducing medium [325].

7.5 Summary

A combined PEEM-MS-XPS approach allows to study *in situ* kinetics of surface reactions under control of the surface chemical composition of the sample, also under reactive atmospheric conditions in the 10^{-5} mbar range. This allows also to trace the reaction induced compositional changes of the sample surface, e.g. as the result of segregation effects or oxide reduction.

In the first part of this chapter the silicon oxide formation resulting from Si-impurity segregation on the polycrystalline Pd foil at oxidizing conditions in the temperature range between 873 K and 1073 K was monitored by XPS and its impact on the global and local (spatially-resolved) kinetics of the CO oxidation was determined by MS and PEEM. The

7 Reactivity of oxides on Pd in CO oxidation

results reveal a drastic inhibiting effect of the silicon oxide formation on the Pd reactivity towards the CO oxidation, manifested in both, the collapse of the global CO₂ formation rate (as measured by MS) and in the changed local properties (as observed by PEEM) of individual Pd micrograins. The presence of the adsorbed oxygen on the Pd surface assists effectively the silicon segregation to the Pd surface, due to energetic reasons.

In the second part, kinetic measurements of the CO oxidation reaction on alumina supported Pd and PdO powder under the same reaction conditions as on the Pd foil were performed. A global kinetic phase diagram for Pd powder pressed into an aluminum foil was constructed by the kinetic transitions measured globally by MS. Isobaric ignition and extinction was proved to match the isothermally obtain kinetic phase diagram, as was already demonstrated for the Pd foil (chapter 5). The comparison with the kinetic phase diagram of Pd foil revealed that the Pd powder sample is generally more tolerant towards CO poisoning, though exhibiting also a broader bistability regime. The Pd oxide powder sample was found to be completely inactive towards CO oxidation until the reduction towards metallic Pd upon Ar⁺ ion sputtering sets in, as was directly demonstrated by XPS.

The present experimental results allow the conclusion, that both the extrinsic SiO_x formed on Pd foil by bulk segregated silicon impurities assisted by the presence of oxygen and the intrinsic palladium oxide lead to a complete deactivation of Pd towards the CO oxidation reaction, at least in the considered pressure regime of $\sim 10^{-5}$ mbar.

CONCLUSIONS

The main objective of this thesis was to study the global and local catalytic properties of different heterogeneous platinum and palladium model systems. For this purpose, a new experimental approach was applied that combines conventional averaging mass spectroscopy (MS) for studying global reaction kinetics with laterally-resolving photoemission electron microscopy (PEEM) allowing for a simultaneous study of the local catalytic properties of heterogeneous samples, such as μm -sized differently oriented (hkl) domains on metal foils, under fully identical reaction conditions.

In this work, the reaction kinetics of the catalytic CO oxidation reaction on individual grains of polycrystalline platinum and palladium foils, as well as on alumina supported Pd and PdO powders, was studied in a laterally-resolving way under high vacuum conditions ($\sim 10^{-5}$ mbar reactants pressure) and compared with the global (averaged) measurements.

To obtain the overall kinetic transitions of the reaction between the steady states of high and low catalytic activity, the hysteresis in the global CO_2 rate was monitored by MS upon cyclic variation of one external parameter (e.g. CO partial pressure at constant temperature and O_2 pressure). For the polycrystalline Pt and Pd foil and for the Pd powder samples, the kinetic transitions τ_A and τ_B , corresponding to the transitions from the high to the low reactivity state and *vice versa*, were plotted in dependence of the reaction temperature providing the *global kinetic phase diagrams*. These kinetic phase diagrams directly illustrate the different regions of reactivity (high and low catalytic activity, bistability) for the particular systems in the (p, T) parameter space, allowing thus a direct comparison of the global reaction behavior of the different catalytic systems.

In turn, by the spatially-resolved intensity analysis of the simultaneously recorded PEEM video-sequences, it was possible to establish *local* kinetic phase diagrams for individual

8 Conclusions

[111]-, [100]- and [110]-oriented domains on Pt and Pd foil. The local image intensity of selected regions of interest in the PEEM video-sequences was correlated with the MS data, thus the kinetic transitions on the individual μm -sized grains could be obtained directly by the intensity changes in the PEEM frames corresponding to a change of the adsorbate coverage on the individual domains. The crystallographic orientation of the individual Pt and Pd (hkl) domains on Pt and Pd foil was first determined with PEEM by comparing the work function values of clean and adsorbate-covered Pt and Pd (hkl) single crystal surfaces with the intensity of the particular domains. The results were validated by independent electron backscatter diffraction (EBSD) measurements providing an unambiguous identification of the crystallographic orientation of the individual domains, also for the case of higher Miller indices, as for example (210).

The comparison between the global (averaged) kinetic phase diagram and the local kinetic phase diagrams of the individual [111]-, [100]- and [110]-oriented domains of Pt foil revealed that the domains behave independently from each other and the whole model system can thus be considered as consisting of μm -sized entities with single-crystal-like behavior. This finding was also confirmed by the confinement of the propagating reaction-diffusion fronts within the grain boundaries. Obviously, the pressure in the applied reaction conditions is not sufficient to synchronize the reactive behavior of the domains via gas-phase coupling. Furthermore, the μm -size of the domains and the grain boundaries effectively hinder diffusion coupling.

A weighted superposition of the local kinetic phase diagrams for the Pt(hkl) domains obtained by PEEM was found to reproduce exactly the MS-measured global kinetic phase diagram for the Pt foil. Thus, all relevant catalytic processes were captured by PEEM and a contribution by the grain boundaries could be excluded.

The PEEM experiments have shown substantial differences in the reactivity regimes of the individual domains of Pt and Pd foil. The reactivity of the (hkl) orientations increases with a decreasing atomic density of the surface, i.e. CO-poisoning occurs in the order $(111) < (100) < (110)$ and reactivation occurs in the opposite order, for both Pt and Pd.

The reaction front propagation on an individual Pt(100) domain on Pt foil was investigated in more detail. The propagating reaction-diffusion fronts were found to be highly anisotropic for both oxygen and CO fronts in a certain temperature range on the seemingly isotropic Pt(100) surface. This front propagation anisotropy could be assigned to the surface phase transition involved in the propagation mechanism. At a certain temperature, the front propagation anisotropy was observed to disappear in case of the oxygen fronts what could be explained by a change of the propagation mechanism. This indicates that

8 Conclusions

the "hill and valley" morphology observed by AFM measurements on the Pt(100) domain in the present study is, though reaction-induced, rather not responsible for the anisotropic front propagation.

The global and local reaction kinetics of Pt and Pd foil and of the individual Pt and Pd (hkl) domains have been compared directly. It was found, that the kinetic phase diagrams of the Pd surfaces were generally located at a higher CO pressure and exhibited a narrower bistability regime. This means in particular, that more CO is needed to poison a Pd surface than a Pt surface at the same oxygen pressure and temperature, i.e. Pd is more CO-tolerant, and that Pd reactivates at a higher CO-to-oxygen pressure ratio compared to Pt. In addition, the bistability region vanishes at lower temperatures for Pd than for Pt, thus CO-poisoning occurs generally at lower temperatures on Pd. These experimental findings were compared to newest micro-kinetic simulations of the CO oxidation reaction on Pt and Pd (hkl) surfaces based on DFT calculated adsorption energies of CO and oxygen and reaction barriers. The results of the simulations were in good agreement with the present experimental findings.

In addition to the usual surface science approach to study kinetic transitions, i.e. variation of the partial pressure of one reactant (here CO) at constant temperature, the kinetic transitions on the individual Pt and Pd surfaces were measured upon *isobaric* temperature variation, resulting in the "ignition" and "extinction" of the reaction, respectively. This concept, more common in technical catalysis, yielded quantitatively the same results. Thus, in the considered pressure regime of $\sim 10^{-5}$ mbar, the phenomenon of ignition in the CO oxidation reaction can be reduced to the pure kinetics since heat generation and mass transport limitations are negligible.

Not only the crystallographic orientation of a surface is important for its catalytic properties, but also the amount of surface defects can be crucial. In order to investigate the role of the defects, additional defects were created artificially on the Pd foil by Ar⁺ ion sputtering. An estimation of the introduced defect density was performed by STM measurements on a Pd(111) single crystal sputtered under the same conditions as was done for the Pd foil. It was found that the global kinetic phase diagram for the additionally sputtered Pd foil is shifted significantly towards higher CO pressures, exhibiting thus generally a higher CO-tolerance and reactivation ability compared to the annealed surface. In addition, the confinement of the reaction fronts within the grain boundaries observed for the annealed Pd foil, was lifted upon Ar⁺ ion sputtering. The independence of the individual domains is apparently lifted due to the creation of a similar amount of defect sites on the differently oriented domains by sputtering.

8 Conclusions

In order to proceed along the complexity axis, kinetic measurements equivalent to those on Pd foil were performed for a Pd powder sample pressed into oxidized Al foil, serving as a more realistic model system for technical catalysts (Al_2O_3 supported Pd particles). A comparison of the obtained global kinetic phase diagram for the Pd powder sample with that of the Pd foil revealed a generally higher CO-tolerance of the supported Pd powder, though also exhibiting a broader bistability range. With PEEM, the nucleation of reaction fronts at highly defected regions, as for example the boundaries between Pd and alumina, and the propagation of reaction-diffusion fronts similar to those on Pd foil could be observed.

In addition to PEEM and MS, X-Ray Photoelectron Spectroscopy (XPS) was integrated into the PEEM apparatus in course of this thesis. This allowed the determination of the chemical state of the sample under the same pressure conditions as during the reaction in the PEEM experiments. Such combined PEEM-MS-XPS approach was applied to study the influence of different oxides on the reactivity of Pd towards the CO oxidation reaction. On Pd foil, an oxygen-enhanced segregation of silicon bulk impurities and the subsequent formation of silicon surface oxide was found under oxidizing conditions. The reactivity of the Pd foil was drastically inhibited with increasing amount of SiO_2 on the surface, as was followed by MS and XPS. A palladium oxide powder sample was found to be inactive towards the CO oxidation reaction under the present reaction conditions until partial reduction to metallic Pd proven by XPS led to an increase in catalytic activity.

As a general conclusion, it can be stated that the combination of laterally-resolving techniques such as PEEM with methods that provide data about the average reaction behavior such as MS and the chemical state of a catalyst such as XPS is highly valuable to reveal local differences in the catalytic properties which can arise due to different crystallographic orientations, local structure variations or chemical composition and can be easily overlooked by the sole usage of averaging techniques. The application of such combined methods provides a promising perspective to find the pace-makers or active sites of a catalyst in different catalytic reactions, thus making the design of catalysts with tailored properties more effective in the future.

REFERENCES

- [1] W. OSTWALD, *Z. Phys. Chem.* **15**, 705 (1894).
- [2] W. OSTWALD, *Nature* **65**, 522 (1902).
- [3] A. D. MCNAUGHT and A. WILKINSON, editors, *IUPAC. Compendium of Chemical Terminology (the "Gold Book")*, Blackwell Scientific Publications, Oxford, 2nd edition, 1997, <http://dx.doi.org/10.1351/goldbook.C00876>.
- [4] I. LANGMUIR, *Trans. Faraday Soc.* **17**, 607 (1922).
- [5] I. LANGMUIR, *Trans. Faraday Soc.* **17**, 621 (1922).
- [6] P. B. RASMUSSEN, B. L. M. HENDRIKSEN, H. ZEIJLEMAKER, H. G. FICKE, and J. W. M. FRENKEN, *Rev. Sci. Instrum.* **69**, 3879 (1998).
- [7] J. PANTFÖRDER, S. PÖLLMANN, J. F. ZHU, D. BORGMANN, R. DENECKE, and H.-P. STEINRÜCK, *Rev. Sci. Instrum.* **76**, 014102 (2005).
- [8] G. RUPPRECHTER, *Adv. Catal.* **51**, 133 (2007).
- [9] G. A. SOMORJAI, *Chem. Rev.* **96**, 1223 (1996).
- [10] G. ERTL, *Angew. Chem. Int. Ed.* **47**, 3524 (2008).
- [11] E. BRÜCHE, *Z. Phys.* **86**, 448 (1933).
- [12] M. E. KORDESCH, W. ENGEL, G. J. LAPEYRE, E. ZEITLER, and A. M. BRADSHAW, *Appl. Phys. A* **49**, 399 (1989).
- [13] W. ENGEL, M. E. KORDESCH, H. H. ROTERMUND, S. KUBALA, and A. VON OERTZEN, *Ultramicroscopy* **36**, 148 (1991).

References

- [14] O. H. GRIFFITH and W. ENGEL, *Ultramicroscopy* **36**, 1 (1991).
- [15] E. BAUER, M. MUNDSCHAU, W. SWIECH, and W. TELIEPS, *Ultramicroscopy* **31**, 49 (1989).
- [16] H. H. ROTERMUND, W. ENGEL, M. KORDESCH, and G. ERTL, *Nature* **343**, 355 (1990).
- [17] H. H. ROTERMUND, W. ENGEL, S. JAKUBITH, A. VON OERTZEN, and G. ERTL, *Ultramicroscopy* **36**, 164 (1991).
- [18] G. ERTL, *Science* **254**, 1750 (1991).
- [19] H. HERTZ, *Ann. Phys.* **267**, 983 (1887).
- [20] W. HALLWACHS, *Ann. Phys.* **269**, 301 (1888).
- [21] A. EINSTEIN, *Ann. Phys.* **322**, 132 (1905).
- [22] M. P. SEAH and W. A. DENCH, *Surf. Interface Anal.* **1**, 2 (1979).
- [23] R. SMOLUCHOWSKI, *Phys. Rev.* **60**, 661 (1941).
- [24] S. HAGSTRÖM, C. NORDLING, and K. SIEGBAHN, *Phys. Lett.* **9**, 235 (1964).
- [25] A. FAHLMAN, K. HAMRIN, J. HEDMAN, R. NORDBERG, C. NORDLING, and K. SIEGBAHN, *Nature* **210**, 4 (1966).
- [26] U. GELIUS, P. F. HEDEN, J. HEDMAN, B. J. LINDBERG, R. MANNE, R. NORDBERG, C. NORDLING, and K. SIEGBAHN, *Phys. Scr.* **2**, 70 (1970).
- [27] J. F. MOULDER, W. F. STICKLE, P. E. SOBOL, and K. D. BOMBEN, *Handbook of X-ray Photoelectron Spectroscopy*, Physical Electronics, Inc., 1995.
- [28] A. JABLONSKI and C. J. POWELL, *J. Vac. Sci. Technol. A* **21**, 274 (2003).
- [29] G. BINNIG, H. ROHRER, C. GERBER, and E. WEIBEL, *Phys. Rev. Lett.* **49**, 57 (1982).
- [30] G. BINNIG, C. F. QUATE, and C. GERBER, *Phys. Rev. Lett.* **56**, 930 (1986).
- [31] A. J. SCHWARTZ, M. KUMAR, B. L. ADAMS, and D. P. FIELD, editors, *Electron backscatter diffraction in materials science*, Springer, US, 2nd edition, 2009.
- [32] S. NISHIKAWA and S. KIKUCHI, *Nature* **121**, 1019 (1928).
- [33] Y. KAINUMA, *Acta Crystallogr.* **8**, 247 (1955).
- [34] J. MARIEN, *Bull. Soc. R. Sci. Liège* **45**, 103 (1976).
- [35] S. NETTESHEIM, A. VON OERTZEN, H. H. ROTERMUND, and G. ERTL, *J. Chem. Phys.* **98**, 9977 (1993).
- [36] B. E. NIEUWENHUYS, R. BOUWMAN, and W. M. H. SACHTLER, *Thin Solid Films* **21**, 51 (1974).

References

- [37] J. LAUTERBACH, G. HAAS, H. H. ROTERMUND, and G. ERTL, *Surf. Sci.* **294**, 116 (1993).
- [38] P. R. NORTON, K. GRIFFITHS, and P. E. BINDNER, *Surf. Sci.* **138**, 125 (1984).
- [39] K. WANDELT and J. E. HULSE, *J. Chem. Phys.* **80**, 1340 (1984).
- [40] K. JACOBI, *4.2 Electron work function of metals and semiconductors*, volume III/42A2, SpringerMaterials - The Landoldt-Börnstein Database.
- [41] M. MCLEAN and H. MYKURA, *Surf. Sci.* **5**, 466 (1966).
- [42] P. HEILMANN, K. HEINZ, and K. MÜLLER, *Surf. Sci.* **83**, 487 (1979).
- [43] P. A. THIEL, R. J. BEHM, P. R. NORTON, and G. ERTL, *Surf. Sci.* **121**, L553 (1982).
- [44] R. J. BEHM, P. A. THIEL, P. R. NORTON, and G. ERTL, *J. Chem. Phys.* **78**, 7437 (1983).
- [45] P. A. THIEL, R. J. BEHM, P. R. NORTON, and G. ERTL, *J. Chem. Phys.* **78**, 7448 (1983).
- [46] R. MARTIN, P. GARDNER, and A. M. BRADSHAW, *Surf. Sci.* **342**, 69 (1995).
- [47] Y. Y. YEO, L. VATTUONE, and D. A. KING, *J. Chem. Phys.* **104**, 3810 (1996).
- [48] M. BARTEAU, E. KO, and R. MADIX, *Surf. Sci.* **102**, 99 (1981).
- [49] K. GRIFFITHS, T. E. JACKMAN, J. A. DAVIES, and P. R. NORTON, *Surf. Sci.* **138**, 113 (1984).
- [50] N. A. DESKINS, J. LAUTERBACH, and K. T. THOMSON, *J. Chem. Phys.* **122**, 184709 (2005).
- [51] G. BRODÉN, G. PIRUG, and H. BONZEL, *Surf. Sci.* **72**, 45 (1978).
- [52] A. BARALDI, E. VESSELLI, L. BIANCHETTIN, G. COMELLI, S. LIZZIT, L. PETACCIA, S. DE GIRONCOLI, A. LOCATELLI, T. ONUR MENTES, L. ABALLE, J. WEISSENRIEDER, and J. ANDERSEN, *J. Chem. Phys.* **127**, 164702 (2007).
- [53] P. R. NORTON, J. A. DAVIES, D. K. CREBER, C. W. SITTER, and T. E. JACKMAN, *Surf. Sci.* **108**, 205 (1981).
- [54] K. HEINZ, E. LANG, K. STRAUSS, and K. MÜLLER, *Appl. Surf. Sci.* **11-12**, 611 (1982).
- [55] R. J. BEHM, W. HÖSLER, E. RITTER, and G. BINNIG, *Phys. Rev. Lett.* **56**, 228 (1986).
- [56] R. J. BEHM, W. HÖSLER, E. RITTER, and G. BINNIG, *J. Vac. Sci. Technol. A* **4**, 1330 (1986).
- [57] E. RITTER, R. J. BEHM, G. PÖTSCHKE, and J. WINTERLIN, *Surf. Sci.* **181**, 403 (1987).
- [58] A. BORG, A.-M. HILMEN, and E. BERGENE, *Surf. Sci.* **306**, 10 (1994).
- [59] G. RITZ, M. SCHMID, P. VARGA, A. BORG, and M. RONNING, *Phys. Rev. B* **56**, 10518 (1997).
- [60] P. VAN BEURDEN, B. S. BUNNIK, G. J. KRAMER, and A. BORG, *Phys. Rev. Lett.* **90**, 066106 (2003).

References

- [61] P. VAN BEURDEN and G. J. KRAMER, *J. Chem. Phys.* **121**, 2317 (2004).
- [62] P. FERY, W. MORITZ, and D. WOLF, *Phys. Rev. B* **38**, 7275 (1988).
- [63] T. GRITSCH, D. COULMAN, R. J. BEHM, and G. ERTL, *Phys. Rev. Lett.* **63**, 1086 (1989).
- [64] K. SWAMY, E. BERTEL, and I. VILFAN, *Surf. Sci.* **425**, L369 (1999).
- [65] K. HEINZ, A. BARTHEL, L. HAMMER, and K. MÜLLER, *Surf. Sci.* **191**, 174 (1987).
- [66] R. IMBIHL, S. LADAS, and G. ERTL, *Surf. Sci.* **206**, L903 (1988).
- [67] P. HOFMANN, S. R. BARE, and D. A. KING, *Surf. Sci.* **117**, 245 (1982).
- [68] T. E. JACKMAN, J. A. DAVIES, O. P. JACKSON, W. N. UNERTL, and P. R. NORTON, *Surf. Sci.* **120**, 389 (1982).
- [69] N. FREYER, M. KISKINOVA, G. PIRUG, and H. P. BONZEL, *Appl. Phys. A* **39**, 209 (1986).
- [70] P. THOSTRUP, E. K. VESTERGAARD, T. AN, E. LAEGSGAARD, and F. BESENBACHER, *J. Chem. Phys.* **118**, 3724 (2003).
- [71] S. LADAS, R. IMBIHL, and G. ERTL, *Surf. Sci.* **197**, 153 (1988).
- [72] R. IMBIHL, A. E. REYNOLDS, and D. KALETTA, *Phys. Rev. Lett.* **67**, 275 (1991).
- [73] J. FALTA, R. IMBIHL, and M. HENZLER, *Phys. Rev. Lett.* **64**, 1409 (1990).
- [74] G. BLYHOLDER, *J. Phys. Chem.* **68**, 2772 (1964).
- [75] H. STEININGER, S. LEHWALD, and H. IBACH, *Surf. Sci.* **123**, 264 (1982).
- [76] R. W. MCCABE and L. D. SCHMIDT, *Surf. Sci.* **60**, 85 (1976).
- [77] C. M. COMRIE and R. M. LAMBERT, *J. Chem. Soc., Faraday Trans. 1* **72**, 1659 (1976).
- [78] J. FAIR and R. J. MADIX, *J. Chem. Phys.* **73**, 3480 (1980).
- [79] C. E. WARTNABY, A. STUCK, Y. Y. YEO, and D. A. KING, *J. Phys. Chem.* **100**, 12483 (1996).
- [80] S. FERRER and H. P. BONZEL, *Surf. Sci.* **119**, 234 (1982).
- [81] T. E. JACKMAN, J. A. DAVIES, D. P. JACKSON, P. R. NORTON, and W. N. UNERTL, *J. Phys. C Solid State* **15**, L99 (1982).
- [82] S. SCHWEGMANN, W. TAPPE, and U. KORTE, *Surf. Sci.* **334**, 55 (1995).
- [83] R. K. SHARMA, W. A. BROWN, and D. A. KING, *Surf. Sci.* **414**, 68 (1998).
- [84] M. NOWICKI, A. EMUNDTS, G. PIRUG, and H. P. BONZEL, *Surf. Sci.* **478**, 180 (2001).

References

- [85] C. T. CAMPBELL, G. ERTL, H. KUIPERS, and J. SEGNER, *Surf. Sci.* **107**, 207 (1981).
- [86] Y. Y. YEO, L. VATTUONE, and D. A. KING, *J. Chem. Phys.* **106**, 392 (1997).
- [87] G. ERTL, M. NEUMANN, and K. M. STREIT, *Surf. Sci.* **64**, 393 (1977).
- [88] H. HOPSTER and H. IBACH, *Surf. Sci.* **77**, 109 (1978).
- [89] Y. Y. YEO, L. VATTUONE, and D. A. KING, *J. Chem. Phys.* **106**, 1990 (1997).
- [90] R. J. BEHM, K. CHRISTMANN, G. ERTL, and M. A. VAN HOVE, *J. Chem. Phys.* **73**, 2984 (1980).
- [91] A. M. BRADSHAW and F. M. HOFFMANN, *Surf. Sci.* **72**, 513 (1978).
- [92] E. M. STUVE, R. J. MADIX, and C. R. BRUNDLE, *Surf. Sci.* **146**, 155 (1984).
- [93] C. BUREAU, *Chem. Phys. Lett.* **269**, 378 (1997).
- [94] J. ROGAL, K. REUTER, and M. SCHEFFLER, *Phys. Rev. B* **75**, 205433 (2007).
- [95] P. UVDAL, P.-A. KARLSSON, C. NYBERG, S. ANDERSSON, and N. V. RICHARDSON, *Surf. Sci.* **202**, 167 (1988).
- [96] G. ERTL and P. RAU, *Surf. Sci.* **15**, 443 (1969).
- [97] J. GOSCHNICK, M. GRUNZE, J. LOBODA-CACKOVIC, and J. H. BLOCK, *Surf. Sci.* **189-190**, 137 (1987).
- [98] H. CONRAD, G. ERTL, J. KOCH, and E. E. LATTI, *Surf. Sci.* **43**, 462 (1974).
- [99] R. RAVAL, S. HAQ, M. A. HARRISON, G. BLYHOLDER, and D. A. KING, *Chem. Phys. Lett.* **167**, 391 (1990).
- [100] P. HU, L. M. DE LA GARZA, R. RAVAL, and D. A. KING, *Surf. Sci.* **249**, 1 (1991).
- [101] M. G. RAMSEY, F. P. LEISENBERGER, F. P. NETZER, A. J. ROBERTS, and R. RAVAL, *Surf. Sci.* **385**, 207 (1997).
- [102] P. HU, D. A. KING, S. CRAMPIN, M.-H. LEE, and M. C. PAYNE, *Chem. Phys. Lett.* **230**, 501 (1994).
- [103] A. LOCATELLI, B. BRENA, S. LIZZIT, G. COMELLI, G. CAUTERO, G. PAOLUCCI, and R. ROSEI, *Phys. Rev. Lett.* **73**, 90 (1994).
- [104] R. RAMPRASAD, K. M. GLASSFORD, J. B. ADAMS, and R. I. MASEL, *Surf. Sci.* **360**, 31 (1996).
- [105] M. KITTEL, R. TERBORG, M. POLCIK, A. M. BRADSHAW, R. L. TOOMES, D. P. WOODRUFF, and E. ROTENBERG, *Surf. Sci.* **511**, 34 (2002).
- [106] J. GOSCHNICK, M. WOLF, M. GRUNZE, W. N. UNERTL, J. H. BLOCK, and J. LOBODA-CACKOVIC, *Surf. Sci.* **178**, 831 (1986).
- [107] T. ENGEL, *J. Chem. Phys.* **69**, 373 (1978).

References

- [108] H. CONRAD, G. ERTL, and J. KÜPPERS, *Surf. Sci.* **76**, 323 (1978).
- [109] X. GUO and J. T. YATES, *J. Chem. Phys.* **90**, 6761 (1989).
- [110] W. K. KUHN, J. SZANYI, and D. W. GOODMAN, *Surf. Sci.* **274**, L611 (1992).
- [111] P. R. NORTON, P. E. BINDNER, and K. GRIFFITHS, *J. Vac. Sci. Technol. A* **2**, 1028 (1984).
- [112] Q. GE, P. HU, D. A. KING, M.-H. LEE, and J. A. WHITE, *J. Chem. Phys.* **106**, 1210 (1997).
- [113] Z. GU and P. B. BALBUENA, *J. Phys. Chem. C* **111**, 9877 (2007).
- [114] Y. OHNO and T. MATSUSHIMA, *Surf. Sci.* **241**, 47 (1991).
- [115] N. FREYER, M. KISKINOVA, G. PIRUG, and H. P. BONZEL, *Surf. Sci.* **166**, 206 (1986).
- [116] J. SCHMIDT, C. STUHLMANN, and H. IBACH, *Surf. Sci.* **284**, 121 (1993).
- [117] R. DUCROS and R. MERRILL, *Surf. Sci.* **55**, 227 (1976).
- [118] A. V. WALKER, B. KLÖTZER, and D. A. KING, *J. Chem. Phys.* **109**, 6879 (1998).
- [119] A. C. LUNTZ, J. GRIMBLLOT, and D. E. FOWLER, *Phys. Rev. B* **39**, 12903 (1989).
- [120] A. ARTSYUKHOVICH, V. UKRAINTSEV, and I. HARRISON, *Surf. Sci.* **347**, 303 (1996).
- [121] J. L. GLAND, B. A. SEXTON, and G. B. FISHER, *Surf. Sci.* **95**, 587 (1980).
- [122] W. WURTH, J. STÖHR, P. FEULNER, X. PAN, K. R. BAUCHSPIESS, Y. BABA, E. HUDEL, G. ROCKER, and D. MENZEL, *Phys. Rev. Lett.* **65**, 2426 (1990).
- [123] H. STEININGER, S. LEHWALD, and H. IBACH, *Surf. Sci.* **123**, 1 (1982).
- [124] C. PUGLIA, A. NILSSON, B. HERNNÄS, O. KARIS, P. BENNICH, and N. MARTENSSON, *Surf. Sci.* **342**, 119 (1995).
- [125] J. L. GLAND, *Surf. Sci.* **93**, 487 (1980).
- [126] C. T. CAMPBELL, G. ERTL, H. KUIPERS, and J. SEGNER, *Surf. Sci.* **107**, 220 (1981).
- [127] D. R. MONROE and R. P. MERRILL, *J. Catal.* **65**, 461 (1980).
- [128] P. R. NORTON, J. A. DAVIES, and T. E. JACKMAN, *Surf. Sci.* **122**, L593 (1982).
- [129] C. NYBERG and C. G. TENGSTAL, *Surf. Sci.* **126**, 163 (1983).
- [130] T. W. ORENT and S. D. BADER, *Surf. Sci.* **115**, 323 (1982).
- [131] A. GERBI, L. SAVIO, L. VATTUONE, F. PIRANI, D. CAPPELLETTI, and M. ROCCA, *Angew. Chem. Int. Ed.* **45**, 6655 (2006).

References

- [132] M. TODOROVA, E. LUNDGREN, V. BLUM, A. MIKKELSEN, S. GRAY, J. GUSTAFSON, M. BORG, J. RO GAL, K. REUTER, J. N. ANDERSEN, and M. SCHEFFLER, *Surf. Sci.* **541**, 101 (2003).
- [133] J.-W. HE, U. MEMMERT, and P. R. NORTON, *J. Chem. Phys.* **90**, 5088 (1989).
- [134] J.-W. HE, U. MEMMERT, K. GRIFFITHS, and P. R. NORTON, *J. Chem. Phys.* **90**, 5082 (1989).
- [135] K. YAGI, D. SEKIBA, and H. FUKUTANI, *Surf. Sci.* **442**, 307 (1999).
- [136] J.-W. HE, U. MEMMERT, K. GRIFFITHS, W. LENNARD, and P. NORTON, *Surf. Sci.* **202**, L555 (1988).
- [137] K. YAGI, K. HIGASHIYAMA, and H. FUKUTANI, *Surf. Sci.* **295**, 230 (1993).
- [138] N. TAKAGI, Y. YASUI, M. SAWADA, A. ATLI, T. ARUGA, and M. NISHIJIMA, *Chem. Phys. Lett.* **232**, 531 (1995).
- [139] H. TANAKA, J. YOSHINOBU, and M. KAWAI, *Surf. Sci.* **327**, L505 (1995).
- [140] B. BRENA, G. COMELLI, L. URSELLA, and G. PAOLUCCI, *Surf. Sci.* **375**, 150 (1997).
- [141] K. YAGI and H. FUKUTANI, *Surf. Sci.* **412-413**, 489 (1998).
- [142] R. A. BENNETT, S. POULSTON, I. Z. JONES, and M. BOWKER, *Surf. Sci.* **401**, 72 (1998).
- [143] A. I. TITKOV, A. N. SALANOV, S. V. KOSCHEEV, and A. I. BORONIN, *Surf. Sci.* **600**, 4119 (2006).
- [144] M. KRALJ, T. PERTRAM, N. SERIANI, F. MITTENDORFER, A. KRUPSKI, C. BECKER, and K. WANDELT, *Surf. Sci.* **602**, 3706 (2008).
- [145] J.-W. HE and P. R. NORTON, *Surf. Sci.* **204**, 26 (1988).
- [146] R. IMBIHL and J. E. DEMUTH, *Surf. Sci.* **173**, 395 (1986).
- [147] P. SJÖVALL and P. UVDAL, *Chem. Phys. Lett.* **282**, 355 (1998).
- [148] H. CONRAD, G. ERTL, J. KÜPPERS, and E. E. LATTA, *Surf. Sci.* **65**, 245 (1977).
- [149] F. P. LEISENBERGER, G. KOLLER, M. SOCK, S. SURNEV, M. G. RAMSEY, F. P. NETZER, B. KLÖTZER, and K. HAYEK, *Surf. Sci.* **445**, 380 (2000).
- [150] B. KLÖTZER, K. HAYEK, C. KONVICKA, E. LUNDGREN, and P. VARGA, *Surf. Sci.* **482-485**, 237 (2001).
- [151] A. STELTENPOHL and N. MEMMEL, *Surf. Sci.* **443**, 13 (1999).
- [152] A. EICHLER, F. MITTENDORFER, and J. HAFNER, *Phys. Rev. B* **62**, 4744 (2000).
- [153] J. LAUTERBACH, K. ASAKURA, and H. H. ROTERMUND, *Surf. Sci.* **313**, 52 (1994).
- [154] N. MCMILLAN, T. LELE, C. SNIVELY, and J. LAUTERBACH, *Catal. Today* **105**, 244 (2005).

References

- [155] H. H. ROTERMUND, *Surf. Sci.* **283**, 87 (1993).
- [156] A. VON OERTZEN, A. MIKHAILOV, H. H. ROTERMUND, and G. ERTL, *Surf. Sci.* **350**, 259 (1996).
- [157] A. V. OERTZEN, A. S. MIKHAILOV, H. H. ROTERMUND, and G. ERTL, *J. Phys. Chem. B* **102**, 4966 (1998).
- [158] M. BERDAU, S. MOLDENHAUER, A. HAMMOUDEH, J. H. BLOCK, and K. CHRISTMANN, *Surf. Sci.* **446**, 323 (2000).
- [159] D. BASHLAKOV, L. JUURLINK, M. KOPER, and A. YANSON, *Catal. Lett.* **142**, 1 (2012).
- [160] H. H. ROTERMUND, M. POLLMANN, and I. G. KEVREKIDIS, *Chaos* **12**, 157 (2002).
- [161] A. V. WALKER, B. KLÖTZER, and D. A. KING, *J. Chem. Phys.* **112**, 8631 (2000).
- [162] S. LADAS, R. IMBIHL, and G. ERTL, *Surf. Sci.* **219**, 88 (1989).
- [163] S. LADAS, R. IMBIHL, and G. ERTL, *Surf. Sci.* **280**, 14 (1993).
- [164] V. A. BONDZIE, P. H. KLEBAN, and D. J. DWYER, *Surf. Sci.* **347**, 319 (1996).
- [165] M. TODOROVA, K. REUTER, and M. SCHEFFLER, *Phys. Rev. B* **71**, 195403 (2005).
- [166] G. ZHENG and E. I. ALTMAN, *Surf. Sci.* **462**, 151 (2000).
- [167] E. LUNDGREN, G. KRESSE, C. KLEIN, M. BORG, J. N. ANDERSEN, M. DE SANTIS, Y. GAUTHIER, C. KONVICKA, M. SCHMID, and P. VARGA, *Phys. Rev. Lett.* **88**, 246103 (2002).
- [168] E. LUNDGREN, A. MIKKELSEN, J. N. ANDERSEN, G. KRESSE, M. SCHMID, and P. VARGA, *J. Phys.: Condens. Matter* **18**, R481 (2006).
- [169] K. REUTER and M. SCHEFFLER, *Appl. Phys. A* **78**, 793 (2004).
- [170] H. GABASCH, W. UNTERBERGER, K. HAYEK, B. KLÖTZER, G. KRESSE, C. KLEIN, M. SCHMID, and P. VARGA, *Surf. Sci.* **600**, 205 (2006).
- [171] J. KLIKOVITS, E. NAPETSCHNIG, M. SCHMID, N. SERIANI, O. DUBAY, G. KRESSE, and P. VARGA, *Phys. Rev. B* **76**, 045405 (2007).
- [172] H. GABASCH, W. UNTERBERGER, K. HAYEK, B. KLÖTZER, E. KLEIMENOV, D. TESCHNER, S. ZAFEIRATOS, M. HÄVECKER, A. KNOP-GERICKE, R. SCHLÖGL, J. HAN, F. H. RIBEIRO, B. ASZALOS-KISS, T. CURTIN, and D. ZEMLYANOV, *Surf. Sci.* **600**, 2980 (2006).
- [173] D. ZEMLYANOV, B. ASZALOS-KISS, E. KLEIMENOV, D. TESCHNER, S. ZAFEIRATOS, M. HÄVECKER, A. KNOP-GERICKE, R. SCHLÖGL, H. GABASCH, W. UNTERBERGER, K. HAYEK, and B. KLÖTZER, *Surf. Sci.* **600**, 983 (2006).
- [174] P. KOSTELNIK, N. SERIANI, G. KRESSE, A. MIKKELSEN, E. LUNDGREN, V. BLUM, T. SIKOLA, P. VARGA, and M. SCHMID, *Surf. Sci.* **601**, 1574 (2007).

References

- [175] E. LUNDGREN, J. GUSTAFSON, A. MIKKELSEN, J. N. ANDERSEN, A. STIERLE, H. DOSCH, M. TODOROVA, J. ROGAL, K. REUTER, and M. SCHEFFLER, *Phys. Rev. Lett.* **92**, 046101 (2004).
- [176] B. L. M. HENDRIKSEN and J. W. M. FRENKEN, *Phys. Rev. Lett.* **89**, 046101 (2002).
- [177] B. L. M. HENDRIKSEN, S. C. BOBARU, and J. W. M. FRENKEN, *Surf. Sci.* **552**, 229 (2004).
- [178] F. GAO, Y. WANG, Y. CAI, and D. W. GOODMAN, *J. Phys. Chem. C* **113**, 174 (2009).
- [179] F. GAO, S. M. MCCLURE, Y. CAI, K. K. GATH, Y. WANG, M. . CHEN, Q. GUO, and D. W. GOODMAN, *Surf. Sci.* **603**, 65 (2009).
- [180] R. VAN RIJN, O. BALMES, R. FELICI, J. GUSTAFSON, D. WERMEILLE, R. WESTERSTRÖM, E. LUNDGREN, and J. W. M. FRENKEN, *J. Phys. Chem. C* **114**, 6875 (2010).
- [181] F. GAO, Y. WANG, and D. W. GOODMAN, *J. Phys. Chem. C* **114**, 6874 (2010).
- [182] M. CHEN, X. V. WANG, L. ZHANG, Z. TANG, and H. WAN, *Langmuir* **26**, 18113 (2010).
- [183] R. VAN RIJN, O. BALMES, A. RESTA, D. WERMEILLE, R. WESTERSTRÖM, J. GUSTAFSON, R. FELICI, E. LUNDGREN, and J. W. M. FRENKEN, *Phys. Chem. Chem. Phys.* **13**, (2011).
- [184] P. LEGARE, L. HILAIRE, G. MAIRE, G. KRILL, and A. AMAMOU, *Surf. Sci.* **107**, 533 (1981).
- [185] E. H. VOOGT, A. J. M. MENS, O. L. J. GIJZEMAN, and J. W. GEUS, *Surf. Sci.* **373**, 210 (1997).
- [186] G. KETTELER, D. F. OGLETREE, H. BLUHM, H. LIU, H. E. L. D., and M. SALMERON, *J. Am. Chem. Soc.* **127**, 18267 (2005).
- [187] J. R. MCBRIDE, K. C. HASS, and W. H. WEBER, *Phys. Rev. B* **44**, 5016 (1991).
- [188] R. WESTERSTRÖM, C. J. WESTSTRATE, J. GUSTAFSON, A. MIKKELSEN, J. SCHNADT, J. N. ANDERSEN, E. LUNDGREN, N. SERIANI, F. MITTENDORFER, G. KRESSE, and A. STIERLE, *Phys. Rev. B* **80**, 125431 (2009).
- [189] J. DICKE, H. H. ROTERMUND, and J. LAUTERBACH, *Surf. Sci.* **454-456**, 352 (2000).
- [190] W. X. LI, L. OESTERLUND, E. K. VESTERGAARD, R. T. VANG, J. MATTHIESEN, T. M. PEDERSEN, E. LAEGSGAARD, B. HAMMER, and F. BESENBACHER, *Phys. Rev. Lett.* **93**, 146104 (2004).
- [191] D. R. BUTCHER, M. E. GRASS, Z. ZENG, F. AKSOY, H. BLUHM, W.-X. LI, B. S. MUN, G. A. SOMORJAI, and Z. LIU, *J. Am. Chem. Soc.* **133**, 20319 (2011).
- [192] N. A. SALIBA, Y.-L. TSAI, C. PANJA, and B. E. KOEL, *Surf. Sci.* **419**, 79 (1999).
- [193] H.-J. FREUND and M. ROBERTS, *Surf. Sci. Rep.* **25**, 225 (1996).
- [194] P. R. NORTON, *Surf. Sci.* **44**, 624 (1974).

References

- [195] P. R. NORTON, *Surf. Sci.* **47**, 98 (1975).
- [196] F. SOLYMOSI and A. BERKO, *J. Catal.* **101**, 458 (1986).
- [197] Z. M. LIU, Y. ZHOU, F. SOLYMOSI, and J. M. WHITE, *J. Phys. Chem.* **93**, 4383 (1989).
- [198] T. ENGEL and G. ERTL, *J. Chem. Phys.* **69**, 1267 (1978).
- [199] T. ENGEL and G. ERTL, *Adv. Catal.* **28**, 1 (1979).
- [200] M. BÄR, C. ZÜLICHE, M. EISWIRTH, and G. ERTL, *J. Chem. Phys.* **96**, 8595 (1992).
- [201] V. P. ZHDANOV and B. KASEMO, *Surf. Sci. Rep.* **20**, 113 (1994).
- [202] M. BÄR, S. NETTESHEIM, H. H. ROTERMUND, M. EISWIRTH, and G. ERTL, *Phys. Rev. Lett.* **74**, 1246 (1995).
- [203] S. KARPITSCHKA, S. WEHNER, and J. KÜPPERS, *J. Chem. Phys.* **130**, 054706 (2009).
- [204] R. M. ZIFF, E. GULARI, and Y. BARSHAD, *Phys. Rev. Lett.* **56**, 2553 (1986).
- [205] S. VÖLKENING and J. WINTERLIN, *J. Chem. Phys.* **114**, 6382 (2001).
- [206] V. P. ZHDANOV, *Surf. Sci. Rep.* **45**, 231 (2002).
- [207] K. FICHTHORN, E. GULARI, and R. ZIFF, *Phys. Rev. Lett.* **63**, 1527 (1989).
- [208] Y. SUCHORSKI, J. BEBEN, E. W. JAMES, J. W. EVANS, and R. IMBIHL, *Phys. Rev. Lett.* **82**, 1907 (1999).
- [209] Y. SUCHORSKI, J. BEBEN, R. IMBIHL, E. W. JAMES, D.-J. LIU, and J. W. EVANS, *Phys. Rev. B* **63**, 165417 (2001).
- [210] V. P. ZHDANOV and B. KASEMO, *J. Statist. Phys.* **101**, 631 (2000).
- [211] K. REUTER and M. SCHEFFLER, *Phys. Rev. B* **73**, 045433 (2006).
- [212] J. ROGAL, K. REUTER, and M. SCHEFFLER, *Phys. Rev. Lett.* **98**, 046101 (2007).
- [213] Y. SUCHORSKI, R. WROBEL, S. BECKER, and H. WEISS, *J. Phys. Chem. C* **112**, 20012 (2008).
- [214] F. SCHLÖGL, *Z. Phys.* **248**, 446 (1971).
- [215] F. SCHLÖGL, *Z. Phys.* **253**, 147 (1972).
- [216] F. SCHLÖGL, *Ber. Bunsen-Ges. Phys. Chem.* **84**, 351 (1980).
- [217] Y. SUCHORSKI, R. IMBIHL, and V. K. MEDVEDEV, *Surf. Sci.* **401**, 392 (1998).
- [218] M. BERDAU, A. KARPOWICZ, G. G. YELENIN, K. CHRISTMANN, and J. H. BLOCK, *J. Chem. Phys.* **106**, 4291 (1997).

References

- [219] M. EHSASI, M. BERDAU, T. REBITZKI, K.-P. CHARLÉ, K. CHRISTMANN, and J. H. BLOCK, *J. Chem. Phys.* **98**, 9177 (1993).
- [220] M. BERDAU, G. G. YELENIN, A. KARPOWICZ, M. EHSASI, K. CHRISTMANN, and J. H. BLOCK, *J. Chem. Phys.* **110**, 11551 (1999).
- [221] G. ERTL, P. R. NORTON, and J. RÜSTIG, *Phys. Rev. Lett.* **49**, 177 (1982).
- [222] R. IMBIHL, M. P. COX, G. ERTL, H. MÜLLER, and W. BRENIG, *J. Chem. Phys.* **83**, 1578 (1985).
- [223] R. IMBIHL, M. P. COX, and G. ERTL, *J. Chem. Phys.* **84**, 3519 (1986).
- [224] K. KRISCHER, M. EISWIRTH, and G. ERTL, *J. Chem. Phys.* **96**, 9161 (1992).
- [225] J. LAUTERBACH and H. H. ROTERMUND, *Surf. Sci.* **311**, 231 (1994).
- [226] R. IMBIHL and G. ERTL, *Chem. Rev.* **95**, 697 (1995).
- [227] R. IMBIHL, *Surf. Sci.* **603**, 1671 (2009).
- [228] B. C. SALES, J. E. TURNER, and M. B. MAPLE, *Surf. Sci.* **114**, 381 (1982).
- [229] H. GABASCH, A. KNOP-GERICKE, R. SCHLÖGL, M. BORASIO, C. WEILACH, G. RUPPRECHTER, S. PENNER, B. JENEWEIN, K. HAYEK, and B. KLÖTZER, *Phys. Chem. Chem. Phys.* **9**, 533 (2006).
- [230] M. S. CHEN, Y. CAI, Z. YAN, K. K. GATH, S. AXNANDA, and D. W. GOODMAN, *Surf. Sci.* **601**, 5326 (2007).
- [231] K. ZORN, S. GIORGIO, E. HALWAX, C. R. HENRY, H. GRÖNBECK, and G. RUPPRECHTER, *J. Phys. Chem. C* **115**, 1103 (2011).
- [232] Y. B. HE, M. KNAPP, E. LUNDGREN, and H. OVER, *J. Phys. Chem. B* **109**, 21825 (2005).
- [233] M. D. ACKERMANN, T. M. PEDERSEN, B. L. M. HENDRIKSEN, O. ROBACH, S. C. BOBARU, I. POPA, C. QUIROS, H. KIM, B. HAMMER, S. FERRER, and J. W. M. FRENKEN, *Phys. Rev. Lett.* **95**, 255505 (2005).
- [234] F. GAO, M. LUNDWALL, and D. W. GOODMAN, *J. Phys. Chem. C* **112**, 6057 (2008).
- [235] T. SCHALOW, M. LAURIN, B. BRANDT, S. SCHAUERMANN, S. GUIMOND, H. KUHNENBECK, D. E. STARR, S. K. SHAIKHUTNIKOV, J. LIBUDA, and H.-J. FREUND, *Angew. Chem. Int. Ed.* **44**, 7601 (2005).
- [236] T. SCHALOW, B. BRANDT, M. LAURIN, S. SCHAUERMANN, J. LIBUDA, and H.-J. FREUND, *J. Catal.* **242**, 58 (2006).
- [237] B. BRANDT, T. SCHALOW, M. LAURIN, S. SCHAUERMANN, J. LIBUDA, and H.-J. FREUND, *J. Phys. Chem. C* **111**, 938 (2007).
- [238] P.-A. CARLSSON, V. P. ZHDANOV, and B. KASEMO, *Appl. Surf. Sci.* **239**, 424 (2005).

References

- [239] J. SINGH, E. M. C. ALAYON, M. TROMP, O. V. SAFONOVA, P. GLATZEL, M. NACHTEGAAL, R. FRAHM, and J. A. VAN BOKHOVEN, *Angew. Chem. Int. Ed.* **47**, 9260 (2008).
- [240] J. SINGH, M. TROMP, O. V. SAFONOVA, P. GLATZEL, and J. A. VAN BOKHOVEN, *Catal. Today* **145**, 300 (2009).
- [241] Y. SUCHORSKI, J. BEBEN, and R. IMBIHL, *Prog. Surf. Sci.* **59**, 343 (1998).
- [242] J. LAUTERBACH and H. H. ROTERMUND, *Catal. Lett.* **27**, 27 (1994).
- [243] M. P. COX, G. ERTL, R. IMBIHL, and J. RÜSTIG, *Surf. Sci.* **134**, L517 (1983).
- [244] H. H. ROTERMUND, S. JAKUBITH, A. VON OERTZEN, and G. ERTL, *J. Chem. Phys.* **91**, 4942 (1989).
- [245] A. VON OERTZEN, H. H. ROTERMUND, S. JAKUBITH, and G. ERTL, *Ultramicroscopy* **36**, 107 (1991).
- [246] B. RAUSENBERGER, W. SWIECH, W. ENGEL, A. M. BRADSHAW, and E. ZEITLER, *Surf. Sci.* **287-288**, 235 (1993).
- [247] B. RAUSENBERGER, W. SWIECH, C. S. RASTOMJEE, M. MUNDSCHAU, W. ENGEL, E. ZEITLER, and A. M. BRADSHAW, *Chem. Phys. Lett.* **215**, 109 (1993).
- [248] W. SWIECH, B. RAUSENBERGER, W. ENGEL, A. M. BRADSHAW, and E. ZEITLER, *Surf. Sci.* **294**, 297 (1993).
- [249] W. SWIECH, C. S. RASTOMJEE, R. IMBIHL, J. W. EVANS, B. RAUSENBERGER, W. ENGEL, A. K. SCHMID, A. M. BRADSHAW, and E. ZEITLER, *Surf. Sci.* **307-309**, 138 (1994).
- [250] H. H. ROTERMUND, J. LAUTERBACH, and G. HAAS, *Appl. Phys. A* **57**, 507 (1993).
- [251] Y. UCHIDA, G. LEHMPFUHL, and R. IMBIHL, *Surf. Sci.* **234**, 27 (1990).
- [252] H. WEI, G. LILIENKAMP, and R. IMBIHL, *Chem. Phys. Lett.* **389**, 284 (2004).
- [253] Y. SUCHORSKI, C. SPIEL, D. VOGEL, W. DRACHSEL, R. SCHLÖGL, and G. RUPPRECHTER, *ChemPhysChem* **11**, 3231 (2010).
- [254] C. SPIEL, D. VOGEL, Y. SUCHORSKI, W. DRACHSEL, R. SCHLÖGL, and G. RUPPRECHTER, *Catal. Lett.* **141**, 625 (2011).
- [255] V. GORODETSKII, J. LAUTERBACH, H.-H. ROTERMUND, J. H. BLOCK, and G. ERTL, *Nature* **370**, 276 (1994).
- [256] M. EHSASI, O. FRANK, J. H. BLOCK, and K. CHRISTMANN, *Chem. Phys. Lett.* **165**, 115 (1990).
- [257] M. SANDER, R. IMBIHL, and G. ERTL, *J. Chem. Phys.* **97**, 5193 (1992).
- [258] S. Y. YAMAMOTO, C. M. SURKO, and M. B. MAPLE, *J. Chem. Phys.* **103**, 8209 (1995).
- [259] M. M. SLINKO, A. A. UKHARSKII, and N. I. JAEGER, *Phys. Chem. Chem. Phys.* **3**, 1015 (2001).

References

- [260] C. SPIEL, *PEEM microscopy and DFT calculations of catalytically active platinum surfaces and interfaces*, PhD thesis, Vienna University of Technology, 2012.
- [261] A. VON OERTZEN, H. H. ROTERMUND, and S. NETTESHEIM, *Surf. Sci.* **311**, 322 (1994).
- [262] R. LUTHER, *Z. Elektrochem.* **12**, 596 (1906).
- [263] Y. SUCHORSKI, J. BEBEN, and R. IMBIHL, *Ultramicroscopy* **73**, 67 (1998).
- [264] C. GONG, K. HUANG, B. DENG, and X. LIU, *Energy* **36**, 53 (2011).
- [265] D. A. FRANK-KAMENETSKII, *Diffusion and heat transfer in chemical kinetics*, Plenum, New York, 2nd edition, 1969.
- [266] M. RINNEMO, D. KULGINOV, S. JOHANSSON, K. L. WONG, V. P. ZHDANOV, and B. KASEMO, *Surf. Sci.* **376**, 297 (1997).
- [267] G. EIGENBERGER, *Chem. Eng. Sci.* **33**, 1255 (1978).
- [268] M. BOWKER, I. Z. JONES, R. A. BENNETT, F. ESCH, A. BARALDI, S. LIZZIT, and G. COMELLI, *Catal. Lett.* **51**, 187 (1998).
- [269] R. A. BENNETT, I. Z. JONES, and M. BOWKER, *Top. Catal.* **42-43**, 373 (2007).
- [270] A. S. MIKHAILOV, *Foundations of Synergetics*, Springer, Berlin, 1990.
- [271] D. VOGEL, C. SPIEL, Y. SUCHORSKI, A. URICH, R. SCHLÖGL, and G. RUPPRECHTER, *Surf. Sci.* **605**, 1999 (2011).
- [272] J. J. MORTENSEN, L. B. HANSEN, and K. W. JACOBSEN, *Phys. Rev. B* **71**, 035109 (2005).
- [273] <https://wiki.fysik.dtu.dk/gpaw>.
- [274] P. E. BLÖCHL, *Phys. Rev. B* **50**, 17953 (1994).
- [275] J. P. PERDEW, K. BURKE, and M. ERNZERHOF, *Phys. Rev. Lett.* **77**, 3865 (1996).
- [276] H. J. MONKHORST and J. D. PACK, *Phys. Rev. B* **13**, 5188 (1976).
- [277] J. D. PACK and H. J. MONKHORST, *Phys. Rev. B* **16**, 1748 (1977).
- [278] G. HENKELMAN, B. P. UBERUAGA, and H. JONSSON, *J. Chem. Phys.* **113**, 9901 (2000).
- [279] P.-A. CARLSSON, M. SKOGLUNDH, P. THORMÄHLEN, and B. ANDERSSON, *Top. Catal.* **30-31**, 375 (2004).
- [280] H. S. TAYLOR, *Proc. R. Soc. London, Ser. A* **108**, 105 (1925).
- [281] J. K. NORSKOV, T. BLIGAARD, B. HVOLBAEK, F. ABILD-PEDERSEN, I. CHORKENDORFF, and C. H. CHRISTENSEN, *Chem. Soc. Rev.* **37**, 2163 (2008).

References

- [282] J. T. YATES, *J. Vac. Sci. Technol. A* **13**, 1359 (1995).
- [283] T. ZAMBELLI, J. WINTTERLIN, J. TROST, and G. ERTL, *Science* **273**, 1688 (1996).
- [284] K. WANDELT, *Surf. Sci.* **251-252**, 387 (1991).
- [285] R. T. VANG, K. HONKALA, S. DAHL, E. K. VESTERGAARD, J. SCHNADT, E. LAEGSGAARD, B. S. CLAUSEN, J. K. NORSKOV, and F. BESENBACHER, *Nat. Mater.* **4**, 160 (2005).
- [286] B. HAMMER, O. NIELSEN, and J. NORSKOV, *Catal. Lett.* **46**, 31 (1997).
- [287] P. J. BERLOWITZ, C. H. F. PEDEN, and D. W. GOODMAN, *J. Phys. Chem.* **92**, 5213 (1988).
- [288] C. J. ZHANG and P. HU, *J. Am. Chem. Soc.* **123**, 1166 (2001).
- [289] J. SZANYI and D. W. GOODMAN, *J. Phys. Chem.* **98**, 2972 (1994).
- [290] J. SZANYI, W. K. KUHN, and D. W. GOODMAN, *J. Phys. Chem.* **98**, 2978 (1994).
- [291] A. K. SANTRA and D. W. GOODMAN, *Electrochim. Acta* **47**, 3595 (2002).
- [292] Y. LI, Q. LIU, and W. SHEN, *Dalton Trans.* **40**, 5811 (2011).
- [293] R. WANG, H. HE, L.-C. LIU, H.-X. DAI, and Z. ZHAO, *Catal. Sci. Technol.* **2**, 575 (2012).
- [294] P. HAN, S. AXNANDA, I. LYUBINETSKY, and D. W. GOODMAN, *J. Am. Chem. Soc.* **129**, 14355 (2007).
- [295] J. XU and J. T. YATES, *J. Chem. Phys.* **99**, 725 (1993).
- [296] J. G. WANG, W. X. LI, M. BORG, J. GUSTAFSON, A. MIKKELSEN, T. M. PEDERSEN, E. LUNDGREN, J. WEISSENRIEDER, J. KLIKOVITS, M. SCHMID, B. HAMMER, and J. N. ANDERSEN, *Phys. Rev. Lett.* **95**, 256102 (2005).
- [297] R. CASTELL, S. REIFF, W. DRACHSEL, and J. BLOCK, *Surf. Sci.* **377-379**, 770 (1997).
- [298] J. KLIKOVITS, M. SCHMID, J. GUSTAFSON, A. MIKKELSEN, A. RESTA, E. LUNDGREN, J. N. ANDERSEN, and P. VARGA, *J. Phys. Chem. B* **110**, 9966 (2006).
- [299] Y. ZHANG, J. ROGAL, and K. REUTER, *Phys. Rev. B* **74**, 125414 (2006).
- [300] R. WESTERSTRÖM, J. GUSTAFSON, A. RESTA, A. MIKKELSEN, J. N. ANDERSEN, E. LUNDGREN, N. SERIANI, F. MITTENDORFER, M. SCHMID, J. KLIKOVITS, P. VARGA, M. D. ACKERMANN, J. W. M. FRENKEN, N. KASPER, and A. STIERLE, *Phys. Rev. B* **76**, 155410 (2007).
- [301] I. V. YUDANOV, R. SAHNOUN, K. M. NEYMAN, N. RÖSCH, J. HOFFMANN, S. SCHAUERMANN, V. JOHANEK, H. UNTERHALT, G. RUPPRECHTER, J. LIBUDA, and H.-J. FREUND, *J. Phys. Chem. B* **107**, 255 (2003).
- [302] R. RAMSIER, K.-W. LEE, and J. YATES JR., *Surf. Sci.* **322**, 243 (1995).
- [303] M. SANDER, R. IMBIHL, R. SCHUSTER, J. V. BARTH, and G. ERTL, *Surf. Sci.* **271**, 159 (1992).

References

- [304] Y. SUCHORSKI and W. DRACHSEL, *Top. Catal.* **46**, 201 (2007).
- [305] D. GOODMAN, C. PEDEN, and M. CHEN, *Surf. Sci.* **601**, L124 (2007).
- [306] F. GAO, Y. CAI, K. K. GATH, Y. WANG, M. S. CHEN, Q. L. GUO, and D. W. GOODMAN, *J. Phys. Chem. C* **113**, 182 (2009).
- [307] G. RUPPRECHTER and C. WEILACH, *J. Phys.: Condens. Matter* **20**, 184019 (2008).
- [308] Y. SUCHORSKI, R. WROBEL, S. BECKER, B. STRZELCZYK, W. DRACHSEL, and H. WEISS, *Surf. Sci.* **601**, 4843 (2007).
- [309] S. BADER, L. RICHTER, and T. ORENT, *Surf. Sci.* **115**, 501 (1982).
- [310] <http://srdata.nist.gov/xps/>.
- [311] B. E. DEAL and A. S. GROVE, *J. Appl. Phys.* **36**, 3770 (1965).
- [312] K. SEKINE, Y. SAITO, M. HIRAYAMA, and T. OHMI, *IEEE T. Electron Dev.* **48**, 1550 (2001).
- [313] K. SAITO, Y. JIN, T. ONO, and M. SHIMADA, *Jpn. J. Appl. Phys.* **43**, L765 (2004).
- [314] M. SALMERON and G. A. SOMORJAI, *J. Vac. Sci. Technol.* **19**, 722 (1981).
- [315] H. P. BONZEL, A. M. FRANKEN, and G. PIRUG, *Surf. Sci.* **104**, 625 (1981).
- [316] H. NIEHUS and G. COMSA, *Surf. Sci.* **102**, L14 (1981).
- [317] V. MEDVEDEV, Y. SUCHORSKI, and J. BLOCK, *Appl. Surf. Sci.* **94-95**, 200 (1996).
- [318] H. MARBACH, S. GÜNTHER, B. LUERSSEN, L. GREGORATTI, M. KISKINOVA, and R. IMBIHL, *Catal. Lett.* **83**, 161 (2002).
- [319] H. MARBACH, G. LILIENKAMP, H. WEI, S. GUNTHER, Y. SUCHORSKI, and R. IMBIHL, *Phys. Chem. Chem. Phys.* **5**, 2730 (2003).
- [320] A. G. NAUMOVETS, *The Chemical Physics of Solid Surfaces*, volume 7, Elsevier, Amsterdam, 1994.
- [321] I. LYUKSYUTOV, A. G. NAUMOVETS, and V. POKROVSKY, *Two-Dimensional Crystals*, Academic Press, Boston, 1992.
- [322] D. C. KERSHNER, M. P. HYMAN, and J. W. MEDLIN, *Surf. Sci.* **602**, 3603 (2008).
- [323] C. KLEIN, G. KRESSE, S. SURNEV, F. P. NETZER, M. SCHMID, and P. VARGA, *Phys. Rev. B* **68**, 235416 (2003).
- [324] J. BLOMQVIST, L. LEHMAN, and P. SALO, *Phys. Status Solidi B* **249**, 1046 (2012).
- [325] Y. SUCHORSKI, L. RIHKO-STRUCKMANN, F. KLOSE, Y. YE, M. ALANDJIYSKA, K. SUNDMACHER, and H. WEISS, *Appl. Surf. Sci.* **249**, 231 (2005).

PUBLICATIONS

Journal articles

1. D. Vogel, C. Spiel, Y. Suchorski, A. Trinchero, R. Schlögl, H. Grönbeck, G. Rupprechter:
"Local catalytic ignition during CO oxidation on low-index Pt and Pd surfaces: a combined PEEM, MS and DFT study",
Angew. Chem. Int. Ed. **51**, 10041 (2012).
2. D. Vogel, C. Spiel, Y. Suchorski, A. Trinchero, R. Schlögl, H. Grönbeck, G. Rupprechter:
"Lokale katalytische Zündung der CO Oxidation auf individuellen niedrig-indizierten Pt und Pd Oberflächen: Kombinierte PEEM, MS und DFT Untersuchungen",
Angew. Chem. **124**, 10185 (2012).
3. D. Vogel, Z. Budinska, Y. Suchorski, C. Spiel, R. Schlögl, G. Rupprechter:
"Silicon oxide surface segregation in CO oxidation on Pd: an in situ PEEM, MS and XPS study",
submitted to *Appl. Surf. Sci.* (2012).
4. D. Vogel, C. Spiel, Y. Suchorski, M. Schmid, M. Stöger-Pollach, R. Schlögl, G. Rupprechter:
"Role of defects in the local reaction kinetics in CO oxidation on low-index Pd surfaces: a PEEM, STM and MS study",
to be submitted (2012).
5. D. Vogel, C. Spiel, Y. Suchorski, R. Schlögl, G. Rupprechter:
"Isobar kinetic transitions in the CO oxidation reaction on Pt: from the mesoscopic to the nanoscale",
in preparation (2012).
6. D. Vogel, C. Spiel, Y. Suchorski, R. Schlögl, G. Rupprechter:
"Local reaction kinetics in catalytic CO oxidation on low-index Pt and Pd surfaces",
Proceedings of the 11th Pannonian International Symposium on Catalysis **1**, 191 (2012).

Publications

7. D. Vogel, C. Spiel, Y. Suchorski, A. Urich, R. Schlögl, G. Rupprechter:
"Mapping the local reaction kinetics by PEEM: CO oxidation on individual (100)-type grains of Pt foil",
Surf. Sci. **605**, 1999 (2011).
8. C. Spiel, D. Vogel, Y. Suchorski, W. Drachsel, R. Schlögl, G. Rupprechter:
"Catalytic CO oxidation on Individual (110) Domains of a Polycrystalline Pt Foil: Local Reaction Kinetics by PEEM",
Catal. Lett. **141**, 625 (2011).
9. Y. Suchorski, C. Spiel, D. Vogel, W. Drachsel, R. Schlögl, G. Rupprechter:
"Local Reaction Kinetics by Imaging: CO Oxidation on Polycrystalline Platinum",
ChemPhysChem **11**, 3231 (2010).
10. C. Spiel, D. Vogel, Y. Suchorski, W. Drachsel, R. Schlögl, G. Rupprechter:
"Catalytic CO oxidation on individual (110) domains of a polycrystalline Pt foil: bistability and reaction front propagation",
Proceedings of the 10th Pannonian International Symposium on Catalysis **1**, 13 (2010).

Conference contributions

1. D. Vogel:
"Local ignition and role of defects in catalytic CO oxidation on low-index Pt and Pd surfaces"
Presentation: PhD Day, Department of Inorganic Chemistry, Fritz-Haber-Institut Berlin, Berlin, Germany, 18.09. - 19.09.2012.
2. D. Vogel, C. Spiel, Y. Suchorski, R. Schlögl, G. Rupprechter:
"Local reaction kinetics in catalytic CO oxidation on low-index Pt and Pd surfaces"
Poster: 11th Pannonian International Symposium on Catalysis, Obergurgl, Austria, 03.09. - 07.09.2012.
3. D. Vogel, C. Spiel, Y. Suchorski, R. Schlögl, G. Rupprechter:
"Local light-off and role of defects in catalytic CO oxidation on low-index Pt and Pd surfaces"
Presentation: 15th Palladium Day, Bad Schandau, Germany, 27.08.2012.
4. Y. Suchorski, D. Vogel, C. Spiel, R. Schlögl, G. Rupprechter:
"Increasing the complexity in CO oxidation on Pd: from micrograins via nanotips to powders"
Presentation: 15th Palladium Day, Bad Schandau, Germany, 27.08.2012.
5. Y. Suchorski, C. Spiel, D. Vogel, R. Schlögl, G. Rupprechter:
"Kinetic transitions and light-off in catalytic CO oxidation on Pt: from mesoscopic to nanoscale"
Presentation: 3S'12 25. Symposium on Surface Science 2012, St. Christoph am Arlberg, Austria, 11.03. - 17.03.2012.
6. D. Vogel, C. Spiel, Y. Suchorski, R. Schlögl, G. Rupprechter:
"CO oxidation on individual grains of polycrystalline Pd: Laterally-resolved reaction kinetics by PEEM"
Poster: 3S'10, 25. Symposium on Surface Science 2012, St. Christoph am Arlberg, Austria, 11.03. - 17.03.2012.
7. D. Vogel, C. Spiel, Y. Suchorski, R. Schlögl, G. Rupprechter:
"Comparison of μm -sized Pd(hkl) and Pt(hkl) domains in CO oxidation: bistability, catalytic ignition, kinetic phase diagrams"
Presentation: 14th Palladium Day, Berlin, Germany, 09.02.2012.
8. D. Vogel:
"Local reaction kinetics and catalytic light-off in CO oxidation on individual grains of Pd foil"
Presentation: Seminar of the doctoral program "Functional Matter", Vienna, Austria, 05.01.2012.
9. D. Vogel, C. Spiel, Y. Suchorski, R. Schlögl, G. Rupprechter:
"CO oxidation on a mesoscopic scale: from individual μm -sized Pd grains to oxides"
Presentation: 13th Palladium Day, Obergurgl, Austria; 04.10. - 05.10.2011.

Publications

10. D. Vogel, C. Spiel, R. Schlögl, G. Rupprechter:
"Catalytic CO oxidation on individual μm -sized grains of a polycrystalline palladium foil"
Poster: SFB "Functional Oxide Surfaces and Interfaces" (FOXSI) 1st Kick-off Meeting, Vienna, Austria, 22.09. - 23.09.2011.
11. C. Spiel, D. Vogel, Y. Suchorski, R. Schlögl, G. Rupprechter:
"Laterally-resolved kinetics of catalytic CO oxidation: from mesoscopic to nano-scale"
Presentation: 5th International Workshop on Surface Physics, Ladek Zdroj, Poland, 02.09. - 05.09.2011.
12. C. Spiel, D. Vogel, Y. Suchorski, A. Urich, R. Schlögl, G. Rupprechter:
"Reaction-diffusion fronts in catalytic CO oxidation on μm -sized Pt(110) and Pt(100) domains: a comparative PEEM study"
Poster: 5th International Workshop on Surface Physics, Ladek Zdroj, Poland; 02.09. - 05.09.2011.
13. Y. Suchorski, C. Spiel, D. Vogel, R. Schlögl, G. Rupprechter:
"Laterally-resolved reaction kinetics by PEEM"
Presentation: 28th European Conference on Surface Science ECOS28, Wroclaw, Poland, 28.08. - 02.09.2011.
14. D. Vogel, C. Spiel, Y. Suchorski, R. Schlögl, G. Rupprechter:
"From single crystal surfaces via defects to surface oxides: Catalytic CO oxidation on an individual μm -sized Pd(110) domain"
Poster: 28th European Conference on Surface Science ECOS28, Wroclaw, Poland, 28.08. - 02.09.2011.
15. D. Vogel:
"Local reaction kinetics and catalytic light-off in CO oxidation on polycrystalline Pd foil"
Presentation: PhD Day, Department of Inorganic Chemistry, Fritz-Haber-Institut Berlin, Berlin, Germany, 24.08. - 25.08.2011.
16. D. Vogel:
"Local reaction kinetics of catalytic CO oxidation on individual grains of Pd foil"
Presentation: Seminar of the doctoral program "Functional Matter", Vienna, Austria, 05.05.2011.
17. D. Vogel, C. Spiel, Y. Suchorski, R. Schlögl, G. Rupprechter: *"Locally resolved reaction kinetics: CO oxidation on individual grains of a polycrystalline platinum foil"*
Poster: 7th Brazilian/German Workshop on Applied Surface Science, Buzios, Brazil, 03.04. - 08.04.2011.
18. D. Vogel:
"PEEM monitoring of reaction fronts in catalytic CO oxidation on individual grains of Pt and Pd foil"
Presentation: PhD Day, Department of Inorganic Chemistry, Fritz-Haber-Institut Berlin, Berlin, Germany, 30.03. - 31.03.2011.

Publications

19. D. Vogel, C. Spiel, Y. Suchorski, R. Schlögl, G. Rupprechter:
"Locally Resolved Study of CO Oxidation on Polycrystalline Pd: Reaction Kinetics and Surface Morphology"
Presentation: 12th Palladium Day, Berlin, Germany, 21.03. - 22.03.2011.
20. D. Vogel:
"Influence of the surface morphology on local reaction kinetics in catalytic CO oxidation on Pt and Pd foil"
Presentation: Seminar of the doctoral program "Functional Matter", Vienna, Austria, 09.11.2010.
21. D. Vogel:
"Surface morphology of individual grains and local reaction kinetics in catalytic CO oxidation on Pt and Pd foil"
Presentation: PhD Day, Department of Inorganic Chemistry, Fritz-Haber-Institut Berlin, Berlin, Germany, 28.10. - 29.10.2010.
22. Y. Suchorski, C. Spiel, D. Vogel, W. Drachsel, R. Schlögl, G. Rupprechter:
"Reaction Kinetics via PEEM Imaging: Laterally-Resolved Studies of Catalytic CO Oxidation on Single Grains of Polycrystalline Pd"
Presentation: 60th Annual Meeting of Austrian Physical Society, Salzburg, Austria, 06.09. - 10.09.2010.
23. C. Spiel, D. Vogel, Y. Suchorski, W. Drachsel, R. Schlögl, G. Rupprechter:
"Catalytic CO oxidation on individual (110) domains of a polycrystalline Pt foil: bistability and reaction front propagation"
Presentation: 10th Pannonian International Symposium on Catalysis, Krakow, Poland, 29.08. - 02.09.2010.
24. C. Spiel, D. Vogel, Y. Suchorski, W. Drachsel, R. Schlögl, G. Rupprechter:
"Catalytic CO Oxidation on Polycrystalline Palladium: Local Reaction Kinetics by PEEM"
Poster: International Symposia on Advancing the Chemical Sciences (ISACS), Budapest, Hungary, 13.07. - 16.07.2010.
25. Y. Suchorski, C. Spiel, D. Vogel, W. Drachsel, R. Schlögl, G. Rupprechter:
"Laterally-resolved reaction kinetics: PEEM microscopy of catalytic CO oxidation on polycrystalline Pt"
Presentation: International Workshop - In situ characterization of near-surface processes, Eisenerz, Austria, 30.05. - 03.06.2010.
26. D. Vogel:
"CO oxidation on individual grains of polycrystalline Pt and Pd: Locally resolved reaction kinetics"
Presentation: Seminar of the doctoral program "Functional Matter", Vienna, Austria, 25.05.2010.
27. D. Vogel, C. Spiel, Y. Suchorski, W. Drachsel, R. Schlögl, G. Rupprechter:
"CO oxidation on individual grains of polycrystalline Pt and Pd: Locally resolved reaction kinetics"
Presentation: 10th Palladium Day, Berlin, Germany, 18.05. - 19.05.2010.

Publications

28. D. Vogel:
"Local reaction kinetics on individual grains of polycrystalline materials: CO oxidation on Pt and Pd"
Presentation: PhD Day, Department of Inorganic Chemistry, Fritz-Haber-Institut Berlin, Berlin, Germany, 03.05. - 04.05.2010.
29. D. Vogel, C. Spiel, Y. Suchorski, W. Drachsel, R. Schlögl, G. Rupprechter:
"Locally resolved kinetics of catalytic CO oxidation on polycrystalline platinum"
Poster: Junior Scientist Conference 2010, Vienna, Austria, 07.04. - 09.04.2010.
30. D. Vogel, C. Spiel, Y. Suchorski, W. Drachsel, R. Schlögl, G. Rupprechter:
"Locally resolved kinetics of catalytic CO oxidation on polycrystalline platinum"
Poster: DPG-Frühjahrstagung der Sektion Kondensierte Materie, Regensburg, Germany, 22.03. - 26.03.2010.
31. Y. Suchorski, C. Spiel, D. Vogel, W. Drachsel, R. Schlögl, G. Rupprechter:
"Visualizing local reaction kinetics: PEEM studies of catalytic CO oxidation on polycrystalline Pt"
Presentation: Workgroup Meeting of COST D41 "Inorganic oxides: Surfaces and Interfaces", Munich, Germany, 18.03. - 19.03.2010.
32. Y. Suchorski, C. Spiel, D. Vogel, W. Drachsel, R. Schlögl, G. Rupprechter:
"Laterally-resolved reaction kinetics: PEEM microscopy of catalytic CO oxidation on polycrystalline Pt"
Presentation: 3S'10, 23. Symposium on Surface Science 2010, St. Christoph/Arlberg, Austria, 07.03. - 13.03.2010.
33. D. Vogel:
"In situ visualization of a catalytic reaction: CO oxidation on polycrystalline Pt"
Presentation: Seminar of the doctoral program "Functional Matter", Vienna, Austria, 11.12.2009.
34. D. Vogel:
"Beyond single crystals: PEEM study of catalytic CO oxidation on polycrystalline Pt"
Presentation: PhD Day, Department of Inorganic Chemistry, Fritz-Haber-Institut Berlin, Berlin, Germany, 27.10. - 28.10.2009.
35. D. Vogel, C. Spiel, Y. Suchorski, W. Drachsel, R. Schlögl, G. Rupprechter:
"PEEM microscopy of catalytic CO oxidation on polycrystalline Pt"
Presentation: 9th Palladium Day, Vienna, Austria, 19.10. - 20.10.2009.
36. Y. Suchorski, W. Drachsel, C. Spiel, D. Vogel, R. Schlögl, G. Rupprechter:
"Along the complexity axis in catalytic CO oxidation on Pt: single crystal, polycrystalline foil, model of a catalytic particle"
Poster: ÖPG, SPS, ÖGA Joint annual Meeting, Innsbruck, Austria, 02.09. - 04.09.2009.
37. C. Spiel, D. Vogel, Y. Suchorski, W. Drachsel, R. Schlögl, G. Rupprechter:
"From single crystals to domain systems: catalytic CO oxidation on Pt"
Presentation: 13th Austrian Chemistry Days 2009, Joint Meeting of the Czech, Slovak & Austrian Chemical Societies, Vienna, Austria, 24.08. - 27.08.2009.

Publications

38. D. Vogel:

"Along the complexity axis in catalytic CO oxidation on Pt: Single crystal, polycrystalline foil, model of a catalytic particle"

Presentation: PhD Day, Department of Inorganic Chemistry, Fritz-Haber-Institut Berlin, Berlin, Germany, 29.04. - 30.04.2009.

CURRICULUM VITAE

Personal Details

Full name: Diana Vogel
Date and place of birth: September 30th, 1982, Moscow, Russia
Citizenship: German
Address: Rueppgasse 27/15, 1020 Wien, Austria
E-mail: diana.vogel@imc.tuwien.ac.at

Education

01/2009-10/2012 PhD studies at the Institute of Materials Chemistry, Vienna University of Technology, Austria;
Supervisors: Prof. G. Rupprechter and Prof. Y. Suchorski;
PhD grant of the Max-Planck-Society (Fritz-Haber-Institute Berlin, Dept. of Inorganic Chemistry, Prof. Robert Schlögl).

10/2008 Dipl.-Phys., University of Heidelberg, Germany;
Thesis title: "Schwingungsspektroskopische Untersuchung der rauen Cu(111)-Oberfläche".

09/2005-06/2006 Studies in Physics at the Saint Petersburg State University, Russia.

10/2002-10/2008 Studies in Physics at the University of Heidelberg, Germany.